Dissertation

submitted to the

Combined Faculty of Mathematics, Engineering and Natural Sciences

of

Heidelberg University, Germany

for the degree of

Doctor of Natural Sciences

Put forward by

Marvin Harald Knapp

born in: Mannheim, Germany

Oral examination: May 28, 2024

Ground-Based Imaging of Carbon Dioxide and Methane Emission Plumes

Referees: Prof. Dr. André Butz
Prof. Dr. Norbert Frank

Abstract

This study presents ground-based imaging of carbon dioxide (CO_2) and methane (CH_4) plumes to derive emission estimates of localized sources. Employing a stationary spectral camera enables rapid scene scanning at approximately one-minute intervals, capturing sky-scattered sunlight in the shortwave infrared spectral range. The developed processing pipeline converts raw hyperspectral data into emission estimates, utilizing an adapted matched filter retrieval for quantifying atmospheric enhancements in CO_2 and CH_4 plumes. The technique facilitates high-frequency imaging of individual sources, thereby complementing existing greenhouse gas monitoring methods like satellite snapshot images.

Field campaigns at point sources of CO_2 and CH_4 show the method's capability. Observing coal mining emissions demonstrates the detection and quantification of CH_4 plumes in single scans, even under challenging conditions. Emission estimates obtained through mass balance methods provide sub-hourly temporal resolution. They reveal considerable diurnal (up to 55 %) and day-to-day (1.56 $tCH_4\ h^{-1}$ to 4.57 $tCH_4\ h^{-1}$) source variability, emphasizing the added value of high-frequent emission monitoring. A proof-of-concept study at a coal-fired power plant provides the first ground-based imaging observations of CO_2 plumes. CO_2 emission estimates require hourly-averaged measurements and a specifically designed observation forward model. The retrieved emissions show reasonable agreement with validation data under favorable conditions, following the power plant's temporal variability and averaging 84 % of the expected emissions with a mean relative uncertainty of 24 %.

Kurzfassung

Diese Arbeit präsentiert bodengestützte Bildgebung von Kohlendioxid- (CO_2) und Methanfahnen (CH_4) zur Ableitung von Emissionsschätzungen von lokalisierten Quellen. Der Einsatz einer stationären Spektralkamera ermöglicht ein schnelles Scannen der Szene in etwa einminütigen Intervallen, wobei das vom Himmel gestreute Sonnenlicht im kurzwelligen Infrarot-Spektralbereich erfasst wird. Die entwickelte Verarbeitungskette wandelt hyperspektrale Rohdaten in Emissionsschätzungen um, wobei ein angepasster Optimalfilter zur Quantifizierung atmosphärischer Überhöhungen in CO_2- und CH_4-Fahnen verwendet wird. Die Technik ermöglicht die hochfrequente Abbildung einzelner Quellen und ergänzt damit die bestehenden Überwachungsmöglichkeiten für Treibhausgasemissionen wie Schnappschussaufnahmen von Satelliten.

Feldkampagnen an Punktquellen von CO_2 und CH_4 zeigen die Fähigkeit der Methode. Beobachtungen von Emissionen aus dem Kohleabbau demonstrieren die Erkennung und Quantifizierung von CH_4-Fahnen in Einzelaufnahmen, selbst unter herausfordernden Bedingungen. Emissionsschätzungen aus Massenbilanz-Methoden bieten eine zeitliche Auflösung von weniger als einer Stunde. Sie zeigen erhebliche tägliche (bis zu 55 %) und Tag-zu-Tag (1,56 $tCH_4\ h^{-1}$ bis zu 4,57 $tCH_4\ h^{-1}$) Quellvariabilität, was den zusätzlichen Nutzen einer hochfrequenten Emissionsüberwachung unterstreicht. Eine Machbarkeitsstudie an einem Kohlekraftwerk lieferte die ersten bodengestützten abbildenden Beobachtungen von CO_2-Abgasfahnen. Die CO_2 Emissionsschätzungen benötigen stündlich gemittelten Messungen und eine speziell entwickelten Vorwärtsmodellierung der Beobachtung. Die ermittelten Emissionen zeigen vernünftige Übereinstimmung mit Validierungsdaten unter günstigen Bedingungen und liegen im Durchschnitt bei 84 % der erwarteten Emissionen mit einer mittleren relativen Unsicherheit von 24 %.

Publications

- **Knapp, M.**, Kleinschek, R., Vardag, S.N., Külheim, F., Haveresch, H., Sindram, M., Siegel, T., Burger, B., Butz, A., 2023. Quantitative imaging of carbon dioxide plumes using a ground-based shortwave infrared spectral camera (accepted). Atmospheric Measurement Techniques. https://doi.org/10.5194/egusphere-2023-1857

  Author Contributions: MK performed the observations, adapted the retrieval algorithm, developed the plume model and the inversion scheme, and wrote the manuscript. RK helped with the instrumental characterization and deployment. SV gave advice on the plume model and inversion scheme. FK, HH, MS, and TS helped with the observations and the retrieval algorithm. MS implemented the AHRS system. BB provided data of the Fraunhofer-Institut für Solare Energiesysteme (ISE). AB developed the research question, supervised the project, and helped with the manuscript.

- **Knapp, M.**, Scheidweiler, L., Külheim, F., Kleinschek, R., Necki, J., Jagoda, P., Butz, A., 2023. Spectrometric imaging of sub-hourly methane emission dynamics from coal mine ventilation. Environ. Res. Lett. 18, 044030. https://doi.org/10.1088/1748-9326/acc346

  Author Contributions: MK developed and performed the evaluation. MK, LS, and FK performed the field measurements in Poland. PJ supported the field observations with real-time in-situ measurements. RK helped to maintain and develop the measurement architecture. JN contributed to the campaign planning and advised the team in Poland with crucial insights in local methane emissions from coal mining operations. AB developed the research question, supervised the project, and helped with the manuscript.

Contents

List of Figures

List of Tables

1 Introduction

The Industrial Revolution initiated an ongoing period of rapid global warming. The most recent Intergovernmental Panel on Climate Change (IPCC) report states: "It is unequivocal that human influence has warmed the atmosphere, ocean, and land. Widespread and rapid changes in the atmosphere, ocean, cryosphere, and biosphere have occurred." (IPCC, 2023, Summary A.1). This anthropogenic climate change is already severely impacting the environment, ecosystems, and human societies (e.g., Collins et al., 2010; Lenton et al., 2023; Flores et al., 2024; Van Westen et al., 2024). Therefore, the signatory countries of the United Nations Framework Convention on Climate Change (UNFCCC) pledged to keep global warming well below 1.5 °C compared to the 1850 - 1900 reference period in the Paris Agreement (UNFCCC, 2015). Figure 1.1 summarizes the drivers and their contributions to the observed global warming following IPCC (2023). It unambiguously identifies well-mixed greenhouse gases (GHGs) as the main driver of the ongoing climate change (see Figure 1.1b). Consequently, parties of the UNFCCC agreed to ambitious goals for reducing anthropogenic GHG emissions. A stock-taking mechanism is in place to monitor the progress of the efforts, which relies on operational emission Monitoring and Verification Support (MVS). The goal of the MVS is to provide a reliable and transparent assessment of the progress towards the emission reduction goals (e.g., Peters et al., 2017; Nisbet et al., 2020; Nisbet et al., 2021). Therefore, the MVS is steadily improved and relies on a holistic approach, including atmospheric observations, bottom-up emission maps, carbon cycle modeling, and data assimilation (Janssens-Maenhout et al., 2020).

Anthropogenic carbon dioxide (CO_2) and methane (CH_4) emissions are the major cause of contemporary global warming (Figure 1.1c). Both gases occur naturally in the Earth's atmosphere and are part of the Earth's natural carbon cycle. However, anthropogenic activities emit a significant amount of CO_2 and CH_4. As the capacity of the natural sinks in the carbon cycle is limited, both gases accumulate in the atmosphere. Increasing CO_2 and CH_4 concentrations cause a positive radiative forcing, i.e., the net change of radiative energy flux due to a change in an external driver. Figure 1.1c shows the contribution of different agents to the observed warming of 1.06 [0.88 to 1.21] °C in 2010 - 2019 relative to 1850 - 1900, emphasizing the contribution of CO_2 and CH_4.

The CO_2 dry air mole fraction in the atmosphere has increased from 178 ppm to 417 ppm between 1750 and 2022 (Friedlingstein et al., 2023). Atmospheric growth rates are still rising and have almost tripled from 0.82 ppm yr^{-1} in the 1960s to 2.39 ppm yr^{-1} in the 2010s (IPCC, 2023, Chapter 5). In total, CO_2 contributes about 80 % to the total radiative forcing (IPCC, 2023, Figure 5.18) since 1850. Thus, CO_2 caused about 0.75 °C of the observed global warming of 1.1 °C (Figure 1.1). The Global Carbon Budget by Friedlingstein et al. (2023) investigates the carbon cycle and its components in detail. Natural fluxes dominate the global carbon cycle, with gross fluxes of about 220 Gt C yr^{-1} between the atmosphere and the other two reservoirs, the ocean and the biosphere

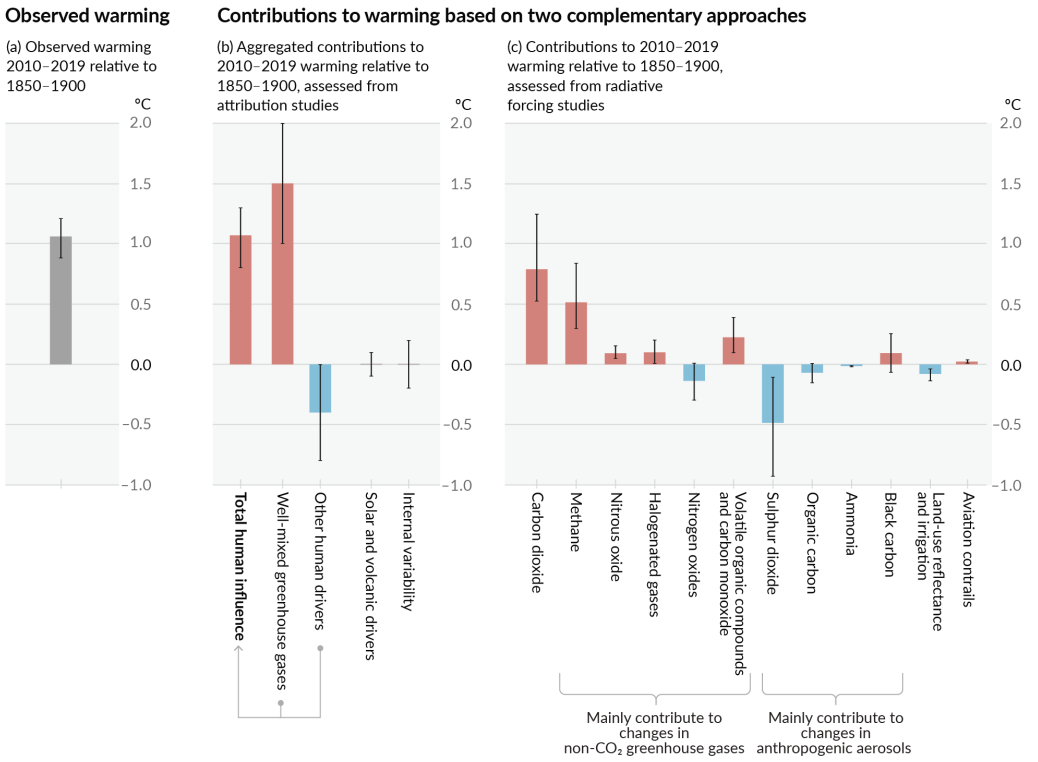

Figure 1.1: Panel (a) shows the observed global surface temperature change from 1850 to 2020. Panel (b) shows contributions based on attribution studies using climate models and observations. Panel (c) shows the evidence gathered based on the radiative forcing and climate sensitivity to different agents. The figure is taken from Masson-Delmotte et al. (2021, Figure SPM.2).

(Friedlingstein et al., 2023, Figure 1). Anthropogenic fluxes are comparatively small at 10.9 Gt C yr^{-1} from fossil fuel combustion and land use change. However, while the natural fluxes balance to net zero between reservoirs, about 50 % of anthropogenic CO_2 accumulates in the atmosphere. Fossil fuel combustion (∼9.6 Gt C yr^{-1}) dominates the anthropogenic contribution, releasing previously stored carbon from the Earth's crust. The energy sector is the largest contributor to anthropogenic CO_2 emissions. Specifically, the combustion of coal has caused steadily increasing CO_2 emissions since the beginning of the Industrial Revolution, reaching ∼4 Gt C yr^{-1} in 2019. Coal-fired power plants contribute ∼2.5 Gt C yr^{-1} to these emissions (IEA, 2018).

Figure 1.1c shows that CH_4 is the second-largest contributor to the observed global warming (Dlugokencky et al., 2011; Saunois et al., 2016; 2020; IPCC, 2023). Its dry air mole fraction has almost tripled since pre-industrial times to a current value of more than 1900 ppb. CH_4 contributes about 23 % to the anthropogenic radiative forcing (Etminan et al., 2016; Smith et al., 2018), although its total carbon emissions are only 4 % of the CO_2 emissions. The reason for this imbalance lies in the warming potential of CH_4, which is a factor of 28 higher than that of CO_2 over 100 years and a factor of 80 over 20 years (Masson-Delmotte et al., 2021). The atmospheric lifetime of CH_4 is only about nine years due to a natural sink in a reaction with the hydroxyl radical (Prather et al.,

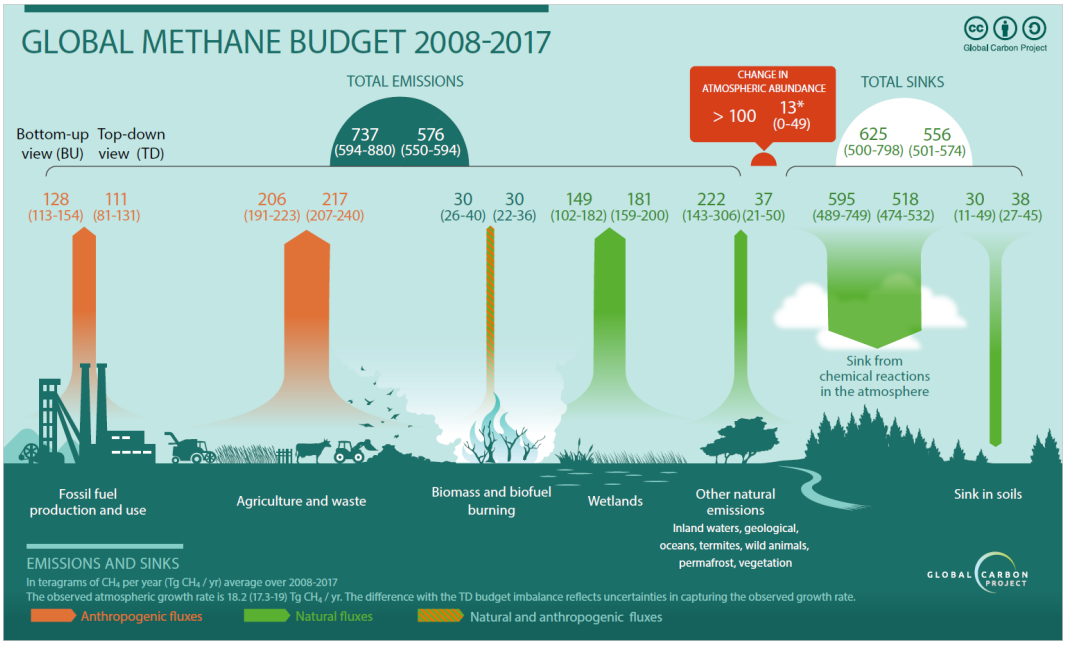

Figure 1.2: The global CH_4 budget (2008 - 2017). Anthropogenic emissions are shown as orange and natural emissions as green arrows. Every flux is associated with two numbers, representing bottom-up and top-down estimates. The figure is taken from Saunois et al. (2020, key figure).

2012). Thus, reducing CH_4 emissions has received particular attention lately as a promising agent to mitigate short-term climate change. Figure 1.2 shows the global CH_4 budget from Saunois et al. (2020), including the contributions from different sources and their uncertainties. Following Saunois et al. (2020, Table 3), 57 [50 to 65] % of the total fluxes are anthropogenic. The agricultural, livestock, and waste sectors are the most significant sources, contributing 60 % to the anthropogenic emissions. Additionally, fossil fuel production and use contribute 31 %, and biomass burning contributes 8 %. While the global budget is reasonably well-constrained, partitioning the sources remains challenging.

Approaches to quantify GHG fluxes fall into two categories: bottom-up and top-down. Bottom-up approaches estimate emissions based on activity data and emission factors, e.g., emitted CO_2 per unit of energy produced. The method scales easily from facilities to national inventories, provided that the activity data is available and emission factors are accurate. Thus, bottom-up approaches are widely used to inform national GHG inventories, e.g., the European Pollutant Release and Transfer Register (E-PRTR). However, the bottom-up framework misses unknown sources or sinks, as their emissions are unavailable *a priori*. Emission factors of CO_2 from combustion processes are well-known and readily available (e.g., Sandau et al., 2021). Activity data, though, is not equally available for sectors and regions. Especially in developing countries, activity data is often incomplete or outdated. Similar issues have an even more significant effect on the CH_4 budget. CH_4 emissions are challenging to predict since they depend on hard-to-constrain factors like meteorological conditions (rice cultivation), animal diet (livestock), and the state of the infrastructure (natural gas distribution). Hence, uncertainties of the sector's fluxes are considerably

higher in the CH_4 budget than for CO_2. Kirschke et al. (2013) report that bottom-up methods suggest ∼30 % higher global CH_4 emissions than top-down inversions, "highlighting the need for more detailed research on emission factors" (Saunois et al., 2020, Abstract).

Top-down approaches use atmospheric observations to infer emissions. Thus, they provide complementary information to bottom-up approaches, serving as an independent validation opportunity to improve the completeness and accuracy of the bottom-up estimates (Ciais et al., 2014; Watanabe et al., 2023). Measurements using in-situ or remote sensing instruments typically provide atmospheric concentrations of GHGs. Concentration enhancements result from the integrated emissions contributing to the observation. Therefore, emission estimates may be inferred from observed concentration enhancements using inversion techniques (e.g., Varon et al., 2018; Nesser et al., 2023). Typical approaches include surrounding a target region with measurement stations or transecting emission plumes (Verhulst et al., 2017; Luther et al., 2019; Dietrich et al., 2021; Gałkowski et al., 2021; Kostinek et al., 2021; Luther et al., 2022). Furthermore, imaging spectroscopy in the shortwave infrared (SWIR) spectral range has proven to be a powerful tool for this purpose. Satellites successfully observe total columns of CO_2 and CH_4 on a global scale (Butz et al., 2011; Jacob et al., 2022). Global area mappers observe CO_2 and CH_4 column concentrations with sub-percent precision, providing invaluable information on large-scale fluxes (e.g., Basu et al., 2013; Feng et al., 2016; Jiang et al., 2022). Recently, point source imager missions enabled observing single sources on the facility to local scale from space (e.g., Guanter et al., 2021; Cusworth et al., 2022). They expand the MVS capabilities by providing independent emission estimates for single sources worldwide, e.g., power plants or landfills, without needing a local campaign. However, while orbiting satellites provide global coverage, observing single sources is only possible with low revisiting rates (Bhardwaj et al., 2022; Jacob et al., 2022). Watine-Guiu et al. (2023) recently illustrated the potential of geostationary satellites to observe intermittent point sources, like methane leaks, with high temporal resolution. In light of the focus of this thesis, Section 2.2.3 provides an overview of the state-of-the-art GHG imaging and related efforts.

Top-down and bottom-up approaches are complementary and can be combined to provide a more comprehensive picture of the GHG fluxes (Ciais et al., 2014). Friedlingstein et al. (2023) point out that a synthesis of both approaches successfully disentangles natural and anthropogenic fluxes of CO_2 and attributes them to sectors. While bottom-up emissions from well-known sources may serve as validation opportunities for emerging observation techniques, established observation frameworks inform bottom-up inventories on missing sources and potential systematic uncertainties.

This thesis investigates the potential of ground-based stationary imaging of CO_2 and CH_4 using a spectral camera in the SWIR spectral range. The camera is a commercially available HySpex SWIR-384 push-broom imaging spectrometer. The spectral specifications of the camera are comparable to those of existing GHG imaging missions conducted by planes or satellites, which have demonstrated the ability to detect emissions of CO_2 and CH_4. However, the stationary setup trades spatial coverage for higher temporal resolution and prolonged observations of a single source. Thus, it is a promising tool for observing source variability and intermittency, providing complementary information to space-borne observations. The major challenge to GHG detection with the HySpex camera is the low signal of sky-scattered sunlight in the SWIR. Furthermore, relative enhancements above the total column of CO_2 are small due to the high background concentration. Therefore, point sources are ideal targets for the camera because their plumes cause signifi-

cant atmospheric enhancement and can be easily attributed to the emitter in an image. This work includes case studies of HySpex field deployments targeting CH_4 emissions from coal mining and CO_2 emissions from a coal-fired power plant. Coal mines vent CH_4 into the atmosphere through ventilation shafts, contributing significantly to the European CH_4 budget. However, past research showed that the currently reported emissions require further validation (e.g., Krautwurst et al., 2017; Fiehn et al., 2020; Kostinek et al., 2021). The observed power plant's CO_2 emissions are well known from bottom-up techniques, providing an excellent validation opportunity for the camera setup.

Alternative ground-based imaging techniques exist for CH_4, which operate using thermal radiation. Thus, they require a thermal contrast between the plume and the background and observe the source from 10 m to 300 m. Gålfalk et al. (2016) report successfully quantifying CH_4 emissions using a ground-based imaging Fourier-transform camera. However, most alternatives are Optical Gas Imaging (OGI) cameras designed for leak detection and incapable of emission quantification. SWIR imaging can observe CH_4 plumes on the kilometer scale, requiring daylight instead of thermal contrast. Thus, it expands current MVS capabilities. Concerning CO_2, no alternative techniques for ground-based imaging exist at the time of writing to the best of the author's knowledge.

The following chapters develop a framework from raw camera observations to emission estimates from strong point sources of CO_2 and CH_4. Chapter 2 provides the essential theoretical background for remote sensing using absorption spectroscopy in the SWIR spectral range. Furthermore, it presents the basic principles of imaging spectroscopy and an overview of the state of the art in GHG imaging. Chapter 3 focuses on the HySpex SWIR-384 camera, including the preprocessing of the raw data and the necessary instrument calibration. It also describes the instrumental field setup and the viewing geometry. Chapter 4 introduces the methods to arrive at emission estimates from the observed spectra. It includes the matched filter retrieval algorithm and emission estimation techniques based on mass balance and Gaussian plume inversion. The methods were adapted from established remote sensing techniques and are tailored to the specific challenges of the ground-based imaging setup. Chapter 5 presents results from two field campaigns at active coal mines in Poland. Chapter 6 presents the first results of CO_2 plume observations from a coal-fired power plant in Germany. Finally, Chapter 7 summarizes the findings and provides an outlook on future work.

2 Background

This chapter presents the physical background for the work and provides a brief overview of the current state of the art in GHG imaging. Section 2.1 explains the interaction of light with molecules in the Earth's atmosphere. It introduces the radiative transfer equation (RTE) and its solution in the single-scattering approximation, which is the basis for retrieving GHG concentrations in this thesis. Section 2.2 introduces the working principles of imaging spectrometers and their application to GHG imaging, including ongoing missions and past efforts.

This thesis employs a spectral camera in the SWIR spectral range to observe atmospheric CO_2 and CH_4 enhancements using absorption spectroscopy. Thus, the following sections focus on the necessary information for this application. The descriptions omit completeness for the sake of brevity and clarity. The following literature provides the foundation of the presented information and includes further details on the topics discussed in this chapter. Petty (2006) yields an excellent introduction to the interaction of radiation with the atmosphere. Stamnes et al. (2017) provide additional or more in-depth descriptions of radiative transfer phenomena. Bransden and Joachain (2003) include a thorough quantum-mechanical description of the interaction of molecules with electromagnetic radiation. Demtröder (2013) and Demtröder (2016) provide basic information on the interaction of light with molecules and the working principles of spectrometers.

2.1 Radiative Transfer in the Atmosphere

2.1.1 The Earth's Atmosphere

The atmosphere plays a vital role in the Earth's radiation budget, i.e., the balance of incoming and outgoing radiative energy. The atmosphere's composition determines the radiative balance since increasing levels of GHGs capture additional energy in the atmosphere. This radiative forcing raises the Earth's surface temperature and causes the contemporary climate change. The following paragraphs describe the atmosphere's structure, composition, and radiation budget.

Structure and Composition

The atmosphere is layered according to the temperature lapse rate, i.e., the vertical temperature gradient. The troposphere extends from the surface up to 8 km at the poles and 16 km at the equator. The surface heats air parcels, causing an unstable layering due to buoyant rise. Thus, the troposphere is well mixed by convection and turbulent mixing. The temperature decreases with height up to the tropopause. At this point, radiative cooling to space and eventually absorption of solar radiation by the ozone layer reverse the trend. The stratosphere extends from the tropopause to the stratopause at approximately 50 km. Air masses are stratified due to the stable layering in the stratosphere and remain distinct for years to decades. Two more temperature lapse

rate changes above the stratopause mark the mesosphere and the thermosphere. The atmospheric pressure profile decreases exponentially with a scale height of around 8 km. Thus, the troposphere and stratosphere dominate the Earth's radiative balance since they contain 99 % of the molecules. Dry air consists mainly of nitrogen (N_2) (78 %), oxygen (O_2) (21 %), and argon (0.9 %). The remaining species are called trace gases due to their low volume concentration. GHGs are trace gases capturing thermal radiation emitted at the Earth's surface. The primary natural GHGs are water vapor (H_2O), CO_2, CH_4, nitrous oxide (N_2O), and ozone (O_3). H_2O reaches concentrations of 0 % to 5 % in the lower atmosphere and contributes most to the greenhouse effect. However, humanity's direct influence[1] on H_2O concentrations is insignificant. Here, discussions focus on anthropogenic emissions of CO_2 and CH_4 since these species contribute most to the man-made radiative forcing.

The Radiative Energy Budget

The Earth's radiative balance is a result of incoming solar radiation and outgoing thermal radiation. Solar radiation dominates the incoming flux at the top of the atmosphere. According to Planck's law, the spectral energy density u_λ emitted by black bodies reads

$$u_\lambda(T) = \frac{8\pi hc}{\lambda^5} \frac{1}{e^{\frac{hc}{\lambda k_B T}} - 1}, \tag{2.1}$$

where λ is the wavelength, T is the temperature, h is the Planck constant, c is the speed of light, and k_B is the Boltzmann constant. The radiation emitted by the Sun can be approximated by the radiation of a black body with an effective temperature of 5770 K. The solar spectrum peaks in the visible (VIS) range around 0.5 µm, with the spectral range from 0.1 µm to 4 µm covering more than 99 % of the radiative energy. The ozone layer in the stratosphere absorbs most radiation in the ultraviolet (UV) range below 320 nm. However, VIS and, in parts, near infrared (NIR) radiation reaches the Earth's surface. The surface reflects a fraction of the light and absorbs the rest as heat. The Earth emits thermal radiation according to Equation (2.1) with an effective emission temperature of 288 K. This radiation peaks in the thermal infrared (TIR) range at 10 µm, radiating most energy between 4 µm and 70 µm. The atmosphere has a so-called "atmospheric window" which is transparent to thermal radiation. It ranges from 8 µm to 12 µm. The atmosphere is opaque for TIR radiation outside this spectral range. Hence, the atmosphere absorbs the major part of the Earth's thermal radiation - only radiation in the "atmospheric window" allows the earth to cool down. Figure 2.1 presents an overview of the Earth's energy budget, as shown in Wild et al. (2017). The incoming solar radiation is approximately 340 W m^{-2}. The outgoing thermal radiation almost equals the incoming flux at the top of the atmosphere. As Figure 2.1 illustrates, GHGs in the atmosphere partially absorb and re-emit thermal radiation. Increasing levels of GHGs cause a net positive radiative imbalance, which is responsible for the rising temperatures of the Earth's surface and troposphere. In 2019, the radiative imbalance amounted to 2.72 [1.96 to 3.48] W m^{-2} relative to 1750 (IPCC, 2023, A.4). CO_2 and CH_4 are responsible for an additional radiative forcing of 2.16 W m^{-2} and 0.54 W m^{-2} since 1750, respectively (IPCC, 2023, p. 69), making them the

[1] Warm air holds more H_2O than cold air. Thus, rising H_2O concentrations in the atmosphere are part of a positive feedback loop of the anthropogenic global warming, but not a result of anthropogenic H_2O emissions.

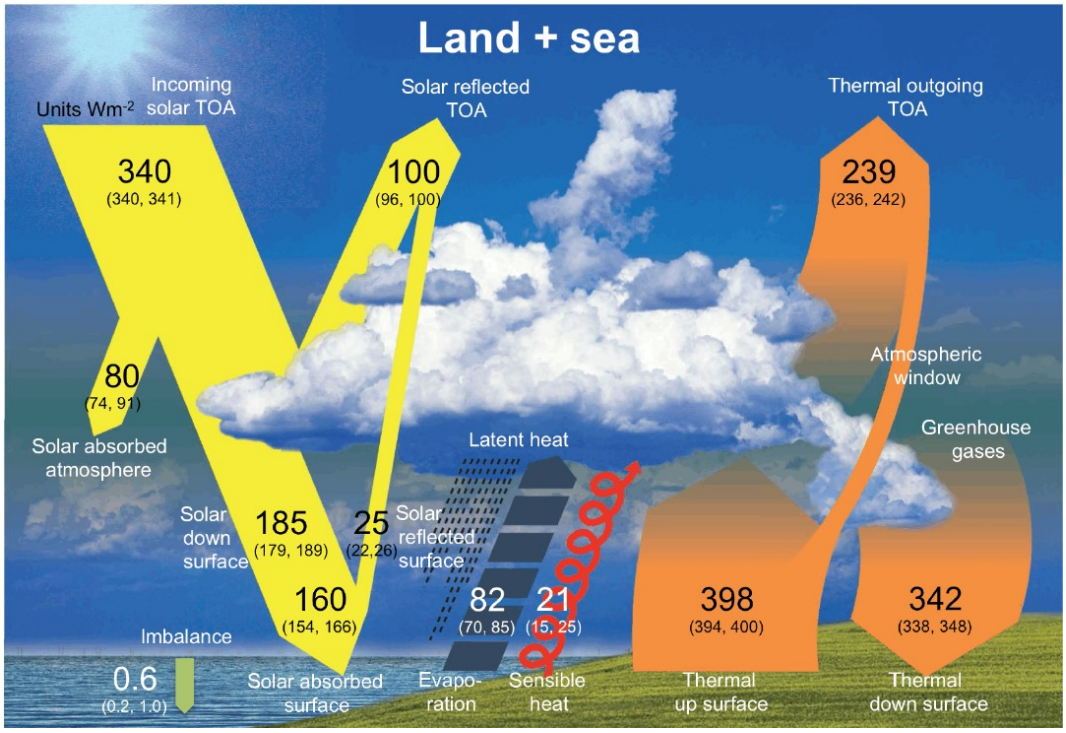

Figure 2.1: The Earth's radiative energy budget taken from Wild et al. (2017). This schematic shows the key solar and thermal radiative fluxes that determine the Earth's energy balance. At the top of the atmosphere, an imbalance is apparent - the Earth captures more energy than it emits. Thus, the Earth's surface and troposphere heat up until the outgoing thermal radiation balances the incoming solar radiation.

two dominant climate agents. As the Earth approaches a higher equilibrium temperature, the radiative imbalance diminishes. The latest period from 2006 to 2018 exhibited global warming corresponding to a radiative forcing of 0.79 [0.52 to 1.06] W m^{-2} (IPCC, 2023, A.4.2).

2.1.2 Interaction of Light and Molecules

Light is electromagnetic radiation, interacting with molecules in three fundamental processes: absorption, emission, and scattering. The following sections describe these processes, primarily focusing on the absorption of CO_2 and CH_4 in the SWIR spectral range from 1.5 µm to 2.5 µm.

Absorption and emission

The electromagnetic field is quantized into photons. Photons exhibit wave-particle-duality, and each photon carries energy according to its wavelength $E_{\text{ph}} = \frac{hc}{\lambda}$. Molecules can emit and absorb photons, thereby exchanging energy with the surrounding field of electromagnetic radiation. The stationary Schrödinger equation describes the energy E a molecule can assume as

$$\hat{H}|\Psi\rangle = E|\Psi\rangle\,, \tag{2.2}$$

where $\hat{H}$ is the time-independent Hamiltonian operator and $|\Psi\rangle$ is the molecule's wave function. The solution of $|\Psi\rangle$ is a linear combination of eigenstates $|\psi_k\rangle$ with corresponding energies E_k. Molecules assume discrete energy levels according to their electronic, vibrational, and rotational state. Transitions due to radiation between energy levels E_i and E_j require the absorption or emission of a photon with $E_{\mathrm{ph}} = |E_i - E_j|$. Photon energies in the SWIR spectral range excite vibrational and rotational transitions, while electronic transitions require photon energies in the UV/VIS range with $\lambda < 1\,\mu\mathrm{m}$. Thus, the following introduction is limited to vibrational and rotational transitions.

Diatomic molecules, like carbon monoxide (CO), provide an opportunity to illustrate the mechanisms of vibration-rotation transitions. The Morse potential describes the interaction potential energy $V(r)$ between the nuclei of a diatomic molecule as

$$V(r) = D_e\Big(1 - e^{-a(r-r_{\mathrm{e}})}\Big)^2 , \tag{2.3}$$

where D_e is the dissociation energy, a is the vibrational constant, r_{e} is the equilibrium bond length, and r is the distance between the nuclei. Solving Equation (2.2) for the stationary states of the Morse potential yields the vibrational energy levels

$$E_\nu = \left(\nu + \frac{1}{2}\right)\hbar\omega_0 - \frac{\left[\left(\nu + \frac{1}{2}\right)\hbar\omega_0\right]^2}{4D_e} , \tag{2.4}$$

where ν is the vibrational quantum number, $\omega_0 = a\sqrt{2D_e/\tilde{m}}$ is the vibrational angular frequency with the reduced mass $\tilde{m}$ of the molecule, and $\hbar$ is the reduced Planck constant. Note that the first term is the harmonic oscillator solution with equidistant energy levels, while the second term is the anharmonic correction. Vibrations are radial oscillations of the nuclei around the equilibrium bond length. Additionally, the molecule can rotate around its center of mass. Without further derivation, the rotational energy levels E_J of a rigid diatomic molecule are given by

$$E_J = \frac{\hbar^2}{2\tilde{m}R^2} J(J+1) , \tag{2.5}$$

where J is the rotational quantum number, and $R = r_{\mathrm{e}}$ is constant for the rigid molecule. The spacing between two rotational energy levels is

$$\Delta E_J = \frac{\hbar^2}{\tilde{m}r_{\mathrm{e}}^2}(J+1) , \tag{2.6}$$

increasing linearly with J. Thus, transition energies ΔE_J are linearly spaced with $\frac{\hbar^2}{\tilde{m}r_{\mathrm{e}}^2}$, where $\tilde{m}$ and r_{e} are molecule-specific. For purely rotational-vibrational transitions, it holds that $\Delta J = \pm 1$ since a photon carries one unit of angular momentum. However, $\Delta J = 0$ is possible in transitions that account for conservation of angular momentum differently. Figure 2.2 illustrates rotational-vibrational transition energies for $\Delta\nu = +1$ and $\Delta J = +1, 0, -1$. Transitions with $\Delta J = -1, 0, +1$ form the P-, Q-, and R-branch, respectively. Since transition energies

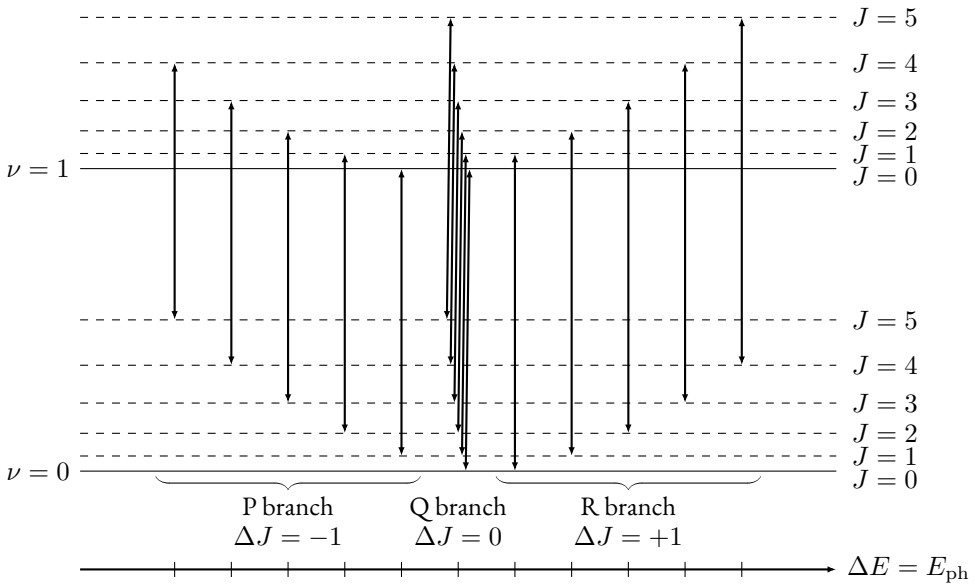

Figure 2.2: Schematic of the energy levels of a diatomic molecule, inspired from Petty (2006). Transitions with $\Delta J = -1, 0, +1$ are called the P-, Q-, and R-branch, respectively. All transition energies ΔE are equidistantly spaced by $\frac{\hbar^2}{\tilde{m} r_e^2}$ around the pure vibrational transition energy from $\nu = 0$ to $\nu = 1$. Molecular transitions either emit or absorb photons carrying energy $E_{\mathrm{ph}} = \Delta E$.

correspond to photons of a certain wavelength, they give rise to a line spectrum of absorption or emission.

Molecules consisting of three or more atoms, like CO_2 and CH_4, have more complex energy level structures than diatomic molecules. Figure 2.3 shows the transmission spectra of CO_2 and CH_4 at atmospheric conditions. Absorption lines appear at wavelengths corresponding to an energy transition of the molecule, decreasing the transmission through the media. CO_2 is a centrosymmetric linear molecule. Thus, it has two equal, non-zero rotational moments of inertia and three modes of vibration. The transmission spectrum in Figure 2.3a around 2000 nm emerges from combined vibrational[2] and rotational transitions. Since the vibrating CO_2 molecule resembles a diatomic molecule, absorption lines follow the transition scheme of Figure 2.2. The two wing-like structures around 2060 nm are the P- and R-branch, while the Q-branch is suppressed. CH_4 is a tetrahedral molecule. Thus, it has three identical moments of inertia and four vibrational modes. Figure 2.3b shows the CH_4 absorption features around 2300 nm. This absorption band emerges from four distinct combinations of at least two vibrational modes (Bransden and Joachain, 2003, Table 81). Thus, the vibration-rotation line spectrum is far more complex than for CO_2.

The following paragraphs introduce the processes that lead to lines of varying shape and strength in the transmission spectrum. Absorption, stimulated emission, and spontaneous emission are the fundamental processes of photon-molecule interaction. Let n_i and n_j be the number of

[2] This transition consists of the symmetric stretching $\tilde{\nu}_1 = 1388\,\mathrm{cm}^{-1}$, asymmetric stretching $\tilde{\nu}_2 = 2349\,\mathrm{cm}^{-1}$, and bending $\tilde{\nu}_3 = 667\,\mathrm{cm}^{-1}$ vibrations. The transition occurs from simultaneous $\tilde{\nu}_2 + 2 \cdot \tilde{\nu}_1$, $\tilde{\nu}_2 + \tilde{\nu}_1 + 2 \cdot \tilde{\nu}_3$, or $\tilde{\nu}_2 + 4 \cdot \tilde{\nu}_3$ transitions (Buback et al., 1986), which add up to approximately the same transition energy.

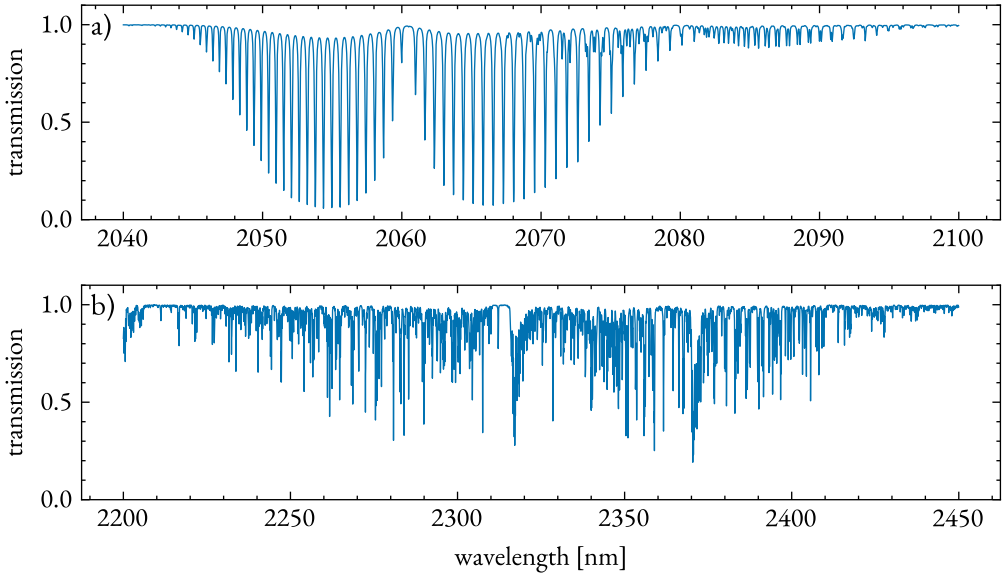

Figure 2.3: Transmission spectra of a) CO_2 and b) CH_4 in the SWIR spectral range. Transmission through a medium decreases when the absorption lines are strong. The transmission spectrum of CO_2 shows the wings of the P- and R-branch, while the transmission spectrum of CH_4 exhibits a much more complex structure.

molecules in the energy states $E_i < E_j$, respectively. The Einstein coefficients A_{ji} [s^{-1}], B_{ij} [$m^3\,W^{-1}\,s^{-1}$], and B_{ji} [$m^3\,W^{-1}\,s^{-1}$] describe the transition probabilities for spontaneous emission, absorption, and stimulated emission, respectively. Quantum electrodynamics provides the necessary framework to derive these coefficients. The rate of change of n_i is

$$\frac{\mathrm{d}n_i}{\mathrm{d}t} = -n_i u_\lambda B_{ij} + n_j u_\lambda B_{ji} + n_j A_{ji}\,, \tag{2.7}$$

where u_λ [$W\,m^{-3}$] is the energy density of the radiation field. Molecules in the troposphere and the stratosphere are, in good approximation, in local thermodynamic equilibrium. Thus, the rate of change between any two energy levels is zero (detailed balance) and the relative number of two states is given by the Boltzmann distribution

$$\frac{n_j}{n_i} = \frac{g_j}{g_i} e^{-\frac{E_j - E_i}{k_\mathrm{B} T}}\,, \tag{2.8}$$

where g_i and g_j are the degeneracies of the states. The aforementioned assumptions of local thermodynamic equilibrium lead to the following relations of the transition probabilities:

$$g_j B_{ji} = g_i B_{ij} \qquad \text{and} \qquad A_{ji} = \frac{8\pi h c}{\lambda^5} B_{ji}\,. \tag{2.9}$$

The occupancy of energy states following the Boltzmann distribution (Equation (2.8)) has some further implications. Typical transition energies of vibrational states are on the order of 100 meV,

while rotational transitions are on the order of 1 meV. Typical thermal energies in the tropo- and stratosphere are well below ∼26 meV (at 300 K). Thus, molecules mostly occupy their vibrational ground state ($\nu = 0$) but extend to higher rotational states ($J \geq 0$). Considering a vibration-rotation transition, the total number density of molecules in the ground state is much higher than in the excited state. Therefore, spontaneous and stimulated emission are small compared to absorption. Furthermore, the Boltzmann distributed rotational energy occupancy in the vibrational ground state explains the wing-like structure of the P- and R-branch in Figure 2.3a. The degeneracy of rotational energy levels is given by $g = 2J + 1$. Thus, the transition probability increases close to the Q-branch with the degeneracy since more states allow for the same energy level. The trend reverses further from the Q-branch, around $J = 10$ in Figure 2.3a. A decreasing population in the transition's ground state causes the reversal, due to the growing energy difference to the molecules ground state at $J = 0$ (see Figure 2.2).

Every transition changes the radiation field's energy by $E_{\mathrm{ph}} = \frac{hc}{\lambda}$. Thus, Equation (2.7) can describe the change in radiative energy. Assuming thermodynamic equilibrium, the energy level population and the transition probabilities are known. Consequently, Equation (2.7) determines the line strength S, that is the change in radiation along a path ds in a volume of molecule density n. Without further derivation, S is given by

$$S = \frac{h}{\lambda} B_{ij} \frac{n_i}{n} \left(1 - e^{-\frac{E_j - E_i}{k_{\mathrm{B}} T}} \right) . \tag{2.10}$$

The medium absorbs light at wavelengths with $B_{ij} \neq 0$. Thus, the absorption spectrum consists of lines as already encountered in Figure 2.3. The derivations above were limited to discrete energy transitions of molecules. However, absorption and emission lines are not infinitely sharp, but have a finite line width caused by three effects. First, the natural line width results from Heisenberg uncertainty principle in the energy-time domain. The molecule's energy levels are not discrete due to the finite lifetime of the excited state. Second, the Doppler effect causes a broadening of the line spectrum due to the thermal motion of molecules in the atmosphere. Third, collisions between molecules distort the energy levels of molecules, which is called pressure broadening. A line shape factor $f(\lambda - \lambda_0)$, normalized to $\int_0^\infty f \, \mathrm{d}\lambda = 1$, describes the absorption line shape around its central wavelength λ_0. The absorption cross-section $\sigma_{\mathrm{a},\lambda_0}$ of a line around λ_0 is defined as

$$\sigma_{\mathrm{a},\lambda_0} = S f(\lambda - \lambda_0) \, , \tag{2.11}$$

such that $\int_0^\infty \sigma_{\mathrm{a},\lambda_0} \, \mathrm{d}\lambda = S$. It describes the effective area of absorption of a molecule at a certain wavelength. Under atmospheric conditions, the natural line width is negligible compared to the Doppler and pressure broadening. Thus, the line shape factor $f(\lambda - \lambda_0)$ results from a combination of the Doppler and pressure broadening. The thermal Doppler broadening causes a Gaussian shape, while the pressure broadening causes a Lorentzian shape. A standard approximation for the resulting line shape is the Voigt profile $V(\lambda)$, which is the normalized convolution of a Gaussian and a Lorentzian profile (for details, see, e.g., Humlíček (1982)). The line spectrum

of discrete absorption lines reads $S(\lambda) = \sum_i^{\text{lines}} S_i \delta(\lambda - \lambda_{0,i})$, where $\delta(\lambda - \lambda_{0,i})$ is the Dirac delta distribution. The total absorption cross-section $\sigma_{\text{a}}(\lambda)$ follows as

$$\sigma_{\text{a},\lambda} = S(\lambda) * V(\lambda) \tag{2.12}$$

$$= \int_0^\infty \sum_i^{\text{lines}} S_i \delta(\lambda' - \lambda_{0,i}) V(\lambda - \lambda') \, \mathrm{d}\lambda' \tag{2.13}$$

$$= \sum_i^{\text{lines}} \sigma_{\text{a},\lambda_{0,i}} \,, \tag{2.14}$$

where $*$ is the convolution operator. More sophisticated line shapes exist, e.g., the Hartmann-Tran profile (Ngo et al., 2013; Tennyson et al., 2014), and are still subject to research. The spectral camera used for the presented thesis cannot resolve single lines of molecular absorption. Thus, the Voigt profile is sufficient for the work presented here. Finally, the absorption coefficient $\beta_{\text{a},\lambda}$ can be written as

$$\beta_{\text{a},\lambda} = \sigma_{\text{a},\lambda} \cdot n \,, \tag{2.15}$$

which is the rate of absorption of radiation passing through a medium.

In conclusion, molecules inside a radiation field absorb and emit photons. The photon energy matches the transition energy between two states of the molecule, giving rise to a line spectrum. Molecules have unique line spectra. Thus, observing absorption lines in the spectrum of light passing through the atmosphere enables the detection and quantification of molecules in the atmosphere.

Scattering

Scattering changes the direction of an electromagnetic wave incident on a molecule. Hence, the loss of radiation in a certain direction is compensated by the gain of radiation in another direction. Scattering processes are described by two quantities: the scattering cross-section and the scattering phase function. The scattering cross-section is the probability of a scattering process at a certain particle, while the phase function describes the angular distribution of the outgoing wave. Both quantities depend on the size regime of the scattering process. The size parameter ζ determines the regime and is defined as

$$\zeta = \frac{2\pi r_{\text{p}}}{\lambda} \,, \tag{2.16}$$

where r_{p} is the radius of the scattering particle and λ is the wavelength incident wave. The following paragraphs introduce the relevant scattering processes for the work presented in this thesis. This encompasses elastic scattering of SWIR waves by molecules and aerosols, which are small particles suspended in the atmosphere.

Rayleigh scattering describes scattering processes for $\zeta < 0.2$ (Petty, 2006, Figure 12.1). Since the molecule is much smaller than the incident wave, every part of it experiences the same electric field. The electric field induces a charge separation inside the molecule, which oscillates with the frequency of the incoming wave. The oscillating dipole emits a secondary wave at the same

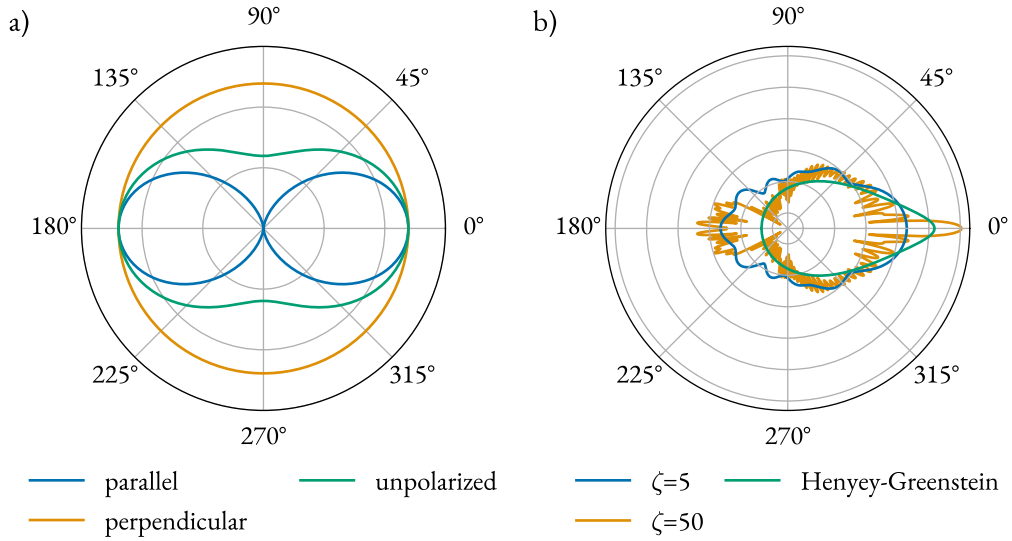

Figure 2.4: Scattering phase functions of a) Rayleigh scattering and b) Mie scattering. Radiation arrives from the left (180°) and is scattered out of beam. Both processes are rotationally symmetric around the direction of propagation of the incoming radiation. For Rayleigh scattering, the phase function changes if the outgoing light is polarized perpendicular (orange), parallel (blue), or unpolarized (green) relative to the scattering plane. For Mie scattering, the phase function changes with the size parameter ζ - a higher size parameter (orange) shows finer structures and stronger forward scattering than a smaller size parameter (blue). In real applications, the scattering phase function of aerosols may be approximated by the Henyey-Greenstein phase function (green, $g = 0.9$). Note that the radial axis in panel b) is logarithmic and scattering phase functions are normalized to unity. Plots produced with Prahl (2023).

frequency as the incoming wave. Thus, Rayleigh scattering is an elastic scattering process. The scattering cross-section σ_s of Rayleigh scattering is given by

$$\sigma_{\mathrm{s,Rayl.}} \propto \frac{\alpha^2 r_\mathrm{p}^6}{\lambda^4}\,, \tag{2.17}$$

where α is the polarizability of the molecule. Equation (2.17) shows that Rayleigh scattering is more efficient at smaller wavelength for constant particle parameters r_p and α. Since Rayleigh scattering emerges from dipole radiation, the emitted light is (partly) polarized even if the incoming light is unpolarized. The induced dipoles are oriented perpendicular to the incoming wave's propagation direction. Thus, the secondary wave is polarized perpendicular to the incoming wave's propagation direction. This results in less light scattered perpendicular to the incoming radiation, as seen in the scattering phase function

$$P_{\mathrm{Rayl.}}(\theta) = \frac{3}{4}(1 + \cos^2\theta)\,, \tag{2.18}$$

where θ is the scattering angle. Figure 2.4a shows the scattering phase functions of Rayleigh scattering. Rayleigh scattering is the dominant scattering process in the UV/VIS spectral range with

size parameters down to $2 \cdot 10^{-3}$. For smaller size parameters, scattering is usually neglected, while for larger size parameters, the assumption of a single oscillating dipole is no longer valid. Scattering of SWIR waves on molecules corresponds to a size parameter of $\zeta \approx 3 \cdot 10^{-4}$. Thus, scattering on molecules is weak in the SWIR spectral range. However, since observations in this thesis focus on pristine atmospheric conditions, Rayleigh scattering is still included in later computations of radiative transfer.

Aerosol scattering is the dominant scattering process in the SWIR spectral range. Larger aerosols ($r > 0.1\,\mu\text{m}$) fall in the size regime of $0.4 \leq \zeta \leq 20$. Mie theory describes the scattering of electromagnetic waves on spherical particles in this size regime[3]. It produces the absorption and scattering cross-section as functions of the size parameter and the refractive index of the particle. For small size parameters, Mie theory reproduces Rayleigh scattering. For large size parameters, the scattering cross-section starts oscillating with ζ, converging to a constant value of $\sigma_{\text{s,Mie}} = 2\pi r_{\text{p}}^2$, twice the geometric cross-section[4]. Mie scattering phase functions show increasingly strong forward scattering for larger size parameters ζ. Furthermore, fine-scale structures emerge in the phase function, which gives rise to optical phenomena like rainbows and halos. Such structures are mostly smoothed away in reality since aerosols exist as a distribution of particles with different size parameters. Thus, the scattering phase function of aerosols may be approximated by the Henyey-Greenstein phase function

$$P_{\text{H-G}}(\theta) = \frac{1 - g^2}{(1 + g^2 - 2g\cos\theta)^{3/2}}\,, \tag{2.19}$$

where g is the asymmetry parameter. The asymmetry parameter determines the pronunciation of the forward scattering, ranging between 0.6 and 0.85 for situations encountered in this thesis. Figure 2.4b shows two scattering phase functions from Mie theory and the Henyey-Greenstein phase function.

Analogous to the absorption coefficient, the scattering coefficient $\beta_{\text{s},\lambda}$ follows from

$$\beta_{\text{s},\lambda} = \sigma_{\text{s},\lambda} \cdot n\,, \tag{2.20}$$

where n is the number density of the scattering particles. The scattering coefficient describes the loss of radiation in traveling direction due to scattering on a path length ds. However, scattering from all other directions may contribute to radiation in the traveling direction according to the scattering phase function. Thus, scattering is also a source of radiation - without scattering, the sky would be dark. The sky-scattered sunlight provides the homogeneous background illumination for the camera observations in this thesis.

[3] Although the theory can be expanded to non-spherical particles, see Van de Hulst (1981).

[4] The fact that the Mie theory predicts twice the geometric cross-section of the particle is called the extinction paradox. There are several theories to explain this phenomenon, e.g., Berg et al. (2011).

2.1.3 The Radiative Transfer Equation

The field of light can be quantified by its spectral radiance

$$I_\lambda = \frac{\mathrm{d}^4 E}{\mathrm{d}A\,\mathrm{d}\Omega\,\mathrm{d}\lambda\,\mathrm{d}t}\,, \tag{2.21}$$

which is the radiant energy $\mathrm{d}E$ transported through an area $\mathrm{d}A$ from a certain solid angle $\mathrm{d}\Omega$ in a spectral interval $\mathrm{d}\lambda$ per time interval $\mathrm{d}t$. The change of radiance in direction $\mathbf{\Omega}$ along a path is described by the radiative transfer equation (RTE)

$$\frac{\mathrm{d}I_\lambda}{\mathrm{d}s} = -\beta_{\mathrm{a},\lambda} I_\lambda - \beta_{\mathrm{s},\lambda} I_\lambda + \frac{\beta_{\mathrm{a},\lambda} c}{4\pi} u_\lambda + \frac{\beta_{\mathrm{s},\lambda}}{4\pi} \int_{4\pi} P_\lambda(\mathbf{\Omega}'; \mathbf{\Omega}) I_\lambda(\mathbf{\Omega}')\,\mathrm{d}\mathbf{\Omega}'\,, \tag{2.22}$$

where s is the path length, $\beta_{\mathrm{a},\lambda}$ is the absorption coefficient, $\beta_{\mathrm{s},\lambda}$ is the scattering coefficient, u_λ is the Planck function (Equation (2.1)), and P_λ is the scattering phase function. The right-hand side of Equation (2.22) describes, from left to right, the absorption of light, the scattering of light from the beam, additional radiance through emission, and the scattering of light from solid angle $\mathbf{\Omega}'$ into the beam traveling into solid angle $\mathbf{\Omega}$. The subscript λ is omitted in the following. The RTE in this form has no analytical solution, though many software solutions exist to solve it numerically (e.g., Berk et al., 2014; Emde et al., 2016). The following sections introduce two special cases of the RTE, which are used in this thesis.

Beer-Lambert Law

The Beer-Lambert law describes the extinction of light over a path length. Thus, only the two first terms of Equation (2.22) are considered. The RTE is easily solved by integration

$$I(s) = I(0) \exp\left(- \int_0^s \beta_\mathrm{e}(s')\,\mathrm{d}s' \right), \tag{2.23}$$

with the extinction coefficient $\beta_\mathrm{e} = \beta_\mathrm{a} + \beta_\mathrm{s}$. The argument of the exponential function is called the optical depth τ. Assuming absorption dominates, the extinction coefficient $\beta_\mathrm{e} \approx \beta_\mathrm{a}$ results from the absorption cross-section $\sigma_{a,\lambda}$ and the number density of the absorbing molecules n (Equation (2.15)), such that

$$\tau = \int_0^s n(s')\sigma_\mathrm{a}(s')\,\mathrm{d}s' \tag{2.24}$$

$$\approx \sigma_\mathrm{a} \cdot \int_0^s n(s')\,\mathrm{d}s'\,, \tag{2.25}$$

where the second line is valid if the absorption cross-section is constant along the path. The attenuation of the light thus depends on the number of molecules integrated along the light path, also called the column density (in molec. cm^{-2}). Therefore, the column density is the physically observable quantity in absorption spectroscopy.

Single Scattering Approximation

The spectral camera used in this thesis observes sky-scattered radiance in the SWIR spectral range. Most complications of the RTE arise from multiple scattering since this requires, in theory, a solution of the equation to infinite scattering orders (i.e., the number of times a photon was scattered until it reached the observer). The single-scattering approximation assumes that the light is scattered just once before it arrives at the observer. Furthermore, thermal emission is neglected for SWIR light at atmospheric temperatures. Thus, the single-scattering approximation considers only photons from the sun that were re-directed once into the observer's viewing direction. The analytical solution of the RTE for a horizontally homogeneous, plane-parallel atmosphere reads

$$I(\lambda) = \frac{S_0(\lambda)\gamma_0}{4\pi(|\gamma| - |\gamma_0|)} \cdot \sum_{k}^{layer} \varpi_k(\lambda) P_k(\lambda; \Omega, \Omega_0) e^{-\frac{\tau_k(\lambda)}{|\gamma_0|-|\gamma|}} \left(1 - e^{-\Delta\tau_k\left(\frac{1}{|\gamma_0|} - \frac{1}{|\gamma|}\right)}\right), \tag{2.26}$$

where S_0 is the top of the atmosphere radiance, $\gamma_0 = \frac{1}{\cos(\text{SZA})}$, $\gamma = \frac{1}{\cos(\text{VZA})}$, ϖ is the single-scattering albedo, and P the scattering phase function for the beam direction before (Ω_0) and after (Ω) the scattering. The solar zenith angle (SZA) and viewing zenith angle (VZA) describe the viewing geometry, while the single-scattering albedo is the ratio of scattering to extinction $\varpi = \frac{\beta_s}{\beta_s+\beta_a}$.

Single scattering approximates radiative transfer well for a small optical depth $\tau \ll 1$, since scattering is overall unlikely, or if absorption dominates over scattering ($\varpi \ll 1$). These assumptions are valid for the SWIR spectral range under clear sky conditions. Scattering on molecules is negligible due to the small size parameter of molecules. Aerosol scattering is more efficient yet still small, making single scattering a good approximation. Thermal emission, again, is negligible since the scattered radiance from the sun is still several magnitudes larger than the radiance emitted from the atmosphere. Since neither scattering of solar photons nor thermal emission efficiently produces observable light in the SWIR spectral range, the sky is dark in this spectral range.

Since the camera observes targets close to the ground, the viewing elevation angle (VEA), with $\text{VEA} = 90° - \text{VZA}$, is small. The assumption of plane-parallel layers is violated for shallow VEAs, yet there are empirical corrections for this effect. For VEAs larger than 0°, i.e., still pointing above the horizon, Kasten and Young (1989) provide a sufficient correction that reads

$$\gamma = \frac{1}{\cos(\text{VZA}) + 0.0572\,(96.07995 - \text{VZA})^{-1.6364}}\,. \tag{2.27}$$

2.2 Imaging Spectrometry

This section introduces the concept of imaging spectrometers and their application to GHG imaging. An imaging spectrometer, also known as a spectral camera, is capable of resolving a spatial scene and providing spectral information for each pixel of the image. The spectral camera used in the context of this thesis is a push-broom imager based on a grating spectrometer. Section 2.2.1 provides the physical principles of grating spectrometers. The concept of push-broom imaging is introduced in Section 2.2.2. Finally, the current state of the art in GHG imaging is laid out in Section 2.2.3, including past and ongoing missions.

2.2.1 Grating Spectrometers

A spectrometer is a tool that observes the spectral components of light, with a common type being the grating spectrometer based on diffraction. Diffraction occurs as light passes through an aperture or encounters an obstacle. The Huygens-Fresnel principle explains this phenomenon by assuming that every point on a wave front acts as a source of spherical waves. The grating spectrometer employs this principle, utilizing a periodic structure of slits as apertures. Therefore, the grating induces an optical path difference for light passing through the grating. This difference is angle-dependent on the observation plane, leading to constructive and destructive interference. The interference pattern, determined by wavelength, allows differentiating spectral components of the light. It can be shown that the far-field diffraction pattern, called Fraunhofer diffraction, of a grating is proportional to the Fourier transform of the grating structure. A periodic grating structure of N slits of width b and a slit distance of d is described by the function

$$G(x) = \Pi(x/b) * \sum_{n=0}^{N} \delta(x - nd)\,, \tag{2.28}$$

where Π is the rectangular distribution. Using the convolution theorem and the geometrical series, the Fourier transform reads

$$\mathcal{F}\{G(x)\} = \mathcal{F}\{\Pi(x/b)\} \cdot \mathcal{F}\left\{\sum_{n=0}^{N} \delta(x - nd)\right\} \tag{2.29}$$

$$\propto \operatorname{sinc}\left(\pi \frac{b}{\lambda} \sin(\Theta)\right) \cdot \frac{1 - \exp(-i2\pi N d \sin(\Theta)/\lambda)}{1 - \exp(-i2\pi d \sin(\Theta)/\lambda)}\,, \tag{2.30}$$

where $\mathcal{F}$ is the Fourier transform operator, λ is the wavelength of the incoming light, and Θ is the observation angle. The intensity of a monochromatic, plane wave is given as its squared amplitude. Thus, the intensity distribution $I(\Theta)$ of the diffraction pattern reads

$$I(\Theta) \propto \operatorname{sinc}\left(\pi \frac{b}{\lambda} \sin(\Theta)\right)^2 \cdot \frac{\sin(\pi N d \sin(\Theta)/\lambda)^2}{\sin(\pi d \sin(\Theta)/\lambda)^2}\,. \tag{2.31}$$

The first term corresponds to the single slit diffraction, while the second term corresponds to the interference of the light passing through the slits. Figure 2.5 shows the diffraction pattern of a grating spectrometer. Maxima in intensity are found at the observation angles

$$\sin(\Theta) = \frac{m\lambda}{d}\,, \tag{2.32}$$

where m is the diffraction order. Equation (2.32) shows that wavelengths may overlap in different orders, effectively limiting the spectral range of the spectrometer. The resolving power of the grating spectrometer is given by

$$R = \frac{\lambda}{\Delta\lambda} = mN\,, \tag{2.33}$$

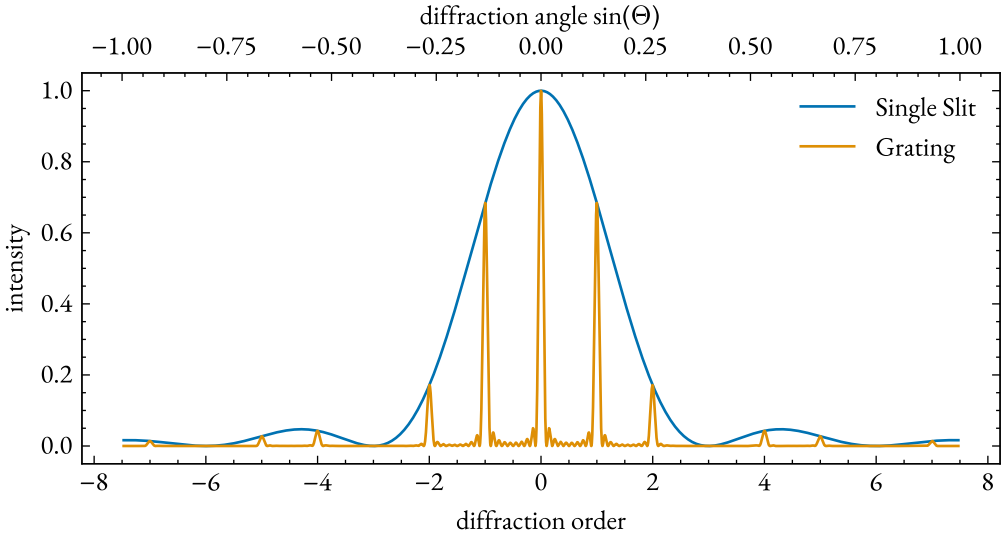

Figure 2.5: Fraunhofer diffraction pattern of a grating spectrometer. The single slit diffraction (blue) envelops the grating diffraction pattern (orange). The spectrum was calculated for a monochromatic light source with $\lambda = 2$ µm and a grating with $N = 10$ slits of width $b = 5$ µm and a slit distance of $d = 15$ µm.

where $\Delta\lambda$ is the spectral resolution, i.e., the smallest wavelength difference that can be detected. The spectral resolution can be improved by increasing the number of slits or the diffraction order. Real grating spectrometers consist of several optical and electrical components, e.g., apertures, a collimator, a grating, and a detector. The response to a monochromatic signal of the detector is called instrument line shape (ILS), and it turns out that for many grating spectrometers a Gaussian profile is a sufficient approximation (Beirle et al., 2017; Mouroulis and Green, 2018). The optical components project the incoming light onto a detector array, which samples the spectrally resolved intensity distribution in discrete channels.

2.2.2 Push-Broom Imaging

Push-broom imaging is a common concept for imaging spectrometers. It requires no moving parts, making it robust and reliable. Figure 2.6 shows the principle configuration of a push-broom imaging spectrometer. The incoming light is focused onto a slit, which cuts out a narrow stripe from the scene. The light passes a collimating mirror, which projects the stripe onto a detector array through a dispersing element and lens optics. The slit is oriented perpendicular to the push-broom direction, denoted as x' in Figure 2.6. Thus, the spectrometer's FOV covers only a narrow angle in the push-broom direction but accepts a larger angle perpendicular to the push-broom direction y'. Radiance from different angles along y' are mapped to different spatial lines y of the detector. The dispersing element splits the light into its spectral components, which are recorded in spectral channels z of the detector element. The spectrometer's FOV moves along the push-broom direction between two detector readouts. Thus, push-broom spectrometer sample the spatial dimension x' over time t. Airborne or satellite push-broom imaging spectrometers scan the scene by moving the instrument platform over the ground. In contrast, the ground-based

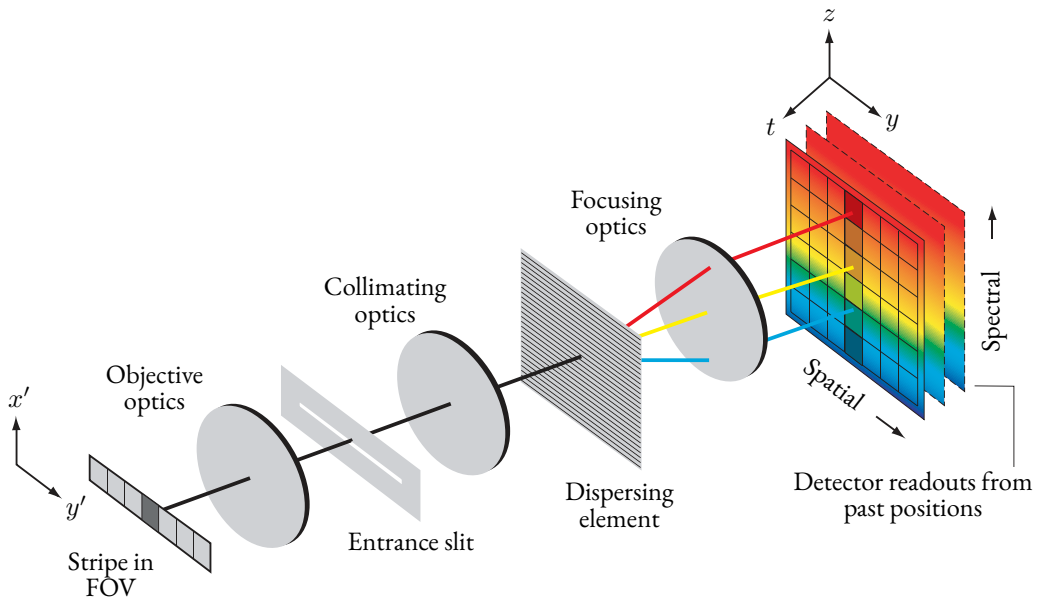

Figure 2.6: Optical setup of a push-broom imaging spectrometer. A stripe of the scene is projected onto a detector array through a dispersing element and a lens and mirror optics. An entrance slit cuts out the stripe from the scene, limiting the field of view (FOV) in push-broom direction. The dispersing element splits the light into its spectral components, which are recorded in spectral channels of the detector array. The scene is scanned along the push-broom direction. The figure was adapted from Shaw and Burke (2003) and Baumgartner (2022).

camera in this thesis scans a horizontal scene by rotating around a vertical axis. In both cases, a hyperspectral image is a three-dimensional data cube consisting of two spatial dimensions and one spectral dimension. This thesis refers to the spectral dimension coordinate as *channel*, the spatial coordinate on the detector as *line*, and the scanning spatial coordinate as *frame*[5].

Interpreting the observed signal requires a characterization of the instrument. Standard procedures include geometric and spectral calibration. The spectral dimension is calibrated similarly to a conventional spectrometer, including the ILS and the wavelength calibration of the channels. The full width at half maximum (FWHM) of the ILS is a typical measure of the instrument's spectral resolution. Similar quantities exist for the spatial dimensions, e.g., the point spread function (PSF) describes the instrument response to a point source in both lines and frames. A geometrical calibration provides the viewing angle of each line, comparable to a wavelength calibration of the channels. However, both calibrations are not independent - the wavelength calibration of the channel typically varies with the line ("smile"), and the geometrical calibration with the wavelength ("keystone"). In addition to the effects induced by the optical setup, the detector affects the recorded signal. Ideally, every detector pixel responds equally and linearly to incoming radiation. In reality, irregularities and the quantum efficiency of the detector material cause a non-uniform response, which can be accounted for by a flatfield correction (e.g., Kokka et al., 2019). Typically,

[5] In airborne applications, the push-broom direction is parallel to the flight direction. The names *across-track pixels* for lines and *along-track pixels* for frames are typically used, but they are confusing in the context of ground-based imaging.

some detector pixels exhibit erratic or non-linear behavior and thus are excluded by a bad pixel mask. Numerous potential instrument specifications (for example, the ILS varies with the incident light angle) inspire ongoing research efforts in specialized calibration facilities (Geladi et al., 2004; Gege et al., 2009; Baumgartner et al., 2012; Baumgartner, 2022). Sections 3.1 and 3.2 present characterization measurements for the spectral camera employed in the context of this thesis.

Every illuminated detector readout contains the radiometric response, a dark signal, and an offset. Thermal electrons cause the dark signal in the detector, which piles up during the image acquisition. Thus, a background correction is required, which is typically performed by taking dark frames before or after the image acquisition. These frames are subtracted from the observed signal. Furthermore, each observation contains an amount of noise. The relevant noise sources in hyperspectral imaging are dark noise, read noise, and photon noise (e.g., Lenhard et al., 2015). The quality of an observation is typically quantified by the signal-to-noise ratio (SNR), which is the ratio of the signal to the standard deviation of the noise signal. The SNR is a function of the integration time, spatial pixel size, and spectral resolution. Detecting a spectral signal at a certain SNR requires a trade-off between the instrument's specifications. For example, improving the spatial resolution requires decreasing spectral resolution or increasing integration time to keep the SNR constant. Depending on the mission objective, sensors are designed to fit the respective requirements, e.g., Hill and Nassar (2019), Strandgren et al. (2020), and Wilzewski et al. (2020).

2.2.3 Imaging of Greenhouse Gases

Imaging of GHGs is a rapidly advancing field of scientific research. Most efforts revolve around images from either satellites or airplanes using a top-down viewing perspective. These platforms offer regional to global coverage within a day to weeks, proving to be invaluable tools for comprehending, among other, the global carbon cycle. Top-down viewing spectrometers observe back-scattered sunlight from the Earth's surface. The observations provide atmospheric trace gas contents and, ultimately, fluxes of source and sinks. Since emission inventories typically rely on bottom-up estimates (e.g., mass of burned coal $\times$ CO_2 per coal mass), satellite observations provide an independent validation of these estimates (e.g., Miller and Michalak, 2017; Palmer et al., 2021). The following section gives a brief overview of past and ongoing GHG observing missions. It is in no way exhaustive, but focuses on CO_2 and CH_4 imaging efforts and closely related research. Although this thesis presents stationary ground-based imaging, most concepts are similar to airborne and satellite applications.

Satellite and Airborne Missions

Satellite missions can broadly be divided into area flux mappers or point source imagers (Jacob et al., 2022). Area flux mappers constrain regional and global fluxes of GHGs. Thus, they measure atmospheric total columns with sub-percentage precision in large ground pixels of 0.1 km to 10 km using a spectral resolution below 1 nm. The longest ongoing mission dedicated to GHG observation is the Greenhouse gases Observing SATellite (GOSAT) mission. It provides global CO_2 and CH_4 maps since 2009 (Kuze et al., 2009; Butz et al., 2011; 2013). Kort et al. (2012) used GOSAT data to detect CO_2 emissions from the LA basin, and especially the long time series provides valuable research opportunities (e.g., Maasakkers et al., 2019; Zhang et al., 2021; Metz et al., 2023). Since 2018, the TROPOspheric Monitoring Instrument (TROPOMI) instrument onboard the Sentinel-5

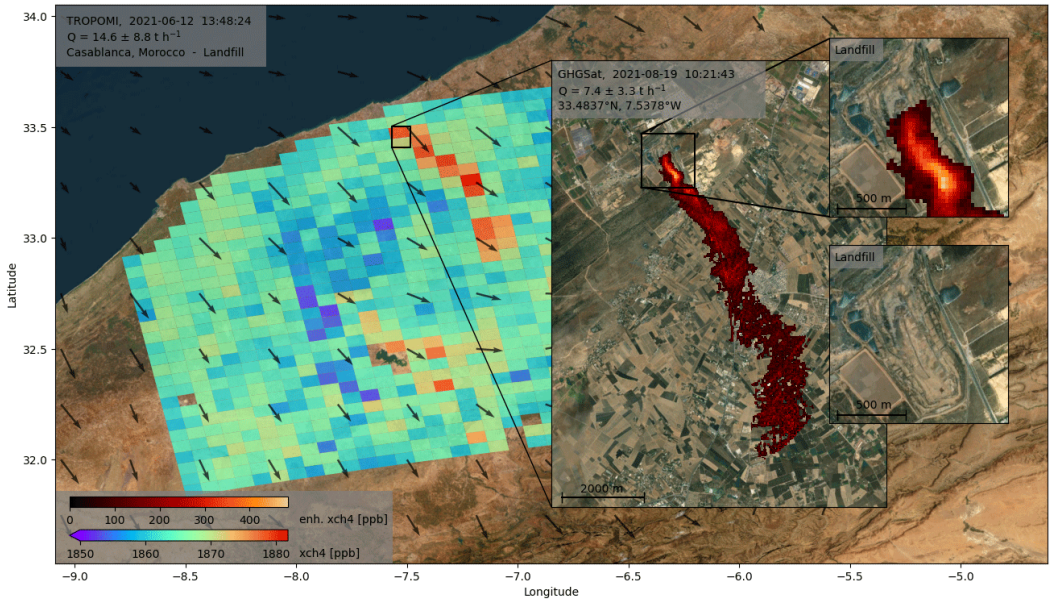

Figure 2.7: Example observations of CH_4 plumes observed with TROPOMI and Greenhouse Gas Satellite (GHGSat) missions taken from Schuit et al. (2023). The increased spatial resolution of GHGSat allows for the identification of individual sources (landfill in Casablanca, Morocco) and turbulent plume features.

Precursor (Sentinel-5P) satellite has been the first European area flux mapper, providing daily global CH_4 and CO maps, among other data (Veefkind et al., 2012; Borsdorff et al., 2018). The CH_4 dataset can provide global maps (Hu et al., 2018) and emission estimates of hotspot regions (Pandey et al., 2019; Varon et al., 2019; Sadavarte et al., 2021; Varon et al., 2021; Lauvaux et al., 2022; Maasakkers et al., 2022). Using TROPOMI, Varon et al. (2023) present weekly CH_4 emissions from the Permian Basin, U.S., which is promising for potential future near-real time applications. Schuit et al. (2023) present the first efforts of a fully automated source identification and quantification pipeline using machine learning techniques. Using annual time series of TROPOMI data, Nesser et al. (2023) shows sensitivity to CH_4 emissions from single landfills in the United States. The National Aeronautics and Space Administration (NASA) dedicated two satellite missions to CO_2, the Orbiting Carbon Observatory 2 (OCO-2) and Orbiting Carbon Observatory 3 (OCO-3) missions, providing global CO_2 maps since 2014 and 2019, respectively (Crisp et al., 2012; Eldering et al., 2017; Eldering et al., 2019). OCO-2 identified fluxes from localized sources (e.g., Schwandner et al., 2017), for the first time down to individual power plants (Nassar et al., 2017). Hakkarainen et al. (2023) use OCO-3 and TROPOMI observations to investigate strong anthropogenic sources in Africa, a region where measurements are typically sparse (Bauwens et al., 2020; Levelt et al., 2023). The upcoming CO2 Monitor (CO2M) (Sierk et al., 2019) mission will be a CO_2 area mapper with the capability to detect CO_2 emissions from cities and power plants in single overpasses (Kuhlmann et al., 2019; 2021).

Point source imagers are dedicated instruments for identifying and quantifying GHG emissions on the local to facility scale, e.g., power plants or the oil and gas industry. Figure 2.7 shows an example of a CH_4 plume observed with GHGSat and TROPOMI taken from Schuit et al. (2023).

The ground pixel size of point source imagers is typically 5 m to 60 m, while the spectral resolution is lower than for area flux mappers and on the order of 5 nm to 13 nm. Spectra from point source imagers typically cover several hundreds of nanometers, providing multipurpose datasets from GHG imaging to surface-type classification. They have recently received particular attention since they provide an effective tool for monitoring sector-specific emissions and identifying mitigation opportunities (Frankenberg et al., 2016; Duren et al., 2019; Nisbet et al., 2020; Thorpe et al., 2020; Ocko et al., 2021). Current in-orbit satellites are the PRecursore IperSpettrale della Missione Applicativa (PRISMA) (Cogliati et al., 2021), Environmental Mapping and Analysis Program (EnMAP) (Guanter et al., 2015), and GHGSat Jervis et al. (2021) missions. They proved to be able to identify and quantify CH_4 emissions from gas leakages, landfills, oil and gas infrastructure, and coal mine activities down to several 100 $kgCH_4\,h^{-1}$ (Varon et al., 2018; Varon et al., 2019; Guanter et al., 2021; Varon et al., 2021; Maasakkers et al., 2022; Roger et al., 2023b). Recently, dedicated CO_2 point source imagers were proposed for monitoring localized sources with emissions down to medium-sized power plants (1 $MtCO_2\,yr^{-1}$ to 10 $MtCO_2\,yr^{-1}$) (Strandgren et al., 2020; Wilzewski et al., 2020).

Airborne missions provide more profound insights into targeted regions. However, using airplanes is typically limited to the period of one to several measurement campaigns. Nonetheless, the high spatial resolution and shorter revisit time enable the detection of smaller sources and a limited option to estimate source variability and intermittency. The Airborne Visible/Infrared Imaging Spectrometer (AVIRIS) (Green et al., 1998) pioneered airborne imaging of CH_4 and CO_2 point sources (Roberts et al., 2010; Dennison et al., 2013; Thorpe et al., 2013). Its successor, the AVIRIS-NG (Next Generation, Hamlin et al., 2011), has been used for a plethora of campaigns observing emission plumes of GHGs (Thorpe et al., 2013; Frankenberg et al., 2016; Thorpe et al., 2016; 2017; Duren et al., 2019; Thorpe et al., 2020; Cusworth et al., 2021a; b; Thorpe et al., 2021; Cusworth et al., 2022; Jongaramrungruang et al., 2022; Yu et al., 2022). The German Methane Airborne MAPper (MAMAP) mission (Gerilowski et al., 2011; Krings et al., 2011) produces similar results, e.g., for power plants in Germany (Krings et al., 2011) and coal mine ventilation shafts in Poland (Krings et al., 2013; Krautwurst et al., 2021), but also operates worldwide (Krautwurst et al., 2017). The MethaneAIR mission (Chulakadabba et al., 2023; Conway et al., 2024) is a precursor to the MethaneSAT satellite, a high-precision point-source imager that is scheduled for 2024.

Ground-Based Observations

Ground-based imaging of GHGs is a relatively new field of research, particularly considering quantitative flux estimations. For CH_4, OGI techniques exist, but they are designed for qualitative leak detection on the meter scale (Zeng and Morris, 2019; Zimmerle et al., 2020). Using a Fourier transform infrared (FTIR) camera in the TIR spectral range, Gålfalk et al. (2016) observed and quantified CH_4 emissions down to 25 $g\,h^{-1}$. Operating in the TIR requires a temperature contrast between the gas and the atmosphere and limits the observation distance to a few hundred meters. The camera successfully operated at waste incineration or wastewater treatment plants (Gålfalk et al., 2017; Gålfalk and Bastviken, 2018; Gålfalk et al., 2022).

Ground-based emission measurements are valuable validation opportunities for the aforementioned satellite and airborne missions. Observations using surface-reflected radiation are challenging due to the significant background concentration of CH_4 and, especially, CO_2. Furthermore,

variations in the spectral albedo of the Earth's surface can introduce artifacts in the retrieval algorithms (e.g., Ayasse et al., 2018; Bell et al., 2023; Roger et al., 2023a). Therefore, complementary validation measurements to satellite observations are essential to ensure the quality of the data products. Ground-based networks like the Total Carbon Column Observing Network (TCCON) (Wunch et al., 2011) and COllaborative Carbon Column Observing Network (COCCON) (Frey et al., 2019) provide high-precision column measurements above land surfaces, while opportunities above the ocean are emerging (Klappenbach et al., 2015; Knapp et al., 2021; Butz et al., 2022). Since point source imagers target fluxes from localized sources, coinciding ground-based emission estimates are a promising tool for validating their emission estimates. Furthermore, controlled release experiments allow testing methods in a single-blind evaluation (e.g., Chulakadabba et al., 2023; Sherwin et al., 2023). Generally, stationary observations trade spatial coverage for temporal resolution. Thus, they can give insights beyond the snapshot images from top-down observations, e.g., source dynamics or biases due to turbulent transport (Bhardwaj et al., 2022; Brunner et al., 2023).

3 Instruments and Observations

The field instrumentation consists of several instruments in addition to the spectral camera, providing a comprehensive data suite for plume image interpretation. The heart of the setup is the HySpex SWIR-384 imaging spectrometer. Section 3.1 introduces the imaging spectrometer and the characterization measurements performed in the laboratory in addition to the manufacturer's specifications. Section 3.2 describes how the observation geometry of the camera is determined in field observations, including the augmentation of the camera with an inertial navigation system (INS). Finally, Section 3.3 introduces the light detection and ranging (LIDAR) system Windranger 200, which provides information on the wind field in the observation area.

3.1 HySpex SWIR-384

The HySpex SWIR-384 camera is a commercially available hyperspectral camera by Norsk Elektro Optikk (NEO). It is a push-broom imager operating in the SWIR spectral range from 950 nm to 2500 nm. The camera accepts light from an FOV of 279 mrad (16°) perpendicular and 0.73 mrad parallel to the push-broom direction. A collimating mirror projects the light onto a transmission grating, which disperses the light onto a mercury cadmium telluride (MCT) detector array. The detector is cooled to 147 K during operation to reduce dark current. It samples the spatial dimension of the image with 384 pixels, called *lines*, and the spectral dimension with 288 pixels, called *channels*. Each line covers an opening angle of approximately 0.73 mrad. The manufacturer provides a linear wavelength calibration of the detector with a constant spectral sampling distance (SSD) of 5.45 nm per channel. A detector readout is in analog-to-digital converter (ADC) units with a 16-bit resolution, representing radiance between 1 DU and $2^{16} - 1$ DU.
Figure 3.1 shows the camera's observation principle. A tripod is the support for the camera's rotation stage. The stage rotates the camera clockwise during operation, so the push-broom direction is horizontal. Each rotation step equals the angular distance of the camera's horizontal opening angle. The detector readout in a rotation step is called a *frame*. Moving the camera's FOV over the target scene results in a data cube with dimensions $\text{number of frames} \times \text{number of lines} \times \text{number of channels}$, called a *scan*. Every pixel in the scan contains a spectrum of the observed scene. At the beginning and end of each scan, a shutter closes the camera to collect 200 dark readouts of the detector. A rugged, field-deployable GETAC® laptop controls the camera and the rotation stage. A Jackery® Explorer 1000 battery (1002 W h) with a Jackery® SolarSaga 100W solar panel provides power to the camera and laptop for more than six hours of consecutive measurements.

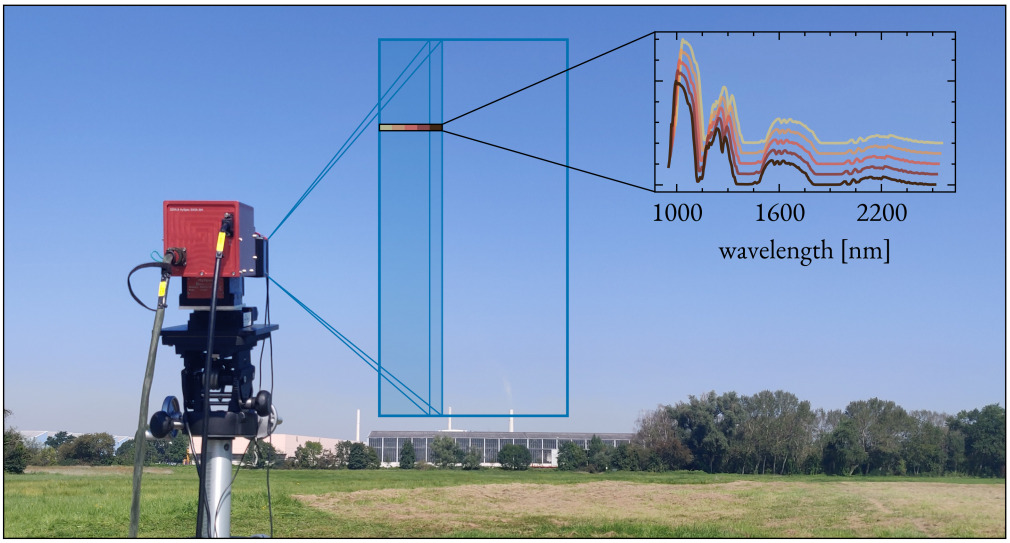

Figure 3.1: The geometry of ground-based push-broom imaging. The stationary camera is mounted on a tripod and rotates around the vertical axis. The blue rectangle indicates the field of view of a scan. The camera's FOV moves over the target scene via rotation. Blue shaded pixels represent the observed part of the scan. One line is highlighted, and the inset axis shows the observed spectra. Colors from red to yellow denote spectra in the line observed in previous frames. The wavelength axis corresponds to the "latest" (dark red) spectrum - "earlier" spectra are shifted to the upper right. The scan's FOV includes the source at the bottom of the image, in this case a chimney of a coal-fired power plant.

3.1.1 Hyperspectral Images

Each scan is a hyperspectral data cube DN_{zjk} where z is the channel, j is the line, and k is the frame. The detector pixels accumulate photo-electrons during the integration time t_{int}. The signal of a frame follows as

$$DN_{zj} = N_{\text{ph},zj} \cdot QE_z \cdot SF \cdot RE_{zj} + BG_{zj} \,, \tag{3.1}$$

where N_{ph} is the incoming number of photons, QE is the quantum efficiency (photo-electron to photon ratio) of a channel, SF is a scaling factor expressing DU per photo-electron, RE is the relative responsitivity matrix, and BG is the dark signal background (NEO, 2014). RE is a matrix with an average value of one that represents sensor non-uniformity. The background contribution is the sum of dark current in the detector and a baseline contribution. The baseline contribution BS ensures positive values for the ADC. Dark current DC describes the number of observed photo-electrons due to thermal fluctuations. Therefore, BG is given by

$$BG_{zj} = DC_{zj}(t_{\text{int}}) + BS_{zj} \tag{3.2}$$

$$= SF \cdot \beta_{zj}(T) \cdot t_{\text{int}} + BS_{zj} \,, \tag{3.3}$$

where $\beta(T)$ is a temperature dependent flux in electrons per second. Appendix A.1.1 presents laboratory measurements for DC_{zj} and BS_{zj} of the detector. It shows a background contribution

of $BG \approx 541\,\mathrm{DU\,ms^{-1}} \cdot t_{\mathrm{int}} + 2702\,\mathrm{DU}$ in the channels of the retrieval. Each scan includes a detector background before $BG_{zj}^{\mathrm{before}}$ and after BG_{zj}^{after} the rotation. The backgrounds are averages of 200 dark detector readouts with the same integration time as used for frames during rotation. The background correction interpolates linearly between $BG_{zj}^{\mathrm{before}}$ and BG_{zj}^{after} to account for drifts during the scan. Thus, the background corrected image LN_{zjk} reads

$$LN_{zjk} = DN_{zjk} - BG_{zj}^{\mathrm{before}} - \frac{BG_{zj}^{\mathrm{after}} - BG_{zj}^{\mathrm{before}}}{\text{number of frames}} \cdot k\,. \tag{3.4}$$

Following Equation (3.1), the signal in each detector element depends on the number of incoming photons $N_{\mathrm{ph},zjk}$. The number of incoming photons is the integrated radiance divided by the photon energy, i.e.,

$$N_{\mathrm{ph},zjk} = \frac{L_{zjk} \cdot t_{\mathrm{int}} \cdot A \cdot \Omega \cdot \Delta\lambda \cdot \lambda_z}{h \cdot c}\,, \tag{3.5}$$

where L is the radiance, t_{int} is the integration time, A is the entrance aperture area, Ω is the solid angle of one detector pixel, and $\Delta\lambda$ is the SSD. Combining Equations (3.1) and (3.5), and assuming the background correction holds, the observed radiance L_{zjk} in each detector pixel and frame fulfills

$$L_{zjk} \propto \frac{LN_{zjk}}{RE_{zj} \cdot QE_z \cdot \lambda_z}\,. \tag{3.6}$$

Preprocessing a raw scan includes correcting the data according to Equation (3.6). This procedure yields spectral measurements proportional to the observed radiance for further processing. The employed retrieval algorithm does not require a radiometric calibration. Therefore, a measurement proportional to radiance is sufficient.

3.1.2 Characterization

The HySpex camera comes with the manufacturer's spectral, spatial, and radiometric calibration. Laboratory measurements were performed to either validate or complement the manufacturer's calibration. The following paragraphs describe the results of these measurements. The first paragraph investigates the camera's noise level and its contributions. The next paragraph presents laboratory measurements of the camera's ILS following Lenhard et al. (2015). Furthermore, a localized correction to the manufacturer's wavelength calibration is introduced. The correction builds on the concept of Guanter et al. (2021) and the results of Siegel (2023) using the matched filter retrieval of Section 4.1. Finally, the manufacturer's bad pixel mask (BPM) is extended with a conservative approach for identifying irregularities in detector pixels.

Noise

The signal from each detector pixel contains three types of noise: photon noise, dark noise, and read noise (e.g., Lenhard et al., 2015; Baumgartner, 2022). The detector electronics read the signal after the integration time. The signal consists of photo-electrons observed due to dark current

or incoming photons. The photo-electron statistics follow a Poisson distribution. The respective noise terms are photon noise σ_{ph} and dark noise σ_{DC}, given by

$$\sigma_{\mathrm{ph}} = SF \cdot \sqrt{QE \cdot N_{\mathrm{ph}}} \propto \sqrt{t_{\mathrm{int}}} \tag{3.7}$$

$$\sigma_{\mathrm{DC}} = SF \cdot \sqrt{\beta(T) \cdot t_{\mathrm{int}}} \propto \sqrt{t_{\mathrm{int}}}\,, \tag{3.8}$$

assuming $N_{\mathrm{ph}} \propto t_{\mathrm{int}}$ (Equation (3.5)). Finally, every spectrum contains additional read noise σ_{r}. This simplified term collects all one-time contributions to the noise from a single readout. It encompasses detector electronics, baseline noise, and quantization noise from the ADC. The read noise typically follows a Gaussian distribution (Baumgartner, 2022). Assuming the noise terms are uncorrelated, the total noise of a single readout σ_{sin} follows from

$$\sigma_{\mathrm{sin}} = \sqrt{\sigma_{\mathrm{ph}}^2 + \sigma_{\mathrm{dc}}^2 + \sigma_{\mathrm{r}}^2} \tag{3.9}$$

$$= \sqrt{SF^2 \cdot QE \cdot N_{\mathrm{ph}} + SF^2 \cdot \beta(T) \cdot t_{\mathrm{int}} + \sigma_{\mathrm{r}}^2}\,. \tag{3.10}$$

The signal-to-noise ratio (SNR) of a single scan follows as

$$\mathrm{SNR}_{\mathrm{sin}} = \frac{SF \cdot QE \cdot N_{\mathrm{ph}}}{\sqrt{SF^2 \cdot QE \cdot N_{\mathrm{ph}} + SF^2 \cdot \beta(T) \cdot t_{\mathrm{int}} + \sigma_{\mathrm{r}}^2}}\,. \tag{3.11}$$

Still assuming that the $N_{\mathrm{ph}} \propto t_{\mathrm{int}}$, Equation (3.11) shows that the SNR increases with $\sqrt{t_{\mathrm{int}}}$ if the signal or the dark noise are the dominant noise contributions, while the SNR increases linearly with t_{int} as long as the read noise dominates.

Typical exposure times for field observations are on the order of 10 ms. Since the sky-scattered sunlight is weak in the SWIR spectral range, the camera observes 500 DU to 1000 DU between 1900 nm and 2500 nm on clear days. This equals a detector signal saturation of 0.8 % to 1.5 % after background subtraction. Dark noise dominates in such observations since

$$\frac{\sigma_{\mathrm{DC}}}{\sigma_{\mathrm{ph}}} = \sqrt{\frac{10\,\mathrm{ms} \cdot 541\,\mathrm{DU\,ms^{-1}}}{1000\,\mathrm{DU}}} \approx 2.3\,.$$

The maximum saturation of the detector pixels limits the integration time. Co-adding of spectra can increase the SNR beyond the limit of single measurements. The total SNR of n co-added spectra is given by

$$\mathrm{SNR}_{\mathrm{tot}} = \frac{SF \cdot QE \cdot \sum_{i=1}^{n} N_{\mathrm{ph},i}}{\sqrt{\sum_{i=1}^{n} \sigma_{\mathrm{sin},i}^2}} \tag{3.12}$$

$$= \frac{\mathrm{SNR}_{\mathrm{sin}}}{\sqrt{n}}\,, \tag{3.13}$$

where Equation (3.13) holds for identical observations. Improving the SNR of an observation is particularly important for CO_2 imaging, as demonstrated later in Chapter 6. Figure 6.3 shows how a plume observation of CO_2 improves for increasing numbers of contributing scans. Pöhler

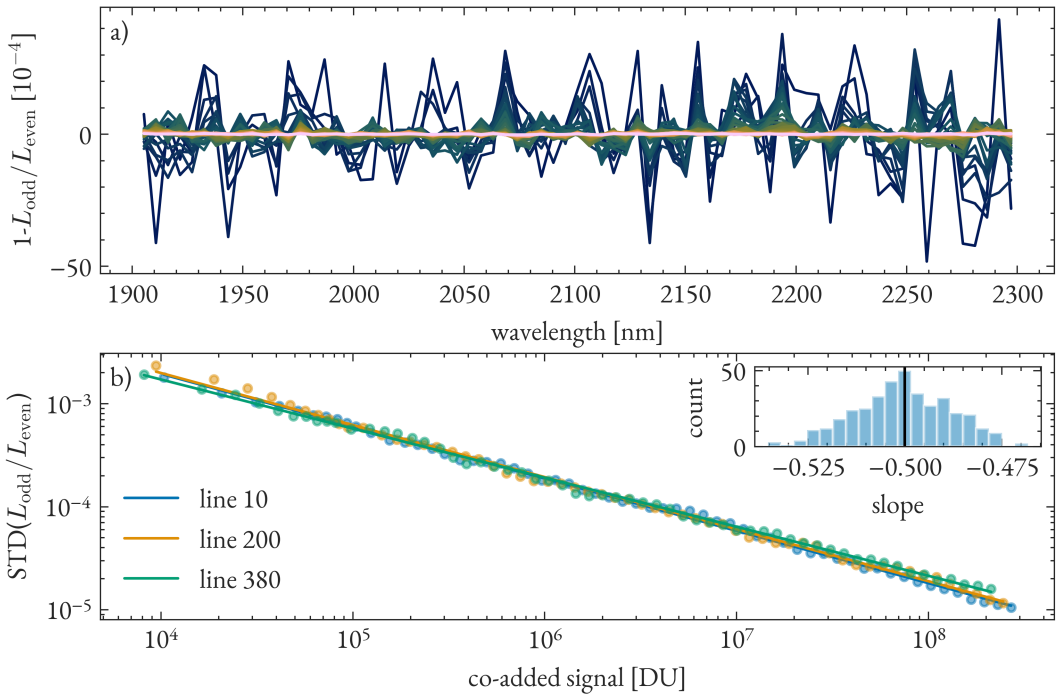

Figure 3.2: Panel a) shows how the division of two spectra evolves with higher numbers of co-addition. The blue-to-white colors represent 58 co-addition levels between 1 and 26 000 spectra. Panel b) shows the evolution of the standard deviation of the divided spectra, representing the remaining noise. The three lines shown are taken in the detector center and on the edges. The inset histogram shows the distribution of fit slopes over all 384 lines, scattering around the theoretical value of −0.5.

(2011) describes a technique to quantify the SNR of co-added spectra and validate the sensor's behavior. An integrating sphere illuminates the camera's entrance homogeneously. The integrating sphere's light sources are four stabilized halogen lamps. Dividing two spectra by each other removes systematic features from the measurements. The division spectra noise increases by a factor of $\sqrt{2}$ compared to a single spectrum's (relative) noise. Co-adding an increasing number of spectra before calculating the division spectrum decreases the spectrum noise according to Equation (3.12). Figure 3.2 shows the results from the total noise test. The camera observed 52 000 spectra ($t_{\mathrm{int}} = 9.8$ ms) in each line while pointing into an integrating sphere. Summing the spectra in an alternating fashion removes systematic changes during the measurement period, e.g., due to the light source. Alternating means adding all odd-numbered and all even-numbered spectra. Thus, the two co-added spectra contain measurements from the start and end of the experiment equally. Figure 3.2a shows how the division spectra noise decreases with increasing co-additions. Figure 3.2b illustrates the dependency of the noise on the total signal for three detector lines. The lines lie in the detector center and on the edges. An inset histogram shows the distribution of the noise behavior of all lines, indicating that the detector behaves as expected.

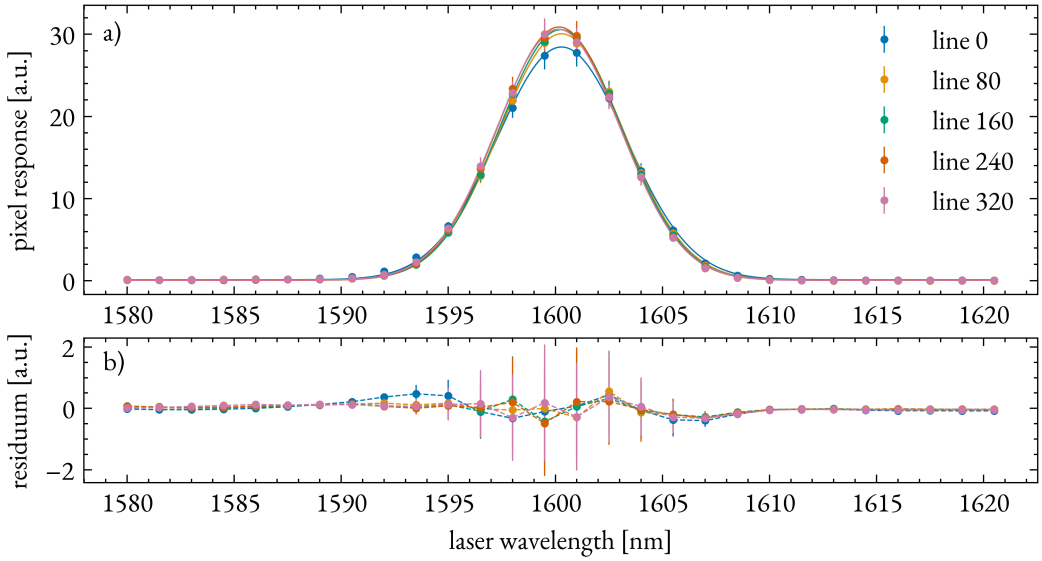

Figure 3.3: Laboratory measured ILS of the HySpex SWIR-384 camera in channel 119. The camera pointed into an integrating sphere illuminated by a tunable diode laser. The laser wavelength was adjusted in 1.5 nm steps so the ILS wanders across the channel. Panel a) shows the measurements at selected lines and a Gaussian fit to the data points. Panel b) shows the residuals to the Gaussian fit. Each data point is a 286-frame mean, and the error bar is the standard deviation.

Instrument Line Shape

The ILS is the response of the spectrometer's optical components to a monochromatic signal. It determines how the at-sensor radiance (ASR), i.e., the true signal entering the spectrometer, arrives at the detector. Thus, the ILS is crucial for interpreting the observations. The spectrum arriving at the detector $L(\lambda)$ is given by the convolution of the ASR $I(\lambda)$ with the ILS:

$$L(\lambda) = I(\lambda) * \mathrm{ILS}(\lambda)\,. \tag{3.14}$$

The ILS emerges from the interplay of all optical components and is typically too complex to be reproduced by a physical model (Beirle et al., 2017). However, it can be measured using quasi-monochromatic light sources in the laboratory.

The manufacturer uses atomic emission lines[1] to characterize the HySpex camera's resolution. The oversampling of the ILS is the ratio of the ILS width, usually taken as its FWHM, to the SSD of the detector. The HySpex camera has an oversampling ratio of approximately 1.3. Thus, the spectrometer resolves the ILS only with 1 to 2 channels. The manufacturer uses the trapezoidal method to calculate the FWHM of the ILS. This method yields a resolution close to the SSD if the ILS peaks in the center of a channel, while it approaches twice the SSD if the ILS falls between two channels. Therefore, the manufacturer provides only an approximate value of the spectral resolution.

[1] The manufacturer characterizes four wavelengths using lamps containing Mercury (1014 nm), Krypton (1443 nm), Argon (1694 nm), or Xenon (2026 nm).

Lenhard et al. (2015) employ a tunable diode laser to improve on the ILS measurements provided by NEO. The laser source illuminates an integrating sphere that completely covers the HySpex camera's FOV. Thus, the sphere illuminates all lines simultaneously, enabling an ILS characterization of the entire detector. The camera takes a scan without rotating, pointing into the sphere during all frames. The procedure alternates between adjusting the laser wavelength and taking a scan with the camera. The laser scans a wavelength interval from 1580.0 nm to 1620.5 nm in 1.5 nm steps. Thus, the ILS moves along the spectral detector dimension. Figure 3.3 shows measurements of channel 119 in selected lines of the detector. The channel response increases as the laser wavelength approaches the channel center wavelength and decreases after the laser passes by it. A Gaussian fit describes the ILS in every line, finding the FWHM and center wavelength. According to the Gaussian model, the spectral resolution of the camera is 6.7 nm to 7 nm. The results agree with the manufacturer's approximate calibration of $1.3 \cdot \mathrm{SSD} = 1.3 \cdot 5.45\,\mathrm{nm} \approx 7\,\mathrm{nm}$ using the 1694 nm Argon line.

Wavelength Calibration

The manufacturer's wavelength calibration assumes a simplified linear mapping from channel to wavelength. Furthermore, the manufacturer reports that the camera's design minimizes the detector's smile, i.e., the wavelength calibration dependency on the spatial detector axis. Observations of the center wavelength of channel 119 from the ILS calibration confirm a peak-to-peak smile of less than 0.5 nm. Thus, every line on the detector has, in good approximation, the same wavelength calibration. The following paragraphs describe a local correction to the manufacturer's wavelength calibration in the spectral intervals of the retrieval. The employed statistical retrieval necessitates this correction because, unlike physical retrieval algorithms, it does not include a wavelength shift when fitting molecular absorption features to observed spectra. Section 4.1 describes the GHG retrieval, a linearized matched filter, in detail. Errors in the wavelength calibration compromise the retrieval performance (Siegel, 2023). Exploiting spectral absorption features from field observations to adjust laboratory calibration data is widely used for hyperspectral sensors (Green et al., 2003; Gao et al., 2004; Brazile et al., 2008). Guanter et al. (2021) use a matched filter retrieval but employ a physical retrieval algorithm to optimize the wavelength calibration of the PRISMA satellite. Here, quality criteria from the matched filter itself serve to correct the camera's wavelength calibration.

According to the results of Siegel (2023), the cost function of the matched filter retrieval is a suitable quality criterion for correcting the spectral calibration. The matched filter minimizes the cost function, derived later in Equation (4.9), by fitting a target spectrum to the observed spectrum. The target spectrum is computed prior to the retrieval and relies on the spectrometer's wavelength calibration. Spectral misalignment of the observation and the target spectrum increases the optimal cost function. The presented method exploits this increase to improve the wavelength calibration in the spectral interval of the retrieval. Figure 3.4 illustrates the procedure, which finds an offset to the manufacturer's calibration. The matched filter performs a retrieval with multiple target spectra to determine the offset. Every target spectrum is computed using a different wavelength shift. The target spectrum facilitating the minimal cost function provides the wavelength calibration offset. Figure 3.4a shows an example observation of a CH_4 plume on June 19, 2022. The matched filter minimizes the cost function for each pixel. Pixels inside the

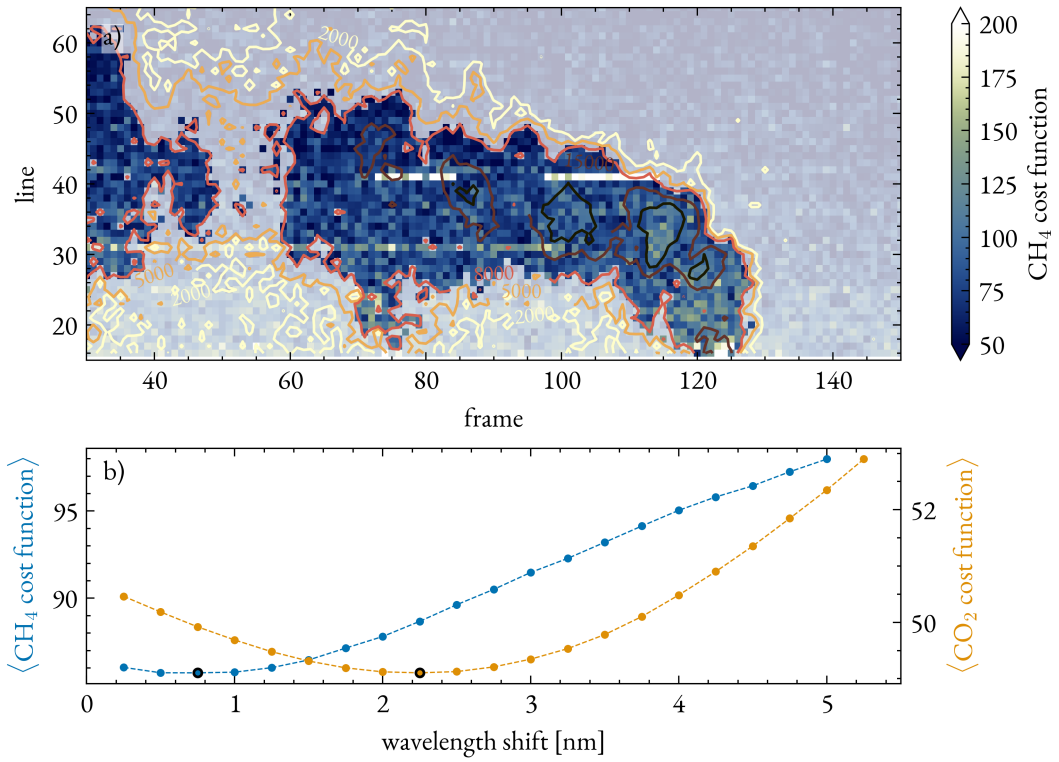

Figure 3.4: Panel a) shows a scene observed in June 2022 in Poland. The blue to white colors are the matched filter cost function of a methane retrieval (Equation (4.9)). The contour levels from yellow to red indicate the plume observation of 2000 ppm · m, 5000 ppm · m, 8000 ppm · m, 12 000 ppm · m, and 20 000 ppm · m. The average cost function is derived from the highlighted pixels with an enhancement above 8000 ppm · m. Panel b) shows mean cost functions within the plume for CH_4 (blue) and CO_2 (orange). The minimum, marked by a black circle, shows the wavelength correction of the respective spectral interval. The CO_2 calibration uses CO_2 enhancements above 250 000 ppm · m in an emission plume from a coal-fired power plant observed on September 9, 2021.

observed plume exhibit the highest enhancements and are affected most by a flawed spectral calibration. Thus, the quality criterion for the wavelength correction is the average cost function of plume pixels. Figure 3.4b shows the quality criterion for 0.25 nm to 5.25 nm wavelength shifts in 0.25 nm steps. The minimum is reached at 2.25 nm and 0.75 nm for the spectral intervals of CO_2 and CH_4, respectively. The spectral intervals of the retrieval are 1967 nm to 2260 nm for CO_2 and 2052 nm to 2395 nm for CH_4. The manufacturer's wavelength calibration is corrected with these offsets for the respective target signatures.

Bad Pixel Mask

The manufacturer provides a BPM for the camera, which, according to their test report, relies on a detailed analysis of observations under varying light conditions. Bad detector pixels respond irregularly to either an illuminated or dark detector, showing exceptionally little ("cold pixel") or high ("hot pixel") sensitivity or significantly increased variability. Lenhard et al. (2015) perform an

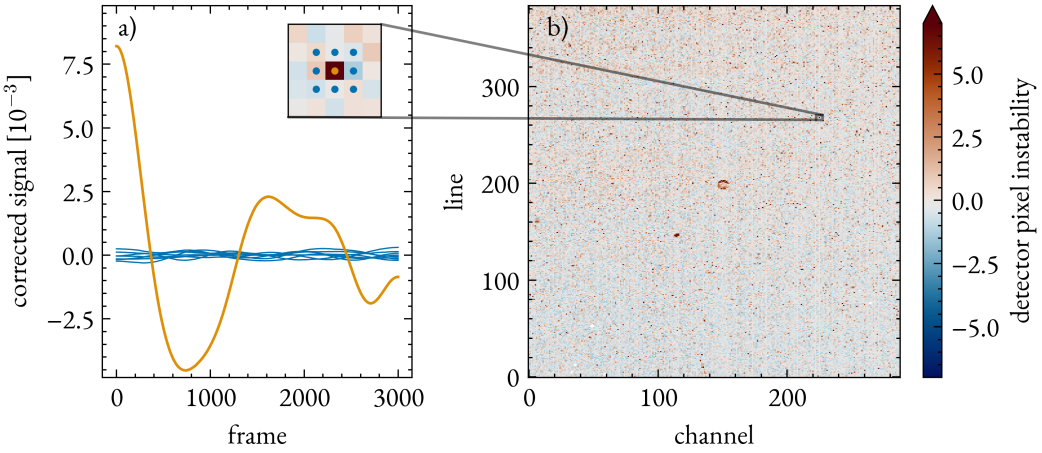

Figure 3.5: The procedure to improve the manufacturer's BPM identifies pixel of increased variability on the detector. Panel a) shows the behavior of an instable pixel (orange) compared to its adjacent pixels (blue). The detector pixel evolution is plotted over 3000 consecutive frames while the camera pointed into an integrating sphere. The inset axis zooms in on the detector area around one newly found bad pixel. The dots mark the origins of the lines. Panel b) shows the instability for each detector pixel.

independent laboratory characterization on two HySpex cameras, identifying a subset of NEO's BPM as bad pixels. Therefore, Lenhard et al. (2015) confirm the manufacturer's calibration, although they acknowledge that their observations are less extensive. The BPM is important in the context of this work to ensure a stable background statistic in the greenhouse gas retrieval, which relies on the observed spectra being alike when coming from the same signal (details in Chapter 4). Therefore, a custom BPM expands on NEO's BPM to conservatively exclude pixels with erratic behavior. The custom BPM extension targets spurious detector pixel fluctuations on the time scales of several hundred frames.

A laboratory experiment investigates the stability of all detector elements. The camera observed an integrating sphere without rotating during a scan. The aperture of the integrating sphere covered the camera's FOV completely. A typical spectrum showed maximum saturation of 50 % to 70 % at 1360 nm. Lenhard et al. (2015) only use pixels with signals above 1000 DU. Here, more than 99.6 % of the observed spectra satisfy this requirement. Thus, the BPM calculations were performed for the whole detector. The camera observed a series of 30 000 frames for each detector pixel. Appendix A.1.2 provides details on the evaluation method, which necessitates several corrections on the raw observations. The concept of bad pixel identification is to (a) identify a temporal evolution that is comparable for all detector pixels and (b) find outliers based on this evolution. The method finds the signal evolution for each detector pixel by accounting for light source instability, integrating sphere heterogeneity, and noise. Figure 3.5a shows the evolution in nine detector pixels after correction, highlighting an outlier. Well-behaved pixels exhibit only small variability in the evolution, represented as the standard deviation over the frames. Typical variability is on the order of 10^{-4}, with higher values in low signal channels above 2000 nm. Figure 3.5a illustrates that some detector pixels show significantly enhanced temporal variability. Figure 3.5b shows the instability of all detector pixels, which is the detector pixels variability

relative to the mean channel variability. The instability was calculated for ten intervals of 3000 frames. Pixels are considered bad if their instability surpasses a critical threshold in over half of these intervals. The extended BPM excludes an additional 291 pixels to the 55 pixels of NEO.

3.2 Camera Attitude and Heading

In the ground-based scanning operation of the HySpex camera, each pixel observes radiance from a distinct VEA and viewing azimuth angle (VAA). Both angles describe the observation geometry of a hyperspectral image. Later interpretation and processing of the data requires accurate knowledge of the observation geometry. Therefore, an MTi-7 Miniature GNSS/INS Module from XSENS® was mounted on the HySpex camera. The attitude and heading reference system (AHRS) model performed well in previous campaigns in ship-borne applications (Dörner et al., 2018). Laboratory performance tests of the AHRS by Sindram (2021) found a precision well below 0.05° for the instrument pitch and roll angle. All data transfers in real-time to the measurement laptop controlling the HySpex camera.

Prior to measurements, the AHRS observes the instrument's roll and pitch for ten minutes. Adjusting for potential offsets after this period results in a camera leveling of (0.0 ± 0.1)°. Subsequently, the camera's pitch is adjusted by tilting the camera such that the lower edge of the image contains the GHG source, usually a chimney or shaft. The sensor does not provide reliable data on the instrument's VAA in stationary operation. Therefore, the observation target serves as a landmark within the image. The forward azimuth angle of the landmark's frame in the image follows from the Global Positioning System (GPS) positions of the camera and landmark (WGS84 reference system, Slater and Malys, 1998). The angular distance between each frame is the horizontal opening angle of the camera of 0.73 mrad. Thus, the VAA of all frames of an image follows from their respective position to the landmark frame. Likewise, the VEA of the line containing the tip of the landmark follows from the landmark as

$$\mathrm{VEA} = \arctan\left(\frac{h}{D}\right), \tag{3.15}$$

where h is the landmark's height and D the distance between camera and landmark. The vertical pointing of each line is not perfectly equidistant, i.e., the vertical spatial resolution depends on the line. Sindram (2021) performed a spatial calibration and found the vertical opening angle of lines increasing from 0.65 mrad to 0.80 mrad from the upper to the lower image region. The VEA of each line is computed using this spatial calibration. Thus, the geometric area of each pixel A_j at the distance D to the target source is

$$A_j = D\tan(\Delta\mathrm{VEA}_j) \cdot D\tan(\Delta\mathrm{VAA}), \tag{3.16}$$

where $\Delta\mathrm{VEA}_j$ and $\Delta\mathrm{VAA}$ are the vertical and horizontal opening angles of the pixel, respectively. The HySpex SWIR-384 provides a spatial resolution of the image between 0.7 m and 3.0 m for typical observation distances of 1.0 km to 4.0 km. The uncertainties of VEA and VAA are below 1° for such distances (Sindram, 2021). If the landmark height is unknown, the AHRS pitch

angle is a substitute. The AHRS is attached to the camera, so its pitch angle measurement equals the center line's VEA.

3.3 Windranger 200

The Windranger 200 is a compact and lightweight wind LIDAR produced by METEK®. It complements the HySpex SWIR-384 field operations since early 2022, providing coinciding observations of wind speed and direction. The model operated successfully in previous campaigns, e.g., Adler et al. (2021) used it to study boundary layer turbulence. The instrument weighs approximately 50 kg, has dimensions of 840 mm x 540 mm x 580 mm, and consumes approximately 60 W during operation. A Jackery® Explorer 500 battery (518 W h) with a Jackery® SolarSaga 100W solar panel provides power for 8 h to 10 h of measurements. A built-in spirit level is used to level out the LIDAR position before the measurements. For absolute reference of wind direction, the Windranger needs to point to the North or another known azimuth reference point. The landmark used for the camera's VAA calibration also serves as the LIDAR reference point. The Windranger can observe wind speed and direction in up to ten levels up to 200 m. During HySpex co-deployment, it measures at six levels of 10 m, 20 m, 50 m, 100 m, 150 m, and 200 m. A laptop displays live observations to the operating personnel, who re-calibrate the height levels if the data quality decreases.

The Windranger uses the Frequency Modulated Continuous Wave (FMCW) technology (Peters, 2018). It continuously transmits light from a 1545 nm laser. The laser beam leaves the Windranger at 10° relative to the zenith and rotates by 360° once per second. A lens optic focuses the laser on a target height from which the LIDAR observes back-reflected radiance. The back-reflected light is Doppler-shifted by a frequency f_D according to

$$f_\mathrm{D} = -2f\frac{v_{||,\mathrm{wind}}}{c}, \tag{3.17}$$

where f is the laser frequency, c is the speed of light, and $v_{||,\mathrm{wind}}$ is the wind component along the laser beam. The frequency shift oscillates with the angular velocity of the laser rotation, assuming a constant wind field. The LIDAR measures the beat frequency of transmitted and received signals at 100 laser positions every rotation. The amplitude and phase of the beat frequency during the laser rotation inform about the wind speed and direction, respectively. Fitting the wind parameter to the data points provides a measurement at the target height. The method is sensitive to turbulent wind fluctuations within one rotation. However, it provides a complete profile approximately every 10 s, such that statistical fluctuations can be reduced by averaging over several rotations.

4 Methods

The methods necessary for measuring source flux from spectral images include retrieval and emission estimation. The retrieval refers to quantifying the amount of the target gas in each image pixel. Current retrieval techniques fall into two categories, namely physical and statistical techniques. This thesis employs a widely used statistical retrieval, the linearized matched filter. Section 4.1 describes the matched filter and its adaption to the specific measurement setup and challenges of ground-based imagery. The image of an active point source yields a two-dimensional projection of the three-dimensional emission plume. Emission estimation methods require correctly identifying the emission plume and subsequently calculating the underlying emission rate. Section 4.2 describes three methods for finding CO_2 and CH_4 emission rates from the spectral images in this thesis.

4.1 Matched Filter Retrieval

The matched filter is a statistical approach for signal identification and quantification in noisy data, e.g., hyperspectral images (Manolakis et al., 2014). It estimates a spectral background variability from the spatial distribution of absorption spectra and identifies a pre-defined spectral signature exceeding this variability. Here, the spectral signatures are absorption features of CO_2 or CH_4 around 2000 nm and 2300 nm, respectively. Alternatives to the matched filter are radiative transfer simulations that sequentially work through all spatial pixels. Such methods are the Iterative Maximum A Posteriori Differential Optical Absorption Spectroscopy (IMAP-DOAS), which has been employed for the evaluation of AVIRIS and AVIRIS-NG images (Thorpe et al., 2017; Borchardt et al., 2021), and full-physics methods applied to measurements with high spectral resolution such as collected by the GOSAT and the OCO-2 (Butz et al., 2011; O'Dell et al., 2012; O'Dell et al., 2018). While physics-based approaches produce a complete atmospheric state vector, e.g., multiple gas profiles, at once, they are computationally expensive, require *a priori* knowledge of the atmospheric state, and depend on complete forward models. In contrast, the matched filter algorithm is computationally cheap and requires only a single absorption spectrum as an input. Despite its simplicity, it has been applied successfully to many remote sensing applications. Dennison et al. (2013) use the matched filter to identify CO_2 emission plumes in AVIRIS images. Thompson et al. (2015) show that the matched filter is fast enough for real-time detection of CH_4 enhancements in AVIRIS-NG data. Guanter et al. (2021) examine images from the PRISMA satellite to showcase its CH_4 mapping capabilities with the matched filter. Zhang et al. (2022) and Cusworth et al. (2021b) quantify CH_4 emission fluxes in the Permian basin from airborne data using the matched filter. Recently, lognormal matched filter algorithms have been investigated to improve the quantification of gases in optically dense plumes (Schaum, 2021; Pei et al., 2023).

Table 4.1: Description of variables used in the matched filter retrieval. Bold symbols denote spectral vectors (dimensionality C) and vector arrows denote spatial vectors (dimensionality N).

Symbol	Description	Symbol	Description
j	image line (vertical)	k	image frame (horizontal)
$i \in N$	number of image pixels (line·frame)	C	number of channel in each pixel
$\boldsymbol{L}$	observed radiance vector	$\boldsymbol{\mu}$	mean radiance vector
$\boldsymbol{t}$	target spectrum	$\boldsymbol{s}$	unit absorption spectrum
$\mathbb{C}$	covariance matrix	α	gas enhancement
$\vec{w}$	regularization weight	$\vec{r}$	brightness factor
$\boldsymbol{l}$	differential spectral vector	σ	noise equivalent enhancement

4.1.1 Classic Matched Filter

The classic matched filter (CMF) is the optimal linear filter for maximizing the SNR of a signal in a noisy dataset (Manolakis et al., 2014). Here, it identifies a pre-defined spectral signature in a hyperspectral image. Let the image consist of N spectra $\boldsymbol{L}_i, i \in \{1, \dots, N\}$, each with C spectral channels[1]. The CMF assumes that the spectra follow a multivariate Gaussian distribution

$$\boldsymbol{L}_i \propto \mathcal{N}(\boldsymbol{\mu}, \mathbb{C}) \,, \tag{4.1}$$

where $\boldsymbol{\mu}$ is the mean spectrum and $\mathbb{C}$ is the covariance matrix. These background parameters follow from the observed spectra $\boldsymbol{L}_i$ as the sample mean $\boldsymbol{\mu}$ and covariance $\mathbb{C}$ with

$$\boldsymbol{\mu} = \frac{1}{N} \sum_{i=1}^{N} \boldsymbol{L}_i \,, \tag{4.2}$$

$$\mathbb{C} = \frac{1}{N-1} \sum_{i=1}^{N} (\boldsymbol{L}_i - \boldsymbol{\mu})(\boldsymbol{L}_i - \boldsymbol{\mu})^\mathsf{T} \,. \tag{4.3}$$

The matched filter identifies a linear target signature $\boldsymbol{t}$ in each spectrum. Assuming a gas enhancement α (in ppm · m) acts on the spectrum following Beer-Lambert's law, a measurement can be written as

$$\begin{aligned} \boldsymbol{L}(\alpha) &= \boldsymbol{\mu} \exp(-\alpha \boldsymbol{s}) + \boldsymbol{\epsilon} && (4.4)\\ &\approx \boldsymbol{\mu} \odot (\mathbf{1} - \alpha \boldsymbol{s}) + \boldsymbol{\epsilon} && (4.5)\\ &= \boldsymbol{\mu} - \alpha \boldsymbol{s} \odot \boldsymbol{\mu} + \boldsymbol{\epsilon} && (4.6)\\ &\equiv \boldsymbol{\mu} + \alpha \boldsymbol{t} + \boldsymbol{\epsilon} \,, && (4.7) \end{aligned}$$

where $\boldsymbol{s}$ is the unit absorption spectrum (UAS) of the target gas [(ppm · m)$^{-1}$], $\mathbf{1}$ is a vector of ones, $\boldsymbol{\epsilon}$ is the measurement error, and $\odot$ denotes the element-wise multiplication. Note that $\boldsymbol{t}$ ab-

[1] The vector $\boldsymbol{L}$ is the radiance vector described in Equation (3.6). The spectral dimension is written as a vector for later convenience. The spatial index i includes all combinations of lines j and frames k.

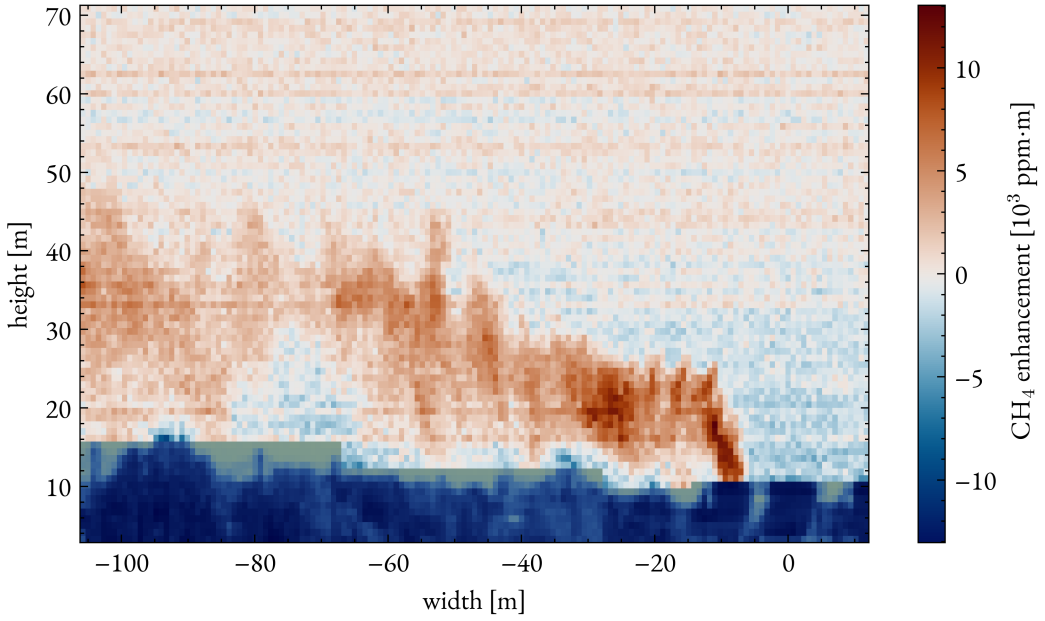

Figure 4.1: Example output of a classic matched filter (CMF) retrieval of CH_4 for a single scan from the sky above a coal mine ventilation shaft. The background (blue to yellow) shows the pixel brightness and the retrieved column enhancements (blue to red) are overlaid. Around 0 m width some rectangular structures mark the location of the ventilation shafts. From the camera's perspective, the left shaft emits are clearly distinguishable CH_4 plume even with the unmodified CMF retrieval.

sorbed a minus for later convenience. The UAS is the relative change of the spectrum for a unit gas enhancement of 1 ppm over 1 m. The linearization of Equation (4.4) only holds for small optical depths $\alpha \boldsymbol{s} \ll 1$. This assumption of Equation (4.4) - Equation (4.7) is only valid due to several circumstances. The retrieval exploits strong absorption lines of CO_2 and CH_4 between 2000 nm and 2500 nm wavelength. The atmosphere's optical depth of these lines is typically much larger than one for ground-based observers. However, the matched filter identifies additional absorption on top of the background. While the *relative* change due to an additional absorption from, e.g., an emission plume, is independent of the background concentration, the *absolute* change is not. An increasing atmospheric background lowers the radiance in absorption lines arriving at the observer. Thus, additional gas leads to a smaller absolute change at higher background concentrations. While Equation (4.4) is similar to Beer-Lambert's law, $\boldsymbol{L}$ is the *observed* radiance vector. The spectral width of the camera's ILS is more than an order of magnitude larger than the absorption lines. Figure 2.2 shows the transmission of CO_2 and CH_4 absorption lines for typical plume densities in the context of this thesis. Single lines reach transmissions close to zero at high resolution, but the transmission is close to one in between. The convolution with the ILS distributes the small absolute change inside the opaque lines into adjacent, more transparent regions. Consequently, observed optical depths are small ($\alpha \boldsymbol{s} < 0.1$) and depend on the atmospheric background concentration.

Using Equation (4.7) as a forward model and assuming the Gaussian distribution, the likelihood of an observation is

$$\begin{aligned}\mathcal{L}(\boldsymbol{L}_1, \ldots, \boldsymbol{L}_N|\vec{\alpha}) =& \frac{1}{\sqrt{(2\pi)^C \det(\mathbb{C})}^N} \\ & \cdot \exp\left(-\frac{1}{2}\sum_{i=1}^{N}(\boldsymbol{L}_i - (\boldsymbol{\mu} + \alpha_i \boldsymbol{t}))^\intercal \mathbb{C}^{-1}(\boldsymbol{L}_i - (\boldsymbol{\mu} + \alpha_i \boldsymbol{t}))\right),\end{aligned} \tag{4.8}$$

where $\vec{\alpha}$ is a vector of gas enhancements α_i for each spectrum. The best estimate of $\vec{\alpha}$ is the one that maximizes the likelihood, which can be calculated from

$$\hat{\vec{\alpha}} = \arg\min_{\vec{\alpha}} \sum_{i=1}^{N} \boldsymbol{d}_i^\intercal \mathbb{C}^{-1} \boldsymbol{d}_i \tag{4.9}$$

$$\boldsymbol{d}_i = \boldsymbol{L}_i - \alpha_i \boldsymbol{t} - \boldsymbol{\mu}\,, \tag{4.10}$$

and solved analytically to

$$\alpha_i = \frac{(\boldsymbol{L}_i - \boldsymbol{\mu})^\intercal \mathbb{C}^{-1} \boldsymbol{t}}{\boldsymbol{t}^\intercal \mathbb{C}^{-1} \boldsymbol{t}}\,. \tag{4.11}$$

Equation (4.11) is the CMF and can be applied to each spectrum individually. It is the computationally fastest form of the matched filter and best suited for signal detection. The retrieval error covariance matrix gives the uncertainty of the matched filter retrieval and depends on $\boldsymbol{t}$ and $\mathbb{C}$ (Köhler et al., 2015). It is given by

$$\sigma^2 = \frac{1}{\boldsymbol{t}^\intercal \mathbb{C}^{-1} \boldsymbol{t}}\,, \tag{4.12}$$

where σ is the noise equivalent enhancement (NEE) of the matched filter. Appendix A.2.1 derives Equation (4.11) and Equation (4.12) in more detail.

Figure 4.1 shows an example of a CMF retrieval of CH_4 from a single scan of the sky above a coal mine ventilation shaft. The plume is clearly visible, yet the image exhibits striping patterns and considerable background variability. Furthermore, several studies suggest that the CMF underestimates the gas enhancement (e.g., Foote et al., 2020; Ayasse et al., 2023). In theory, the CMF is unbiased, i.e., the expected value of the estimated gas enhancement is equal to the true gas enhancement. However, non-compliance of real data with the assumptions typically leads to underestimating the gas enhancement. Section 4.1.2 to Section 4.1.4 describe several refinements to the CMF.

4.1.2 Iterative Matched Filter

Foote et al. (2020) present refinements to the CMF to increase the accuracy of the gas enhancement retrieval, which they call the Matched filter with Albedo correction and reweiGhted L1 sparsity Code (MAG1C) algorithm. The first adaption is an albedo factor $\vec{r}$ defined as

$$r_i = \frac{\boldsymbol{L}_i^\intercal \boldsymbol{\mu}}{\boldsymbol{\mu}^\intercal \boldsymbol{\mu}}\,, \tag{4.13}$$

accounting for each pixel's relative brightness to the mean spectrum. Furthermore, MAG1C introduces an iteration scheme excluding enhancements from the background estimation using a sparsity constraint. The sparsity constraint exploits that enhanced pixels typically comprise less than 1 % of the image. Thus, an L_0-regularization is used to minimize the number of enhanced pixels. An L_0-regularization forces pixels with insignificant enhancement to zero, clearly distinguishing background and signal regions. However, an L_0-regularization makes the minimizer non-differentiable. Candès et al. (2008) show that a re-weighted L_1-regularization can approximate the minimizer. The iteratively re-weighted least squares (IRLS) algorithm (e.g., Aster and Thurber, 2013, Chapter 7.5) provides the solution to the L_1-regularized problem by solving a sequence of regular least-squares problems. The MAG1C algorithm exploits the necessary iteration scheme to update each iteration step's background mean and covariance. The cost function takes the form

$$\hat{\vec{\alpha}}_m = \arg\min_{\vec{\alpha}} \sum_{i=1}^{N} \left[\boldsymbol{d}_{i,m}^{\intercal} \mathbb{C}_m^{-1} \boldsymbol{d}_{i,m} + r_i w_{i,m} ||\alpha_{i,m}||_1 \right] \tag{4.14}$$

$$\text{with } \boldsymbol{d}_{i,m} = \boldsymbol{L}_i - r_i \alpha_{i,m} \boldsymbol{t}(\boldsymbol{\mu}_m) - \boldsymbol{\mu}_m \tag{4.15}$$

$$\text{and } w_{i,m} = \frac{1}{\alpha_{i,m-1} + \kappa} , \tag{4.16}$$

where m is the iteration step, $\boldsymbol{d}_{i,m}$ is the residual vector, w_i^k is the regularization weight, and κ is a small constant to avoid division by zero. Solving for $\hat{\vec{\alpha}}$ yields

$$\hat{\alpha}_{i,m} = \max\left(\frac{(\boldsymbol{L}_i - \boldsymbol{\mu}_m)^{\intercal} \mathbb{C}_{i,m}^{-1} \boldsymbol{t}_{i,m} - w_{i,m}}{r_i \boldsymbol{t}_m^{\intercal} \mathbb{C}_m^{-1} \boldsymbol{t}_m}, 0 \right) , \tag{4.17}$$

which includes a physically motivated positivity constraint on gas enhancements. MAG1C updates the background mean and covariance in each iteration step by correcting for the absorption structure like

$$\boldsymbol{\mu}_m = \frac{1}{N} \sum_{i=1}^{N} \boldsymbol{L}'_{i,m} , \tag{4.18}$$

$$\mathbb{C}_m = \frac{1}{N-1} \sum_{i=1}^{N} (\boldsymbol{L}'_{i,m} - \boldsymbol{\mu}_m)(\boldsymbol{L}'_{i,m} - \boldsymbol{\mu}_m)^{\intercal} , \tag{4.19}$$

$$\text{with } \boldsymbol{L}'_{i,m} = \boldsymbol{L}_i - \alpha_{i,m-1} \boldsymbol{t}_{m-1} . \tag{4.20}$$

The iteration scheme requires the step number as an input. Foote et al. (2020) suggest a value of 30, which is used throughout this thesis. Furthermore, MAG1C forces most enhancements artificially to zero. A final CMF step fills these null enhancements to avoid systematic biases in the emission estimates. This step uses the mean and covariance from the last iteration to ensure the retrieval benefits from the iteration. Foote et al. (2020) show that the MAG1C algorithm reduces root mean square error (RMSE) by up to 60.7 % in simulated data and the NEE in real data by 36.3 % to 47.1 %.

4.1.3 Differential Matched Filter

A common systematic feature in spectral imaging is the striping pattern in physical and statistical retrievals (e.g., Borsdorff et al., 2018; Guanter et al., 2021). The instrument's detector array causes the stripes since every line is an independent spectrometer. Thus, the stripes occur along the scanning direction. In terms of the matched filter, this implies that each line has a different background mean and covariance. Estimating a background distribution from the whole image (a) reduces the sensitivity of the matched filter and (b) introduces striping in the retrieval (Figure 4.1). Images from satellite or airborne applications contain several million spectra in each across-track line, allowing for reduced striping by applying a matched filter to each line separately (e.g., Thompson et al., 2015). Stationary images contain only several hundred spectra in each line, which is insufficient for a line-wise matched filter (Ayasse et al., 2023).

The differential matched filter (DMF) was developed within this work to circumvent line-specific detector non-uniformities. Comparable to Differential Optical Absorption Spectroscopy (DOAS) applications, the DMF divides the observed spectra by a reference spectrum (e.g., Platt and Wagner, 1998; Frankenberg et al., 2005; Platt, 2017). The reference spectrum $\boldsymbol{L}_{\text{ref}}$ is a 30-frame (k) mean of a background region, e.g., upwind from the source. It is calculated for each line j separately as

$$\boldsymbol{L}_{\text{ref},j} = \langle \boldsymbol{L}_{j,k} \rangle_{\text{backgr.}} \,. \tag{4.21}$$

The DMF uses the reference spectrum to calculate a differential spectral vector $\boldsymbol{l}_{jk}$ for each spectrum $\boldsymbol{L}_{jk}$ in the image

$$\boldsymbol{l}_{jk} = \frac{\boldsymbol{L}_{jk}}{\boldsymbol{L}_{\text{ref},j}} \,, \tag{4.22}$$

which, in theory, scatters around $\mathbf{1}$ for background spectra and $\mathbf{1} - \alpha \boldsymbol{s}$ for enhanced spectra (Equation (4.4)). Note that the target signature $\boldsymbol{t}$ changes from $\boldsymbol{\mu} \odot \boldsymbol{s}$ in the CMF to $\boldsymbol{s}$ in the DMF, following the derivation of Equation (4.4)ff. Furthermore, the brightness factor $\vec{r}$ is now defined relative to the reference spectrum

$$r_{jk} = \frac{\boldsymbol{L}_{jk}^{\intercal} \boldsymbol{L}_{\text{ref},j}}{\boldsymbol{L}_{\text{ref},j}^{\intercal} \boldsymbol{L}_{\text{ref},j}} \,. \tag{4.23}$$

Referencing each spectrum in a line with a line-specific mean background spectrum provides several advantages. Firstly, it removes detector non-uniformities across the lines. Secondly, it corrects for the different VEA each line in a ground-based image corresponds to. The VEA alters the radiative transfer through the atmosphere, an effect also included in the reference spectrum. Thus, the differential spectral vectors comply with the assumptions of the CMF better than the observed spectra. In practice, residual striping effects are still expected and visible. Striping is a result of detector effects. Temporally constant striping may result from an incomplete detector characterization, e.g., omitting effects like smile, keystone, and wavelength calibration non-linearity (see Section 3.1). Furthermore, the detector exhibits sporadic instabilities in single detector pixels, causing stripes if they appear in channels of the retrieval's target signature. Nevertheless, the DMF outperforms the CMF method for CH_4 (Chapter 5) and enables the first CO_2 retrieval from a stationary ground-based image (Chapter 6).

Clustering

Referencing all spectra within each line using a background spectrum assumes no significant changes in radiative transfer with the VAA. This assumption is generally valid for a homogeneous sky, evident from the UAS presented later in Figure 4.5. However, clouds induce scene heterogeneity, changing the radiative transfer depending on the horizontal and vertical viewing direction. Clouds in the reference region of the DMF introduce a systematic change between the reference spectrum and all pixels in the affected lines. A simple clustering approach can compensate for this by grouping spectra into similar clusters (Funk et al., 2001; Thorpe et al., 2013; Hochstaffl et al., 2023). A k-means algorithm (e.g., Theiler and Gisler, 1997) clusters the spectra, and the reference spectrum is calculated for each line and cluster separately. Thus, a line- and cluster-specific reference spectrum exists, reducing the systematic error clouds introduced in the reference region. Figure 4.2 shows how the filter quantities $(\boldsymbol{\mu}, \mathbb{C})$ change for the CMF and DMF in clear and cloudy conditions. In clear sky conditions, the DMF produces a spectral mean vector around one. The relative uncertainty[2] of spectral channels decreases by a factor of 2 to 8 for the differential spectrum. The smaller uncertainty suggests that the DMF outperforms the CMF in clear skies. Cloudy conditions pose challenges to the CMF and the clustered DMF retrieval. The DMF spectral mean is offset against one, indicating imperfect referencing as the observed spectra within a cluster are not identical. Consequently, the covariances increase significantly for the CMF and DMF under cloudy conditions. Section 5.2.2 discusses the effect of clustering and the DMF in more detail using field observations of CH_4 plumes.

4.1.4 Combo Matched Filter

Roger et al. (2023b) propose the combo matched filter (CoMF) to mitigate false positives in the retrieval. It combines two separate (but overlapping) spectral regions in a single matched filter retrieval. The combination of both regimes increases the contrast of the background to the plume signal. Roger et al. (2023b) suggest using the CoMF for plume detection rather than quantification due to its heuristic nature. The CoMF technique is applied to methane retrievals in Chapter 5 for plume masking and artifact suppression in cloudy scenes.

The CoMF employed in this thesis uses the 1600 nm and 2300 nm absorption features of CH_4. The "narrowband"- and "broadband"-windows cover intervals from 2053 nm to 2396 nm and 1524 nm to 2396 nm, respectively. Hence, the "broadband"-window covers methane's 1600 nm absorption features and includes additional information on the background variability. Covering additional channels makes the window less susceptible to background artifacts. The CoMF enhancements are calculated from

$$\alpha_{\text{combo}} = \begin{cases} \alpha_{\text{bb}} \cdot f & \text{if } \alpha_{\text{bb}} < \alpha_{\text{nb}} \\ \alpha_{\text{nb}} & \text{if } \alpha_{\text{bb}} \geq \alpha_{\text{nb}} \end{cases}, \tag{4.24}$$

[2] The relative uncertainty of a channel is the square root of the diagonal elements of the covariance matrix divided by the mean spectrum.

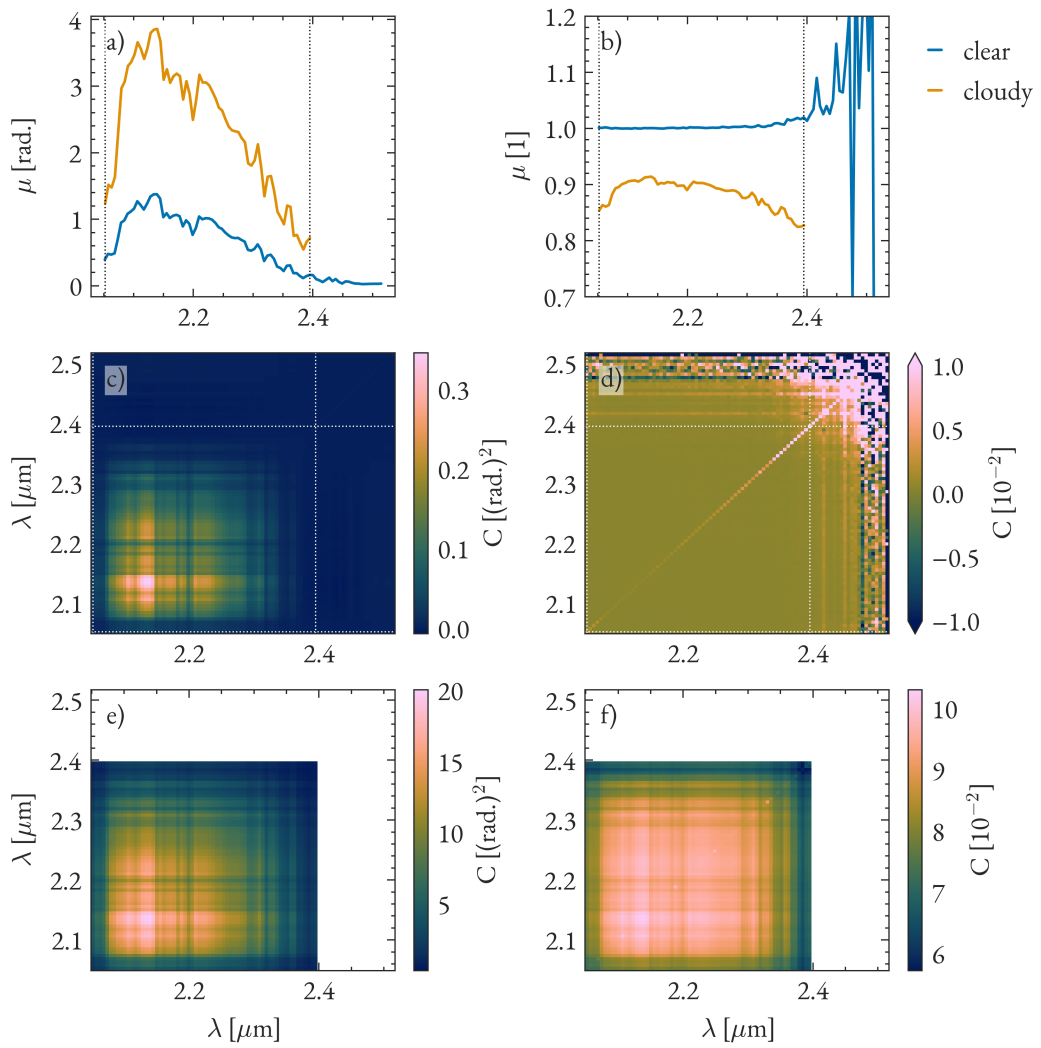

Figure 4.2: Estimated background mean and covariance matrix for a classic (panels a), c), e)) and differential (panels b), d), f)) matched filter retrieval of CH_4 from a single scan of the sky above a coal mine ventilation shaft. The background mean (panels a), b)) of an observation in clear (blue) and cloudy (orange) conditions show that the DMF referencing works as intended in clear sky conditions but produces a biased mean spectrum under cloudy conditions. The background covariance (panels c), d)) in clear sky conditions support that finding since the DMF covariance is significantly less structured than the CMF covariance. The effect does not translate to the cloudy condition covariances (panels e), f)), which are similar for both methods (see Chapter 5). The clear sky retrieval uses a broader spectral interval, illustrating matched filer performance in low signal regions. The CMF and DMF deal with low radiance by suppressing the absorption features and increasing the variances, respectively.

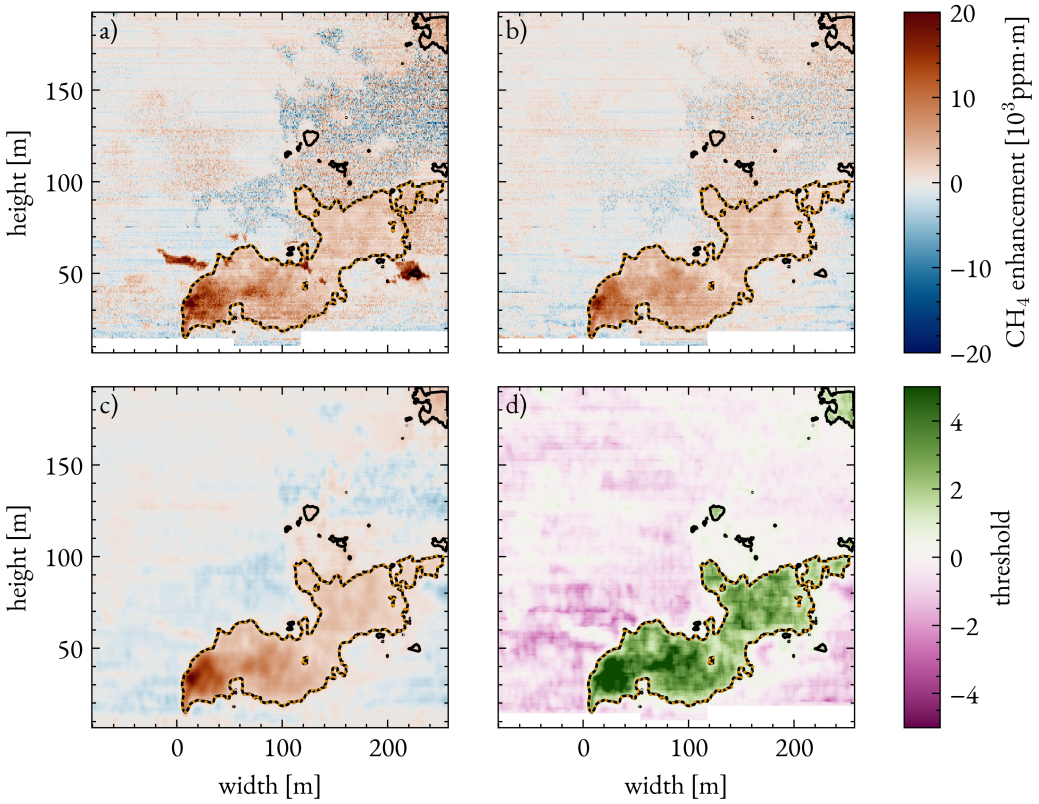

Figure 4.3: Workflow of the CoMF plume masking algorithm. Panel a) shows the narrowband enhancement map, panel b) shows the broadband enhancement map, panel c) shows the smoothed combo enhancement map, and panel d) shows the plume masking approach. The black contours show the pixels above the plume mask thresholding, and the orange dashed contour shows the final plume mask.

where α_{bb} and α_{nb} are the broadband and narrowband enhancements, respectively, and f is a scaling factor. The scaling factor is defined as

$$f = \frac{\sigma_{\mathrm{bb}}}{\sigma_{\mathrm{nb}}}\,, \tag{4.25}$$

where σ_{bb} and σ_{nb} are the NEEs of the broadband and narrowband retrieval, respectively. The scaling factor accounts for the typically smaller variability of the broadband retrieval. Figure 4.3 illustrates the CoMF workflow for an exemplary observation of a CH_4 plume during a cloudy scene. The narrowband retrieval exhibits artifacts (panel a)) from clouds, which the broadband retrieval suppresses (panel b)). Both retrievals identify enhanced plume pixels. The CoMF combines the retrieved images into a single enhancement map. Median filtering (7×7 pixels) further suppresses the background variability (panel c)). The local mean and standard deviation of the smoothed map are calculated for each pixel (panel d)). Potential plume pixels are those in which the local mean surpasses the local standard deviation (black contour). The plume mask is the largest patch of connected pixels and all patches that correspond in the vertical (for details, see

Appendix A.3.2). This approach covers patches of the plume that were separated from the main body, likely due to a portion of the plume being diluted below the detection limit. Roger et al. (2023b) recommend applying the final plume mask (black and orange contour) to the narrowband enhancement map for emission estimation. They find a systematic underestimation of the retrieved enhancements in the broadband retrieval based on synthetic enhancements added to a PRISMA dataset. Thus, emission estimates use the unbiased narrowband enhancement map, as it is common in large parts of the literature (e.g., Nesme et al., 2020; Thorpe et al., 2020; Guanter et al., 2021). The results in Chapter 5 confirm the relative bias of the retrieval windows found by Roger et al. (2023b). The bias becomes most apparent for cloudy retrievals, which points to a systematic effect from the covariance matrix (see Figure A.3). Another possible explanation for this underestimation is the linear wavelength calibration of the camera. This assumption worsens with an increasing wavelength interval. Further investigation of this underestimation is a promising approach to increase the retrieval's precision by including the 1600 nm absorption feature of CH_4.

4.1.5 Unit Absorption Spectra

The UAS $\boldsymbol{s}$ is the only external input of the matched filter retrieval and plays a pivotal role in the retrieval. It is defined as the relative change of an observed spectrum for a column enhancement of 1 ppm · m, and it determines the target signature $\boldsymbol{t}$ of the matched filter.

The generation of the UAS consists of two steps. First, a radiative transfer model provides the ASR, i.e., the radiance arriving at the instrument entrance. The model simulates the ASR for an atmosphere with ($\boldsymbol{I}_\lambda(\alpha)$) and without ($\boldsymbol{I}_\lambda(0)$) a target gas enhancement. Second, an observation model of the spectrometer provides the theoretical observation of the ASR ($\boldsymbol{L}(\alpha)$ and $\boldsymbol{L}(0)$). A simplistic observation model includes the instrument's ILS and the detector's spectral sampling, but can be increased in complexity by including effects like smile, keystone, and non-linear wavelength calibration. The UAS follows from

$$\boldsymbol{s} = -\frac{\partial}{\partial \alpha} \ln\left(\frac{\boldsymbol{L}(\alpha)}{\boldsymbol{L}(0)}\right), \tag{4.26}$$

which results from the assumption that an additional absorbing column acts on the observed radiance according to Beer-Lamberts law (Equation (4.4)).

The radiative transfer model used in this thesis is the single-scattering solution of the RTE given in Equation (2.26). The model calculates the $\boldsymbol{I}_\lambda(0)$ at a resolution of 0.001 nm in an 100 layer atmosphere of 400 m thickness. The HITRAN database (Kochanov et al., 2016; Gordon et al., 2017) provides absorption cross-sections of H_2O, CO_2, and CH_4. Anderson et al. (1986) provide atmospheric standard profiles. However, the background concentrations of CO_2 and CH_4 were scaled to 420 ppm and 1.85 ppm, respectively. Molecular scattering employs the Rayleigh phase function, and aerosol scattering employs the Henyey-Greenstein phase function. Nearby AERONET stations (Holben et al., 1998) provide the aerosol optical depth (AOD), namely the stations in Karlsruhe, Germany, for results discussed in Chapter 6 and from Raciborz, Poland, in Chapter 5. The AOD at the target wavelength (2000 nm for CO_2 and 2300 nm for CH_4) follows from the AOD at 870 nm and the Ångström exponent. The above parameters comprise all the necessary infor-

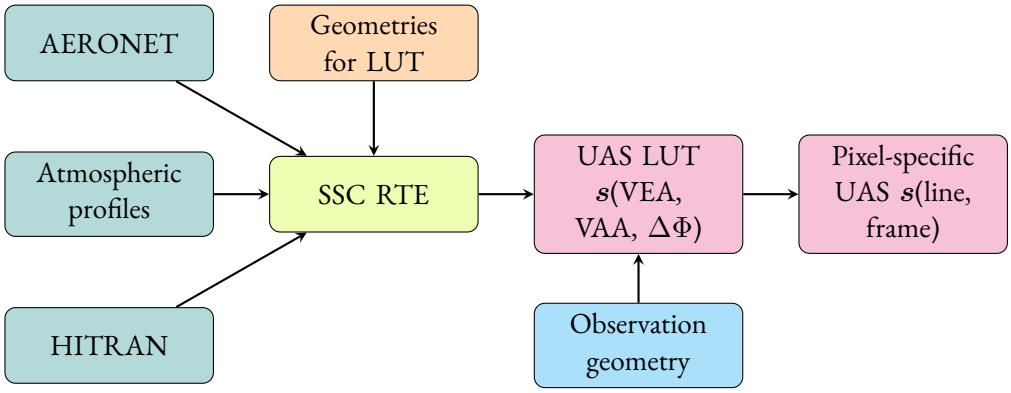

Figure 4.4: Flowchart of the UAS generation. The single scattering approximation of the RTE (SSC RTE) builds on generic atmospheric profiles, HIgh-resolution TRANsmission molecular absorption database (HITRAN) cross-sections, and specific AErosol RObotic NETwork (AERONET) data. A set of pre-chosen viewing geometries are used to calculate the UAS look-up table (LUT). Each image contains its observation geometry, which is used to interpolate the LUT and assign each pixel a specific UAS. Processes are yellow, settings are orange, (interim) results are red, and internal and external data are blue and green, respectively.

mation for calculating each model layer's absorption and scattering cross-sections. Thus, the RTE provides the ASR in single-scattering approximation $I_\lambda(0)$.

The influence of an additional optical density τ, e.g., due to an emission plume of CO_2, acts on $\boldsymbol{I}_\lambda(0)$ according to Beer-Lambert's law (Equation (2.23)). The optical density due to an enhancement is

$$\tau = n_{CO_2} \cdot \sigma_{CO_2} \cdot \Delta z \tag{4.27}$$

$$= n_{\text{air}} \cdot \sigma_{CO_2} \cdot \alpha \cdot 10^{-4}\,, \tag{4.28}$$

where n_{CO_2} and n_{air} are the number density of CO_2 and air [molec. cm^{-3}], respectively, σ_{CO_2} is the absorption cross-section of CO_2 [cm^2 molec.$^{-1}$], Δz is the layer thickness [cm], α is the gas enhancement [ppm · m], and 10^{-4} is a unit conversion factor. Using the optical density, the ASR with an additional enhancement reads

$$I_\lambda(\alpha) = I_\lambda(0) \cdot \exp(-n_{\text{air}} \cdot \sigma_{CO_2} \cdot \alpha \cdot 10^{-4})\,. \tag{4.29}$$

The observation operator is simplified to the convolution of the ASR with the ILS of the instrument

$$L_\lambda(\alpha) = I_\lambda(\alpha) * \text{ILS}\,, \tag{4.30}$$

which represents the radiance after the optical setup reaching the detector. The ILS is approximated by a Gaussian with a FWHM of 7 nm as found in Section 3.1. In a final step, the observed

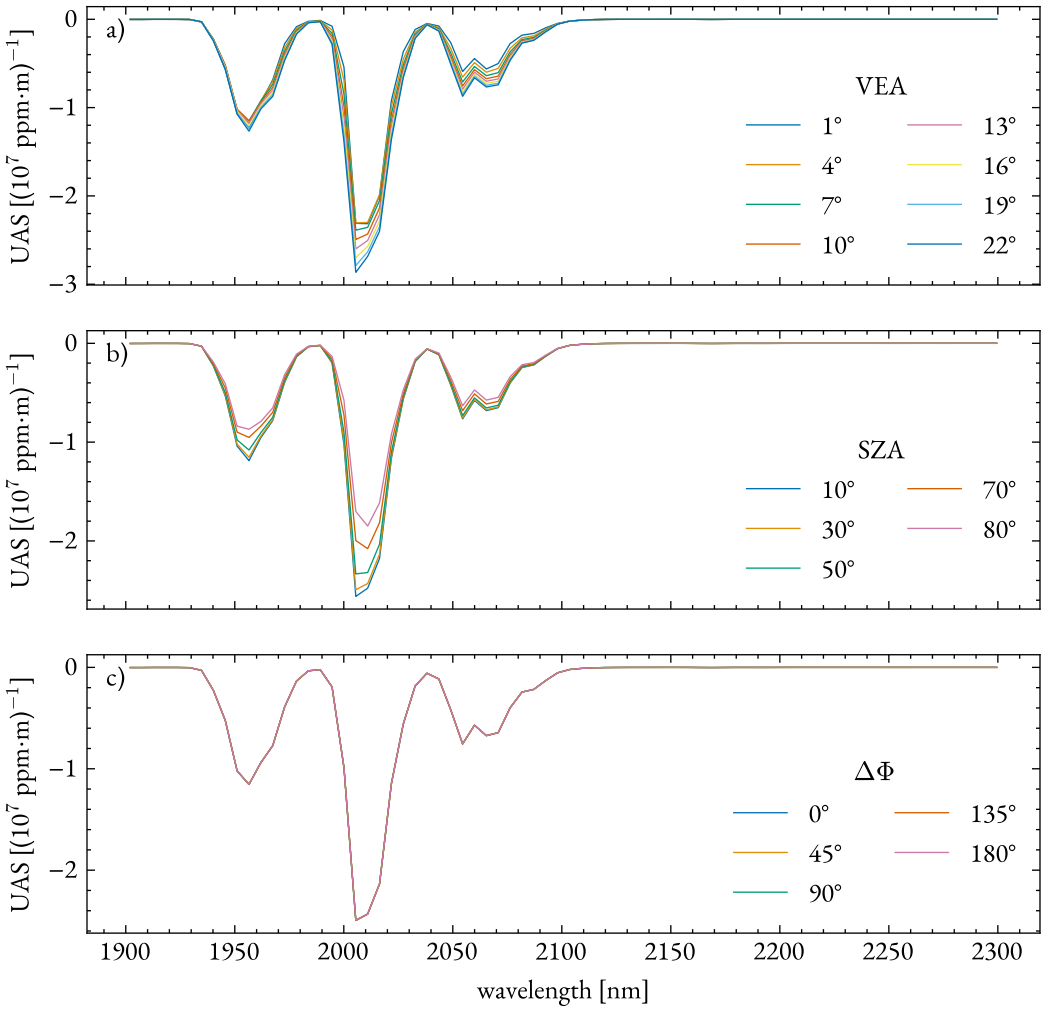

Figure 4.5: Variations of the CO_2 UAS with the VEA, SZA, and VAA. Increasing SZA (lower Sun) and decreasing VEA (closer to horizon) increase the effective path length of photons through the atmosphere. As expected, this leads to smaller UAS values (in an absolute sense). The influence of $\Delta\Phi$ is in the per mill range of the UAS, since this angle does not change the effective light path significantly. The UAS is calculated for a representative AOD of 0.01 and an asymmetry factor of 0.6 (Pandolfi et al., 2018).

radiance vector $\boldsymbol{L}(\alpha)$ follows from binning $L_\lambda(\alpha)$ into the spectral channels of the instrument. Equation (4.26) is solved using finite differences, i.e.,

$$\boldsymbol{s} = -\frac{\ln(\boldsymbol{L}(\alpha)) - \ln(\boldsymbol{L}(0))}{\alpha}\,, \tag{4.31}$$

where α are typical plume gas enhancements of 1 000 000 ppm · m and 20 000 ppm · m for CO_2 and CH_4, respectively. The retrieval uses a CO_2 UAS from 1967 nm to 2260 nm. For CH_4, the narrowband and broadband UAS window covers 2052 nm to 2395 nm and 1524 nm to 2395 nm, respectively. The broadband UAS excludes the wavelength range from 1725 nm to 2052 nm to avoid strong water absorption, as suggested by Roger et al. (2023a).

Foote et al. (2021) emphasize the importance of scene-specific UAS for the matched filter retrieval, showing for a set of top-down images that the UAS varies with parameters like the SZA or observer altitude. Since both CO_2 and CH_4 have considerable background concentrations, the effective light path through the atmosphere significantly influences the UAS. The longer the light path, the less an additional enhancement will alter the observed radiance, and thus, the absolute UAS will be smaller. UAS in this work are calculated using a daily AOD from AERONET for CO_2 observations (Chapter 6) and the June monthly mean for CH_4 observations (Chapter 5).

Figure 4.4 shows the flowchart of the UAS generation, and Figure 4.5 shows the resulting UAS for CO_2. Figure A.4 shows the UAS for CH_4 in the narrowband window. For ground-based observations in single scattering geometry, the effective light path follows from SZA, VEA, and the relative azimuth angle $\Delta\Phi$ between the Sun and the camera pointing. Thus, instead of a single UAS for a scan, a pixel-specific UAS is calculated for each pixel in the image. This is realized by calculating the UAS for a grid of SZA (10°, 30°, 50°, 70°), VEA (1°, 4°, 7°, 10°, 13°, 16°, 19°, 16°, 22°), and $\Delta\Phi$ (0°, 45°, 90°, 135°, 180°). The preprocessing of a scan assigns the respective VEA and VAA to each pixel (Section 3.2). The solar position (SZA, solar azimuth angle (SAA)) follows from the time and location of the camera using Holmgren et al. (2018). The matched filter assigns each pixel a specific UAS by interpolating the LUT of pre-computed UAS using the pixel-specific VEA and $\Delta\Phi$ and the scan-specific SZA. As expected, the UAS decreases with increasing SZA and decreasing VEA since the effective light path through the atmosphere increases. Since $\Delta\Phi$ does not change the effective light path significantly, its influence is in the per mill range of the UAS.

4.2 Emission Estimation

A plethora of techniques exist to estimate gas emission rates of point sources from imaging data. They divide in four categories: (a) optical flow analysis, (b) mass balance methods, (c) plume inversion, and (d) machine learning.

Optical flow methods are commonly used in stationary imaging applications (Klein et al., 2017; Gålfalk et al., 2022; Kuhn et al., 2022) and rely on tracking plume features in between images. Thus, they require a temporal resolution of more than 1 Hz, which is not available for the presented data. The other three techniques are commonly employed for top-down observations of greenhouse gases (Varon et al., 2018; Jacob et al., 2022), yet they can be easily adapted to ground-based observations. Mass balance methods are based on the conservation of mass and, e.g., use the flux

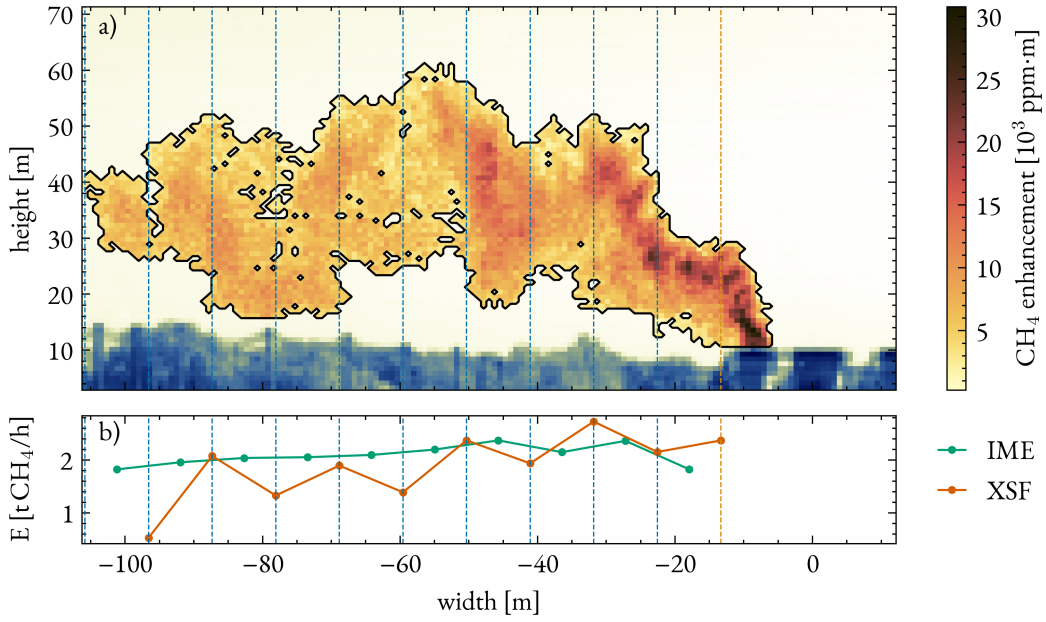

Figure 4.6: Example of the working principle of the mass balance methods IME and XSF. Panel a) shows a plume in a single image, evaluated with the DMF algorithm. The observed plume is split into 10 segments of equal length (blue dashed). Panel b) shows the IME emission estimates (green) for increasing box sizes from the shaft (dashed orange) alongside XSF estimates for the frames between each segment (dark orange).

through a plume cross-section or simple box models to estimate the emission rate (e.g., Krings et al., 2011; 2013; Frankenberg et al., 2016; Cusworth et al., 2021a; Fuentes Andrade et al., 2023). Plume inversion methods use a simulated plume to fit the emission by minimizing the difference between the observed and simulated plume (e.g., Zheng et al., 2019; Wang et al., 2020). Typically, a Gaussian plume model is used to approximate the plume shape, even though the snapshot nature of single overpasses may cause significant deviations from the Gaussian shape (Bovensmann et al., 2010; Krings et al., 2011; Jongaramrungruang et al., 2019; Brunner et al., 2023). Machine learning approaches have been introduced by Jongaramrungruang et al. (2022) and can be used to process large amounts of data, which is a valuable asset for satellite applications (Radman et al., 2023; Schuit et al., 2023).

The following sections introduce the cross-sectional flux (XSF) and integrated mass enhancement (IME) mass balance approaches and a Gaussian plume inversion scheme which was developed in this thesis. Emission estimates are the final step of the data evaluation chain since they are comparable to any measurement technique and inventories.

4.2.1 Mass Balance Methods

Integrated Mass Enhancement

The IME is a simple mass balance approach which was applied to ground-based images of methane plumes from coal mining activities (Knapp et al., 2023a, see Chapter 5). It is adapted from satellite and airborne applications, in which it was extensively used and evaluated (e.g., Frankenberg et al.,

2016; Varon et al., 2018; Duren et al., 2019; Ayasse et al., 2022). The IME method relates the total observed mass M to its residence time τ in the plume to the emissions E by

$$E = \frac{M}{\tau} \,. \tag{4.32}$$

The plume mass is defined as the total excess mass inside all plume pixels with respect to the background. Since the matched filter algorithm inherently provides column enhancements in units of ppm · m, the mass is calculated from

$$M = k \cdot \sum_{i=1}^{N_\mathrm{p}} \alpha_i \cdot A_i \,, \tag{4.33}$$

where N_p is the set of plume pixels, α_i is the column enhancement of pixel i, and A_i is the geometric pixel area. The factor k converts column enhancements to mass using the molar mass and volume of the target species, i.e., $k_{\mathrm{CH_4}} \approx 6.7\,\mathrm{g\,ppm^{-1}\,m^{-3}}$ at normal conditions. The pixel area follows from the distance between camera and target and the opening angle of the pixel (Equation (3.16)). The residence time τ is calculated using the plume speed and length by

$$\tau = \frac{d_\mathrm{im,c}}{u} = \frac{d_\mathrm{im}}{u_\mathrm{eff}} = \frac{d_\mathrm{im}}{u \cdot \sin(\phi)} \,, \tag{4.34}$$

where d_im is the plume length projected on the plane of observation using the angle ϕ between the plume direction and the camera pointing by $d_\mathrm{im} = d_\mathrm{im,c} \cdot \sin(\phi)$. Likewise, u is the true plume speed and $u_\mathrm{eff} = u \cdot \sin(\phi)$ is the speed projected onto the observation plane. Plume speed and travel direction are assumed to be the ambient wind field at mass-weighted mean plume height, while d_im is the distance between two vertical cross-sections in the image. Thus, the emission estimate for a plume segment of length d_im is given by

$$E = \frac{M}{d_\mathrm{im}} \cdot u \cdot \sin(\phi) \,. \tag{4.35}$$

Figure 4.6 shows an example for an emission estimate using the IME method. The plume length is always taken from a line shortly downwind the emission shaft to the end of a plume segment of increasing size. Thus, several emission estimates can be calculated from a single image, which are then averaged to a final estimate similar to Duren et al. (2019) and Fuentes Andrade et al. (2023). An empirical error of a single image emission estimate follows from the error propagation of Equation (4.35) to

$$\left(\frac{\Delta E}{E}\right)^2 = \left(\frac{\Delta \rho}{\rho}\right)^2 + \left(\frac{\Delta u}{u}\right)^2 + \left(\frac{\cos(\phi)}{\sin(\phi)} \Delta\phi\right)^2 , \tag{4.36}$$

where $\rho = M/d_\mathrm{im}$ is the mean line density of the plume, $\Delta\rho$ its standard deviation over the plume segments, and Δu and $\Delta\phi$ are the standard deviations of the wind speed and wind direction, respectively. The contribution of $\Delta\rho$ includes, in particular, the assumption of a constant

emission rate during the time of observation, fluctuations due to turbulence, and mass loss due to plume dilution below the detection limit.

Chapter 5 presents time series of CH_4 emissions using the IME. The IME method is computationally cheap and can be applied to single images, if these exhibit sufficiently large and clear plumes. This makes it advantageous for retrieving emission time series encompassing several hundred images per day. The IME is typically prone to uncertainties in the wind field, yet the addition of the wind LIDAR to the field setup of this thesis mitigates that uncertainty to some extent. Note that especially the uncertainty due to turbulent transport is not covered within one image, but requires averaging several of the images to one emission estimate (Woitischek et al., 2021a; Brunner et al., 2023). This phenomenon can be amplified by the scanning observation of the camera, especially in a scenario when the plume is moving with the field of view of the camera. Section 5.3 discusses this effect in more detail.

Cross-Sectional Flux

The XSF method estimates the flux within a plume at a certain cross-section (Varon et al., 2018). The cross-sections normal vector is chosen to align with the plume flow direction, such that the flux is calculated from

$$E = \int_{-\infty}^{\infty} k \cdot \alpha(x, y) \cdot u(x, y)\, \mathrm{d}y\,, \tag{4.37}$$

where $k\alpha$ is the mass enhancement in units of $\mathrm{g\,m^{-2}}$, $u(x, y)$ is the wind speed normal to the cross-section, and $\mathrm{d}y$ is an infinitesimal distance along the cross-section. In practice, the cross-section is discretized into N pixels, and the flux is calculated from

$$E = \sum_{i=1}^{N} k \cdot \alpha_i \cdot u_{\mathrm{eff}} \cdot h_i \cdot w\,, \tag{4.38}$$

where i runs over all plume pixels within an image frame, u_{eff} is the projected plume speed, h_i is the pixel height, and w is the pixel width. The uncertainty follows from Gaussian error propagation from the wind speed, wind direction, and the standard deviation of the emission estimates of the individual frames within a scan. Taking a frame as the cross-section assumes a horizontal plume flow, which is given for low vertical wind speeds and plumes at ambient temperature in good approximation. The XSF method is applied to camera observations in a fixed geometry, i.e., the camera did not rotate on the tripod, but the plume was passively moving through the field of view. Thus, the XSF method enables emission estimates at the frame rate of the camera, which is typically 3 Hz to 10 Hz. Figure 4.6 demonstrates the XSF method applied to a single image in scanning geometry. Section 5.2.3 discusses the application of the XSF method to methane plumes in more detail.

4.2.2 Gaussian Plume Inversion

Fitting a plume model to an observation enables the inversion of the emission source strength. A point-by-point comparison of the observed and simulated plume requires an accurate forward

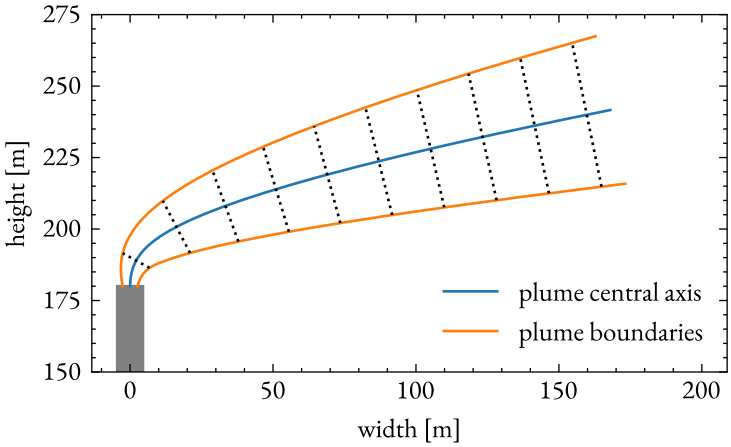

Figure 4.7: Example for the output of the Gaussian plume model IBJpluris with a chimney of 180 m height. The central axis (blue) contains the plume properties like the plume width (orange) at every cross-section (every 20th shown dotted black). The examples input parameters are the ambient wind velocity (5.2 m s^{-1}), ambient temperature (27 °C), and relative humidity (40 %) at 200 m height. Furthermore, the initial velocity (13.4 m s^{-1}), temperature (63.0 °C), and concentration (189 g m^{-3}) of the exhaust gas are given. Output parameters like the concentration of CO_2 are provided along the central plume axis. Figure adapted from Knapp et al. (2023b).

model. The comparison is especially challenging for snapshot observations of turbulent plumes (Zheng et al., 2019; Wang et al., 2020; Brunner et al., 2023). In contrast to airborne and satellite observations, the ground-based camera setup of this thesis enables repeated observations of an emission plume with a temporal resolution of approximately 1 min. Thus, every image contains a turbulent ensemble member of the emission plume under quasi-stationary conditions. Averaging over many of these images blurs the turbulent features of the plume, and the plume shape approaches a Gaussian shape (e.g., Woitischek et al., 2021b). This enables the application of a Gaussian plume model to the observed plume, which is then fitted to the observed plume to estimate the emission rate. The technique is demonstrated for CO_2 observations from a coal-fired power plant in Chapter 6.

Section 4.2.2 introduces the Gaussian plume model that simulates the plumes for the inversion. Section 4.2.2 presents the observation forward model, used to simulate an observation from the modelled plume. Finally, Section 4.2.2 explains the inversion scheme that fits the simulated to the observed plume and estimates the emission rate. This procedure has been published in Knapp et al. (2023b) and the following sections are adapted from this publication.

Gaussian Plume Model

Since the camera observes plumes in a horizontal viewing geometry, the model needs to account for the bent-over plume shape (Figure 4.7). The plume rise presents a fundamental difference from top-down viewing observations. These Gaussian inversions rely on a simplified model that only accounts for horizontal transport, which is insufficient in ground-based applications. Janicke and Janicke (2001) published a plume rise model which calculates plume properties along the cen-

tral plume travel axis. The model is called IBJpluris and considers the evolution of cross-sectional plume properties along the plume axis in three spatial dimensions. It is an integral model which solves the flow $Q = A\rho u$ of air with density ρ and velocity u through a cross-section of area A. IBJpluris computes the plume parameters for plume segments of length $\mathrm{d}s$. The flow evolution is determined by the conservation of mass, momentum, and energy, which are given by

$$\frac{\mathrm{d}}{\mathrm{d}s}(Q) = 2\pi\tilde{\rho}F\,, \tag{4.39}$$

$$\frac{\mathrm{d}}{\mathrm{d}s}(Qu) = 2\pi\tilde{\rho}F\tilde{u} - f_B\,, \tag{4.40}$$

$$\frac{\mathrm{d}}{\mathrm{d}s}\left(Q(\frac{u^2}{2} + \frac{u'^2}{2} + gz + c_pT)\right) = 0\,, \tag{4.41}$$

where F is the entrainment function, $\tilde{\rho}$ and $\tilde{u}$ are the mass density and velocity of the entrained air, f_B is the buoyancy force, u' is the turbulent velocity, g is the gravitational acceleration, z is the height, c_p is the specific heat capacity of air, and T is the temperature. Energy conservation assumes an adiabatic plume evolution - in the case of non-zero entrainment the evolution is solved sequentially using a separated adiabatic and entrainment step. Likewise, the conservation of a carried scalar quantity c is given by

$$\frac{\mathrm{d}}{\mathrm{d}s}(Acu) = 2\pi F\tilde{c}\,, \tag{4.42}$$

where $\tilde{c}$ is the concentration of the entrained air. Figure 4.7 shows the simulated plume shape for a set of initial conditions.

The plume properties are given at discrete points, containing the plume radius R, the distance along the plume axis s, and the mass concentration of a carried quantity c at the spatial coordinates (x, y, z). The model input parameters encompass ambient parameters such as wind speed u_a, temperature T_a, pressure p_a, and relative humidity RH_a. Furthermore, source information like the exhaust gas initial velocity u_e, temperature T_e, and concentration c_0 are required. The total gas enhancement in the plume depends linearly on the emission rate E. The mean concentration c_0 in the plume segment right above the chimney follows from

$$c_0 = \frac{E}{\dot{V}}\,, \tag{4.43}$$

where $\dot{V}$ is the air volume flux from the chimney. The concentration c_0 holds for a homogeneous plume segment of cylindrical form and radius R. A Gaussian profile containing the same mass as the cylindrical plume segment is given by

$$c(r) = c^* \exp\left(-\frac{r^2}{b^2}\right), \tag{4.44}$$

where c^* is the core concentration, r the distance to the central axis, and b the plume width. Thus, c^* follows from the conservation of mass compared to a cylindrical plume segment with concentration c from

$$c \cdot \pi R^2 \Delta s = \int_{s_0}^{s_1} \mathrm{d}s \int_0^{2\pi} \mathrm{d}\phi \int_0^{\infty} r \mathrm{d}r \, c(r) \tag{4.45}$$

$$= \Delta s \cdot 2\pi \cdot \frac{c^* b^2}{2} \tag{4.46}$$

$$\Rightarrow c^* = \frac{R^2}{b^2} c \,, \tag{4.47}$$

where s is the distance along the plume axis, i.e., Δs the plume cross-section segment thickness.

The observation model requires a plume simulation on a three-dimensional grid. For a set of input parameters, the model output is a set of plume properties of a plume traveling in y-direction. A domain around the central plume axis serves as the model domain, which covers at least a $4b$ radius around each point on the plume axis. The spatial resolution of the domain cells is approximately 1 m, a third of the HySpex pixel width. Each domain cell is assigned its closest plume axis point and the radius r to this point. For domain cells in the vicinity of the plume ($\exp(r^2/b^2) > 10^{-6}$), the mass concentration $c(r)$ follows from Equation (4.44). For domain cells further away, the concentration is set to zero.

In order to allow the inversion of the source strength later on, two additional parameters are introduced to Equation (4.44). The first parameter is a scaling factor k_c of the concentration c^*, which is used to scale the total mass of the plume. Since the mass of the plume is linearly related to the emission rate E, the scaling factor k_c is linearly related to the emission rate. The second parameter is a scaling factor k_b of the plume width b. It accounts for potential changes in transport during the averaging period and incomplete knowledge on the turbulent diffusion of the plume (Carhart and Policastro, 1991). The parameters are introduced such that k_c linearly scales the total mass of the plume, while k_b linearly scales the plume width without changing the total mass. The mass M_s in each slice of the plume is given by

$$M_s = \int_{s_0}^{s_1} \mathrm{d}s \int_0^{2\pi} \mathrm{d}\phi \int_0^{\infty} r \mathrm{d}r \, c(r, b; k_c, k_b) \tag{4.48}$$

$$= \int_{s_0}^{s_1} \mathrm{d}s \int_0^{2\pi} \mathrm{d}\phi \int_0^{\infty} r \mathrm{d}r \, \frac{k_c}{k_b^2} \, c_s^* \, \exp\left(-\frac{r^2}{(k_b b_s)^2}\right) \tag{4.49}$$

$$= \pi \cdot \Delta s \cdot b_s^2 \cdot k_c c_s^* \,, \tag{4.50}$$

where b_s and c_s^* are the radial width and core concentration of the segment from s_0 to s_1, respectively. Since each domain cell already carries its distance r and the plume width b, computing the concentration $c(r, b; k_c, k_b)$ requires only a single computation in each domain cell. The emission associated with such a plume is $E = k_c E_{\mathrm{ap}}$, where E_{ap} is the *a priori* emission estimate used for the initial plume simulation following Equation (4.43).

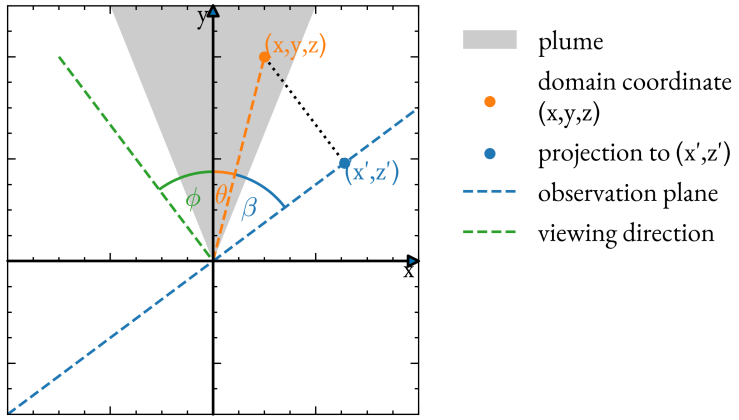

Figure 4.8: Sketch of the projection of a plume cell at (x, y, z) onto the observation plane (x', z'). The gray shading shows a conceptual top-down view on a horizontal plume cross-section - the triangular shape is chosen for simplicity and does not represent the actual plume shape. The camera viewing direction is marked by the green line, such that the angle ϕ is the angle between the viewing direction and the plume axis. The orange line points to an arbitrary plume cell at (x, y, z), with a plume cell angle of $\theta = \arctan(x/y)$. The blue line marks the projection plane which is perpendicular to the viewing direction. Figure adapted from Knapp et al. (2023b).

Observation Forward Model

The simulated plume observation follows from the modelled concentrations in the three-dimensional domain by projecting the cells on the plane of observation and aggregating the mass according to the image pixels. Figure 4.8 shows a sketch which explains the projection in a horizontal slice through the plume. The observation angle ϕ is the angle between the plume travel direction and the viewing direction of the camera. It determines the observation plane, which is perpendicular to the viewing direction. Each plume cell at (x, y, z) is at an angle $\theta = \arctan(x/y)$ to the plume travel direction. The projection angle β is the angle between the plume cell and the observation plane and given by $\beta = 90° - \phi - \theta$. This treatment neglects any vertical component of the projection, which is considered small for observations in this thesis since the plume is observed in viewing elevation angles of 2° to 7°. The observation angle is defined between -180° and +180°, where a negative angle denotes a plume moving to the left, a positive angle a plume moving to the right, and a zero angle a plume moving straight away from camera. The projection of the cell location (x, y, z) to the observation plane (x', z') follows from geometry and is given by

$$\begin{aligned} x' &= \sqrt{x^2 + y^2} \cdot \sin(\phi + \arctan(x/y)) \,, \\ z' &= z \,. \end{aligned} \tag{4.51}$$

The mass of each plume cell is given by the product of the concentration and the cell volume, and applying the projection of Equation (4.51) yields the mass distribution $m(x', z')$ in the observation plane. The mass distribution is then aggregated to the image pixels as m_{jk} by summing up

all mass points $m(x', z')$ which are located in the pixel jk. The conversion to a simulated column enhancement $\tilde{\alpha}_{jk}$ follows from

$$\tilde{\alpha}_{jk} = \frac{m_{jk}\, \nu_{\mathrm{CO_2}}}{A_{jk}}\,, \tag{4.52}$$

where $\nu_{\mathrm{CO_2}} \approx 0.546\,\mathrm{m^3\,kg^{-1}}$ is the specific volume of CO_2 at normal conditions and A_{jk} is the pixel area.

Plume Inversion

The emission estimate from the Gaussian plume inversion results from minimizing the χ^2_r-distance between the observed and simulated plume. The observation forward model has four independent input parameters: the ambient wind speed u_a, the observation angle ϕ, the emission scaling k_c, and the plume width scaling k_b. Wind information is provided by the wind LIDAR, yet the measurements are performed at kilometer distance from the source, and typical plume heights are above the LIDAR's top height of 200 m. Thus, the wind speed u_a and the observation angle ϕ are used as free parameters. All remaining input parameters are imposed *a priori* and considered constant for an observation.

The χ^2_r-minimization is performed as a brute-force scan over a sufficiently large parameter space to find the optimum and constrain the error of the independent parameters. Albeit computationally costly, this approach allows for a detailed analysis of the parameter space. For each parameter set, the reduced χ^2_r difference between the simulated and observed plume is calculated by

$$\chi^2_\mathrm{r} = \frac{1}{N-4} \sum_{jk}^{\mathrm{fitmask}} \left(\frac{\tilde{\alpha}_{jk}(k_b, k_c, u_\mathrm{a}, \phi) - \alpha_{jk}}{\sigma_{jk}} \right)^2 , \tag{4.53}$$

where N is the number of pixels in the fit mask, $\tilde{\alpha}_{jk}(k_b, k_c, u_\mathrm{a}, \phi)$ is the simulated column enhancement for the parameter set $(k_b, k_c, u_\mathrm{a}, \phi)$, α_{jk} is the observed column enhancement, and σ_{jk} is the uncertainty of the observed column enhancement in pixel jk. The uncertainty σ follows from Equation (4.12) and is specific to each scene from the covariance dependency and each pixel from the UAS.

The fit mask results from the union of the observation plume mask and all pixels with a simulated column enhancement above 2σ. The plume mask is defined as the largest continuous patch of enhancements above 2σ in the observation. Enhancements above 2σ noise level are well above the detection limit; thus, the matched filter retrieval should detect them. The combination of both masks ensures that the simulation stays close to the observation outside the observed plume mask. Background pixels from the observation contribute to the χ^2_r-distance, preventing unrealistic fit scenarios as presented in Figure 4.9b. If only the observation plume mask is used as a fit mask, the inversion scheme can move emitted mass outside the fit mask by increasing the plume width k_b and compensate for the loss by increasing k_c. The scenarios are similar in the χ^2_r-metric, yet including the background pixel from the observation identifies the unrealistic fit scenario. Using the whole image as a fit mask is not feasible since the image background typically includes systematic features which cannot be captured by the model.

Panels a) and b) in Figure 4.10 show an example of an observed and simulated plume from a coal-fired power plant, respectively. Measurements in the same frames as the chimney are excluded

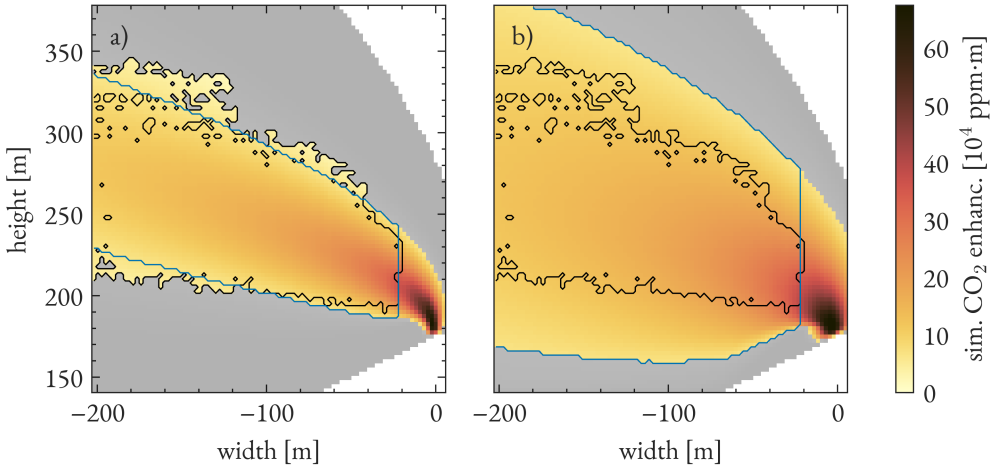

Figure 4.9: Two simulated plumes describing an observation from March 26, 2022, 13:31 - 17:36 UTC. Panel a) shows the result for the optimal plume parameter set ($k_c = 0.9$, $k_b = 1.6$). Panel b) shows the result for a plume with a larger plume width and emission ($k_c = 2.3$, $k_b = 3.7$). The black contour marks the observation plume mask, while the blue marks all simulated pixels with an enhancement above 2σ. The gray shaded area are non-zero simulated enhancements below 2σ, while the colored pixel are within the fit mask. If only the observation plume mask is used as a fit mask, both simulations result in $\chi^2_\mathrm{r} = 1.1$, even though panel a) reproduces the observation much better. The combined plume mask accounts for the mass outside the observation plume mask and yields $\chi^2_\mathrm{r} = 1.5$ and $\chi^2_\mathrm{r} = 6.8$ for panels a) and b), respectively.

since the comparatively high brightness of the chimney affects the other spectra in the frame. The translucent area of the simulated plume is below the detection limit, while the colored area is above the detection limit and thus contributes to the fit mask. Figure 4.10c shows the residual within the fit mask of the best fitting scenario.

Scanning the parameter space in a brute-force manner results in a χ^2_r for each parameter set. The optimal parameter set ($\hat{k}_b$, $\hat{k}_c$, $\hat{u}_\mathrm{a}$, $\hat{\phi}$) corresponds t the lowest χ^2_r and provides the emission estimate. The χ^2_r-landscape is used to estimate the uncertainty of the emissions. Figure 4.11 shows an illustrative χ^2_r hypersurface of the four-dimensional parameter space along the cross-sections for an exemplary observation. The χ^2_r surfaces are smooth, indicating that χ^2_r is a continuous function of the parameters. Each hypersurface shows a unique minimum, marked by a blue dot, around which the χ^2_r increases monotonically. For purely statistical errors, an increase of one in χ^2_r corresponds to a mean deviation of one standard deviation between the simulated and observed image due to parameter changes (Bevington et al., 1993). Since the concentration scaling factor k_c determines the emission estimate by $E = k_c E_\mathrm{ap}$, its uncertainty is the uncertainty of the emission estimate. Fixing ($\hat{k}_b$, $\hat{u}_\mathrm{a}$, $\hat{\phi}$) to the optimal parameter set and varying k_c within

$$\chi^2_\mathrm{r} < \min(\chi^2_\mathrm{r}) + 1 \tag{4.54}$$

results in a minimal and maximal emission estimate complying with the χ^2_r criterion. These estimates are used as the uncertainty range of the emission estimate. It is an approximation of the

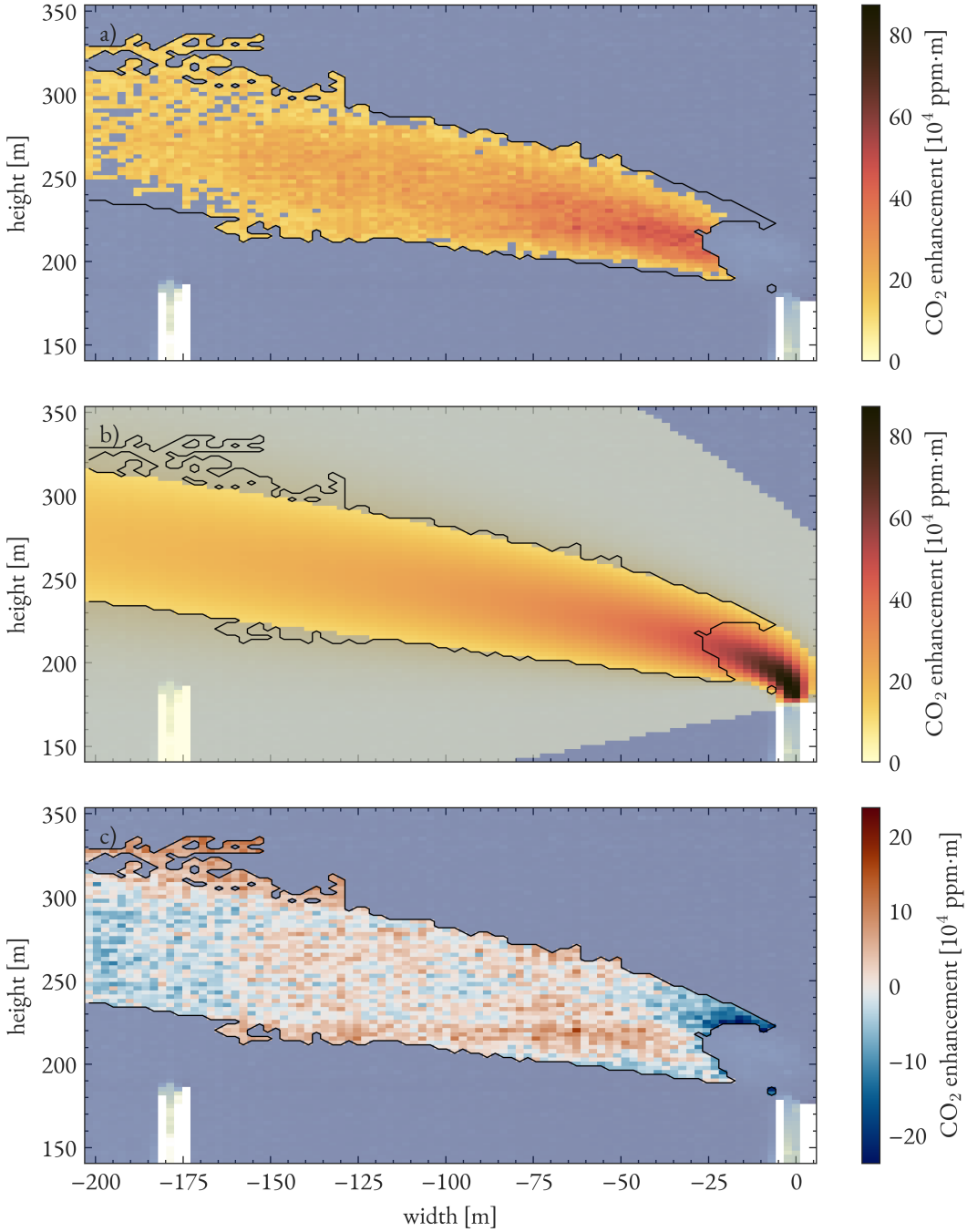

Figure 4.10: Panel a) shows an observed CO_2 emission plume from a coal-fired power plant. Panel b) shows the simulated plume for the optimal parameter set ($k_c = 1.0$, $k_b = 1.4$, $u_a = 3.8\,\mathrm{m\,s^{-1}}$, $\phi = -111°$). Panel c) shows the residual between the observed and simulated plume. Each panel shows the fit mask as a black contour. The early stages of the plume could not be observed due to condensation. The example is the observation from March 26, 2022, 15:56 - 17:36 UTC. Figure adapted from Knapp et al. (2023b).

true uncertainty since it neglects systematic errors between observation and simulation, which are challenging to account for.

The χ^2_r hypersurfaces provide the optimal parameter set and the uncertainty of the emission estimate. Furthermore, the shape and depth of the χ^2_r well convey information about the observation and the fit. A deep well indicates that the observation successfully constrains a parameter. Circular wells imply uncorrelated parameters, while a slanted well points to a correlation between the parameters. Figure 4.11 shows all six possible combinations of χ^2_r wells, each passing through the optimal parameter set. The χ^2_r surfaces indicate that the wind speed u_a and plume width parameters k_b are independent. The observation angle ϕ is the least constrained parameter and correlates with the wind speed. This behavior results from an ambiguity in the observed plume shape for horizontally viewing observers. A plume traveling toward the observer at high speed will appear similar to a slower plume traveling at a perpendicular angle. The estimated emissions are unaffected by this, following a mass balance argument comparable to the IME method. The total mass observed in the plume is fixed, and the lifetime of the plume is given by the plume length divided by the plume speed. Both the observed plume length and speed are subject to the same geometrical projection factor, thus canceling out in the emission estimate. There remains a correlation between the plume width scaling k_b and the emission scaling k_c, which results from the effect shown in Figure 4.9 and indicates that the fit mask cannot fully compensate for the correlation. Observations under favorable conditions constrain the ambiguity effectively since they provide enough information on plume width. The plume width is less constrained in observations under challenging conditions such as clouds or low emission rates. Such observations lead to a flat, slant well in the plume width (k_b) - emission scaling (k_c) plane.

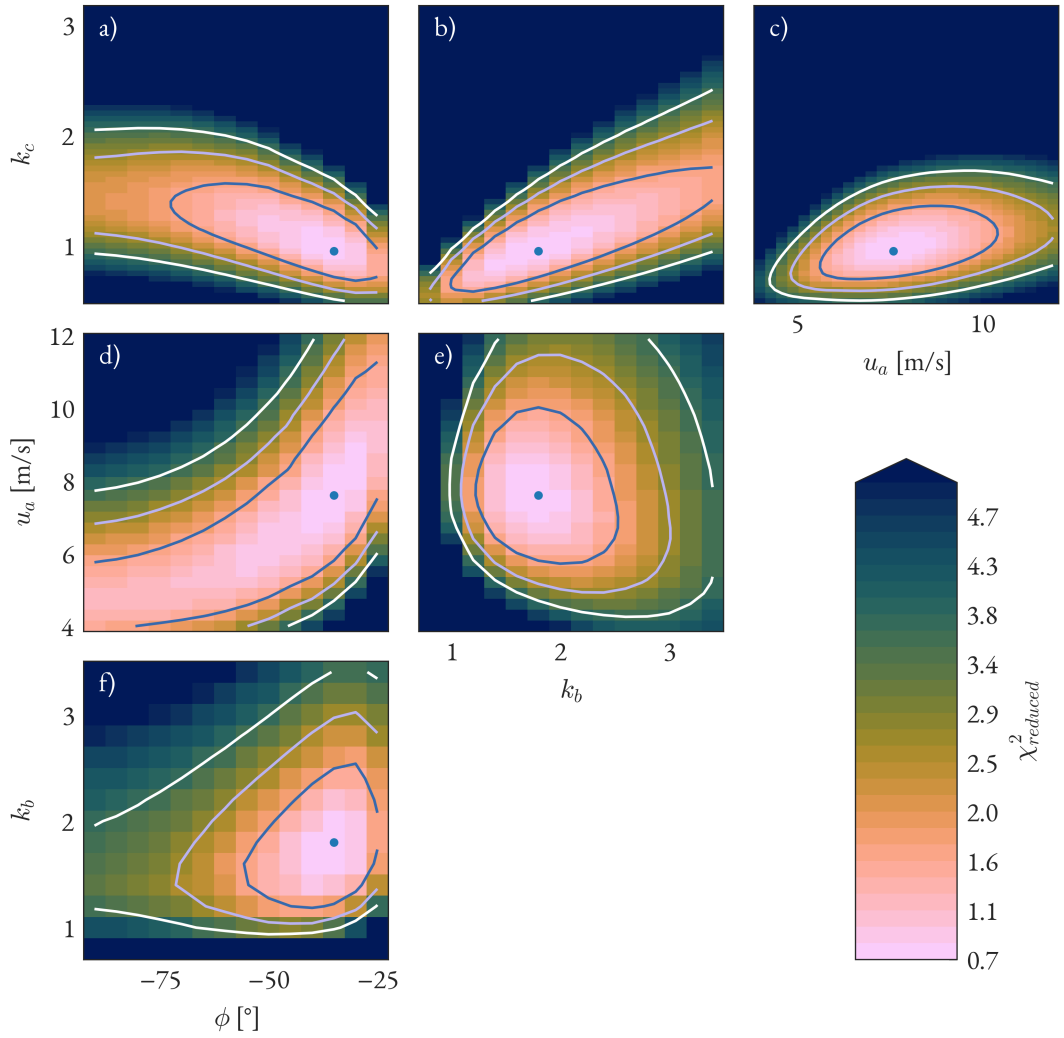

Figure 4.11: Cross-sections through the χ^2_r hypersurfaces (color coded) for the four-dimensional parameter space: emission scaling factor k_c, plume width factor k_b, wind speed u_a, and observation angle ϕ. The contour lines mark where the χ^2_r increases by 1, 2, and 3. The blue dot marks the minimal χ^2_r. Note that all cross-sections involving the observation angle are symmetric around -90°, since a plume moving away from or towards the camera looks identical. The example is the observation from September 8, 2021, 14:24 - 15:26 UTC. Figure adapted from Knapp et al. (2023b).

5 Methane Emissions From Coal Mining Operations

The ground-based HySpex camera operated at coal mine ventilation shafts in the Upper Silesian Coal Basin (USCB), Poland. Its observations enable CH_4 emission measurements from coal mining. While certain sections of this chapter have been previously published in Knapp et al. (2023a), it is noteworthy that methodological enhancements have been implemented subsequently. Section 5.1 provides an overview of the coal mining operations in the USCB, detailing two field campaigns that were conducted there. Section 5.2 describes the retrieval and emission estimation of single scans, including the challenges that arise from clouds. It presents the best-performing techniques and their limitations. Section 5.3 discusses the resulting time series of CH_4 emissions and their variability, particularly concerning the influence of turbulent transport.

5.1 Upper Silesian Coal Basin Campaigns

Globally, coal mining contributes about a third to CH_4 emissions from the fossil fuel sector (Saunois et al., 2020). Poland is currently the largest producer of hard coal in the European Union and emits about 1800 $ktCH_4$ per year (NIR, 2018). Coal mining in the USCB contributes about 500 $ktCH_4$ to these emissions. Fossil fuel related emissions are not well constrained (e.g., Kirschke et al., 2013; Saunois et al., 2020), partly due to the temporal variability. For coal mining emissions, the wide range of CH_4 content in coal seams and missing activity data cause incomplete knowledge (Swolkień, 2020). Methane forms in coal beds during the carbonization of organic matter and is released when the ambient pressure drops, e.g., during coal mining operations. In order to avoid hazardous concentrations inside the mine ($\geq 5\%$), CH_4 is continuously vented into the atmosphere through ventilation shafts. The E-PRTR lists more than 50 active shafts emitting between 0.3 $ktCH_4\ yr^{-1}$ and 40 $ktCH_4\ yr^{-1}$ in the USCB in 2018. The extraordinary accumulation and strength of the point sources make the USCB a particularly interesting target for CH_4 emission quantification (Swolkień, 2020).

A major effort was conducted with the Carbon Dioxide and Methane (COMET) mission 1.0 in 2018, using a plethora of instruments to quantify CH_4 emissions. Luther et al. (2019) and Luther et al. (2022) measured total column CH_4 using ground-based FTIR spectrometers, either on a mobile platform or as a network. Aircraft observations using in-situ (Gałkowski et al., 2021; Kostinek et al., 2021), column (Krautwurst et al., 2021), or imaging (Hochstaffl et al., 2023) sensors were used to either quantify area or single shaft emissions. Fiehn et al. (2020) combined aircraft and ground-based in-situ observations to constrain emissions from the whole area. Unmanned aerial vehicles flew plume transects downwind of the shafts to estimate the emissions from these curtains (Andersen et al., 2021; Shi et al., 2022; Andersen et al., 2023). Many more studies of the USCB connect

to the COMET campaign, e.g., using satellite observations (Tu et al., 2022) or improving the understanding of top-down emission quantification (Brunner et al., 2023). The COMET campaign demonstrates the added value of comprehensive and independent top-down observations of coal mining emissions and inspired further research in the USCB, including the presented results.

5.1.1 Proof of Concept Campaign 2022

The HySpex SWIR-384 camera operated in the USCB in June 2022. It was the first time ground-based imaging spectroscopy in the SWIR spectral range was used to observe CH_4 plumes from point sources. Thus, the campaign was a proof of concept for quantifying CH_4 emissions from the spectral images. The goal was to identify the best practices and challenges that must be overcome in future campaigns. The team comprised researchers from Heidelberg University and the AGH University of Science and Technology in Kraków. Camera observations were conducted for 11 days between June 14 and June 27, 2022, at five different coal mine ventilation shafts around Katowice, Poland.

The camera and the portable wind LIDAR operated between 0.6 km and 1.3 km from the shafts. Figure 5.1 shows a typical setup of the instruments during observations at the Pniówek V coal mine ventilation shaft. In addition to the wind LIDAR, mobile on-ground in-situ measurements of CH_4 gave real-time information on the plume travel direction, supporting the selection of a suitable observation location for the camera. Since the method requires an unobstructed view of the ventilation shaft, which is approximately 11 m high, obstacles like tree lines or buildings limit the choice of observation locations. The coal mine ventilation shaft Pniówek V (49.9753°N, 18.7354°E) was chosen as the main observation target due to its high CH_4 emissions in the past of at least 18 ktCH_4 yr^{-1} (E-PRTR 2018) and the availability of a suitable observation location in the west and north of the shaft. Figure 5.2 shows the observation locations on a map. Knapp et al. (2023a) present results from four days of observations at Pniówek V under varying atmospheric conditions, including several levels of cloud cover and wind conditions. These results are discussed again in this chapter using an improved evaluation technique. Other shafts than Pniówek V were observed on a single day each. However, low emissions, observation locations that were too close, and bad weather conditions prevented a successful retrieval of CH_4 emissions from these observations.

5.1.2 Collaborative Campaign 2023

In June 2023, a collaborative campaign in the context of the International Methane Emissions Observatory (IMEO) program from the United Nations Environment Programme (UNEP) took place in the USCB. The campaign aimed to cross-validate different methods for quantifying CH_4 emissions from single coal mine ventilation shafts. The Pniówek V shaft served as the main observation target since it was best located and accessible for all instruments. A team from the Technische Universität München operated a ground-based network of three FTIR spectrometers around the shaft, observing the total column CH_4. The AGH Kraków mounted a tunable diode laser absorption spectroscopy (TDLAS) instrument on top of Pniówek V. It measured the CH_4 column in an open path above the outlet in addition to AGH's mobile ground-based measurements. The HySpex camera operated for ten days between June 4 and June 17, 2023. During the campaign,

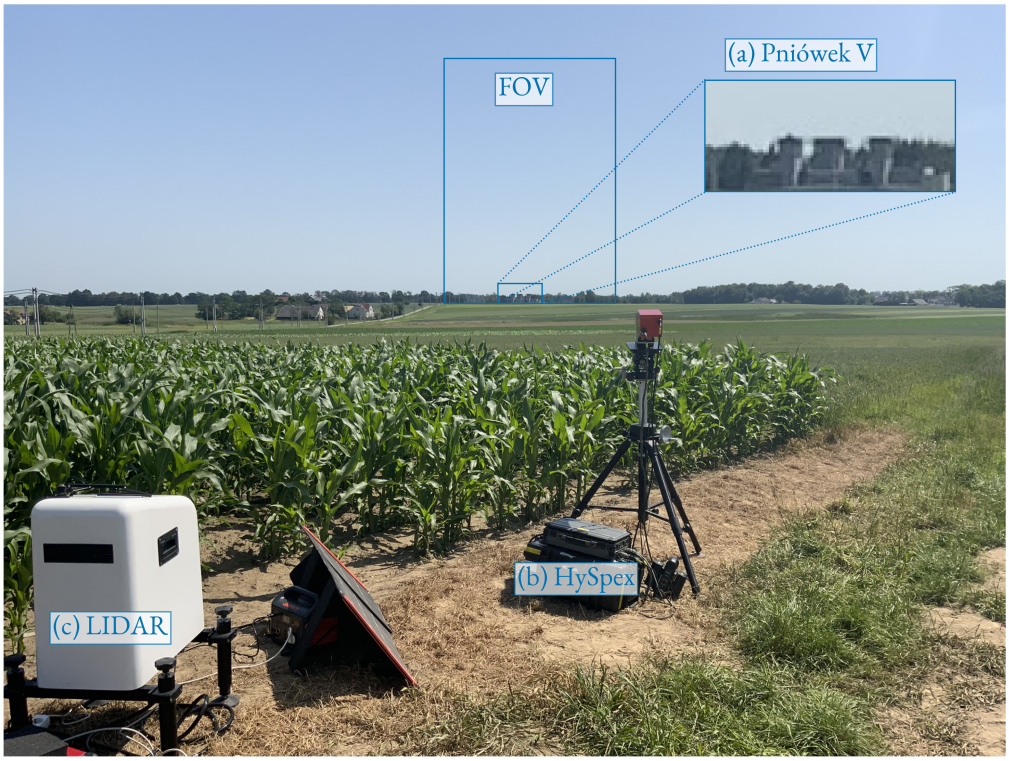

Figure 5.1: Field setup of the instruments during observations at the Pniówek V coal mine ventilation shaft (a). The FOV of the HySpex camera (b) is indicated by the blue rectangle, in the lower part lies the shaft. Beside the camera the wind LIDAR (c) is visible. Figure as shown in Knapp et al. (2023a).

a persistent cloud cover posed challenging measurement conditions to the camera and the direct-sun viewing FTIR spectrometers. This chapter presents camera observations on June 8, 11, 12, and 13, 2023, which had ideal wind conditions. Section 5.2.2 discusses approaches to overcome issues from scene heterogeneity using the matched filter algorithm. Section 5.2.3 presents observations of the camera operating in a fixed observation geometry, i.e., the camera was not rotating during the scan. UNEP kindly allowed the inclusion of preliminary in-situ data in this thesis. The TDLAS instrument operated continuously after June 13, allowing a comparison of its emission estimates to the imaging setup. Furthermore, a continuously operated safety network of low-cost pellistor sensors monitors the CH_4 concentration in the mine shaft with a resolution of 0.1 % (Swolkień et al., 2022). A pellistor sensor operates by oxidizing gases at a catalytic bead, inducing a change in electric resistance for the concentration measurement. These measurements are available for all campaign days.

5.2 Methane Imaging and Emission Estimation

The following sections present the retrieval and emission estimation techniques for CH_4 plume observations. Section 5.2.1 compares the performance of several matched filter retrieval algo-

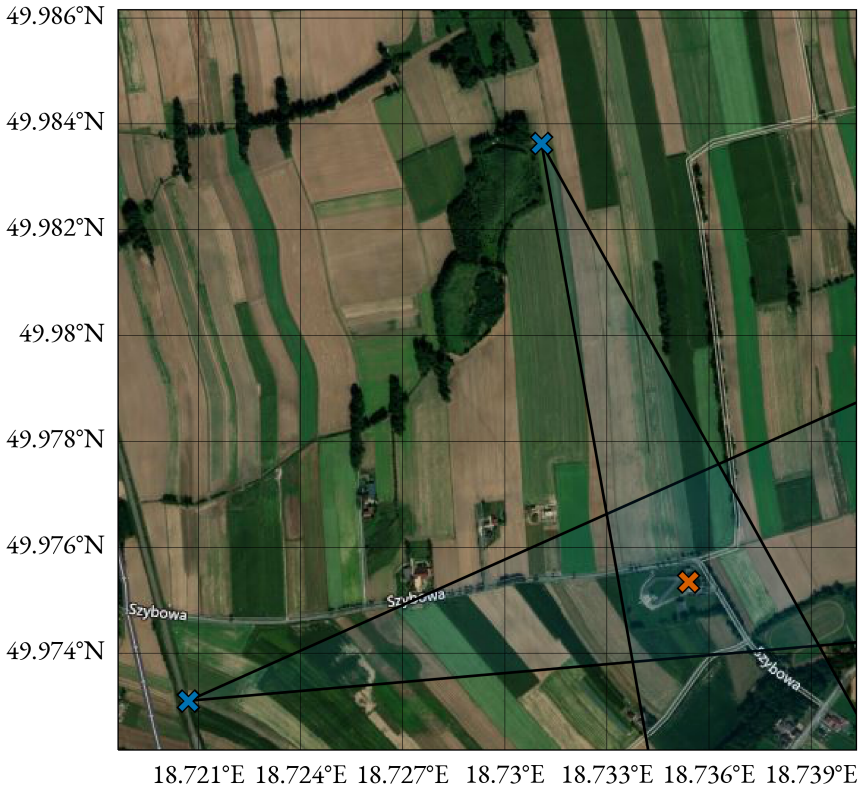

Figure 5.2: Map of the Pniówek V coal mine ventilation shaft (orange) and the observation locations (blue). The FOV of the camera is indicated by the blue triangle. The actual FOV depends on the settings of the individual experiment. The observation location is chosen according to the wind direction, such that the plume moves laterally through the FOV. Background map from OpenStreetMap (openstreetmap.org).

rithms and presents mass balance emission estimates using observations from the 2022 campaign. Scene heterogeneity caused by clouds, as encountered in 2023, requires a more sophisticated approach to the matched filter retrieval, which is discussed in Section 5.2.2. Section 5.2.3 presents the first results from the fixed viewing geometry.

5.2.1 Image Evaluation Technique

The image evaluation pipeline comprises the preprocessing of raw images, the retrieval of atmospheric CH_4 enhancements, and emission estimates based on plume observations. This section compares the performance of several matched filter algorithms for retrieving CH_4 enhancements. Furthermore, it discusses mass balance methods in the context of ground-based imaging. Figure 5.3 shows the workflow from the raw camera scan to the emission estimate. Every scan is preprocessed according to Section 3.1.1. The coal mine ventilation shaft serves as a landmark, which, combined with the GPS sensor, constrains the camera's VEA and VAA. Since every image contains the shaft in the lower part, there are also near-surface structures like trees in the image. Such structures compromise the matched filter performance and are excluded manually from further

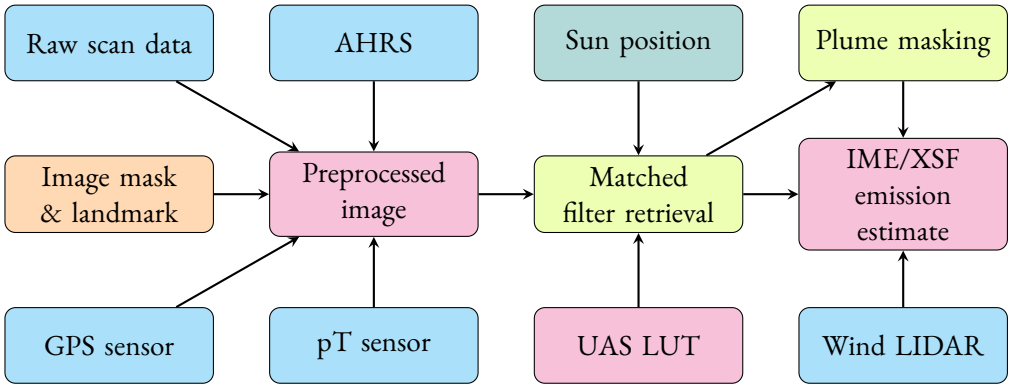

Figure 5.3: Flowchart of the CH_4 imaging and emission estimation technique. A pressure and temperature (pT) sensor observes the ambient conditions. A GPS sensor provides the camera position and time, and the AHRS and a landmark provide the camera orientation. The visually defined image mask excludes pixels that observe the tree line, for example, from the retrieval. The preprocessing applies necessary corrections to the raw data, see Equation (3.6). The retrieval requires a UAS LUT (Figure 4.4) and thus, the solar position. The emission estimate uses the coinciding wind LIDAR observations and observed enhancements inside the plume mask. Processes are yellow, settings are orange, (interim) results are red, and internal and external data are blue and green, respectively.

processing. Thus, every preprocessed image includes the necessary information for the subsequent retrieval.

Retrieval performance comparisons for the matched filter algorithms consider two quality criteria. The matched filter maximizes the SNR of the target signature with respect to the background. Thus, the SNR of the retrieval serves as one quality criterion. It follows from Equation (4.11) and Equation (4.12) in every pixel i in the image as $\mathrm{SNR}_i = \hat{\alpha}_i/\sigma_i$. A higher SNR indicates a clearer separation of the plume from the background. The plume size is the second quality criterion as it is relevant for mass balance emission estimates since missing plume parts cause an underestimation of the emission. The comparison of different matched filter algorithms relies on the reliably observed plume pixels. Image pixels are considered reliable plume observations if they fulfill the following conditions. First, the CoMF plume masking algorithm of Section 4.1.4 identifies them as plume pixels. Second, the plume satisfies additional sanity criteria to ensure correct plume identification. The additional criteria are chosen following Knapp et al. (2023a) and are empirical for ill-suited observation conditions or incorrect plume masks. They assert that the plume mask contains pixels close ($\leq$ 7 m) to the shaft outlet. Furthermore, the plume must be located downwind from the shaft (85 % of the enhanced pixels). Lastly, a wind direction filter criterion removes plumes that are moving at an acute angle towards or away from the observer ($|\sin(\phi)| \geq 0.45$). Such wind directions impair the IME's ability to infer the plume length, compromising the emission estimate. Knapp et al. (2023a) also exclude small plumes with less than 900 pixels. The improved retrieval and plume masking algorithms make this criterion obsolete since it only removes already excluded observations. Table A.1 provides an overview of the filter effects.

Observation conditions were ideal on June 19, 2022, with a clear sky and prevailing winds from the south. Thus, observations of this day are suitable for evaluating the performance of

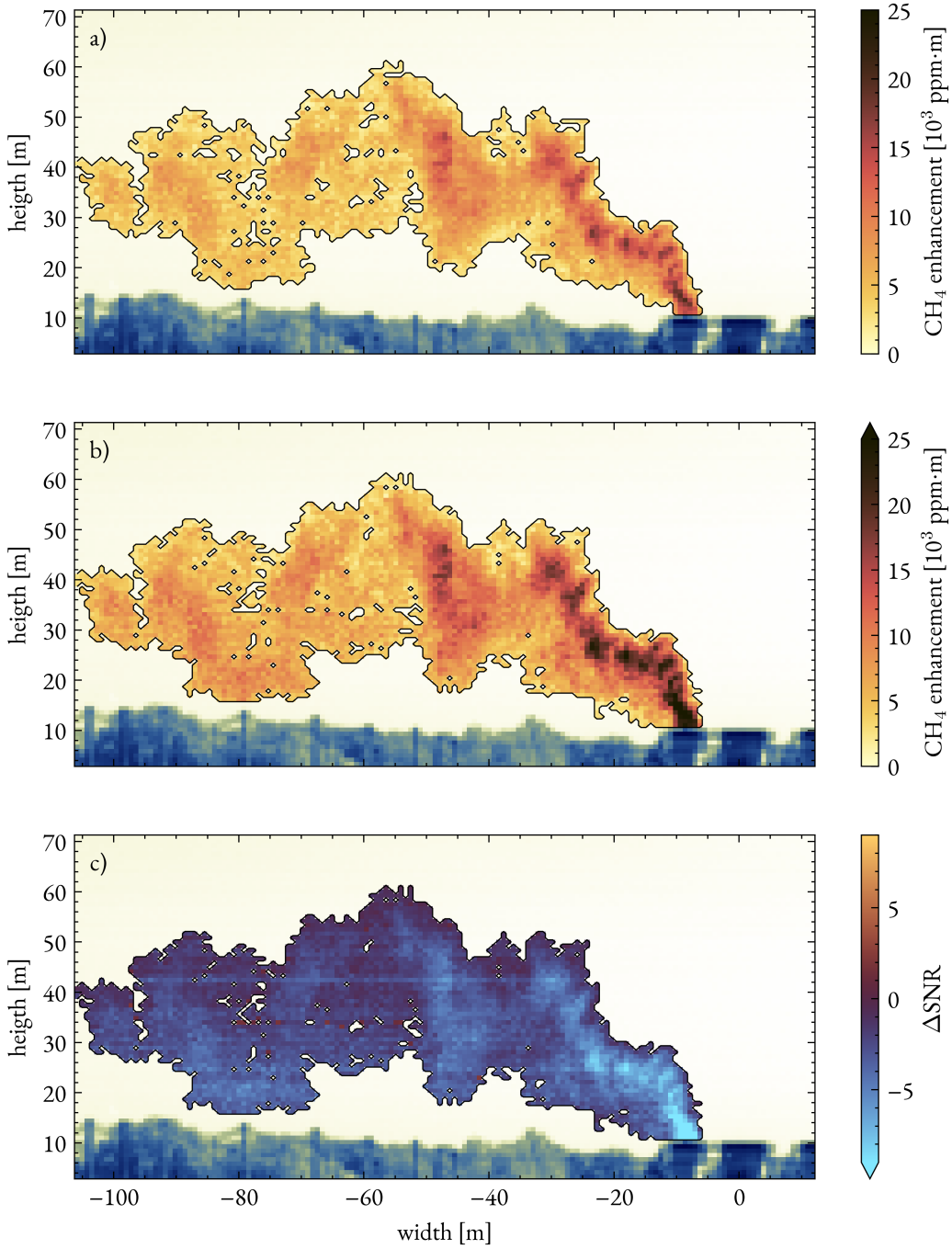

Figure 5.4: Comparison of the a) CMF and b) DMF retrieval for an observation on June 19, 2022. The plume is identified in front of a cloudless, blue sky, and plume pixels are identified using a simple thresholding approach. Panel c) shows the difference in SNR (CMF-DMF) for the plume pixels. The DMF algorithm outperforms the CMF in terms of SNR and plume size.

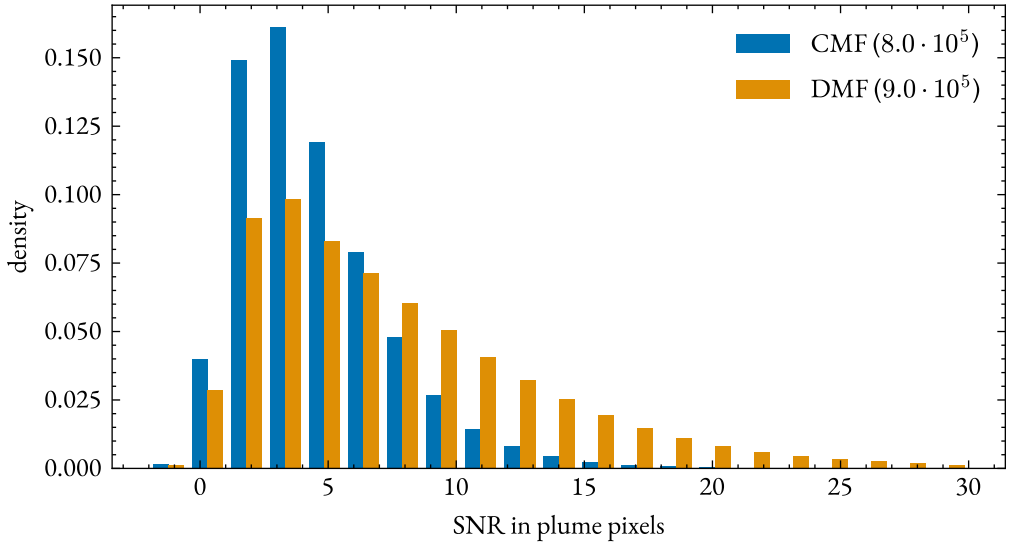

Figure 5.5: Comparison of CMF and DMF retrieval SNR for plume pixels from observations on June 19, 2022. The number in brackets is the total amount of confidently identified plume pixels. The DMF shows a higher SNR within the plume pixels. Note that the lowest SNR bins are included in the plume mask due to the CoMF plume masking algorithm, which includes a median smoothing.

the matched filter retrieval algorithms under favorable conditions. Due to wind gusts, corn plants sporadically obstructed parts of the FOV between 11 am and 2 pm UTC, and these trivial cases are visually identified and removed. Figure 5.4 shows exemplary CH_4 plume images retrieved using a) the CMF and b) the DMF for this day. Both retrievals employ the iterative background optimization and brightness correction described in Section 4.1.2. Thus, the line-wise referencing of the spectra in the DMF causes the performance difference. Here, the plume is identified as the largest continuous patch of CH_4 enhancement in the image following Knapp et al. (2023a). This simplified plume mask emphasizes the differences between the CMF and DMF retrieval. While the CMF identifies nearly the same plume pixels as the DMF, the DMF shows larger enhancements and a higher SNR for all plume pixels (Figure 5.4c). This finding points to an increased capability of the DMF to detect CH_4 enhancements, which is consistent for all observations during favorable conditions. Figure 5.5 shows the SNR distribution for all plume observations from the CMF and DMF retrieval on June 19, 2022. The DMF identifies more plume pixels ($9.0 \cdot 10^5$) than the CMF ($8.0 \cdot 10^5$) over the day, as illustrated in panels a) and b) of Figure 5.4. Furthermore, the SNR distribution shifts towards higher values for the DMF retrieval. Since the DMF outperforms the CMF in clear sky conditions in both plume pixel identification and SNR, it is favored for the following analysis.

The emission estimate from each image is calculated using the IME method described in Section 4.2.1. The observed plumes are spatially well resolved with a pixel size of approximately 0.73 m × 0.73 m. The resolution allows the identification of density fluctuations within the plume. A single image provides ten emission estimates with increasing segment length, following Duren et al. (2019). The average of the segments' emissions is the scan's emission estimate. The spread of the

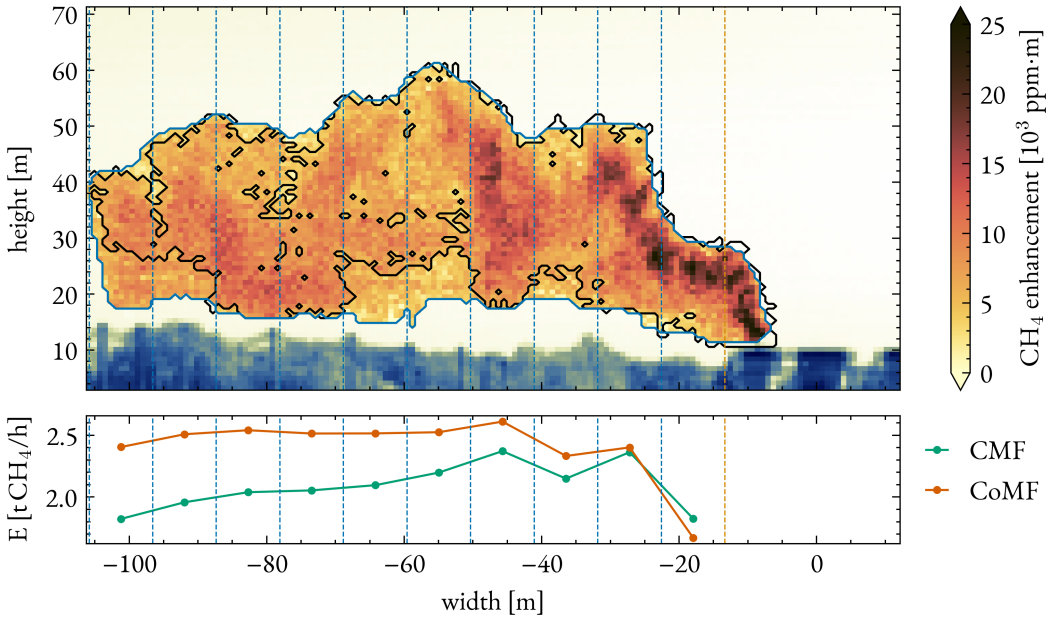

Figure 5.6: Effect of CoMF masking on emission estimation under clear sky conditions. The CoMF masking includes low SNR pixels in the plume's fringes, partly compensating for the dilution of the plume below a detection limit tresholding. Segment-wise emission estimates are displayed in the lower panel, which remain more stable with increasing distance from the source for the CoMF masking (orange) while they decrease for the MAG1C (green) thresholding.

segments' estimates arises from turbulent transport, dilution below the detection limit, and emission variability during the scan. The uncertainty for the emission estimate follows using Gaussian error propagation as described in Equation (4.36). It uses the distribution of the ten emission estimates and the co-located wind LIDAR observations. The mean and standard deviation of a ten-minute interval around each image provide the wind speed and direction and their respective uncertainties. Note that the emission uncertainty does not include systematic uncertainties from, e.g., the UAS generation or the linearity assumption of the matched filter. The horizontal viewing geometry enables a direct assessment of the plume height. Thus, the emission estimate uses the wind information at the mass-weighted plume height. This technique provides a single emission estimate with an uncertainty from each plume image, which is used for further analysis in Section 5.3.

Figure 5.6 shows the effect of the CoMF plume masking algorithm from Roger et al. (2023b) on a CH_4 plume image from June 19, 2022. The CoMF uses a combination of spectral retrieval intervals to suppress artifacts from scene heterogeneity and to improve the plume mask (Section 4.1.4). Figure 5.6 shows how the plume mask includes low SNR pixels at the plume fringes, improving emission estimates from mass balance methods. The MAG1C algorithm of Foote et al. (2020) effectively sets pixel enhancements below a detection limit of 2σ to zero. Thus, it provides a plume mask using a thresholding approach, which is included in Figure 5.6 for comparison. Due to mixing with ambient air and the resulting dilution of the plume, as the distance from the source

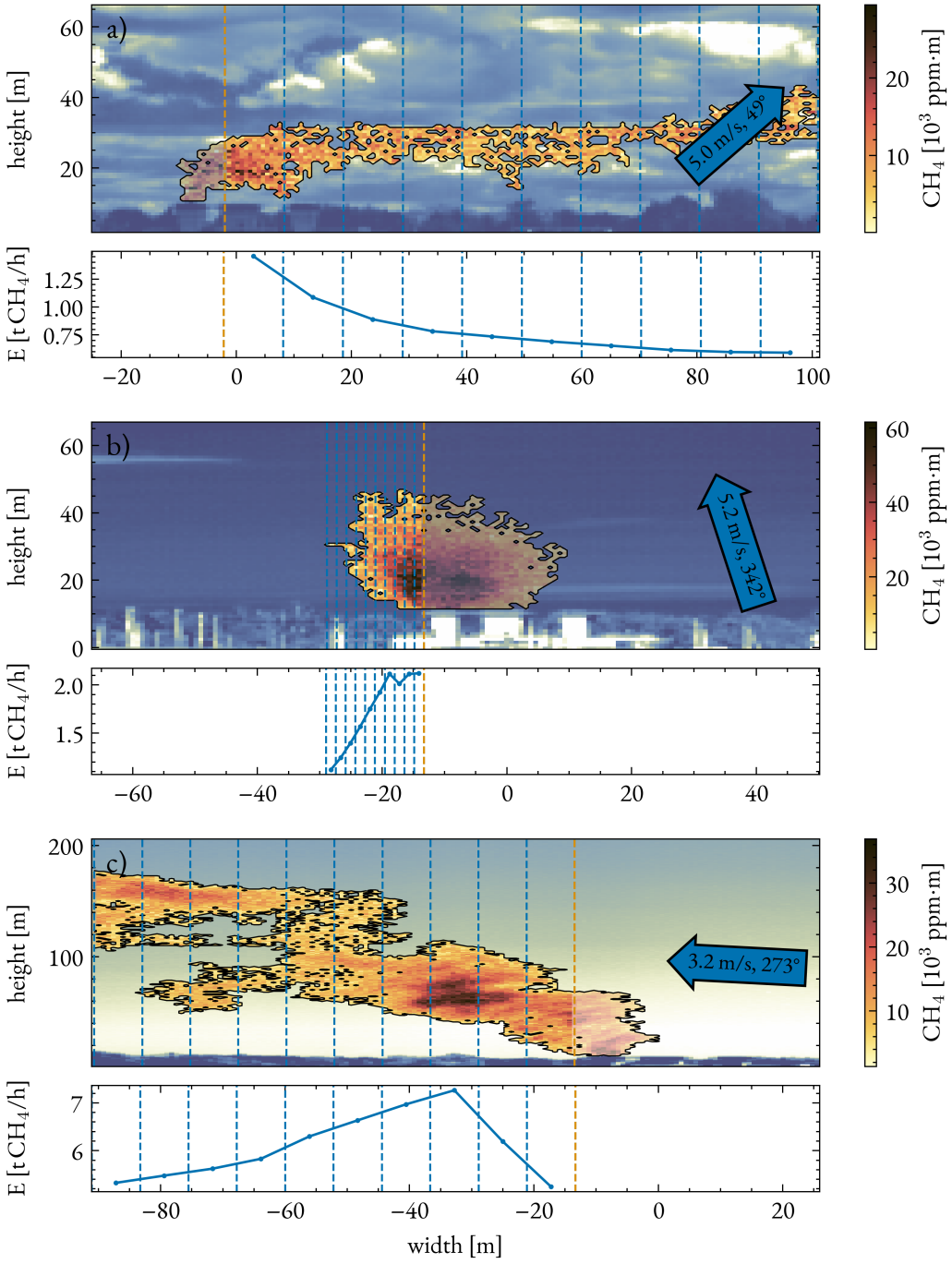

Figure 5.7: Limits of the IME technique by a) clouds, b) wind direction, and c) wind speed. From a) June 17 10:58 UTC, b) June 18 14:31 UTC, and c) June 20 08:48 UTC in 2022. The plumes are identified with a tresholding approach to highlight the effect of scene heterogeneity. The arrows in each panel show the wind direction and speed, where an upward arrow denotes a plume moving away from the observer, a downward arrow denotes a plume moving towards the observer, and left and right arrows denote a plume moving left and right, respectively. Figure adapted from Knapp et al. (2023a, Supplement).

increases, more of the emitted mass falls below the detection limit. Since the CoMF improves the contrast of background and plume pixels, it enables the inclusion of low-enhancement pixels in the plume mask. On average, emission estimates using a thresholding approach decrease with distance from the shaft by 8 % to 12 %, while the CoMF masking reduces this to 0 % to 5 %. Thus, the CoMF plume mask is used for further analysis.

Imaging observations face some limitations that may compromise successful emission estimates. Figure 5.7 shows three examples of such limitations identified in the 2022 campaign (Knapp et al., 2023a). Figure 5.7a shows the CMF result of a cloudy scene. In general, clouds can cause the algorithm to either miss a significant fraction of the plume or identify artifacts as the plume. They act similarly to surface heterogeneity in top-down viewing applications. The CoMF mitigates this effect efficiently and is discussed in more detail in Section 5.2.2. Figure 5.7b shows an example of a plume moving towards the observer. This is a trivial case of unfavorable wind conditions since the advection-driven plume extent cannot be derived from the image. The wind direction filter criterion excludes such observations from further processing. Figure 5.7c shows an example of a plume at relatively low wind speed, causing unstable plumes with enhanced turbulent features. While this behavior does not prevent the emission estimation per se, it increases the uncertainty of the emission estimate from a single image. Wind speeds ranged between 1.6 m s^{-1} and 3.9 m s^{-1} on June 20, significantly lower than those observed on June 19 (4.0 m s^{-1} to 7.6 m s^{-1}). The relative emission error of single scans increased from 10.7 % to 15.5 %, even though both days featured a blue sky.

5.2.2 Clouds and Their Impact on Methane Imaging

The blue sky is, to the advantage of the matched filter retrieval, a spectrally smooth and spatially homogeneous background in the SWIR spectral range. Background heterogeneity challenges physics-based and statistical retrievals and is a well-known problem in top-down observations (e.g., Ayasse et al., 2018; Borchardt et al., 2021; Roger et al., 2023b). Surface features induce artifacts if their spectral reflectivity is similar to the target gas absorption features. Clouds introduce comparable background heterogeneity to ground-based observations by altering the radiative transfer through the atmosphere. Thus, they may be treated using similar techniques. Cloudy pixels are typically an order of magnitude brighter than the blue sky and favor multiple scattering, violating the single scattering assumption for the UAS generation. Furthermore, the introduced spatial variability of spectra translates to increasing covariance matrix elements. Generally, the covariance elements inform the retrieval of the correlation between channels. Thus, they recover information about the spectra from the target scene. The spatial covariance makes the matched filter retrieval more robust against scene heterogeneity than physics-based retrievals, which treat every pixel independently (e.g., Hochstaffl et al., 2023). However, the spectral reflectance of clouds is not the same as that of molecules and aerosols. Cloud-scattered pixels show systematically different spectra than the blue sky, violating the Gaussian assumption of the matched filter retrieval. Thus, the matched filter's capability to detect and quantify the target gas decreases. While the average SNR of plume pixels on clear days ranges from 5 to 6, it drops to 2 to 3 on cloudy days (Figures 5.5 and 5.10).

Figure 5.8 shows several realizations of the matched filter algorithm dealing with scene heterogeneity caused by clouds on June 13, 2023. The scene is only mildly affected by clouds in the lower parts, but it illustrates the relevant features. All algorithms use the CoMF approach to suppress

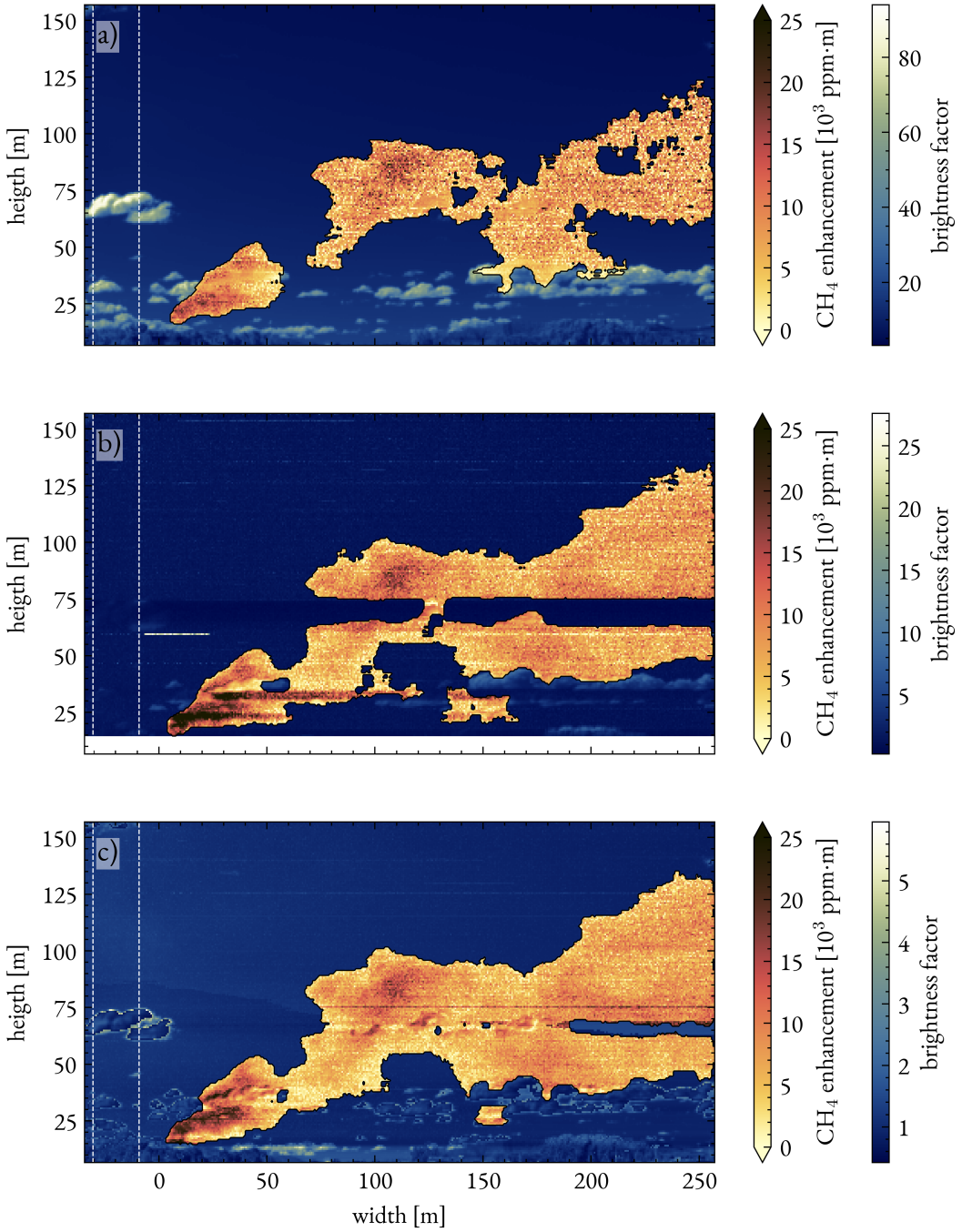

Figure 5.8: Comparison of the a) CMF, b) DMF, and c) clustered differential matched filter (CLU) retrieval for an observation on June 13, 2023. The identified plumes (yellow to red) are shown in front of the brightness factor (blue to white) of the respective retrieval. The clouds are easily identified in the CMF retrieval as the bright spots. For the DMF and CLU retrieval, the dashed white lines mark the background region. A cloud at 75 m height causes a major artifact in the DMF retrieval, which is partly removed by the CLU retrieval.

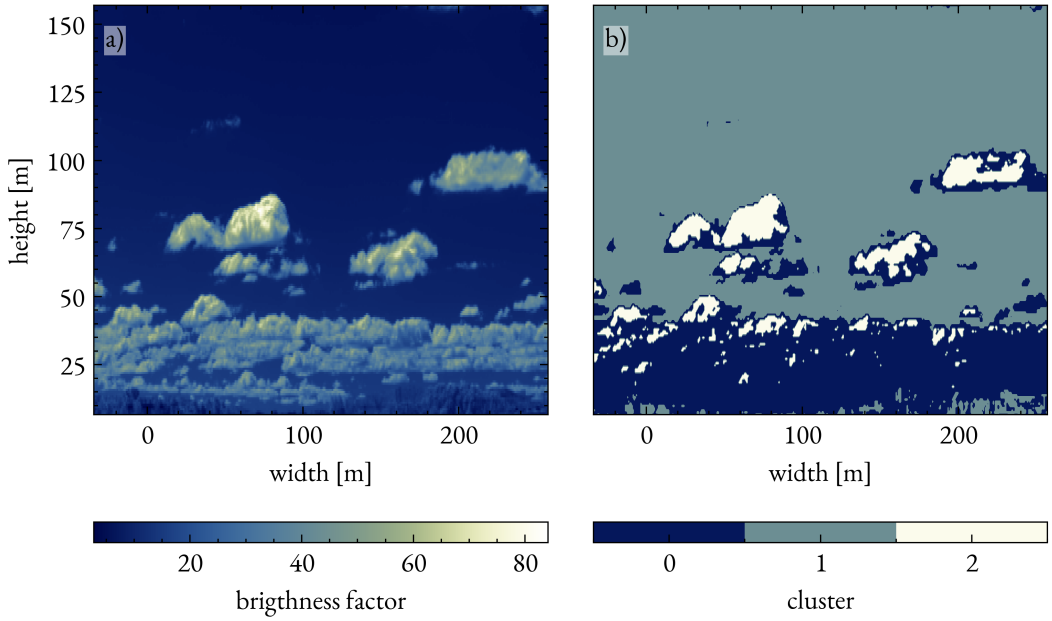

Figure 5.9: Clustering of pixels into similar spectra to improve referencing for the CLU. Panel a) shows the pixel brightness and panel b) the clustering result.

background artifacts and improve the plume mask. Figure 5.8a shows the CMF retrieval of the scene, revealing a tube-like plume moving upwards and to the right. A darker background corresponds to higher noise levels within the identified plume pixels. Furthermore, enhancements appear in front of clouds in the lower plume parts around 150 m to 200 m downwind of the shaft. These enhancements may be due to cloud scatter artifacts or the higher brightness for better enhancement detection. While the DMF outperforms the CMF under favorable conditions, Figure 5.8b shows that this is not necessarily the case for cloudy scenes. The differential approach requires a reference spectrum from the background pixels upwind of the source. The background region is marked in Figure 5.8, and spectra from this region are taken as representative of the whole line of the image. The assumption fails for a heterogeneous background, as is apparent around 75 m in height. A cloud drifted into the background region, so the reference spectrum does not fit the other spectra in the line. Consequently, the DMF cannot identify the plume in these lines. Similar features are apparent in the earlier stages of the plume, around 25 m in height, where clouds introduce stripes of higher enhancements. Despite these shortcomings, the DMF identifies an overall larger plume and closes gaps in the CMF retrieval.

Clustering of the pixels improved the matched filter performance in the presence of heterogeneous data in past studies (Funk et al., 2001; Thorpe et al., 2013). These studies use a simple k-means clustering to aggregate all pixels of the scene and apply a different matched filter to each cluster. However, clusters may contain an insufficient pixel number to support a robust background estimation for the matched filter. Therefore, the presented clustered differential matched filter (CLU) aims to unify the spectral input vectors of the whole image and apply the matched filter to all pixels. As described in Section 4.1.3, the CLU requires reference spectra depending on the line

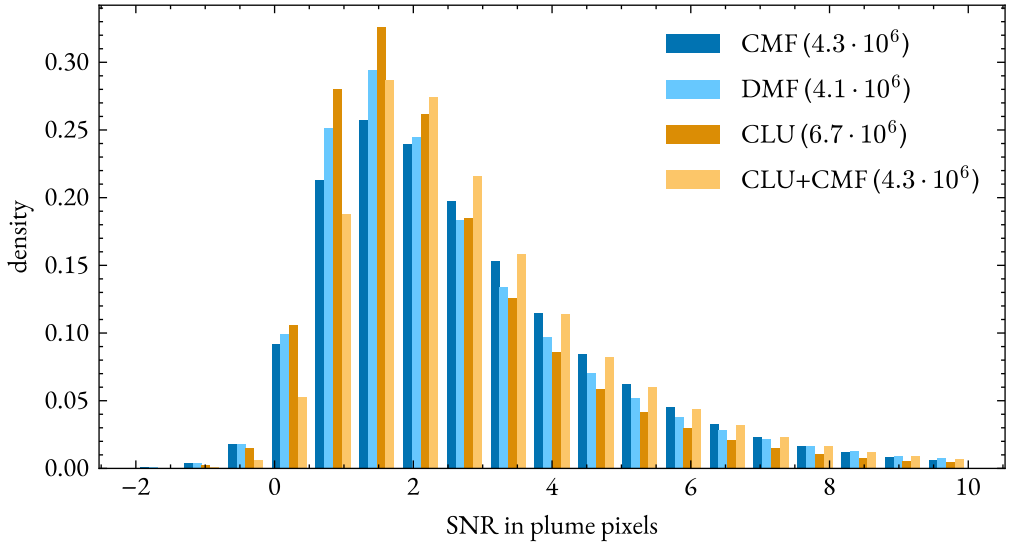

Figure 5.10: Comparison of CMF, DMF, and CLU retrieval SNR within the plume mask for all pixels during a cloudy observation day (June 13, 2023). As expected, the overall SNR is lower than for clear sky observations. Furthermore, the comparison of the three algorithms is inconclusive when all plume pixels are considered. Yet, the CLU identifies many more plume pixels than the other algorithms, and outperforms the CMF in shared plume pixels (CLU+CMF). Numbers in brackets denote the total number of plume pixels contributing to the histogram.

and the cluster. The k-means clustering sorts pixels from 30 consecutive images into three clusters. Figure 5.9 shows that the algorithm clusters the pixels according to their brightness, which can be loosely associated with blue sky and directly and indirectly illuminated clouds. The clustering uses four channels[1] from the whole spectral range of the instrument to limit the required computational resources. A reference spectrum of the same cluster and line references each spectrum in a line, removing systematic features from the input data. If the background region of the line includes no matching reference spectrum, the cluster mean reference spectrum is used. Figure 5.8c shows the result of the CLU retrieval. The image's background shows that clustering decreases the brightness range of the background pixels, as was to be expected. The striping in the 25 m height region vanishes, and the missing stripe in the 75 m height nearly closes. The remaining missing values align with a cluster change of the pixels. Enhancements in cluster 1 are detected, and the gap in the plume consists of pixels in cluster 2. While a line-specific reference spectrum exists for cluster 1, cluster 2 falls back on the cluster mean reference spectrum. Thus, the referencing performance suffers, and the plume cannot be identified in cluster 2. Potential paths to improve the clustering approach are (a) choosing reference spectra from the same cluster and line from other images or (b) applying the DMF for each cluster separately, given that the cluster sizes support a robust background estimation.

Figure 5.10 compares the three retrieval algorithms for a cloudy observation day on June 13, 2023. In contrast to the clear sky case, the SNR histogram shows no separation between the CMF,

[1] The channels are chosen in the transparent parts of the spectrum at 1007, 1279, 1606, and 2204 nm.

DMF, and CLU retrieval. In the case of scene heterogeneity, a major challenge of the matched filter retrieval is the identification of the plume pixels. The DMF is not feasible in cloudy scenes due to the shortcomings mentioned earlier, as reflected in the low number of plume pixels identified ($4.1 \cdot 10^6$). The CLU identifies $6.7 \cdot 10^6$ plume pixels, over 50 % more than the CMF ($4.3 \cdot 10^6$). Furthermore, the CLU outperforms the CMF in plume pixels identified by both retrievals regarding the SNR. A visual inspection of the images shows that the CLU plumes typically (a) close holes in the CMF plume or (b) expand the plume outwards. Although the CLU technique is not flawless, it enhances the retrieval of plume mask and SNR in comparison to the CMF for heterogeneous backgrounds. Therefore, it is preferred for analyzing cloudy scenes.

5.2.3 Fixed Viewing Geometry

During the 2023 campaign, the camera operated in a fixed viewing geometry for several hours on three of the four days presented here. The camera does not rotate in this observation mode, such that each frame observes the same vertical stripe of the scene. Thus, these pseudo-scans lose the imaging capability, but several advantages arise from this setup. If the camera points a few degrees downwind of the shaft, the ambient wind transports the emitted plume through the camera's FOV. Every frame captures a cross-section of the plume, which provides a time series of the plume evolution at a certain distance downwind of the source. The camera's frame dimension is effectively transformed into a temporal dimension, allowing for observing the plume's evolution over time instead of a spatial image of the bent-over plume shape. The camera's integration time and co-adding settings determine the sampling rate of frames, typically ranging from 3 Hz to 10 Hz.

The fixed geometry has some implications for the differential retrieval and emission estimation technique. As the fixed viewing geometry lacks an upwind region, the DMF and CLU techniques necessitate a background image for the reference spectrum. The camera pointed 2° upwind of the shaft for background observations. These images were captured either before or after the fixed geometry observation. Taking ten or more background scans is recommended to improve the SNR in the reference spectra and provide sufficient spectra in each cluster. The k-means clustering algorithm sorts the spectra from the background scans and 20 consecutive plume scans into three clusters. Every pixel in the plume scans is assigned a line- and cluster-specific reference spectra from the background scans.

The fixed geometry is ideal for emission estimates using the XSF method, as each frame provides a cross-sectional plume measurement. Therefore, the XSF provides emission estimates at the same frequency as the frame rate. However, single-frame emission estimates show considerable variability due to turbulent transport processes at this temporal scale (e.g., Woitischek et al., 2021a). Like in the scanning geometry, each pseudo-scan provides a mean emission estimate with uncertainty. The mean emission is the frame average, while the uncertainty follows from the wind observations at observation time and the emission standard deviation over the frames. Note that the uncertainty is generally higher than for the scanning observations since the frames may include no plume pixels, yielding 0 $tCH_4\ h^{-1}$ as the frame emissions, and are not binned into segments.

Figure 5.11 displays two observations obtained with the CMF and CLU using the fixed geometry on June 8, 2023. Observations using the fixed geometry during a clear sky day were impossible due to the weather conditions. Therefore, the current analysis is limited to cloudy scenes. The background brightness exhibits greater variability in the vertical direction than in the horizontal

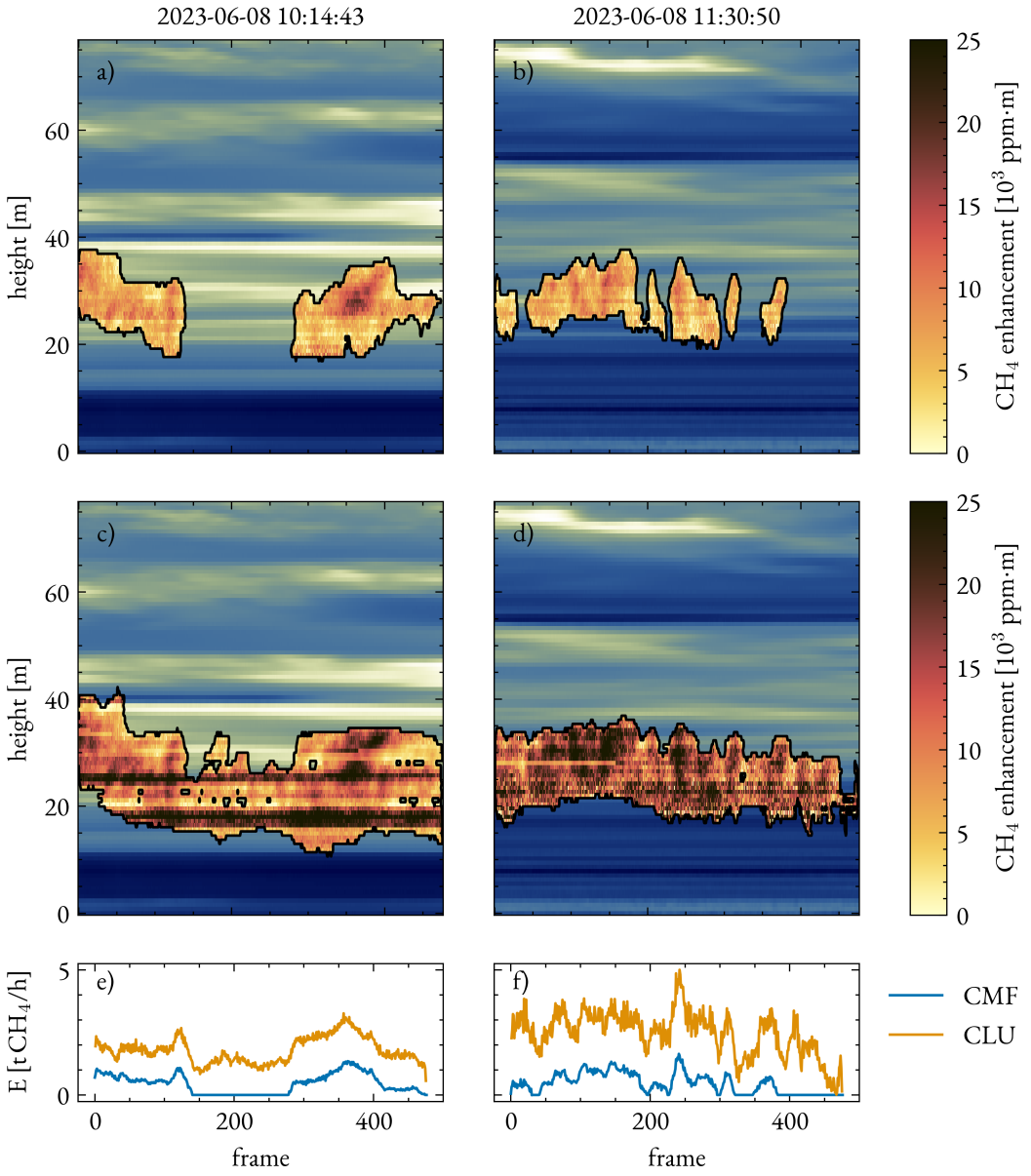

Figure 5.11: Comparison of the CMF and CLU retrieval for two scans during a fixed geometry observation on June 8, 2023. Both observations are 1 h 16 min apart and show backgrounds of different cloudy scenes. Panels a) and b) show the CMF retrieval, while panels c) and d) show the CLU retrieval. The CLU retrieval closes gaps in the plume, but shows striping patterns. Panels e) and f) show the emission estimates from the XSF method. The emission estimates of both retrievals follow the same trend, but the CLU retrieval provides more continuous estimates since many frames of the CMF retrieval are zero.

direction due to the movement of distant clouds. The CH_4 plume is easily identifiable as a band of enhancements between 20 m and 30 m height. While the CMF retrieval shows several gaps in the plume observations, the CLU retrieval fills these gaps. As in the scanning geometry, the CLU method can detect parts of the plume that are too faint for the CMF retrieval. However, the CLU plume observations exhibit striping features, particularly in Figure 5.11c. Striping across several lines suggests shortcomings in the referencing, e.g., due to the temporal distance of approximately one hour between the plume and background observation. The frame-wise emission estimates are shown in panels e) and f) of Figure 5.11. Gaps in the plume cause the XSF estimate to drop to zero, while the CLU estimate still produces a non-zero value. Comparing the XSF results from the CMF and CLU retrievals, they follow the same trend, with the CMF falling to zero for the smaller CLU values.

Clear-sky observations are necessary to evaluate the performance of the fixed geometry in more detail. The following discussion is thus preliminary. The first results of the fixed geometry are promising. The plume appears as a band in the images, likely continuous under favorable conditions. Thus, it provides high-frequent flux estimates through a vertical cross-section. The geometry necessitates explicit background scans for differential matched filter methods. Ideally, the camera alternates automatically between background scans upwind of the shaft and plume scans downwind. During the 2023 campaign, the first fixed geometry observations required manual alternation between background and plume scans, which was time-consuming. At the time, the necessity of background scans was unclear, so they were taken only after prolonged periods (hours) of plume scans. Taking background scans more frequently is likely to benefit the retrieval since the referencing of the spectra improves. The fixed geometry may provide a higher temporal resolution of the plume evolution compared to the scanning geometry. Additionally, the co-moving effect of the camera and plume (as discussed later in Section 5.3.1) is eliminated, making the data easier to interpret. In future applications, this geometry offers new possibilities for analyzing point-source emissions. For example, the camera can be positioned sideways to observe a horizontal cross-section above the shaft outlet.

5.3 Emission Time Series

The following sections present time series of CH_4 emissions from the Pniówek V coal mine ventilation shaft. As explained in Section 5.2, applying a matched filter retrieval on hyperspectral images enables the identification of emitted CH_4 plumes. Each image provides a single estimate of the emission and an error based on the IME method for scanning observations and the XSF method for fixed geometry observations.
Section 5.3.1 discusses the impact of atmospheric turbulence on the emission estimates. The error estimate of the single image already includes small-scale turbulence, but the scanning geometry requires a more detailed analysis. Section 5.3.2 presents the emission time series for eight campaign days, with several hundred plume observations per day. Four days are from the 2022 campaign and four from the 2023 campaign. Preliminary emission estimates from in-situ sensors in the shaft are compared to the emission estimates from the camera for the collaborative data in 2023.

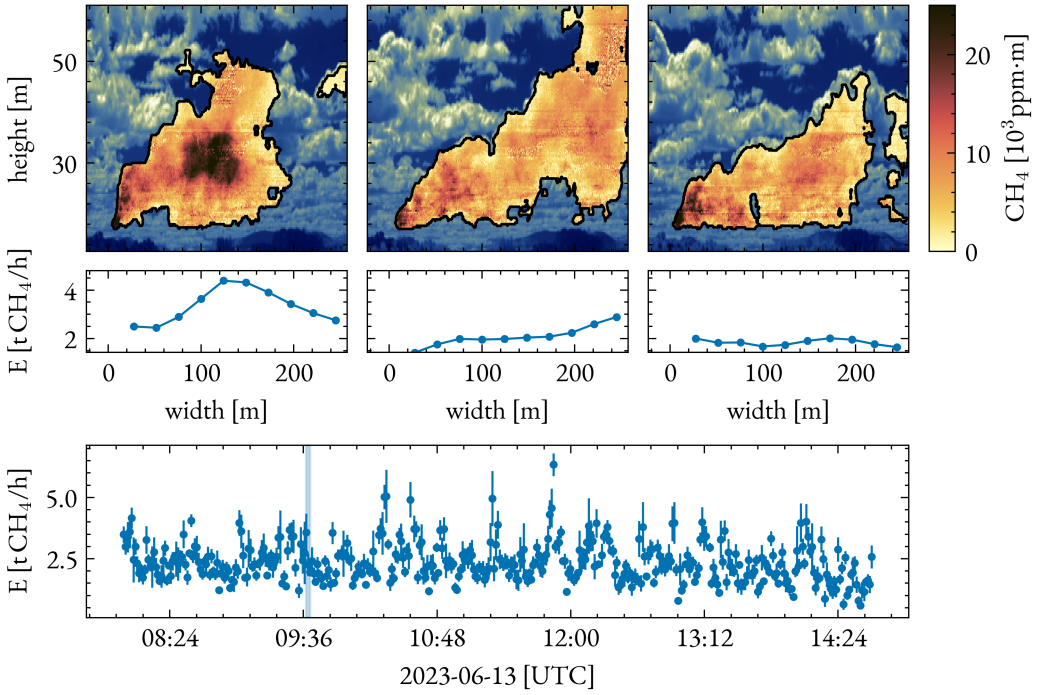

Figure 5.12: Scan to scan variability of emission estimates on June 13, 2023. Three consecutive scans are shown, taken 1 min apart. The panels below the observations show the emission estimates from the IME method, revealing substantial short term variability. The emission estimates decrease from 3.33 $tCH_4\ h^{-1}$ to 1.86 $tCH_4\ h^{-1}$. The lowest panel shows the whole emission time series of the day, highlighting the period of the three observations above.

5.3.1 Impact of Turbulence on Emission Estimation

Typical measurement days yield several hundred emission estimates. A single scan emission estimate includes uncertainty based on the observed plume mass variability along the plume, wind speed, and wind direction. Plume variability along the trajectory is the dominant source of uncertainty in the single emission estimates on all days (Table 5.1). Mass balance methods assume constant emissions over the timescale they are applied. Since they rely on the conservation of mass, they require the flux in the observed region (area for IME, cross-section for XSF) to represent the source. Various factors contribute to the observed plume mass variability, namely (a) background artifacts, (b) dilution below the detection limit, (c) turbulent transport, and (d) source variability. The method aims to observe source variability and distinguish it from the other features outlined below. Background artifacts within the plume mask may lead to either underestimating or overestimating distinct plume parts. The CoMF retrieval suppresses artifacts outside the plume mask but is unable to handle artifacts inside the plume mask. Visual inspection suggests rare background artifacts under cloudy conditions inside the plume, but these cases account for less than 1 % of the scans. Based on this investigation, spurious artifacts inside the plume have no substantial influence on the time series. Entrainment of ambient air causes the dilution of the CH_4 plume, an effect that accumulates as the plume travels away from the source. The retrieval

detection limit and the plume masking algorithm determine which part of the plume is lost to dilution. Figure 5.6 demonstrates that the combo masking effectively reduces the mass portion lost to dilution. Typically, it amounts to a few percent for the observations presented here, as the plume is observed near the source. Turbulent transport causes prominent density fluctuations in the observed plume. Turbulence arises when the external forces on a fluid exceed the viscous forces. The Reynolds number of typical atmospheric flows is on the order of 10^6 to 10^7, leading to rich turbulence structures (e.g., Woitischek et al., 2021a). Density fluctuations along the plume cause variability of the emission estimates between each segment. The following paragraphs propose a technique to differentiate between turbulent transport and source variability.

Figure 5.12 displays the variability of emission estimates from the CLU retrieval on June 13, 2023. Visually, every plume observation is reasonable despite the cloudy conditions. The emission estimates change significantly within the three minutes of observation. However, simultaneous observations inside the shaft suggest that the emissions change only on longer time scales (see Section 5.3.2). Furthermore, Woitischek et al. (2021a) performed a laboratory experiment using a constant source and measured plume thickness at cross-sections along the plume. They find significant variability at all distances from the source, although the magnitude and frequency of the density fluctuations decrease with distance. Thus, variability caused by turbulence is expected to contribute to the observed scan-to-scan variability. For CH_4 plume observations, turbulent transport (a) displaces mass in the plume, inducing concentration gradients, and (b) causes differences between the wind field above the shaft and the camera, where the LIDAR is located. Mass displacements happen simultaneously with the advective transport of the plume and evolve over time. As turbulence in the atmosphere is a statistical process, averaging the emission estimate over a long enough temporal or spatial interval removes the turbulent variability from a flux estimate. However, Woitischek et al. (2021a) point out that source variability can only be detected on time scales longer than the averaging interval. Therefore, the averaging interval should balance a length sufficient to mitigate turbulent variability with brevity to optimize temporal resolution for source variability.

The observed plume length in each scan represents its averaging interval, and the emission estimate already accounts for density variations within the observed plume. The scanning geometry of the camera interacts with the observed plume length in an image. For snapshot images, the observed plume length equals the plume length in the image. This is not true for scanning observations since the plume moves while the camera rotates to scan the FOV. The scan speed v_{scan} at the plume is given by

$$v_{\mathrm{scan}} = \omega_{\mathrm{rot}} \cdot D \,, \tag{5.1}$$

where ω_{rot} is the camera's angular velocity and D is the distance between camera and shaft. In the most extreme case, the plume moves at the scan speed, causing the camera to follow the same plume segment along the scan. In this case, the observed plume length is zero, and the camera observes only temporal variability in a plume cross-section. This effect causes increased scan-to-scan variability when the camera follows a diluted or enhanced part of the plume. For example, it might cause the strong enhancement feature in the first plume observation in Figure 5.12.

Calculating the observed plume length requires considering the camera's rotation, the ambient wind speed, and the observation geometry. As in the derivation of the IME method, a plume of length $d_{\mathrm{im,c}}$ appears with a length of $d_{\mathrm{im}} = d_{\mathrm{im,c}} \cdot \sin(\phi)$ in an image, where ϕ is the angle

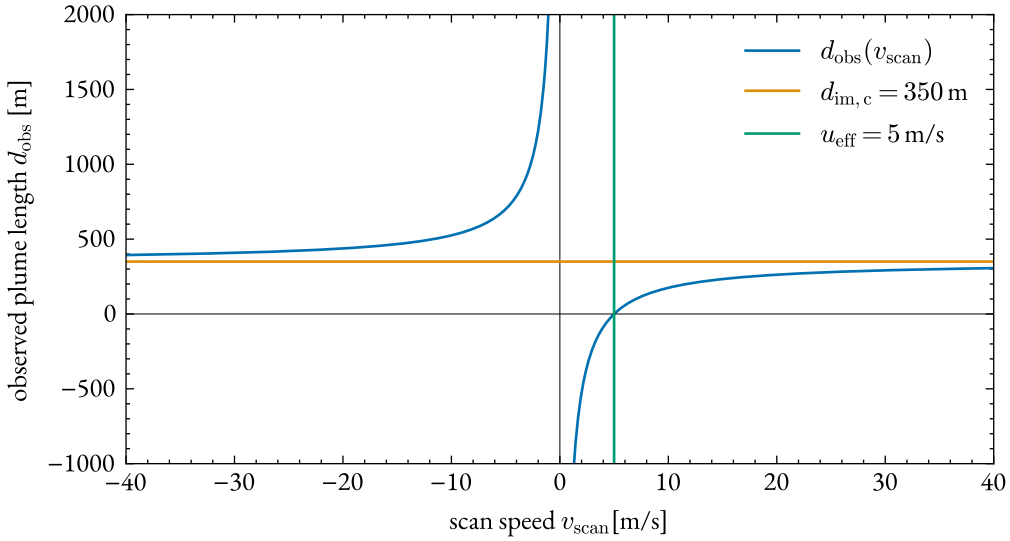

Figure 5.13: Effect of the convolution of plume and scan speed during a scan. The plume is assumed to move with a constant speed of 5 m s^{-1} (green) to the right and the camera scans over 350 m (orange) of the plume. The observed plume length d_{obs} (blue) is shown in dependence of the scan speed v_{scan}.

between the plume travel direction and the camera's viewing direction. Likewise, the effective plume speed in the image is $u_{\mathrm{eff}} = u \cdot \sin(\phi)$, where u is the plume speed. The observed plume length d_{obs} reads

$$d_{\mathrm{obs}} = d_{\mathrm{im,c}} \cdot \left(1 - \frac{u_{\mathrm{eff}}}{v_{\mathrm{scan}}}\right), \tag{5.2}$$

following from the ambient wind and the camera's settings. Negative plume speeds indicate that the camera moves against the plume, while positive speeds indicate that the camera moves with the plume. Figure 5.13 shows the effect of the convolution of the plume and scan speed during a scan on d_{obs}. Note that low scan speeds correspond to longer scan times. The observation approaches a snapshot image for a scan speed much higher than the plume speed. The observed plume length is zero for a scan speed equal to the plume speed and negative if the plume overtakes the camera's FOV during the scan. If the camera scans against the plume, each frame observes a wider plume interval than expected from the camera's horizontal opening angle. Thus, scanning against the plume travel direction causes $d_{\mathrm{obs}} > d_{\mathrm{im,c}}$. Observing the plume in the fixed geometry of the camera simplifies calculating d_{obs}. Assuming that the plume moves constantly through the camera's FOV, the observed plume length reads

$$d_{\mathrm{obs,fix}} = u_{\mathrm{eff}} \cdot n_{\mathrm{ca}} t_{\mathrm{int}} \cdot N_{\mathrm{frames}}\,, \tag{5.3}$$

where n_{ca} is the number of co-added spectra of integration time t_{int} in each frame and N_{frames} is the number of frames in a scan. Scanning and fixed geometry experiments are assigned an observed plume length according to Equations (5.2) and (5.3), respectively. An experiment consists

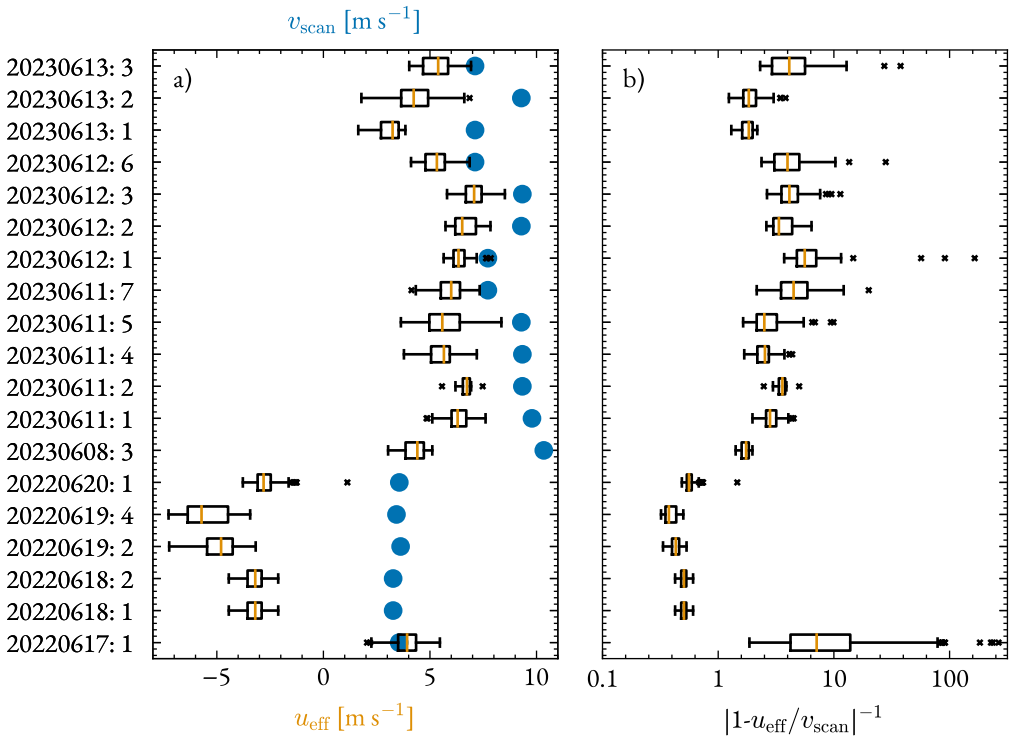

Figure 5.14: Panel a) shows the effective plume (orange) and scan (blue) speeds for all scanning experiments of the USCB campaigns. Panel b) shows the factor $|1 - u_{\mathrm{eff}}/v_{\mathrm{scan}}|^{-1}$, which modulates the observed plume length in each scan. Boxes extend from the first to the third quartile of the data, with a line (orange) at the median. The whiskers extend to the farthest data point lying within 1.5 times the inter-quartile range from the box, and crosses show outliers. Note the logarithmic x-axis in panel b).

of consecutive scans with identical settings, like scanning angle, detector exposure time, and viewing geometry.

The turbulent mixing length d_{turb} is assumed to represent the optimal trade-off between mitigating turbulence and achieving temporal resolution. Observing plumes of sufficient length d_{turb} requires a total of η scans, given by

$$\eta = \frac{d_{\mathrm{turb}}}{d_{\mathrm{obs}}} = \frac{d_{\mathrm{turb}}}{d_{\mathrm{im,c}}} \cdot \left| 1 - \frac{u_{\mathrm{eff}}}{v_{\mathrm{scan}}} \right|^{-1}, \tag{5.4}$$

assuming every scan observes the same plume length. Figure 5.14 shows the effective plume and scan speeds for all scanning experiments of the USCB campaigns. Moreover, Figure 5.14 lists the corresponding factor $|1 - u_{\mathrm{eff}}/v_{\mathrm{scan}}|^{-1}$ modulating η. The effective plume speed for each experiment is the mean plume speed during the experiment. For the 2023 campaign, all of these factors are larger than one since the wind consistently drove the plume to the right. Thus, additional scans are required to observe a plume of sufficient length. For June 18 to 20, 2022, the factors are below one, which benefits the temporal resolution.

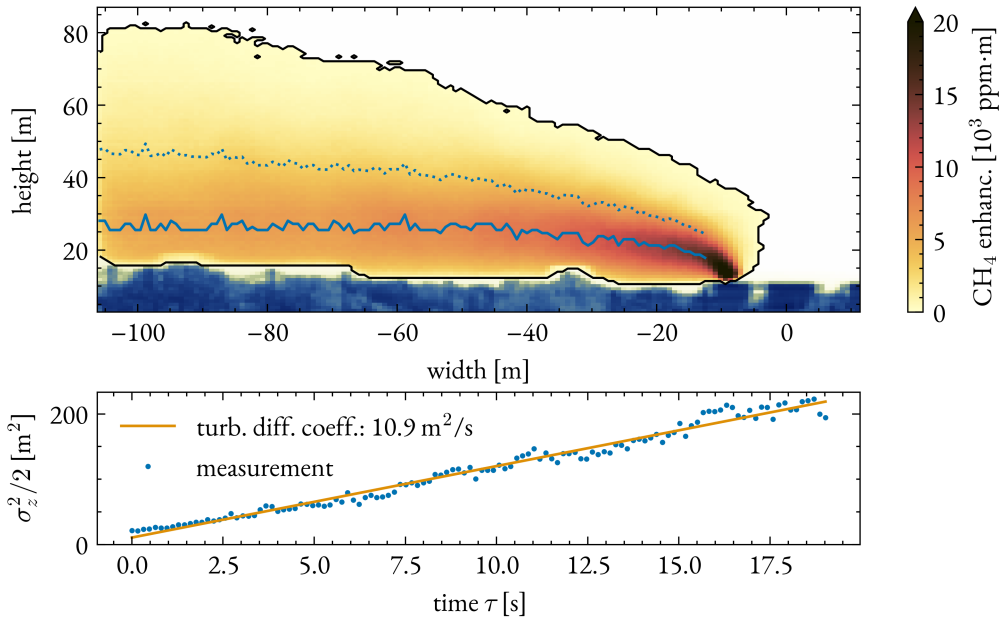

Figure 5.15: Turbulent diffusion coefficient estimated from the observations of June 19, 2022. The plume shown is the averaged CH_4 enhancement of 266 observations between 07:28 - 13:28 UTC. The mean plume height (blue) is at the maximum concentration of the plume, while σ_z is calculated according to Equation (5.7) for each downwind frame (dotted blue). From the dispersion width, the turbulent diffusion coefficient is estimated to $K = 10.9\,\mathrm{m^2\,s^{-1}}$ from a linear fit (orange) between the plume area and the plume lifetime.

The turbulent mixing length d_{turb} is an empirical concept, and it depends on atmospheric conditions like boundary layer height, surface roughness and temperature, and source parameters. Thus, calculating a precise value for d_{turb} poses significant challenges. A dimensional analysis is used to estimate d_{turb} based on the available information. The Péclet Number Pe is a dimensionless number that relates the advective transport to the diffusive transport of some physical quantity. It can be derived from the advection-diffusion equation, see Appendix A.3.1 (Brasseur and Jacob, 2017). Using turbulent instead of molecular diffusion, as done by Varon et al. (2018), Pe is defined as

$$\mathrm{Pe} = \frac{u \cdot d_{\mathrm{Pe}}}{K}\,, \tag{5.5}$$

where u is the wind speed, d_{Pe} is the mixing length, and K is the turbulent diffusion coefficient. The turbulent diffusion coefficient is a function of the turbulent mixing length and the turbulent velocity scale. It acts similarly to the molecular diffusion coefficient in the diffusion equation (e.g., Roedel and Wagner, 2011, Chapter 6). The turbulent mixing length is the correlation length scale of the turbulent velocity fluctuations. It is analog to the mean free path length in molecular diffusion. Usually, the turbulent diffusion coefficient is unknown, and a literature value for an atmospheric stability class is taken. On local scales, K typically ranges between $10\,\mathrm{m^2\,s^{-1}}$ and $50\,\mathrm{m^2\,s^{-1}}$ (Gifford, 1968; D'Isidoro et al., 2010; Varon et al., 2018). Since our observations provide repeated images of emission plumes, the turbulent diffusion coefficient can be estimated from

the time series. The plume width is expected to grow proportional to the square root of the time at long distances from the source (e.g., Taylor, 1922; Weil et al., 2002). Roedel and Wagner (2011) derive the expression

$$\sigma^2 = 2 \cdot K \cdot \tau \,, \tag{5.6}$$

where σ is the standard deviation of the concentration distribution, i.e., a measure of the plume width, and τ is the time. Dosio (2005) provides a method to estimate K from a plume observation if the mean height is known. Averaging single scans over extended periods yields a smooth plume observation, as shown in Figure 5.15. The maximum concentration is taken as the mean plume height in each frame. According to Nieuwstadt (1992), the vertical dispersion of a plume is given by

$$\sigma_z^2 = \frac{\int c \cdot z'^2 dV}{\int c \cdot dV} \,, \tag{5.7}$$

where c is the observed CH_4 concentration and z' is the vertical distance from the mean plume height. Figure 5.15 shows the turbulent diffusion coefficient estimated from the June 19, 2022, observations between 07:28 and 13:28 UTC. Equation (5.7) yields σ_z for each distance d downwind of the source. The lifetime of the plume is estimated by $\tau = d_{\mathrm{im}}/u_{\mathrm{eff}}$. The plume dispersion σ_z^2 increases linearly with the plume lifetime. Thus, K follows from a linear fit using Equation (5.6). Empirically, more than 150 plume images are required to obtain a smooth plume observation. Thus, the temporal trend of boundary layer turbulence can not be observed. Performing the analysis yields six estimates of K from four days, falling between 8 $\mathrm{m^2\ s^{-1}}$ and 14 $\mathrm{m^2\ s^{-1}}$.

The length scale d_{Pe} determines if advection dominates over the turbulent diffusion. Table A.2 lists the key quantities for all experiments of the USCB campaigns. Typical image plume lengths $d_{\mathrm{im,c}}$ range from 110 m to 270 m, while the observed plume lengths d_{obs} range from 13 m to 420 m per scan. Wind speeds range from 3 $\mathrm{m\ s^{-1}}$ to 8 $\mathrm{m\ s^{-1}}$, and a turbulent diffusion coefficient of $K = 10\ \mathrm{m^2\ s^{-1}}$ is assumed for all experiments. For large Péclet numbers of $\mathrm{Pe} = 100$ to 1000, the length scale d_{Pe} ranges from 140 m to 3700 m. Since this is only a rough estimate, a conservative turbulent mixing length of $d_{\mathrm{turb}} = 3000$ m is taken for all experiments. Choosing a value close to the upper limit provides an observation of sufficient length to mitigate the turbulent variability, requiring η scans in the respective experiment. Section 5.3.2 discusses the resulting averaging intervals in more detail. However, Brunner et al. (2023) suggest that airborne snapshot observations of plumes still only allow an accuracy of 20 % in IME emission estimates due to turbulence, even though their simulated plumes are nearly 100 km long.

The proposed assessment for distinguishing between turbulent and source variability has limitations. It does not account for temporal variability observed in scanning experiments, the camera's opening angle, and the dead times between frames. Additionally, the turbulent mixing length is not a well-defined physical quantity but rather a length scale loosely associated with fluid dynamic processes. However, the method described above uses standard tools of turbulent transport to provide a reasonable estimate for the turbulent mixing length. It relies on an independent observation of the turbulent diffusion coefficient, which is unavailable in most studies. This information is available here through the repeated imaging of the plume, presenting an advantage of the technique at hand.

Table 5.1: Daily average emission estimates $\overline{E}$ [$tCH_4\,h^{-1}$] and average error $\overline{\Delta E}$ [$tCH_4\,h^{-1}$] from a total of N_{scan} scans. Furthermore, the averaged relative error $\overline{\Delta E/E}$ [%] with its contributions from the wind speed $\overline{\Delta u}$ [%], the wind direction $\overline{\Delta\phi}$ [%], and the plume density $\overline{\Delta\rho}$ [%] of Equation (4.36). The range of the E_{roll} [$tCH_4\,h^{-1}$] is the range from the minimal to the maximal rolling-mean emission estimate. The rolling mean kernel size η_{rep} is calculated from the fixed and scanning experiments' η.

Date	N_{scan}	η_{rep}	$\overline{E}$	range of E_{roll}	$\overline{\Delta E}$	$\overline{\Delta E/E}$	$\overline{\Delta\rho}$	$\overline{\Delta u}$	$\overline{\Delta\phi}$
2022-06-17	247	232	1.56	n.a.	0.21	14.1	12.1	4.2	4.6
2022-06-18	293	7	2.15	0.92 - 4.00	0.40	18.1	16.1	3.3	6.7
2022-06-19	457	11	2.16	1.41 - 2.88	0.23	10.7	9.4	3.5	2.8
2022-06-20	160	16	4.57	3.01 - 5.59	0.72	15.5	12.1	5.0	5.5
2023-06-08	275	18	2.02	1.33 - 2.91	0.38	15.0	14.0	4.3	1.7
2023-06-11	315	35	1.85	1.14 - 2.34	0.28	15.9	15.3	3.5	0.7
2023-06-12	436	41	1.87	1.29 - 2.90	0.26	15.5	15.1	3.3	0.7
2023-06-13	477	24	2.15	1.42 - 2.89	0.34	15.9	14.8	4.0	2.7

5.3.2 Emission Variability From Coal Mine Operations

HySpex observations of the Pniówek V coal mine ventilation shaft took place during the 2022 and 2023 campaigns, spanning a comprehensive eight-day period characterized by diverse observation conditions. On June 17, 2022, there was cloud cover and unfavorable wind conditions because the plume was moving at nearly the same speed as the camera's FOV. In the following days, the background conditions were mainly homogeneous and cloud-free. The wind direction error for emission estimates on June 18, 2022, is larger than on the other days since the plume travel direction was close to the critical threshold. On June 19, 2022, favorable observation conditions prevailed, effectively showcasing the method's capabilities. The final day of the 2022 time series, June 20, consists of observations with relatively low wind speeds ($\leq$ 3 m s^{-1}). Thus, the plumes rise higher within the images and develop more pronounced transport features, increasing the plume density error. During the 2023 campaign, observation conditions were stable over the four days. The wind speed was ideal, and the plume traveled perpendicular to the camera's line of sight. The plume was consistently co-moving with the camera's FOV, and a persistent cloud cover extended over the whole campaign period. Technical problems prevented scanning observations on June 8, 2023, after 09:30 UTC, but fixed observations were possible for the remaining day. Figures 5.17 and 5.19 show example images from each day.
As described in Section 5.2.1, quality criteria remove scans with flawed plume masking or compromising wind direction. Table A.1 lists the number of scans before and after the quality filter for each day and which filter criteria are responsible for removing the scans. Depending on the observation conditions, they remove between 1 % and 44 % of the scans. Wind direction is the dominant factor in the data yield. An unfortunate wind direction can remove observations over prolonged periods (morning of June 20, 2022) or sporadically if the wind direction fluctuates around the critical threshold (June 18, 2022).

Table 5.1 lists the daily average emission estimates $\overline{E}$ and the average error $\overline{\Delta E}$ for every presented observation day. Each day encompasses between 160 and 477 scans after quality filtering.

The average relative error ranges between 10.7 % and 18.1 % for a single scan, with smaller errors in favorable observation conditions. As expected from Equation (4.36), the wind direction error is situational. If the wind drives the plume perpendicular to the camera's viewing direction, the wind direction error is well below 3 %. Unstable wind conditions around the critical threshold of $\sin\phi = 0.45$ cause the highest mean wind direction error of 6.7 %. The wind speed error ranges between 3 % and 5 %, with low wind speeds causing a higher relative uncertainty. The wind LIDAR is a valuable addition to the setup since it accurately constrains the ambient wind field. Most top-down plume observations rely on meteorological wind models, which are known to have significant uncertainties in the boundary layer (e.g., Jongaramrungruang et al., 2019; 2022; Brunner et al., 2023; Roger et al., 2023b). For the ground-based observations, the plume density variability dominates the error budget in single scans with 9.4 % to 16.1 %.

As described in Section 5.3.1, distinguishing source variability from turbulent transport requires averaging η scans. Since the observed plume length depends on the wind- and scan speed, η changes for each experiment. Table A.2 lists η for each experiment, and Table 5.1 lists a representative η_{rep} for each day. Here, η_{rep} is the experiment-average η weighted by each experiment's scans. η_{rep} corresponds to the daily temporal resolution of the method since each image acquisition takes approximately one minute. In terms of the temporal resolution, the June 17, 2022, observations can be considered the worst-case scenario. The effective wind speed matches the scanning speed within 10 %, so the observation contains only minimal spatial variability during a single scan. The temporal resolution is estimated at 232 min, which is insufficient for inferring the diurnal variability of the coal mine ventilation shaft. Generally, plumes co-moving with the scan direction will impede the temporal resolution of the method. Except for June 17, 2022, the temporal resolution ranges between 20 min and 76 min for co-moving plumes. Ideally, the plume moves against the scanning direction, which enables a temporal resolution below 16 min, as of June 18 to 20, 2022. The fixed geometry falls between the two scan cases, yielding a temporal resolution between 12 min and 20 min for the three presented cases. Thus, an option to set the camera rotation direction based on the wind direction is planned for future applications.
Figures 5.16 and 5.18 show the observed time series during the presented days. Every panel includes the single scan emission estimates after quality filtering, excluding scans with flawed plume masking or compromising wind direction (Knapp et al., 2023a). A moving mean of different kernel sizes within the expected temporal resolution range $(\min(\eta), \eta_{\mathrm{rep}}, \max(\eta))$ on that day illustrates the observed diurnal variability. The range of η is computed for fixed and scanning experiments separately. Smaller kernel sizes increase the observed diurnal variability. Figure 5.18c suggests that the fixed geometry observations fit well with the scanning observations, i.e., no apparent biases exist between the methods. Table 5.1 lists the rolling mean range alongside a daily temporal resolution. The data show that shaft emissions can deviate from the daily mean by as much as 34 % to 55 %. The only exception is June 18, 2022, which shows maximum deviations between 57 % and 86 %.

In-situ instruments observed shaft emissions alongside the HySpex camera, providing preliminary emission estimates for comparison. One source is pellistor sensors in the shaft, as used in Swolkień et al. (2022). These sensors measure the CH_4 concentration in 0.1 % steps every second and report them as a mean over 60 s. The pellistors provide low-quality observations since their purpose is to detect dangerous CH_4 concentrations in the shaft. However, they are installed in ev-

ery shaft and operate continuously[2]. The pellistor sensors provide a continuous data set in 2023 but, due to extended downtime, only a few reliable data points in 2022. Furthermore, a TDLAS open path experiment was mounted on top of Pniówek V on June 13, 2023. It observed the CH_4 column along a transect across the shaft outlet. A Prandtl tube inside the shaft provides the flow speed to convert the TDLAS and pellistor concentration measurements to emission fluxes.
In comparing the emission estimates of the 2023 campaign, HySpex consistently yielded smaller values than the observations from TDLAS and pellistor sensors. The CLU retrieval estimates result in 30 %, 22 %, 22 %, and 20 % lower daily emissions than the pellistor observations on June 8, 11, 12, and 13, 2023, respectively. However, the CLU observations improve the consistency between the observations significantly compared to the CMF method, which results in approximately 50 % lower emissions than the CLU. Several potential explanations exist for the inconsistency between the in-situ and HySpex observations. The observation conditions were challenging for the matched filter retrieval due to heavy cloud coverage. Additionally, the UAS generation relies on the single-scattering approximation of the RTE, which is deficient for the observed cloud coverage. Albeit these challenging conditions, the daily mean emissions follow a similar trend, showing comparable day-to-day variabilities ($(E_{\max} - E_{\min})/E_{\mathrm{mean}}$) of 15 % and 19 % for the HySpex and pellistor, respectively. During the 2022 campaign, the HySpex observations show increasing emissions from 1.55 $tCH_4\ h^{-1}$ to 4.57 $tCH_4\ h^{-1}$ between June 17 and 20. The available pellistor observations show a similar trend for the first three days (1.23 $tCH_4\ h^{-1}$ to 2.39 $tCH_4\ h^{-1}$) yet disagree with the observations on June 20 (1.08 $tCH_4\ h^{-1}$). However, the comparison is inconclusive since the pellistor was not operational during most of the observation periods. The TDLAS and pellistor observations exhibit less diurnal variability than the HySpex observations during the 2023 campaign. The HySpex observations display some residual correlation with the effective plume speed, with a Pearson correlation coefficient ranging from 0.00 to 0.26 (see Figure A.7). However, the correlation does not explain the observed discrepancy in diurnal variability. An upcoming publication led by the IMEO and the AGH Kraków will focus on a detailed comparison of the emission estimates based on the strengths and weaknesses of all participating methods.

In summary, the presented observations demonstrate that the camera observations can observe the diurnal variability of coal mining emissions. The temporal resolution ranges from 10 min to 232 min, depending on observation conditions. However, choosing a scanning direction opposite to the plume travel direction can reliably improve the temporal resolution for future scanning observations. Typical uncertainties are below 20 % for a single scan, with the plume density variability dominating the error budget. Although clouds challenge the matched filter retrieval, plume identification and emission quantification are still possible. However, non-compliance of the radiative transfer model with the observed cloud coverage may introduce systematic errors. The supplementary information of Knapp et al. (2023a) includes several videos of the observations, providing a more intuitive understanding of the method's capabilities. In addition to the source emission, these observations also provide information on the turbulent state of the atmosphere (see Figure 5.15) or the CH_4 injection height into the atmosphere.

[2] At least in theory. In practice, there can be long periods when the sensor does not observe a new data point and only reports the last value recorded (J. Swolkień, pers. communication).

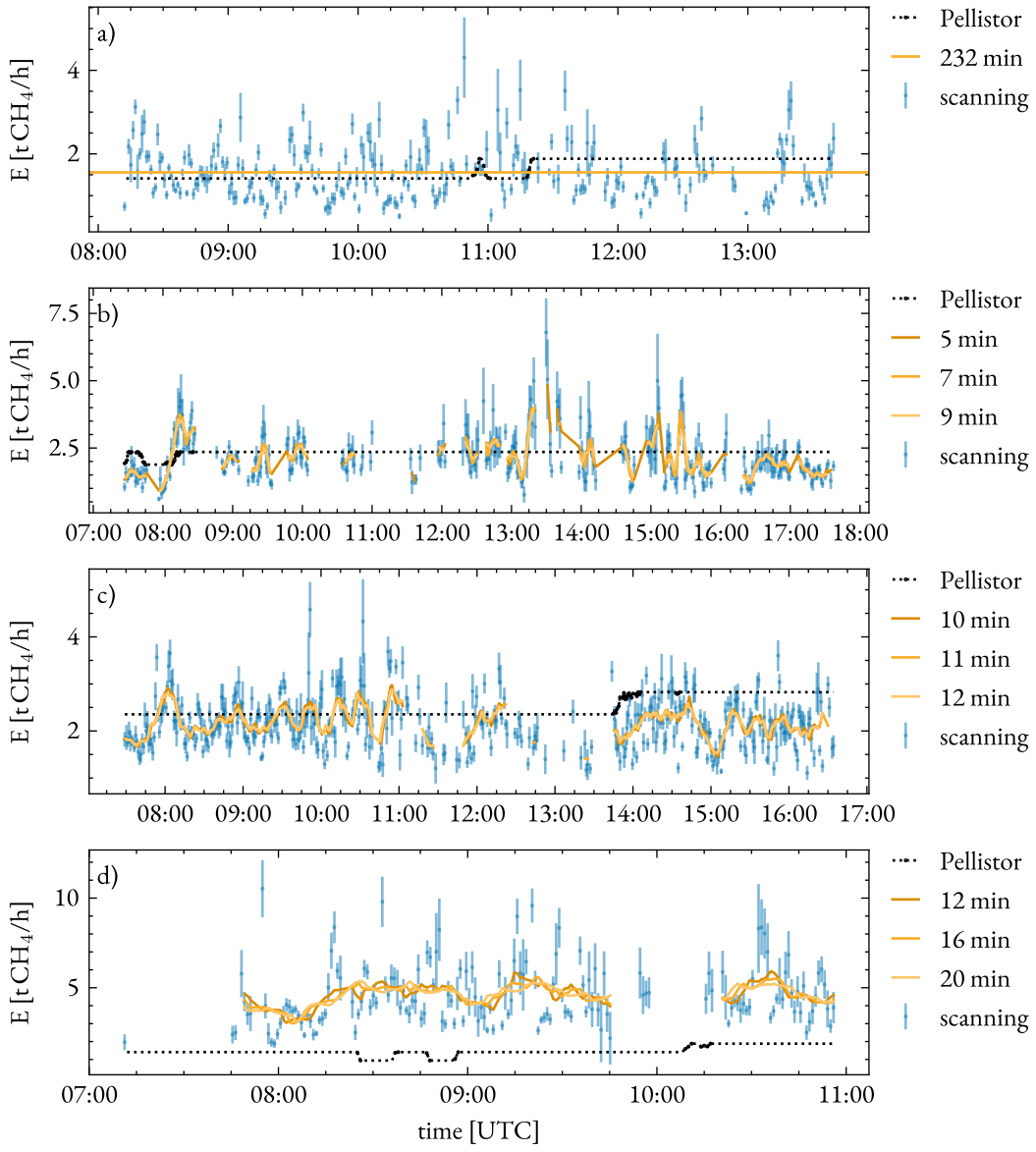

Figure 5.16: Emission time series observed during the 2022 campaign. Panels a) to d) show measurements from June 17, 18, 19, and 20, respectively. Single HySpex observations using the DMF method (blue) are shown. Rolling averages (orange) illustrate the diurnal variability. The kernel sizes are $\min(\eta)$, η_{rep}, and $\max(\eta)$ of the respective day following Table A.2. There was only one experiment conducted on June 18, 2022, so the range in panel b) is for illustration only. Simultaneous emission estimates using in-situ data is given (black) whenever available, with the dotted line marking detector downtimes.

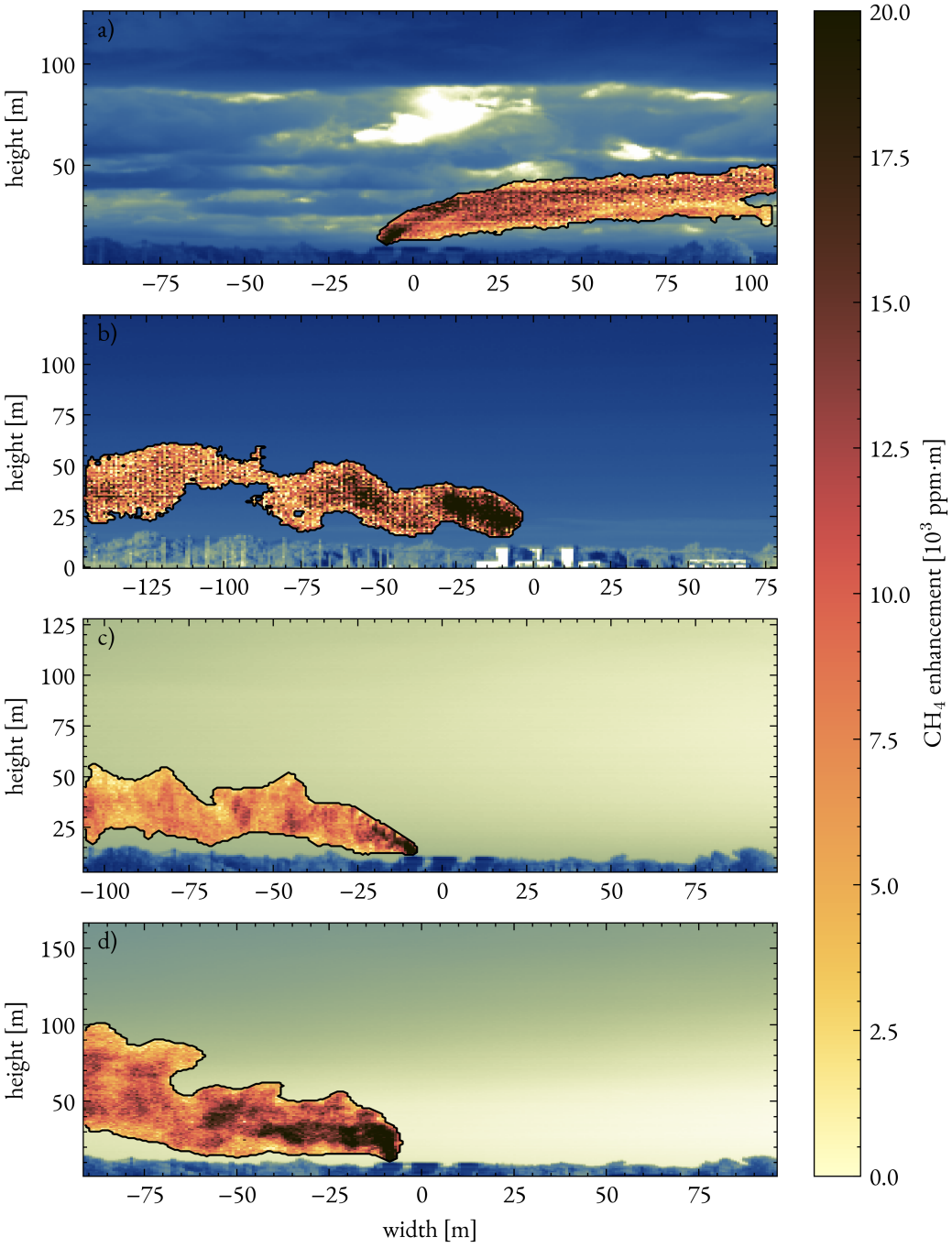

Figure 5.17: Example observations from June 17, 18, 19, and 20 in 2022 (panels a) to d)).

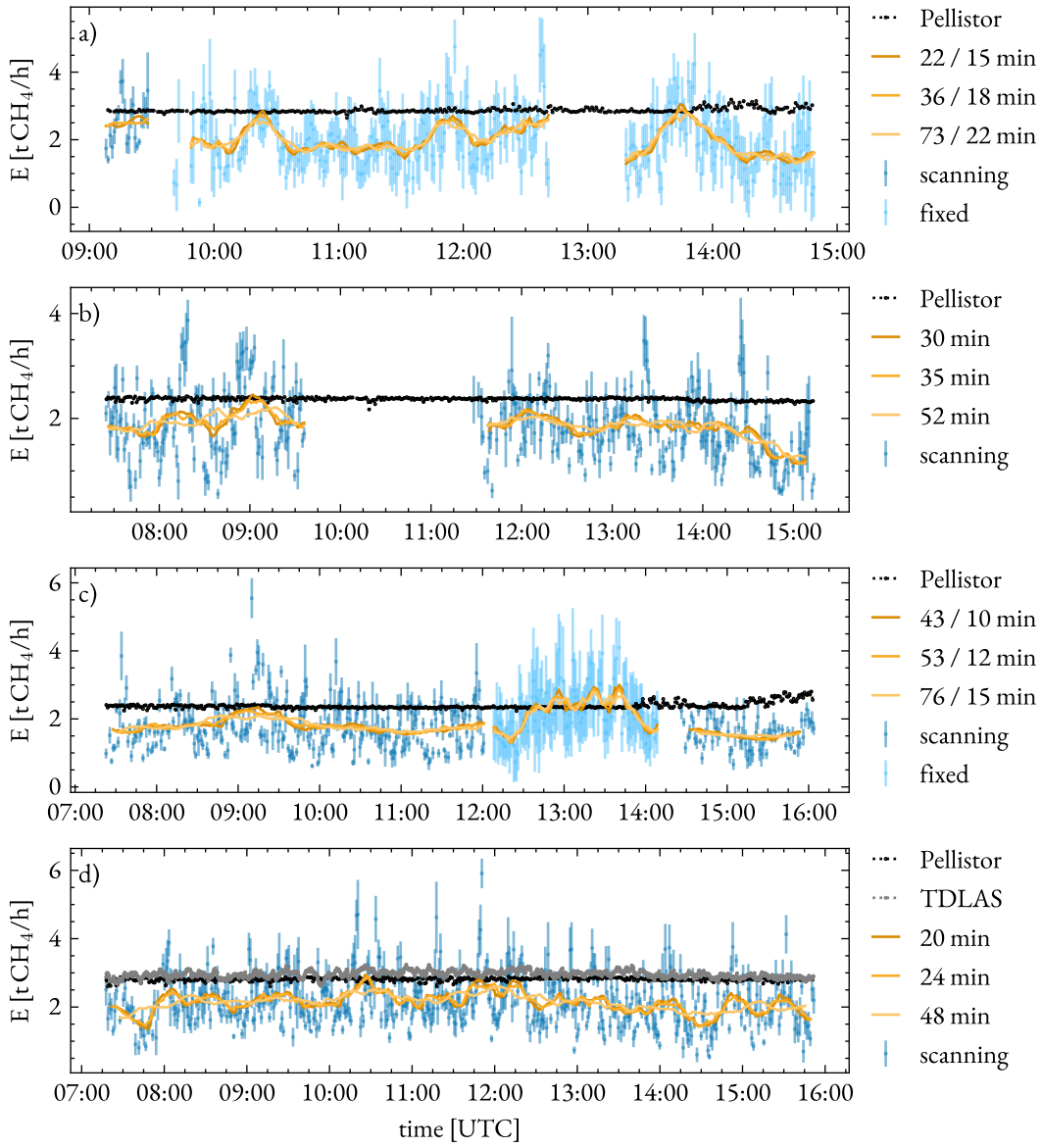

Figure 5.18: Same as Figure 5.16, but for June 8, 11, 12, and 13 in 2023. HySpex observations were performed in a scanning (dark blue) and fixed (light blue) observation geometry. Panels a) and b) include extended intervals without observations. These are due to technical problems on June 8 and fixed viewing geometry data without corresponding background scans on June 11. Averaging kernel sizes in panel a) and c) are given for the scanning and fixed experiments separately, the scanning being the one before the slash. Panel d) includes the coinciding TDLAS observations (gray).

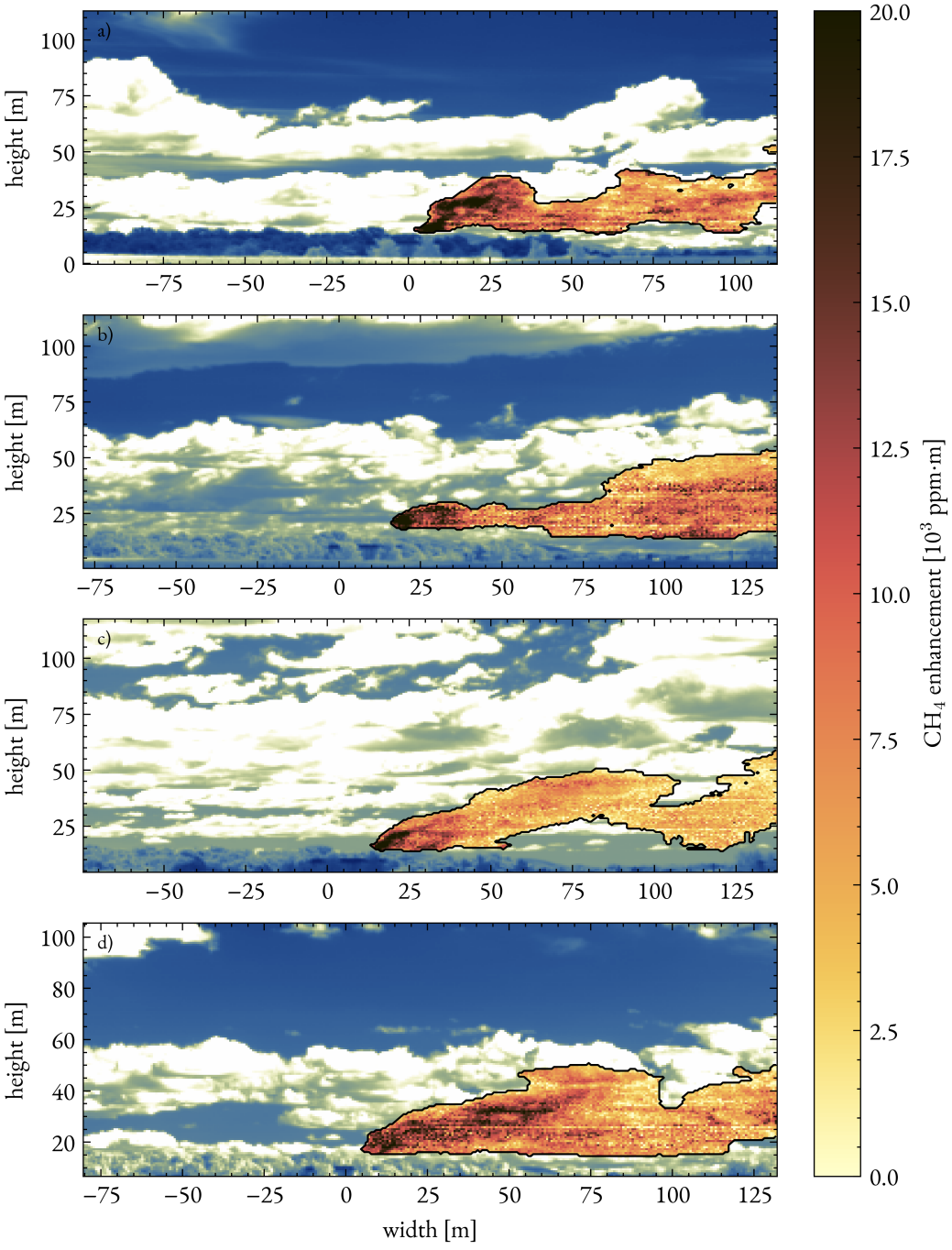

Figure 5.19: Example observations from June 8, 11, 12, and 13 in 2023 (panels a) to d)).

6 Carbon Dioxide Emissions From a Coal-Fired Power Plant

This chapter presents the first ground-based imaging observations of CO_2 plumes. The observations were performed at the Grosskraftwerk Mannheim (GKM), which is the largest coal-fired power plant in Baden-Württemberg, Germany. It serves as a validation target for the methods presented in this thesis. Knapp et al. (2023b) covers most results presented in this chapter. However, this chapter contains a more detailed description of all field observations and the advantages of the DMF retrieval compared to the CMF retrieval. Section 6.1 introduces the GKM, the available information on the power plant, and the performed observations. Section 6.2 describes the image processing and the retrieval of the CO_2 column enhancements. Finally, Section 6.3 presents the emission estimates and compares them to the bottom-up emissions of the GKM.

6.1 Grosskraftwerk Mannheim

The GKM is a coal-fired power plant in Mannheim, Germany (49.44 °N, 8.50 °E). It burns hard coal and uses cogeneration to simultaneously produce electricity and district heating. The maximum capacity of the GKM is 2146 MW of electrical power and 1500 MW of district heating. From the 2146 MW of electrical power, 1958 MW are available for the public grid, and 188 MW are used for the internal power consumption of the power plant. The power plant consists of nine units, numbered from 1 to 9. Only units 6 to 9 are still in operation, of which unit 9 was last commissioned in 2015.

The GKM reports their annual emissions to the E-PRTR. Its yearly reports contain energy production and fuel consumption, e.g., Grosskraftwerk (2015). On average, the GKM released $\eta_{\mathrm{tot}} = 955.1\,\mathrm{gCO_2\,kWh^{-1}}$ between the years 2015 and 2021 (Table A.3). The Umweltbundesamt (UBA) provides a German average emission factor of $\eta = 335.2\,\mathrm{gCO_2\,kWh^{-1}}$ for hard coal at 100 % efficiency (Sandau et al., 2021). Unit 9 has a maximum capacity of 911 MW and operates at a net efficiency of 46.5 % (Grosskraftwerk, 2015), translating to an emission factor of $\eta_9 = 722\,\mathrm{gCO_2\,kWh^{-1}}$. Assuming that units 6 ($P_6 = 475$ MW), 7 ($P_7 = 480$ MW), and 8 ($P_8 = 280$ MW) have the same efficiency, their emission factor η_{6-8} follows from

$$\eta_{\mathrm{tot}} = \frac{1}{P_{\mathrm{tot}}}(P_9 \cdot \eta_9 + (P_6 + P_7 + P_8) \cdot \eta_{6-8}) \tag{6.1}$$

$$\Rightarrow \eta_{6-8} = 1127\,\mathrm{gCO_2\,kWh^{-1}}\,, \tag{6.2}$$

where $P_{\mathrm{tot}} = 2146$ MW is the total power production. Units 6 to 8 were built in 1975, 1983, and 1993, respectively, explaining their lower efficiency compared to unit 9. Therefore, the GKM

operates unit 9 preferentially, and the other units are only used when the demand for electricity and district heating is high.

6.1.1 Field Observations

Two suitable locations are available for the GKM observations. The first is located south of the GKM at Backofen-Riedwiesen, Brühl (49.41 °N, 8.51 °E), and the second is located in the west at Kiefweiher, Altrip (49.44 °N, 8.45 °E). Both options provide an unobstructed view of the GKM's chimneys from a distance of 3 km to 4 km. The wind direction forecast determines the best observation spot since favorable conditions drive the plume perpendicular to the camera's line of sight. The camera observed the GKM on 12 days between 2021 and 2023. Since the GKM operates unit 9 preferentially, the camera observes unit 9 on 10 of these days. From early 2022, the wind LIDAR was available for the observations and positioned near the camera.

Prior to the measurements, the camera's roll angle is levelled using the AHRS. The camera is then tilted such that its vertical FOV covers primarily the blue sky, and only the tips of the chimneys are visible in the lower part of the image. The horizontal FOV extends from approximately 1° upwind of the chimney to up to 20° downwind of the chimney. Thus, the FOV contains the plume, upwind frames for reference spectra, and the blue sky background for the matched filter retrieval. The chimney tip serves as a landmark for calculating the camera's VEA and VAA in all pixels. Typical exposure times range between 8 ms and 20 ms. Every frame co-adds 5 to 10 individual exposures, such that a typical scan of 10° takes 40 s to 90 s. At the observing distance, the spatial resolution of the image is 2 m to 3 m. Table A.4 lists information on all days of observations, including the camera settings.

Observations were planned according to the weather forecast. Ideal conditions feature a clear sky to ensure scene homogeneity for the matched filter retrieval. Condensation in the exhaust plume prevents the CO_2 retrieval in affected pixels. Thus, the ambient temperature should be high enough to prevent water condensation in the plume. Finally, stable wind directions over the observation period are favored since relocating between the observation spots takes about 2 h. Since the campaigns at the GKM are a proof-of-concept study for CO_2 observations, the weather conditions requirements were relaxed on some days to test the limits of the method. Therefore, the measurement conditions prevented successful CO_2 retrieval or emission inversion on several days. Common problems were condensation in the plume or scene heterogeneity due to clouds or aerosols. As described above, preventing such problems requires sunny and warm days. Renewable energy, like solar power, produces cheaper energy than coal-fired power plants. Thus, the GKM reduces its power production or even shuts down on such days, preventing plume observations. In the end, observations from five of the 12 days were suitable for evaluating the developed method. From the other seven days, two suffered from low emissions, two from unfavorable wind directions, and three from scene heterogeneity. Table A.4 includes a short description of the observation conditions for all days.

6.1.2 *A Priori* Data

Both the retrieval and the inversion require *a priori* information about the atmosphere and the power plant. The operator of the GKM kindly provided proprietary information about the power

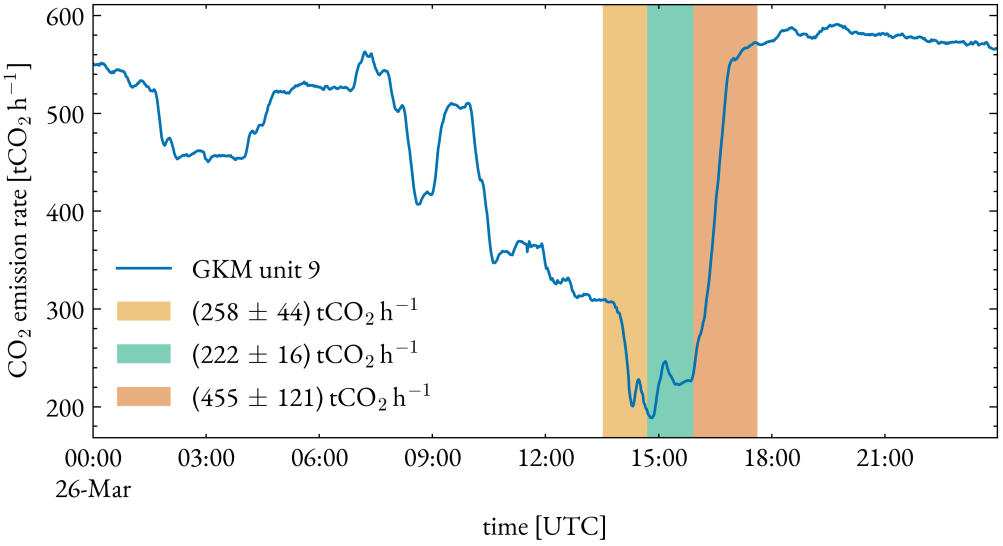

Figure 6.1: Bottom-up emission estimate for unit 9 of the GKM on March 26, 2022. The emissions follow from the instantaneous power production and the emission factor of 722 $gCO_2\,kWh^{-1}$ for unit 9. The colored time span shows the time of the observations. Every color represents a different averaging interval, for which the mean bottom-up emissions are shown.

plant for the days of observations. The data includes 10 m meteorological observations at the power plant, consisting of wind speed and direction, temperature, pressure, and relative humidity. Furthermore, operational data of the power plant is available, including the coal consumption, the exhaust volume flow rate at the chimney top, the chimney tip diameter, and the exhaust gas temperature. Both the meteorological and operational datasets have a resolution of 1 min. Similar information can be taken from literature, e.g., Pregger and Friedrich (2009), in case such data is unavailable. However, the data from the operator is more reliable and specific to the GKM. It provides coinciding information to the camera observations, which is not the case for literature data. Table A.5 lists the *a priori* information for each observation period detailed in Section 6.2, taken as the mean value of the available data.

The instantaneous power production of the GKM provides a bottom-up estimate of the CO_2 emissions using the emission factors from Section 6.1. The GKM proprietary data includes the power production of unit 9 but not for the other units. Four of the five observation days target unit 9. Only on May 13, 2022, unit 6 was observed since unit 9 malfunctioned. The Fraunhofer-Institut für Solare Energiesysteme (ISE) allocates German power plant energy production with 15 min resolution. Since the GKM data shows that unit 6 was the only operational unit on May 13, 2022, we use the ISE data to estimate the CO_2 emissions of unit 6 on that day. These high-resolution and site-specific emissions serve as a validation opportunity for the inversion results. Figure 6.1 shows an example of the bottom-up emission estimate for the observation periods.

Wind information is available from both the GKM data and the LIDAR observations. Typical observations at chimney height show a wind speed of 3 $m\,s^{-1}$ to 8 $m\,s^{-1}$ with hourly standard deviations of 0.9 $m\,s^{-1}$. The LIDAR data covers all observation days except September 8, 2021.

Table 6.1: The first three columns list the time (UTC) interval of the observations, the unit number of the power plant that was observed, and if the Windranger 200 was available. Column 5 lists the camera's mean VAA, approximately aligning with north (N) or east (E), and column 6 lists the distance D to the observed unit. Columns 7 and 8 list the AERONET AOD at 2000 nm and the asymmetry parameter (g) of the scattering phase function. Column 9 lists if condensation was observed in the plume. For more detailed atmospheric conditions, see Tables A.4 and A.5.

Date & time	Unit	LIDAR	VAA [°]	D [m]	AOD	g	Cond.
2021-09-08 12:13 - 16:36	9	No	347 (N)	3183	0.012	0.82	No
2022-03-23 14:51 - 17:36	9	Yes	94 (E)	3760	0.022	0.78	Yes
2022-03-26 13:31 - 17:36	9	Yes	347 (N)	3179	0.035	0.77	Yes
2022-03-28 15:35 - 16:28	9	Yes	91 (E)	3760	0.063	0.76	Yes
2022-05-13 12:21 - 15:39	6	Yes	333 (N)	4098	0.065	0.76	No

The *a priori* wind data for September 8, 2021, follows from scaling the GKM wind speed to the chimney height using Copernicus Atmosphere Monitoring Service (CAMS) reanalysis data (Inness et al., 2019). Figure A.8 shows the CAMS scaling and a typical wind LIDAR profile. Since the emission inversion simultaneously retrieves the wind field, these observations provide a starting point for the inversion grid.

Calculating the UAS for the matched filter employs the atmospheric aerosol content. The closest AERONET station to Mannheim is located in Karlsruhe, Germany (49.10 °N, 8.44 °E). It provides the daily mean AOD at 2000 nm and the asymmetry factor of each observation day. Thus, the UAS generation of the matched filter retrieval utilizes the daily aerosol information for the solution of the RTE. However, the AERONET station is located 50 km south of the GKM. Since AOD may vary significantly over such distances, the AERONET data may not represent the aerosol load at the GKM. Table 6.1 lists the AERONET parameters for all observation days. Furthermore, it lists the observed unit, mean VAA of the camera, the target distance, and whether condensation occurred in the plume.

6.2 Image Processing

Each observation day provides several hundred scans, which are preprocessed according to Section 3.1. In contrast to the CH_4 observations presented in Chapter 5, the SNR in single scans is too low to retrieve CO_2 column enhancements. The high atmospheric background concentration of 420 ppm means that the additional absorption signal of the plume is small. Therefore, the CO_2 retrieval requires averaging of the scans to increase the SNR in the observation. Section 6.2.1 describes the averaging and the generation of a plume condensation mask. Section 6.2.2 compares the CMF to the DMF retrieval approach for several examples. Finally, Section 6.2.3 describes the process and settings of the emission estimation.

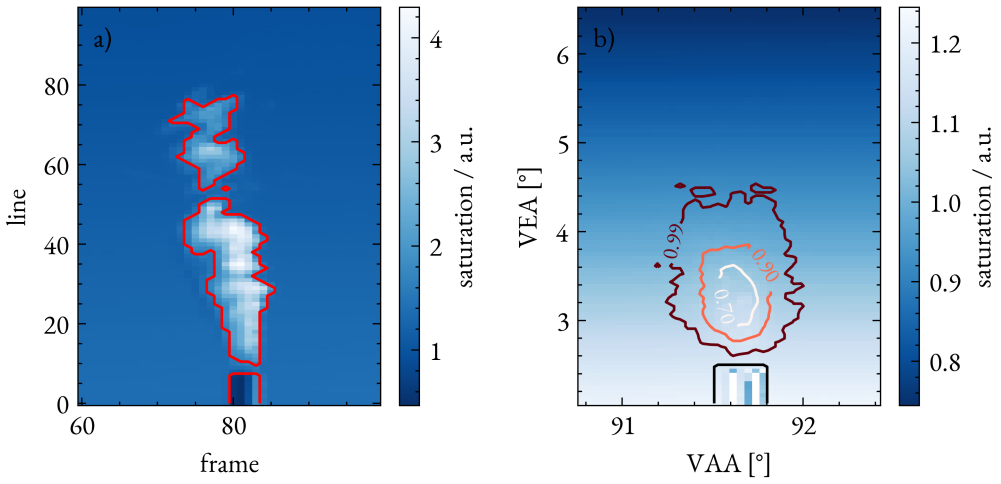

Figure 6.2: Panel a) shows the saturation of a single image. The red border surrounds pixels showing an enhanced saturation, either from reflectance at the chimney or condensation in the plume. Panel b) shows the saturation of the averaged image. The colored lines mark the areas to which a certain fraction of the scans have contributed. The black line marks a manual mask excluding the tip of the chimney. Note that the averaged image has dimensions of VEA and VAA, while the single scan has dimensions of line and frame. Plot adapted from Knapp et al. (2023b).

6.2.1 Averaging and Condensation Mask

The CO_2 retrieval operates on averaged scans from 50 min to 90 min. All scans are scanned visually for corruption, e.g., due to obstacles in the FOV or a significant change in cloud coverage. Only scans passing the visual inspection proceed to the averaging. Emission plumes may show condensation due to co-emitted water vapor in the early stages of the plume development, depending on the ambient conditions. The condensation is visible as a white cloud in the plume and significantly changes the photon path length in the plume. Thus, evaluating this part of the plume would lead to large uncertainties in the retrieval. A plume condensation mask identifies and excludes these pixels from further processing. Figure 6.2 illustrates the principle of the condensation mask. Since condensation increases the saturation of the observed spectrum significantly compared to the blue sky background, the mask is generated from the saturation of the images. The pixel saturation S_{jk} is defined as the maximum of the spectrum $\boldsymbol{L}_{jk}$ in the pixel at frame j and line k, i.e., $S_{jk} = \max_{\text{channel}}(\boldsymbol{L}_{jk})$. The blue sky background saturation follows from

$$B_{jk} = \underset{j}{\text{med}}(S_{jk}) \cdot \left(\frac{\underset{k}{\text{med}}(S_{jk})}{\left\langle \underset{k}{\text{med}}(S_{jk}) \right\rangle_j} \right)^{\mathsf{T}}, \tag{6.3}$$

where med is the median and $\langle \cdot \rangle_j$ is the mean over the scan. Equation (6.3) is the outer product of the saturation median along the frames and the normalized median along the lines. Thus, B_{jk}

represents a smoothed background saturation of the image. The use of the median asserts that the exceptionally high saturation of condensation pixels does not influence the calculation of B_{jk}. The mask identifies condensation pixels by subtracting B_{jk} from the image saturation S_{jk}. Each pixel deviating by more than 3σ from the residual distribution is identified as a condensation pixel. Flagged pixels in a scan do not contribute to the averaged image. If less than 90 % of scans contribute to a pixel in the averaged image, the pixel is removed from the retrieval. This procedure assumes that condensation affects only a small fraction of a scan.

DMF retrieval algorithms require dividing each spectrum by a reference. The referencing of each spectrum within a line to the background spectrum is performed for each scan individually, before averaging the scans. Thus, the background spectrum is specific to the situation of every scan. It is taken as a 20-frame mean upwind of the source.

6.2.2 Carbon Dioxide Observations

The following section describes the CMF and DMF retrieval performance for the CO_2 plume observations. Figure 6.3 illustrates how an increasing averaging period improves the plume observation as more pixel enhancements exceed the detection limit. Averages from 50 min to 90 min provide a good compromise between the plume observation quality and the temporal resolution of the emission estimates for the presented cases. The matched filter retrieval of the averaged image employs a UAS LUT generated from daily AERONET data as described in Section 4.1.5. It uses the observation mean SAA and SZA and the pixel-specific VAA and VEA to compute the UAS. Knapp et al. (2023b) describe observations using the DMF retrieval, while the comparison to CMF retrievals is added here to underline the performance difference.

Seven of the 12 observation days were not suitable for emission estimates. Figure A.10 shows two example plumes excluded from further processing due to unfavorable wind and scene heterogeneity. Panel a) shows an observation on September 6, 2021, where the plume rises straight from the chimney to approximately 350 m height before seemingly turning left. Slow winds or wind directions parallel to the camera's line of sight cause the plume to rise vertically in the image. It is impossible to discern plume transport from these observations, and the forward model cannot accurately replicate the plume's shape. Panel b) shows an observation on March 24, 2022, where the plume is only visible close to the plume and subject to significant striping. Again, the plume shape is indiscernible, making an emission estimation impossible.

The five days chosen for further processing cover a range of observation conditions. The conditions were fine on June 8, 2022, with clear skies and *a priori* observation angles of $(-53 \pm 13)°$. However, the sky became increasingly dark and heterogeneous in the afternoon, causing the retrieval noise to increase. On March 23, 2023, significant condensation in the early stages of the plume and an acute observation angle $(33 \pm 28)°$ posed challenges to the retrieval. March 26, 2023, again showed favorable conditions. The ambient temperature increased steadily, reaching 20 °C around 14:30 UTC. While condensation prevents a plume observation before this time, the following two periods yield a discernible plume of connected enhancements above the detection limit. A Sahara dust event increased the aerosol load on March 28, 2023, causing the sky to be hazy and relatively bright in the shortwave infrared. Finally, the camera observed power plant unit 6 instead of unit 9 on May 13, 2023, under fair weather and favorable wind.

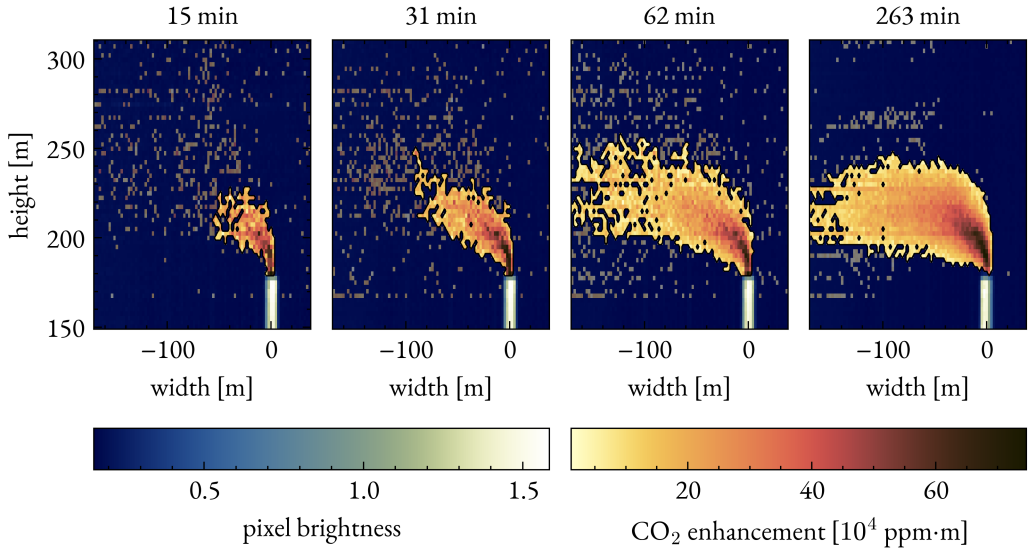

Figure 6.3: Improvement of the plume observation with increasing temporal averaging using the DMF. All observations are from September 8, 2021, starting at 12:13 UTC. The averaging period is in each panel's title and increases from left to right. CO_2 enhancements above the detection limit are colored yellow to red, and a black border marks the observation plume mask. Enhancements outside the mask but above the detection limit are shown slightly transparent. The observed plume becomes clearer with each increase in temporal averaging.

Figure 6.4 shows retrieved CO_2 enhancements using the CMF and DMF for March 26 and May 13, 2023. The days illustrate how the DMF outperforms the CMF retrieval. Enhancements exceeding the 2σ detection limit are potential plume pixels. The observation plume mask is the largest contiguous area of such pixels. The CMF retrieval is prone to striping, visible as vertical lines in the images. Panels a) and b) in Figure 6.4 illustrate how the CMF retrieval may fail to identify faint plumes due to striping or a low SNR. While the CMF is capable to identify CO_2 plumes, the DMF retrieval mitigates the striping and identifies larger parts of the plume (Figure 6.4, panels c) and d)). Figure 6.5 shows the SNR of the CMF and DMF retrievals for the two days shown in Figure 6.4. The histogram compares SNR values from the observation plume mask of the DMF retrieval. Thus, the DMF histogram contains no SNR values below two since this serves as the plume masking threshold. Note that the SNR reaches similar values for CO_2 in hourly averaged spectra as for CH_4 in single scans (see Figures 5.5 and 5.10). While the CMF can still identify most of the plumes in the presented observations, the DMF retrieval performs persistently better regarding SNR and observed plume size. Furthermore, striping is particularly problematic for emission estimates using plume fitting, as the striping signal is not included in the forward model. Thus, the DMF retrieval is the preferred method for the CO_2 observations.

Figure 6.6 shows the DMF retrievals for all five observation days, yielding 11 plumes images. All observations show an evident plume beginning at the chimney. The ambient wind carries the plumes downwind as they rise and disperse. As the images are long-term averages, turbulent features are blurred out in the ensemble, similar to, e.g., volcanic plume observations in Woitischek

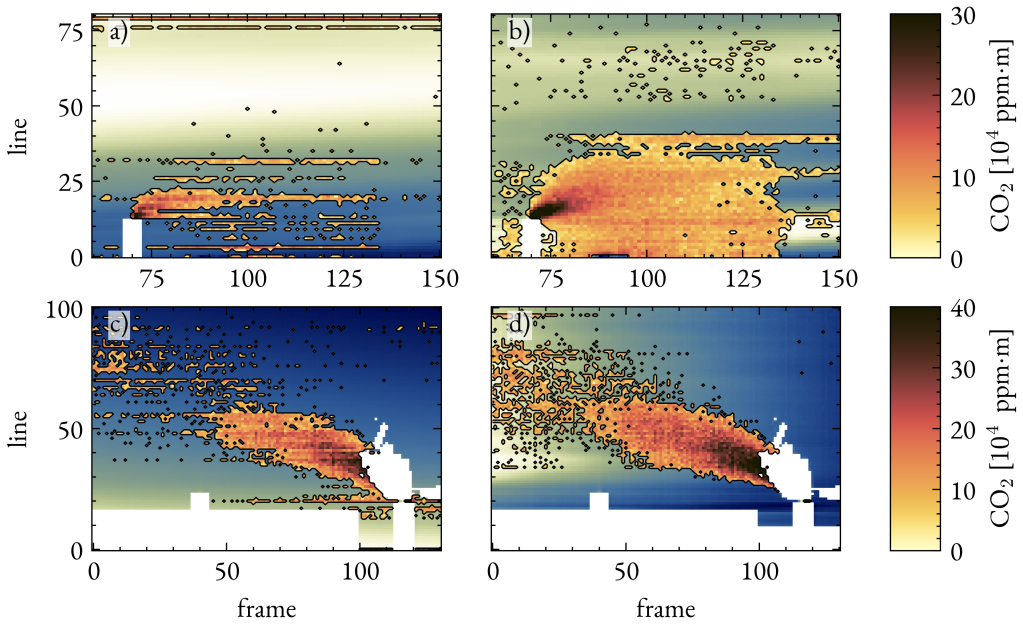

Figure 6.4: Comparison of the CMF and DMF retrieval performance. Panels a) and b) show observations from May 13, 2022, between 12:21 and 15:39 UTC. Panels c) and d) show observations from March 26, 2022, between 15:56 and 17:36 UTC. The left panels, a) and c), show the CMF retrieval results, while the right panels, b) and d), show the DMF retrieval results. The images show enhancements above the 2σ detection limit. The DMF enhancements show overall higher enhancements, less striping, and a larger and more realistic plume shape. Colors from yellow to red indicate increasing CO_2 column enhancements. The pixel brightness is shown in blue (dark) to white (bright). Missing values result from manual masking or condensation.

et al. (2021b). Plume observations in March 2022 show missing pixels close to the chimney due to condensation, and the plume on May 13 shows a stripe-like pattern in the plume mask. These observations are included to illustrate the limitations of the method.

6.2.3 Emission Estimation

A Gaussian plume inversion yields an emission estimate for each plume in Figure 6.6. Section 4.2.2 describes the inversion method in detail. Figure 6.7 gives an overview of the evaluation process of CO_2 emission estimates. For each ambient wind speed in the parameter space, the IBJpluris model of Janicke and Janicke (2001) calculates the plume shape. The wind LIDAR observations provide an adequate initial range for the parameter grid, yet the grid is expanded if the inversion yields no minimum in the initial range. The meteorological and proprietary data of the GKM provide all further information required by IBJpluris specifically for the observation period. Table A.5 lists the *a priori* data used for the plume generation. The inversion minimizes the χ^2_r-distance between the observed plume and the simulated plumes. The brute-force grid samples the χ^2_r-surfaces with step sizes of 0.2 m s^{-1} to 0.3 m s^{-1} for the ambient wind speed, 5° for the wind direction, 0.1 for the emission scaling k_c, and 0.1 - 0.4 for the plume width scaling k_b. Since k_c represents the emission

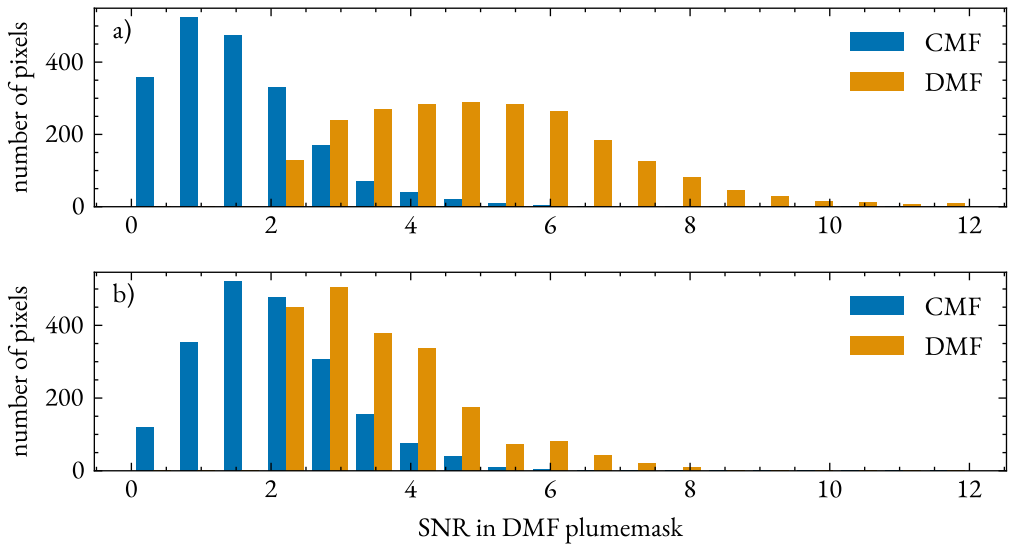

Figure 6.5: Comparison of the SNR of the retrievals in Figure 6.4. Panel a) and b) show data from May 13 and March 26, 2022, respectively. The DMF retrieval shows a higher SNR for all observations. The SNR is taken from all pixels in the observation plume mask of the DMF retrieval.

estimate, it is sampled a final time in 0.01 steps at the optimal parameters ($\hat{k}_b$, $\hat{u}_\mathrm{a}$, $\hat{\phi}$) to improve the emission estimate given the other three parameters.

Seven plumes from three days fulfill the requirements for the inversion procedure. On September 08, 2021, March 26, and 28, 2022, measurements yielded clear plume observations with little to no condensation and favorable wind conditions. Plume observations show comparatively small plumes after 14:24 UTC on September 8, 2021, and before 15:55 on March 26, 2022. The small plume sizes were caused by low background brightness and power plant activity, respectively. However, a visual inspection reveals no obvious non-compliance with the Gaussian plume shape assumption. Low wind speeds of $\hat{u}_\mathrm{a} = 1.4\,\mathrm{m\,s^{-1}}$ and a high aerosol load on March 28, 2022, cause slow transport of the emitted CO_2 and a bright background illumination. Thus, the observation reveals a particularly large plume. The plume observation is coarsened to constrain the computational cost by averaging two by two neighboring pixels.

The plume images collected under unfavorable conditions on March 23 and May 13, 2022, are particularly well-suited to illustrate the method's limitations. On March 23, 2022, an acute observation angle reduces the apparent plume size due to the unfavorable projection. Furthermore, condensation removes a considerable part from the early stages of the plume. Thus, the observation contains fewer pixels to inform the inversion. On May 13, 2022, wind conditions were favorable with $5.5\,\mathrm{m\,s^{-1}}$ at 62° observation angle, and the AOD was comparatively high with 0.065 at 2000 nm. However, the observed plumes show two enhancement patches, one above and one below the expected plume shape. Figure A.9 shows the retrieved image between 12:21 and 14:01 UTC on May 13, 2022. The stripe-like patches follow the background saturation and cause enhanced patches in the plume edges. Scene heterogeneity may cause such features, similar to sur-

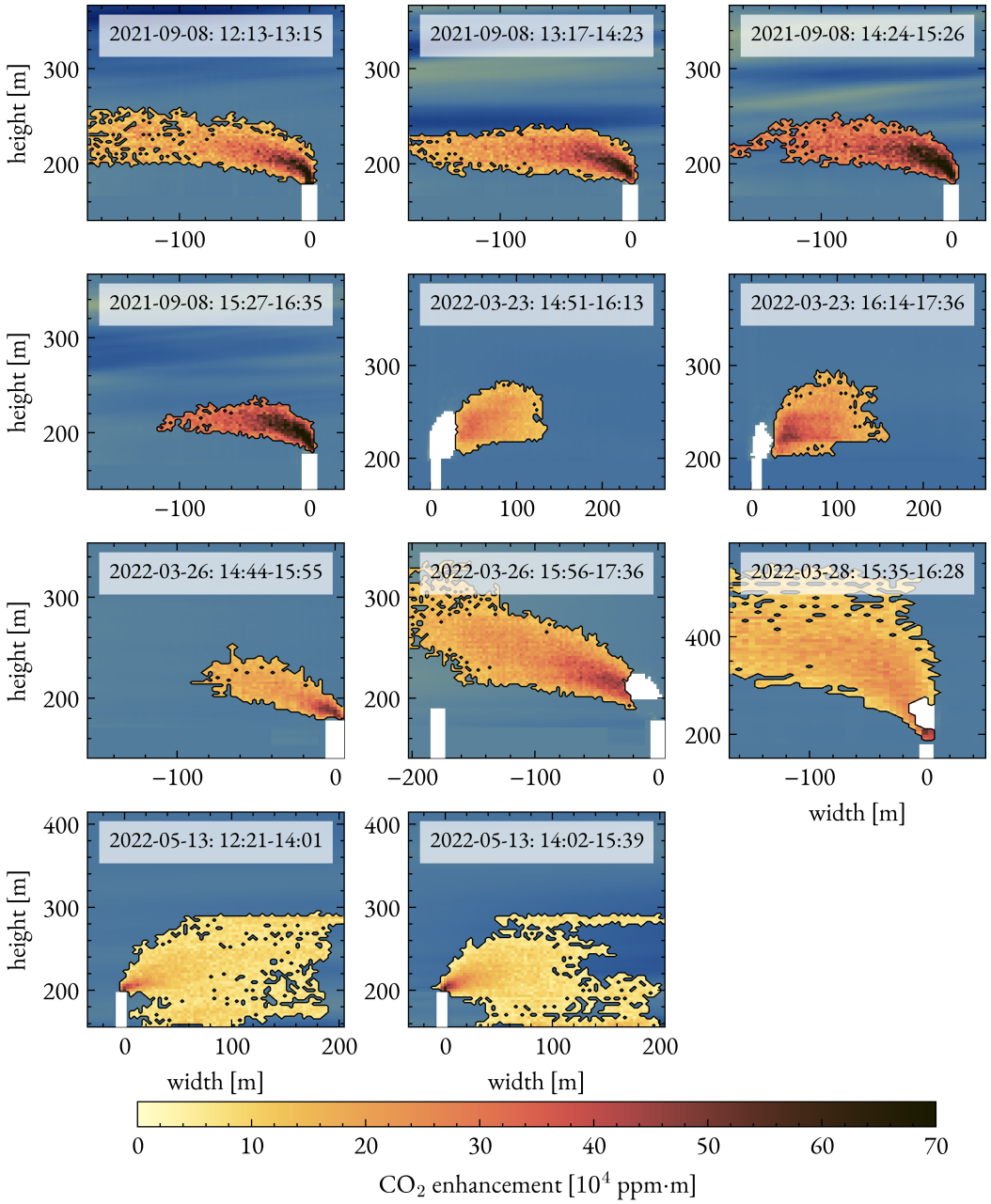

Figure 6.6: Plume images for all periods of the five observation days. The images share the yellow to red colorbar for the CO_2 column enhancements. The blue (dark) to white (bright) color in the background shows the pixel brightness. The white rectangular shapes in the lower part of the images are masks excluding the chimney tip. Plumes as shown in Knapp et al. (2023b).

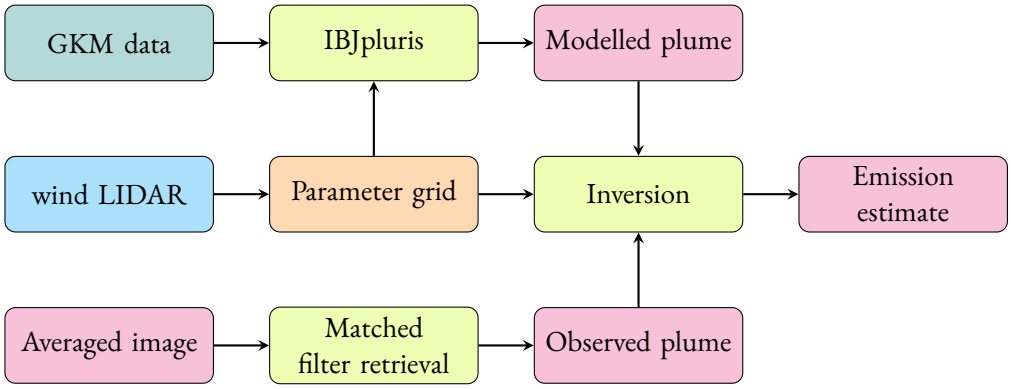

Figure 6.7: Flowchart of the CO_2 emission estimation technique. The IBJpluris model of Janicke and Janicke (2001) models a plume shape given the input parameters from the GKM and a range of wind speeds. The wind LIDAR provides *a priori* wind information. The averaged observation image is used as input for the matched filter retrieval, which operates with an observation-specific UAS. The inversion scans over a parameter grid in a brute-force manner. The emission estimate is given by minimum χ^2_r distance. Processes are yellow, settings are orange, (interim) results are red, and internal and external data are blue and green, respectively.

face albedo variations in top-down measurements. Irrespective of the origin of these artifacts, the Gaussian model cannot represent these patterns.

Mass balance methods like the IME or XSF do not rely on the observation complying with a model assumption. Obvious enhancement artifacts from scene heterogeneity can be removed via visual inspection, avoiding a systematic bias. However, there are several shortcomings to the mass balance methods. Plume parts lost below the detection bias the emission estimate low. The Gaussian plume model enables an estimate of the plume mass lost to the detection limit. Mass balance methods use the observed mass inside a plume mask, as done for CH_4 in Chapter 5. The model informs on the mass outside the plume mask. Only the frames containing the plume are used for the IME and XSF calculations. The lost mass fraction is the ratio of the total simulated mass to the observed mass in these frames. Typical lost mass fractions fall between 20 % and 25 % for the larger plume observations but may reach up to 46 % for fainter plumes like on March 26, 2022, 14:44 - 15:55 UTC (Figure A.11). Applying mass balance techniques to the CO_2 observations will underestimate the emissions by the same amount. Furthermore, mass balance methods require knowledge on the plume's flow direction and speed. The wind LIDAR delivers the necessary information for the CH_4 emission estimates since it observes the wind field at plume height at a distance of 1 km. However, the CO_2 plumes extend above the wind LIDAR range since the chimneys of the GKM are 180 m (unit 9) and 200 m (units 6 - 8) high. The thermal plume rise in the early stages of the plume development further complicates mass balance methods. At a plume cross-section, the IME requires the time since the emission and the XSF the plume velocity perpendicular to the travel direction. Both quantities are hard to compute reliably for the observed bent-over plume shapes. In fact, it also requires fitting a model to the observations. Thus, the Gaussian plume inversion is the preferred emission estimation method for the presented CO_2 observations.

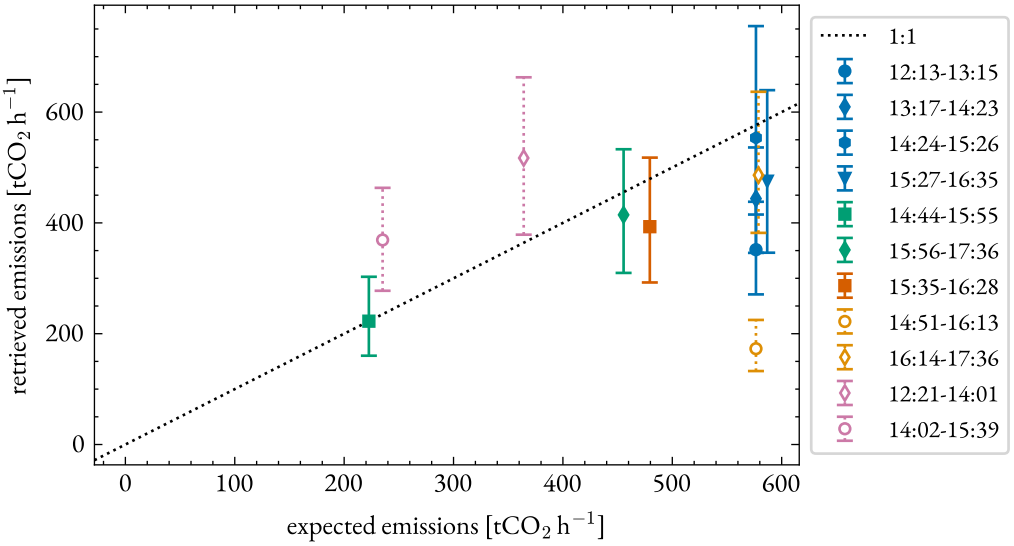

Figure 6.8: Correlation plot of the expected and retrieved emissions. The dotted line marks the 1:1 line. Each color represents a day: September 8, 2021 (blue), March 23, 2022 (yellow), March 26, 2022 (green), March 28, 2022 (orange), and May 13, 2022 (pink). The symbols represent observation periods. Solid markers denote days with favorable and open markers denote days with unfavorable conditions. Adapted from Knapp et al. (2023b).

6.3 Comparison to Validation Data

The optimal parameter set from the Gaussian plume inversion yields a retrieved emission estimate for each plume observation. Table 6.2 lists the parameters and the corresponding retrieved and expected power plant emissions. The GKM dataset provides precise knowledge of the power plant's energy production. Thus, the correlative bottom-up emissions serve as validation data for the retrieved emissions. Figure 6.8 shows the correlation plot for the emission values. Observation conditions have been favorable in seven of 11 plume observations. The retrieved emissions from these plumes show an overall reasonable agreement with the expected emissions. On average, they amount to 84 % of the expected emissions and have a relative uncertainty of 24 %. Five of the seven observations agree with the expected emissions within their uncertainties. The power plant emissions increased during the observation period on March 26, 2022, from 223 $tCO_2\ h^{-1}$ to 445 $tCO_2\ h^{-1}$ between 14:44 - 15:55 and 15:56 - 17:36 UTC. The emission estimates from the plume observations follow the source variability, indicating that the method can observe diurnal changes in emission rates. The March 28, 2022, observation provides a preliminary lower limit for the wind speed necessary for the method to work. It agrees with the expected emissions at an ambient wind speed of $\hat{u}_a = 1.4\ m\ s^{-1}$. Observations on September 8, 2021, between 14:24 and 16:35 UTC, agree with the expected emissions within the uncertainty range, while observations between 12:13 and 14:23 UTC underestimate the expected emissions. The estimated observation angle $\hat{\phi}$ is between -35° and -30° for these observations. This angle is significantly steeper than the *a priori* observation angle of (−53 ± 13)°, which was derived from ERA5 data since there is no wind LIDAR data on September 8, 2021. Observations on March 23, 2022, indicate that acute obser-

Table 6.2: Column one lists the observation time period, and column two the expected emissions E_{exp} [$tCO_2\ h^{-1}$] (Section 6.1.2). The retrieved emissions E_{ret} are listed in column three, with the uncertainty range in parentheses. Columns four to seven give the optimal inversion parameters $\hat{k}_c$, $\hat{k}_b$, $\hat{\phi}$ [°], and $\hat{u}_{\mathrm{a}}$ [$m\ s^{-1}$]. Note that $\hat{k}_c$ is the relative scaling between retrieved and expected emissions, i.e., it represents the relative deviation. The last column shows the minimum χ^2_{r} for each observation.

Date & time	E_{exp}	E_{ret}	$\hat{k}_c$	$\hat{k}_b$	$\hat{\phi}$	$\hat{u}_{\mathrm{a}}$	$\hat{\chi}^2_{\mathrm{r}}$
2021-09-08							
12:13 - 13:15	576	352 [271 to 438]	0.61 [0.47 to 0.76]	1.5	-34	8.3	1.88
13:17 - 14:23	576	444 [346 to 536]	0.77 [0.60 to 0.93]	1.8	-30	10.4	3.24
14:24 - 15:26	576	553 [415 to 755]	0.96 [0.72 to 1.31]	1.8	-35	7.6	0.66
15:27 - 16:35	587	475 [346 to 640]	0.81 [0.59 to 1.09]	1.9	-25	9.2	0.65
2022-03-26							
14:44 - 15:55	223	223 [160 to 303]	1.00 [0.72 to 1.36]	2.0	-131	3.4	0.30
15:56 - 17:36	455	414 [310 to 533]	0.91 [0.68 to 1.17]	1.4	-116	3.8	0.62
2022-03-28							
15:35 - 16:28	479	393 [292 to 518]	0.82 [0.61 to 1.08]	1.9	-65	1.4	0.85
2022-03-23							
14:51 - 16:13	576	173 [133 to 225]	0.30 [0.23 to 0.39]	1.2	15	5.7	1.34
16:14 - 17:36	579	486 [382 to 637]	0.84 [0.66 to 1.10]	1.8	65	3.9	1.24
2022-05-13							
12:21 - 14:01	364	517 [379 to 663]	1.42 [1.04 to 1.82]	7.0	40	6.2	1.77
14:02 - 15:39	235	369 [277 to 463]	1.57 [1.18 to 1.97]	7.0	85	6.6	3.00

vation angles may cause emission underestimation, which might also apply to the observations on September 8, 2021. Potential sources of systematic errors in the retrievals are background heterogeneity of the scene, CO_2 features in the image region of the reference spectrum, or assumptions in the unit absorption spectrum calculations like aerosol content.

Figure 6.8 shows that observations taken under challenging conditions do not agree with the bottom-up estimates of the power plant emissions. Two plume observations from March 23, 2022, illustrate the effect of acute observation angles and condensation. The wind LIDAR provides an *a priori* observation angle of (33 ± 30)° and (33 ± 25)° for the observation between 14:51 and 16:13 UTC and 16:14 to 17:36 UTC, respectively. The ideal fitting parameter $\hat{\phi} = 15°$ for the earlier observation agrees with the *a priori* value, but the retrieved emissions underestimate the expected emissions significantly by 70 [61 to 77] %. The later observation agrees with the expected emissions, yet the retrieved observation angle of 65° is inconsistent with the LIDAR observations. The results indicate that acute observation angles and plume condensation limit the applicability of the method. Thus, both features may serve as filter criteria in future observations. Plume observations on May 13, 2022, do not comply with the Gaussian plume assumption due to stripe-like features close to the plume. Retrieved emissions significantly overestimate the power plant emissions for both observations. The stripes appear at the plume edges, causing an overestimation of the width scaling factor k_b. Typical values for k_b range between 1.2 and 2.0, while they reach 7.0 for both plumes on May 13, 2022. The forward model compensates for the stripes by

increasing the overall observed mass, attributing higher emissions to the source. In this case, the non-compliance of the observations with the Gaussian plume shape could be identified, and the emission estimates excluded from the validation. However, in other cases, the effect might be too small to be recognized visually but still large enough to propagate in the emission estimate.

7 Conclusions and Outlook

This work presents ground-based observations of atmospheric CO_2 and CH_4 plumes using a stationary HySpex SWIR-384 spectral camera. It comprises a complete processing chain for estimating point source emissions from raw hyperspectral data. Proof-of-concept field studies at sources of CO_2 and CH_4 demonstrate the method's capabilities. The stationary camera allows for repeated observation of the same source with a temporal resolution of approximately one minute, yielding several hundred hyperspectral images per day. A statistical retrieval enables quantifying atmospheric enhancements of CO_2 and CH_4 in emission plumes. Emission estimates based on plume images provide time series with hourly (CO_2) to sub-hourly (CH_4) resolution. Particular advantages of the described methods are (a) a high specificity to the target gas by spectroscopically resolving the absorption features, (b) imaging capability enabling unambiguous source attribution, (c) operating distances spanning the kilometer scale, and (d) observation of diurnal and day-to-day emission variability of the source. Additionally, all required instruments fit inside a single car and can operate on batteries for a full day, allowing for flexible target selection.

Incorporating stationary imaging of atmospheric CO_2 and CH_4 into existing greenhouse gas observation techniques enhances Monitoring and Verification Support (MVS) capabilities for greenhouse gas emissions. The methods developed in this study provide complementary information to snapshot images obtained from aircraft and satellite platforms, enabling emission estimates on shorter time scales and, particularly for CH_4, in conditions characterized by cloud cover. Additionally, imaging CH_4 plumes in the SWIR spectral range complements established methods, such as put forward by Gålfalk et al. (2016) and Zimmerle et al. (2020), which rely on the thermal contrast of the gas. The observations made possible by this technique facilitate the estimation of CH_4 source variability on time scales ranging from minutes to days. The presented technique enabled ground-based imaging of CO_2 emission plumes for the first time. It allows for estimating hourly emissions of strong point sources under favorable observation conditions. Thus, this work demonstrates promising results in fulfilling remote sensing needs for measuring greenhouse gas fluxes (Bastviken et al., 2022). Ground-based emission estimates may serve to validate snapshot images and offer insights into the accuracy of their instantaneous source flux estimates concerning source variability and intermittency. The application of remote sensing at the kilometer scale extends the array of potential targets to include hard-to-reach sources, such as volcanoes or restricted areas. Operating at ill-constrained sources holds the potential for independent emission verification, providing valuable contributions to bottom-up inventories in the future. For example, Wang et al. (2024) point out systematic underestimation of landfill CH_4 bottom-up emissions and their potential for low-cost abatement. Moreover, imaging local sources could be a valuable tool to increase public awareness of local emissions and promote emission reduction measures (Jungmann et al., 2022). The following paragraphs outline the development of the retrieval and the results from the proof-of-concept studies at CO_2 and CH_4 point sources.

The first methodological development of this thesis concerns quantifying atmospheric column enhancements of CO_2 and CH_4 in image pixels containing an emission plume. A linearized matched filter algorithm exploits molecular absorption features of CO_2 and CH_4 around 2.0 µm and 2.3 µm, respectively. The method incorporates various refinements from the literature, namely an iterative scheme from Foote et al. (2020) to improve accuracy and a robust plume masking from Roger et al. (2023a) in cloudy conditions. However, the matched filter requires additional adaptations due to the horizontal viewing geometry. First, the target signature depends significantly on the observation geometry. Thus, the developed matched filter employs a pixel-specific target signature based on the camera's FOV. Second, retrieving ground-based observations requires the whole image for sufficient background statistics, while airborne applications usually treat lines independently to reduce striping. A differential matched filter (DMF) mitigates this effect in the presented data. The DMF outperforms the classic matched filter regarding SNR and observed plume size in all observation conditions, especially in homogeneous, clear skies.
Potential future methodological advancements include refinements in the retrieval and target signature calculation. Log-normal matched filter approaches, such as those presented by Pei et al. (2023), may improve accuracy, particularly in pixels with high optical depths. Furthermore, the target signature calculation could benefit from refinements in the instrument characterization or the radiative transfer description. Haveresch (2023) develops a physical inversion routine based on the single-scattering solution of the RTE. This routine enables the simultaneous retrieval of effective aerosol parameters and atmospheric CO_2 and CH_4 column concentrations. Processing hyperspectral images on a pixel-by-pixel basis is more computationally expensive than using the matched filter. The physical retrieval is favorable for complex scenes, such as co-emitted aerosols, which are inherently challenging for matched filter retrievals. Combining complementary aspects from statistical and physical retrievals, such as providing the spectral sample covariance matrix to the physical inversion, has shown promising results in reducing the correlation of CH_4 enhancements and background heterogeneity (Hochstaffl et al., 2023).

The thesis expands on CH_4 emission time series from coal mine ventilation shafts previously published in Knapp et al. (2023a). A co-located wind LIDAR provides precise wind information for emission estimates based on mass balance methods. Favorable conditions comprise a clear sky and wind speeds above approximately 2 m s^{-1} perpendicular to the camera's line of sight. However, the method successfully identifies emission plumes from single scans in clear-sky and cloudy conditions. The dataset comprises 2660 quality-filtered plume images captured over eight days with varying observation conditions. Single-scan emission estimates show relative uncertainties between 10 % and 18 %. Higher uncertainties coincide with background heterogeneity, low wind speeds, or unfavorable wind direction. In order to discern the emission variability of the source from turbulent transport features, averaging the emission estimates over several scans becomes necessary. The temporal resolution varies between 10 min and 232 min. Considering this, rolling-averaged emission estimates are between 34 % and 55 % lower or higher than the daily mean. However, always scanning against the wind direction will reliably push the temporal resolution to its lower limit in future applications. The daily estimates of CH_4 emissions from the observed coal mine shaft range from 1.56 tCH_4 h^{-1} to 4.57 tCH_4 h^{-1}. The source strength is consistent with previous studies (Luther et al., 2019; Andersen et al., 2021; Swolkień et al., 2022) and the observed variability emphasizes the added value of temporally resolving the emissions. Preliminary comparisons with coinciding in-situ observations indicate that day-to-day variability is similar, but in-

situ emission estimates are consistently higher than camera measurements and exhibit less diurnal variability. Further investigation and extended side-by-side observations are required to understand the differences between the two methods better.
Future deployments at CH_4 sources include a controlled release experiment to validate the method against well-known bottom-up emissions. Furthermore, other CH_4 sources like the oil and gas sector (Bhardwaj et al., 2022; Foulds et al., 2022) and landfills (Cusworth et al., 2020; Kumar et al., 2023) also show considerable emission variability and are potential targets for stationary imaging. Diffuse sources like landfills may not produce a distinct enhancement plume, yet mass balance techniques independent of plume masking, such as divergence methods (Liu et al., 2021; Chulakadabba et al., 2023), can effectively overcome such challenges.

Repeated ground-based observations of a localized CO_2 source enable imaging of the emission plume (Knapp et al., 2023b). Proof-of-concept observations come from a medium-sized coal-fired power plant in Mannheim, Germany, with an annual emission of approximately 4.9 $MtCO_2$. Plume observations of CO_2 require averaging images over 50 min to 90 min to increase the SNR. Temporal averages of plume observations allow fitting a Gaussian plume model to the observation in good approximation. A newly developed forward model based on bent-over Gaussian plume shapes simulates a plume observation. An inversion minimizes the χ^2_r-difference between simulated and observed plumes, providing the best estimate of the source emissions. As expected, the method is sensible to non-compliance of the observation with Gaussian model assumptions, e.g., striping or background artifacts. However, plume observations with stable, homogeneous backgrounds typically comply with the assumptions. Seven plume observations under such conditions were recorded between 2021 and 2023. Temporally resolved bottom-up emissions based on activity data supplied by the power plant's operator serve as a validation opportunity for each observation period. The estimated emission rates of these seven observations average 84 % of the expected emissions with a mean relative uncertainty of 24 %. Thus, they agree reasonably well with the expected emissions. Furthermore, measurements on March 26, 2022, indicate that the retrieved emission estimates follow diurnal trends in the power plant's bottom-up emissions.
Ongoing observation efforts at the power plant provide a growing dataset for methodological refinements. Further development of the technique could provide independent verification for CO_2 emissions, especially for less well-known anthropogenic sources or natural sources such as volcanoes.

A Appendix

A.1 Appendix to Instrument Chapter

A.1.1 Detector Background

Each detector reading contains a background signal according to Equation (3.1):

$$DN_{zj} = N_{\mathrm{ph},zj} \cdot QE_z \cdot SF \cdot RE_{zj} + BG_{zj} \,. \tag{A.1}$$

The background contribution BG is due to a pixel dark current DC and an offset OS. It follows for each detector pixel from

$$BG = SF \cdot \beta(T) \cdot t_{\mathrm{int}} + OS \,, \tag{A.2}$$

where $\beta(T)$ is a temperature dependent flux in photo-electrons per second and SF the scaling factor of photo-electrons to digital numbers [DU]. Figure A.1 shows the dark current and offset for each detector pixel. The values follow from background observations of the camera with increasing integration times. Background observations are detector readouts while the shutter of the camera prevents ambient light from falling onto the detector. The times were chosen as multiples of the minimum frame period of 2.332 ms up to 13.992 ms. The background signal was between 4000 DU and 12 000 DU. For each pixel, a linear fit following Equation (A.2) yields OS and $SF \cdot \beta(T)$. The retrieval of CO_2 and CH_4 uses the spectral interval above channel 190. The background contributes an average of

$$OS = (2702 \pm 569)\,\mathrm{DU} \tag{A.3}$$

$$SF \cdot \beta(T) = (541 \pm 52)\,\mathrm{DU\,ms^{-1}} \tag{A.4}$$

to the signal in this detector area.

A.1.2 Bad Pixel Mask Generation

This section provides additional information on the extended bad pixel mask presented in Section 3.1.2. A stable power supply provided 13.0 V and 2.1 A to four halogen lamps. The lamps illuminate the integrating sphere's interior. The system was allowed to stabilize thermally for two hours prior to measurements. The detector temperature remained stable at 147 K during the measurements. Each frame exposed the detector 4.7 ms to the light source. 150 scans of 200 frames provide a 30 000 frames time series for each detector pixel. The technique is designed to find variability in the detector pixel response over several scans. Thus, the following steps are performed:

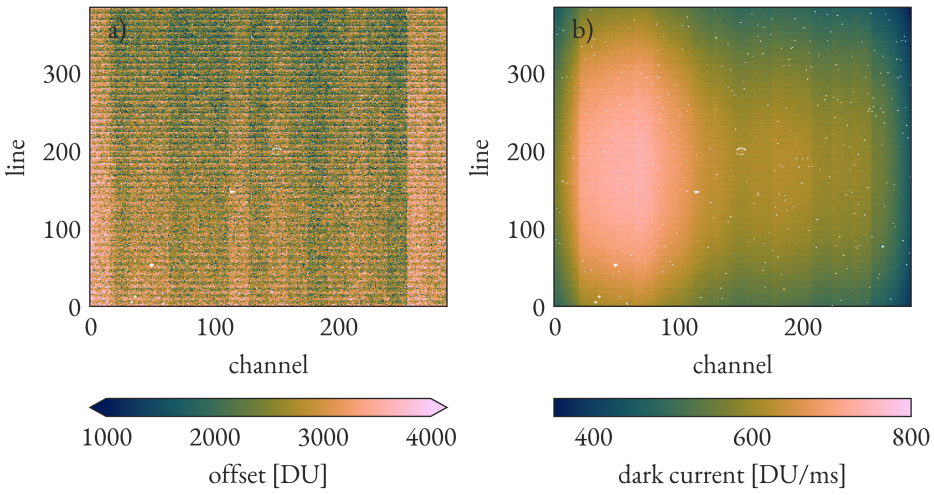

Figure A.1: Panel a) shows the detector offset signal and panel b) the detector dark current. Both values follow from a detector pixel-wise interpolation of dark signals.

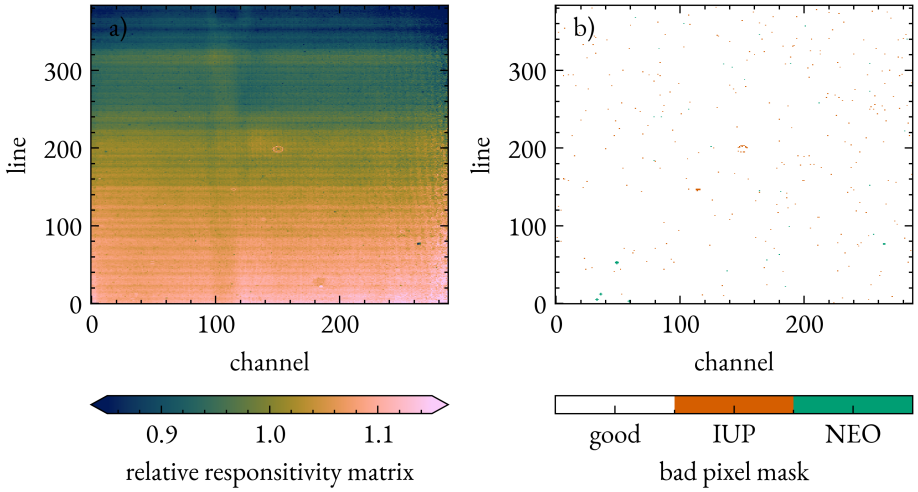

Figure A.2: Panel a) shows the relative responsitivity matrix provided by NEO. Panel b) shows the bad pixel mask, including the bad pixels identified by NEO (green) and additional bad pixels from the Institut für Umweltphysik (IUP) (orange). Note that the additional pixel partly correspond with a circular feature in the detector center that can also be seen in panel a).

1. A Gaussian filter removes the frame-to-frame variability. This step removes noise from the time series to observe a "baseline" of each pixel.

2. The integrating sphere is not perfectly homogeneous. Thus, every line observes a different brightness. Furthermore, the detector sensitivity also introduces some residual spatial heterogeneity. All baselines are normalized by their temporal mean, correcting for integrating sphere and detector pixel heterogeneity.

3. The integrating sphere's brightness shows small temporal variability despite the stable power supply. This source variability acts on all pixels identically. Thus, subtracting the median signal in each time step from the normalized baseline corrects for source variability. Figure 3.5a shows this as "corrected signal".

4. For each pixel, the standard deviation along the frames $\tilde{\sigma}$(channel, line) is computed. Temporally stable detector pixels show only little remaining variability, since the previous steps remove variability from noise and light source.

5. Higher signal channels show lesser standard deviations. Therefore, the instability is defined with respect to the channel. Every channel exists in all 384 spatial lines. For each line, the mean and standard deviation of $\tilde{\sigma}$ is computed.

6. The instability of Figure 3.5b is the number of standard deviation each pixel's $\tilde{\sigma}$ deviates from the channel's mean.

7. The whole time series of 30 000 frames is divided into ten intervals. If the instability is larger than five in at least half of the intervals, the corresponding pixel is considered bad.

Note that step 7 is included since the behavior of the detector pixels was not unambiguous. The newly found bad pixels are likely to exhibit increased temporal variability but may also perform "normally" over limited periods. Likewise, other detector pixels show erratic behavior in rare cases. The procedure aims to minimize the contribution of flawed detector pixels to the image. However, striping in the matched filter retrievals indicates that flawed detector pixels still contribute to the evaluation. The flawed detector pixel is usually easily identified from the (differential) spectrum. Manually excluding the pixel and repeating the retrieval is a feasible but cumbersome solution. Figure A.2 shows the camera's relative responsitivity matrix and the bad pixel mask. The method identifies pixels in a circular shape in the detector center as bad. This feature is also visible in the relative responsitivity matrix, indicating that the area differs from the remaining detector. The stripe around channel 100 in the detector responsitivity results from an additional optical filter on the detector.

A.2 Appendix to Method Chapter

A.2.1 Matched Filter Derivation

This section provides more detailed derivations of the matched filter retrieval than Section 4.1. There are several ways to derive the matched filter. It follows from maximizing the signal-to-noise ratio, and a derivation can be found on https://en.wikipedia.org/wiki/Matched_filter (accessed January 2024). This section will derive the matched filter from maximizing the likelihood of an observation, using a similar approach as Foote et al. (2020). Furthermore, a derivation using the normal equations following Rodgers (2000) is given. The latter helps to understand the implementation of pixel-specific UAS and the iterative solution of the sparsity constraint. The notation of this chapter follows Section 4.1.

From the Likelihood

The likelihood of an observation describes how likely it was to make this observation given a theoretical description. The theoretical description of the matched filter retrieval is a multivariate Gaussian distribution with mean vector $\boldsymbol{\mu}$ and covariance $\mathbb{C}$. Furthermore, the model includes a linear attenuation $\boldsymbol{t}$ scaled with the signal strength α in each pixel. As stated in Equation (4.8), the likelihood of the retrieval is given by

$$\begin{aligned}\mathcal{L}(\boldsymbol{L}_1, \dots, \boldsymbol{L}_N|\vec{\alpha}) =& \frac{1}{\sqrt{(2\pi)^C \det(\mathbb{C})}^N} \\ & \cdot \exp\left(-\frac{1}{2}\sum_{i=1}^{N}(\boldsymbol{L}_i - (\boldsymbol{\mu} + \alpha_i \boldsymbol{t}))^\intercal \mathbb{C}^{-1}(\boldsymbol{L}_i - (\boldsymbol{\mu} + \alpha_i \boldsymbol{t}))\right).\end{aligned} \tag{A.5}$$

The closed-form solution of the matched filter follows from maximizing the observation's likelihood with respect to $\vec{\alpha}$. Maximizing this likelihood is the same as minimizing the negative log-likelihood:

$$\hat{\vec{\alpha}} = \arg\min_{\alpha} \sum_{i=1}^{N} \boldsymbol{d}_i^\intercal \mathbb{C}^{-1} \boldsymbol{d}_i \tag{A.6}$$

$$\boldsymbol{d}_i = \boldsymbol{L}_i - \alpha_i \boldsymbol{t} - \boldsymbol{\mu}\,. \tag{A.7}$$

The log-likelihood can be differentiated analytically to

$$0 = -\vec{\nabla}_\alpha \ln(\mathcal{L}) \tag{A.8}$$

$$\begin{aligned} = & -\vec{\nabla}_\alpha \ln\left(\frac{1}{\sqrt{(2\pi)^C \det(\mathbb{C})}^N}\right) \\ & + \frac{1}{2}\vec{\nabla}_\alpha\left(\sum_{i=1}^{N}(\boldsymbol{L}_i - \alpha_i \boldsymbol{t} - \boldsymbol{\mu})^\intercal \mathbb{C}^{-1}(\boldsymbol{L}_i - \alpha_i \boldsymbol{t} - \boldsymbol{\mu})\right) \end{aligned} \tag{A.9}$$

$$= \vec{\nabla}_\alpha \sum_{i=1}^{N}(\boldsymbol{L}_i - \alpha_i \boldsymbol{t} - \boldsymbol{\mu})^\intercal \mathbb{C}^{-1}(\boldsymbol{L}_i - \alpha_i \boldsymbol{t} - \boldsymbol{\mu}) \tag{A.10}$$

The minimizer $\hat{\vec{\alpha}}$ follows from minimizing the individual terms, i.e., finding α for each pixel. Thus, the following holds for each pixel $i \in N$:

$$0 = \frac{\partial}{\partial \alpha}(\boldsymbol{L} - \alpha \boldsymbol{t} - \boldsymbol{\mu})^\intercal \mathbb{C}^{-1}(\boldsymbol{L} - \alpha \boldsymbol{t} - \boldsymbol{\mu}) \tag{A.11}$$

$$= -2\boldsymbol{L}^\intercal \mathbb{C}^{-1}\boldsymbol{t} + 2\boldsymbol{\mu}^\intercal \mathbb{C}^{-1}\boldsymbol{t} + 2\alpha \boldsymbol{t}^\intercal \mathbb{C}^{-1}\boldsymbol{t} \tag{A.12}$$

$$= (\boldsymbol{\mu} - \boldsymbol{L})^\intercal \mathbb{C}^{-1}\boldsymbol{t} + \alpha \boldsymbol{t}^\intercal \mathbb{C}^{-1}\boldsymbol{t}\,, \tag{A.13}$$

leading to the CMF equation

$$\alpha_i = \frac{(\boldsymbol{L}_i - \boldsymbol{\mu})^\intercal \mathbb{C}^{-1}\boldsymbol{t}}{\boldsymbol{t}^\intercal \mathbb{C}^{-1}\boldsymbol{t}}\,. \tag{A.14}$$

From the Normal Equations

Consider a measurement vector $\boldsymbol{L}$, which has dimensions pixels times channels ($N \times C$). The forward model describes each entry in a Lambert-Bert fashion, with a pixel-specific UAS. It can be written as

$$\begin{pmatrix} L_{11} \\ L_{12} \\ \vdots \\ L_{1C} \\ L_{21} \\ \vdots \\ L_{NC} \end{pmatrix} = \boldsymbol{L} = \boldsymbol{F}(\vec{\alpha}) = \begin{pmatrix} \mu_1 e^{-\alpha_1 s_{11}} \\ \mu_2 e^{-\alpha_1 s_{12}} \\ \vdots \\ \mu_C e^{-\alpha_1 s_{1C}} \\ \mu_1 e^{-\alpha_2 s_{21}} \\ \vdots \\ \mu_C e^{-\alpha_N s_{NC}} \end{pmatrix}. \tag{A.15}$$

The Taylor expansion of the forward model around $\alpha = 0$ up to the linear term is

$$\boldsymbol{L} = \boldsymbol{F}(\vec{\alpha})|_{\alpha=0} + \left(\frac{\partial \boldsymbol{F}}{\partial \vec{\alpha}}\right)\Bigg|_{\alpha=0} \vec{\alpha} \tag{A.16}$$

$$= \boldsymbol{\mu'} + \mathbb{K}\vec{\alpha}\,, \tag{A.17}$$

where the vector $\boldsymbol{L}$ contains the observed spectra in all pixels, the vector $\vec{\alpha}$ contains the enhancements in all pixels, and $\boldsymbol{\mu'}$ repeats the mean radiance vector $\boldsymbol{\mu}$ N times for dimensional consistency. Note that vectors of dimension $N \times C$ (spatial pixels times channel) are written bold and vectors of dimension N use the vector arrow. The *weighting function matrix* $\mathbb{K}$ is given by

$$\mathbb{K} = \begin{pmatrix} -\mu_1 s_{11} & 0 & \cdots & 0 \\ -\mu_2 s_{12} & 0 & \cdots & 0 \\ \vdots & \vdots & \vdots & \vdots \\ -\mu_2 s_{1C} & 0 & \cdots & 0 \\ \vdots & \vdots & \ddots & \vdots \\ 0 & 0 & \cdots & -\mu_C s_{NC} \end{pmatrix} \tag{A.18}$$

$$\equiv \begin{pmatrix} t_{11} & 0 & \cdots & 0 \\ t_{12} & 0 & \cdots & 0 \\ \vdots & \vdots & \vdots & \vdots \\ t_{1C} & 0 & \cdots & 0 \\ \vdots & \vdots & \ddots & \vdots \\ 0 & 0 & \cdots & t_{NC} \end{pmatrix} \tag{A.19}$$

$$\dim(\mathbb{K}) = NC \times N\,, \tag{A.20}$$

with $t_{iz} \equiv -\mu_z s_{iz}$, where i is the pixel and z the channel.
Defining the "data vector" $\boldsymbol{y}$ as $\boldsymbol{y} = \boldsymbol{L} - \boldsymbol{\mu'}$, the forward model assumes the form

$$\boldsymbol{y} = \mathbb{K}\vec{\alpha}\,, \tag{A.21}$$

which is the well-known form of a linear system. Since $\boldsymbol{y}$ is subject to uncertainties, $\mathbb{K}$ is not trivially invertible. The matched filter assumes that the measurements are prone to a multivariate normally distributed error with expected value 0 and covariance matrix $\mathbb{C}$ in each pixel. Furthermore, the pixels are assumed to be independent, such that the mean radiance vector $\boldsymbol{\mu}$, $\dim(\boldsymbol{\mu}) = C$, and covariance matrix $\mathbb{C}$, $\dim(\mathbb{C}) = C \times C$, follow as the sample mean and sample covariance of the observation. The error covariance matrix $\mathbb{S}_y$ therefore becomes

$$\mathbb{S}_y = \begin{pmatrix} \mathbb{C} & 0 & \cdots & 0 \\ 0 & \mathbb{C} & \cdots & 0 \\ \vdots & \vdots & \ddots & \vdots \\ 0 & 0 & \cdots & \mathbb{C} \end{pmatrix}, \tag{A.22}$$

repeating $\mathbb{C}$ N times on the diagonal, i.e., assuming all observed spectra are prone to the same error. The problem described above can be solved as a weighted least-squares problem, i.e., the

optimal solution is the one that minimizes the residual distance of $\boldsymbol{y}$ and $\mathbb{K}\vec{\alpha}$ in a least-squares sense. Thus, the solution follows from

$$\hat{\vec{\alpha}} = \arg\min_{\vec{\alpha}} (\boldsymbol{y} - \mathbb{K}\vec{\alpha})^{\mathsf{T}} \mathbb{S}_y^{-1} (\boldsymbol{y} - \mathbb{K}\vec{\alpha}) \,. \tag{A.23}$$

This equation may be solved using the Cholesky factorization $\mathbb{S}_y = \mathbb{Z}\mathbb{Z}^{\mathsf{T}}$:

$$\begin{aligned}
(\boldsymbol{y} - \mathbb{K}\vec{\alpha})^{\mathsf{T}} \mathbb{S}_y^{-1} (\boldsymbol{y} - \mathbb{K}\vec{\alpha}) &= (\boldsymbol{y} - \mathbb{K}\vec{\alpha})^{\mathsf{T}} (\mathbb{Z}\mathbb{Z}^{\mathsf{T}})^{-1} (\boldsymbol{y} - \mathbb{K}\vec{\alpha}) && \text{(A.24)} \\
&= (\mathbb{Z}^{-1}\boldsymbol{y} - \mathbb{Z}^{-1}\mathbb{K}\vec{\alpha})^{\mathsf{T}} (\mathbb{Z}^{-1}\boldsymbol{y} - \mathbb{Z}^{-1}\mathbb{K}\vec{\alpha}) && \text{(A.25)} \\
&\equiv (\tilde{\boldsymbol{y}} - \tilde{\mathbb{K}}\vec{\alpha})^{\mathsf{T}} (\tilde{\boldsymbol{y}} - \tilde{\mathbb{K}}\vec{\alpha}) && \text{(A.26)} \\
&= ||\tilde{\boldsymbol{y}} - \tilde{\mathbb{K}}\vec{\alpha}||_2^2 \,. && \text{(A.27)}
\end{aligned}$$

Building on the solution of the linear least squares problem (e.g., Aster and Thurber, 2013, Equation 2.3), the solution to the original problem is given by

$$\begin{aligned}
\hat{\vec{\alpha}} &= (\tilde{\mathbb{K}}^{\mathsf{T}}\tilde{\mathbb{K}})^{-1}\tilde{\mathbb{K}}^{\mathsf{T}}\tilde{\boldsymbol{y}} && \text{(A.28)} \\
&= ((\mathbb{Z}^{-1}\mathbb{K})^{\mathsf{T}}\mathbb{Z}^{-1}\mathbb{K})^{-1}(\mathbb{Z}^{-1}\mathbb{K})^{\mathsf{T}}\mathbb{Z}^{-1}\boldsymbol{y} && \text{(A.29)} \\
&= (\mathbb{K}^{\mathsf{T}}\mathbb{S}_y^{-1}\mathbb{K})^{-1}\mathbb{K}^{\mathsf{T}}\mathbb{S}_y^{-1}\boldsymbol{y} && \text{(A.30)} \\
&\equiv \mathbb{G}\boldsymbol{y} \,. && \text{(A.31)}
\end{aligned}$$

The treatment of least-squares optimization allows propagating the measurement error covariance $\mathbb{S}_y$ to the estimate of the parameters $\mathbb{S}_\alpha$:

$$\begin{aligned}
\mathbb{S}_\alpha &= \mathbb{G}\mathbb{S}_y\mathbb{G}^{\mathsf{T}} && \text{(A.32)} \\
&= \cdots && \text{(A.33)} \\
&= (\mathbb{K}^{\mathsf{T}}\mathbb{S}_y^{-1}\mathbb{K})^{-1} \,. && \text{(A.34)}
\end{aligned}$$

Calculating the matrices in Equation (A.30) shows that the presented derivations of the matched filter are consistent. The multiplication of

$$\mathbb{K}^{\mathsf{T}}\mathbb{S}_y^{-1} = \begin{pmatrix} t_{11} & t_{12} & \cdots & 0 & 0 \\ 0 & 0 & \cdots & 0 & 0 \\ \vdots & \vdots & \ddots & \vdots & \vdots \\ 0 & 0 & \cdots & t_{NC-1} & t_{NC} \end{pmatrix} \times \begin{pmatrix} \mathbb{C}^{-1} & 0 & \cdots & 0 \\ 0 & \mathbb{C}^{-1} & \cdots & 0 \\ \vdots & \vdots & \ddots & \vdots \\ 0 & 0 & \cdots & \mathbb{C}^{-1} \end{pmatrix} \tag{A.35}$$

yields a matrix that can be multiplied on a vector of length $N \times C$, e.g., the measurement vector $\boldsymbol{y}$. It will result in a vector of the parameter vector size N that reads

$$\mathbb{K}^\intercal \mathbb{S}_y^{-1} \boldsymbol{y} = \begin{pmatrix} \sum_j^C \sum_i^C t_{1i} \mathbb{C}_{ij}^{-1} (L_{1j} - \mu_j) \\ \sum_j^C \sum_i^C t_{2i} \mathbb{C}_{ij}^{-1} (L_{2j} - \mu_j) \\ \vdots \\ \sum_j^C \sum_i^C t_{Ni} \mathbb{C}_{ij}^{-1} (L_{Nj} - \mu_j) \end{pmatrix} = \begin{pmatrix} \boldsymbol{t}_1^\intercal \mathbb{C}^{-1} \boldsymbol{y}_1 \\ \boldsymbol{t}_2^\intercal \mathbb{C}^{-1} \boldsymbol{y}_2 \\ \vdots \\ \boldsymbol{t}_N^\intercal \mathbb{C}^{-1} \boldsymbol{y}_N \end{pmatrix}, \tag{A.36}$$

where $\boldsymbol{y}_i$ denotes the spectral measurement in pixel i (minus the mean spectral vector) and $\boldsymbol{t}_i$ the corresponding target signature.
Calculating the remaining term of Equation (A.30) in analogy leads to

$$\mathbb{K}^\intercal \mathbb{S}_y^{-1} \mathbb{K} = \begin{pmatrix} \boldsymbol{t}_1^\intercal \mathbb{C}^{-1} \boldsymbol{t}_1 & 0 & \cdots & 0 \\ 0 & \boldsymbol{t}_2^\intercal \mathbb{C}^{-1} \boldsymbol{t}_2 & \cdots & 0 \\ \vdots & \vdots & \ddots & \vdots \\ 0 & \cdots & 0 & \boldsymbol{t}_N^\intercal \mathbb{C}^{-1} \boldsymbol{t}_N \end{pmatrix}, \tag{A.37}$$

which is a diagonal matrix. Thus, it is trivially inverted to

$$(\mathbb{K}^\intercal \mathbb{S}_y^{-1} \mathbb{K})_{ii}^{-1} = (\boldsymbol{t}_i^\intercal \mathbb{C}^{-1} \boldsymbol{t}_i)^{-1}. \tag{A.38}$$

Note that this is the parameter error covariance matrix $\mathbb{S}_\alpha$ as given by Köhler et al. (2015).
Solving the linear least squares problem for $\vec{\alpha}$ leads to

$$\hat{\vec{\alpha}} = \begin{pmatrix} (\boldsymbol{t}_1^\intercal \mathbb{C}^{-1} \boldsymbol{t}_1)^{-1} (\boldsymbol{t}_1^\intercal \mathbb{C}^{-1} \boldsymbol{y}_1) \\ (\boldsymbol{t}_2^\intercal \mathbb{C}^{-1} \boldsymbol{t}_2)^{-1} (\boldsymbol{t}_2^\intercal \mathbb{C}^{-1} \boldsymbol{y}_2) \\ \vdots \\ (\boldsymbol{t}_N^\intercal \mathbb{C}^{-1} \boldsymbol{t}_N)^{-1} (\boldsymbol{t}_N^\intercal \mathbb{C}^{-1} \boldsymbol{y}_N) \end{pmatrix}, \tag{A.39}$$

which is the classic matched filter in each pixel with a pixel-wise unit enhancement spectra.
It may be noted here that the matched filter follows a so-called "unity-gain constrained" in most publications of greenhouse gas imaging. This constraint means a signal strength of one $\boldsymbol{t}$ will give 1 as the output. That is merely a design choice, and many applications of the matched filter provide the signal-to-noise ratio as the result. Thus, the matched filter may read

$$\alpha_i = \frac{(\boldsymbol{L}_i - \boldsymbol{\mu})^\intercal \mathbb{C}^{-1} \boldsymbol{t}}{\sqrt{\boldsymbol{t}^\intercal \mathbb{C}^{-1} \boldsymbol{t}}}, \tag{A.40}$$

in some sources.

The derivation via the normal equation allows a natural introduction of the sparsity constraint. Foote et al. (2020) introduce it as a L0-regularization on the retrieved enhancements. Candès et al. (2008) trace the L0-regularization from

$$\hat{\vec{\alpha}} = \arg\min_{\alpha}\Big(||\tilde{\boldsymbol{y}} - \tilde{\mathbb{K}}\vec{\alpha}||_2^2 + ||\vec{\alpha}||_0\Big) \tag{A.41}$$

back to a L1-regularization

$$\hat{\vec{\alpha}} = \arg\min_{\alpha}\Big(||\tilde{\boldsymbol{y}} - \tilde{\mathbb{K}}\vec{\alpha}||_2^2 + ||\mathbb{L}\vec{\alpha}||_1\Big) \tag{A.42}$$

with updating weights $\mathbb{L}$. The matrix entries have the form $\mathrm{L}_{ii} = \alpha_{i,m-1}^{-1}$, where m is the number of iterations. Aster and Thurber (2013, Chapter 7) provides several algorithms to solve a L1-regularized least-squares problem. Choosing the Iterative Reweighted Least Squares (IRLS) algorithm leads to

$$\hat{\vec{\alpha}} = \arg\min_{\alpha}\Big(||\tilde{\boldsymbol{y}} - \tilde{\mathbb{K}}\vec{\alpha}||_2^2 + \beta||\mathbb{L}\vec{\alpha}||_1\Big) \tag{A.43}$$

with the regularization parameter β. Following the derivation in the book and using the positivity constraint on α, the solution to the constrained problem is given by

$$F(\vec{\alpha}) = ||\tilde{\mathbb{K}}\vec{\alpha} - \tilde{\boldsymbol{y}}||_2^2 + \beta||\mathbb{L}\vec{\alpha}||_1 \tag{A.44}$$

$$\nabla_\alpha F(\vec{\alpha}) = 2\tilde{\mathbb{K}}^\intercal\tilde{\mathbb{K}}\vec{\alpha} - 2\tilde{\mathbb{K}}^\intercal\tilde{\boldsymbol{y}} + \beta\vec{\nabla}_\alpha\sum_{i,j}^{N}|\mathbb{L}_{ij}\alpha_j| \qquad \mathbb{L}\text{ diagonal} \tag{A.45}$$

$$0 = 2\tilde{\mathbb{K}}^\intercal\tilde{\mathbb{K}}\vec{\alpha} - 2\tilde{\mathbb{K}}^\intercal\tilde{\boldsymbol{y}} + \beta\vec{\nabla}_\alpha\sum_{i}^{N}|\mathbb{L}_{ii}\alpha_i| \qquad \alpha\text{ positive} \tag{A.46}$$

$$0 = 2\tilde{\mathbb{K}}^\intercal\tilde{\mathbb{K}}\vec{\alpha} - 2\tilde{\mathbb{K}}^\intercal\tilde{\boldsymbol{y}} + \beta\vec{\nabla}_\alpha\sum_{i}^{N}\mathbb{L}_{ii}\alpha_i \tag{A.47}$$

$$0 = 2\tilde{\mathbb{K}}^\intercal\tilde{\mathbb{K}}\vec{\alpha} - 2\tilde{\mathbb{K}}^\intercal\tilde{\boldsymbol{y}} + \beta\mathrm{diag}^{-1}(\mathbb{L}) \tag{A.48}$$

$$\Rightarrow \hat{\vec{\alpha}} = (\tilde{\mathbb{K}}^\intercal\tilde{\mathbb{K}})^{-1}(\tilde{\mathbb{K}}^\intercal\tilde{\boldsymbol{y}} - \frac{\beta}{2}\mathrm{diag}^{-1}(\mathbb{L}))\,, \tag{A.49}$$

where $\mathrm{diag}^{-1}(\mathbb{L})$ is the N-dimensional vector consisting of the diagonal entries of $\mathbb{L}$. This is in agreement with the results of Foote et al. (2020) for $\beta = 2$. Since $\mathbb{L}$ depends on $\vec{\alpha}$, again an iterative solution is required. The initialization step computes $\vec{\alpha}$ based on the classic matched filter. Subsequently, $\mathbb{L}$ and α are updated iteratively until convergence. The MAG1C algorithm exploits the iterative solution by simultaneously optimizing $\boldsymbol{\mu}$ and $\mathbb{C}$.

A.2.2 Combo Matched Filter

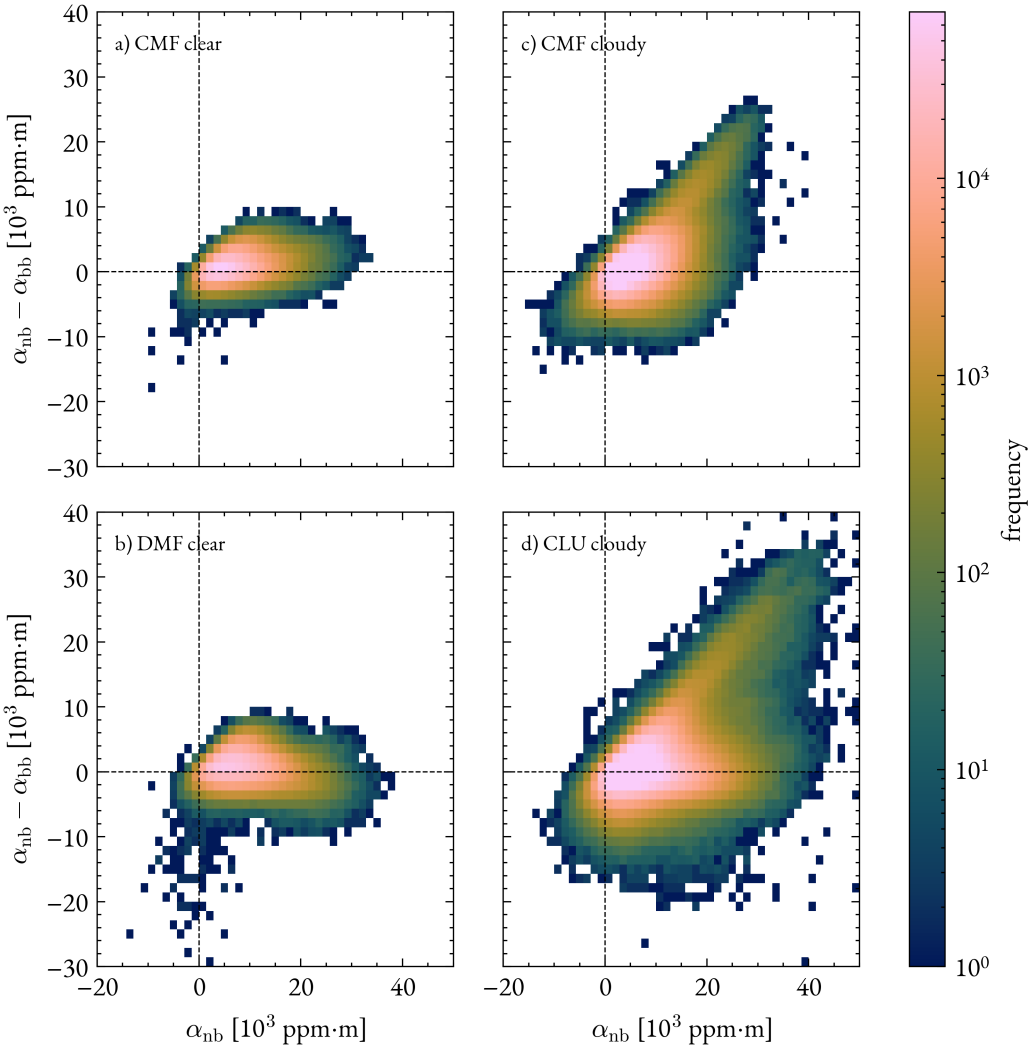

Figure A.3: Comparison of the narrowband and broadband enhancements of the CoMF for all pixels inside the plume mask. The data is taken from a clear (June 19, 2022, panels a+b) and a cloudy (June 13, 2023, panels c+d) measurement day. With increasing enhancements, the broadband enhancement is systematically biased low against the narrowband enhancement in cloudy cases. The bias is insignificant for clear sky conditions. This behavior is consistent for the CMF and DMF retrievals and also reported in Roger et al. (2023b).

A.2.3 Methane UAS

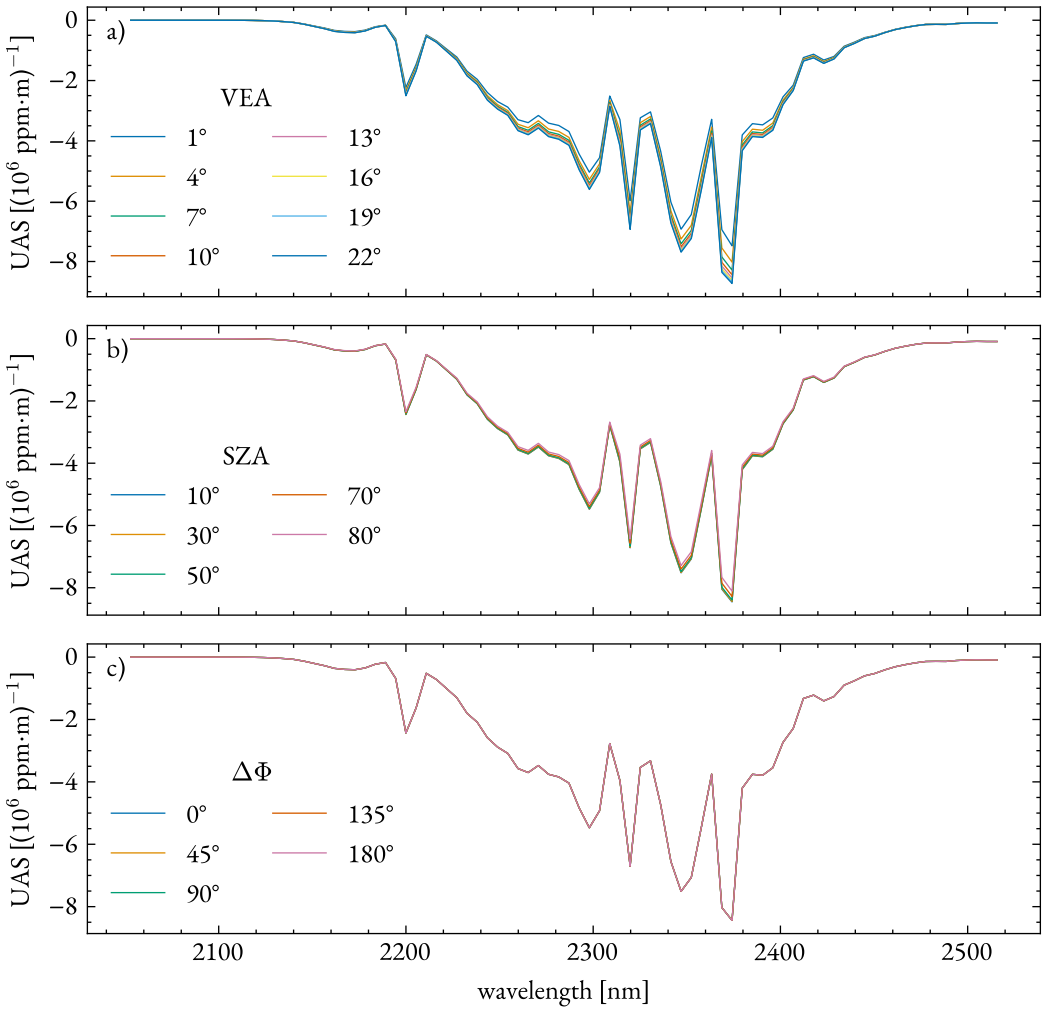

Figure A.4: Unit absorption spectra of methane from 2050 nm to 2525 nm. Panels a) to c) show the dependency on the viewing geometry. While one observation angle varies, the other two are fixed to SZA = 30°, VEA = 10°, and $\Delta\Phi$ = 180°.

A.3 Appendix to Methane Chapter

A.3.1 The Péclet Number

The Péclet number is a dimensionless number used in transport phenomena. It follows, similar to the Reynolds number, from a dimensional analysis of the transport equation (Brasseur and Jacob, 2017). The continuity equation (without sources) for a scalar quantity c and its flux $\vec{j}$ reads

$$\frac{\partial c}{\partial t} + \nabla \vec{j} = 0\,. \tag{A.50}$$

The advection-diffusion equation follows from the flux being the sum of an advective and a diffusive term

$$\vec{j} = \vec{v}c - D\nabla c\,, \tag{A.51}$$

where $\vec{v}$ is the advection velocity and D is the diffusion coefficient. Thus, the continuity equation becomes

$$\frac{\partial c}{\partial t} + \nabla(\vec{v}\cdot c) - D\nabla^2 c = 0\,. \tag{A.52}$$

The dimensionless form of Equation (A.52) transforms each term to dimensionless numbers using characteristic values for each quantity. The Péclet number is defined as the ratio of the advective to the diffusive term

$$\mathrm{Pe} = \frac{\nabla(\vec{v}\cdot c)}{D\nabla^2 c} = \frac{u/L}{D/L^2} = \frac{uL}{D}\,, \tag{A.53}$$

where L is a characteristic length scale and u a characteristic velocity. Figure A.5 illustrates the temporal evolution of a scalar quantity c in a one-dimensional domain.

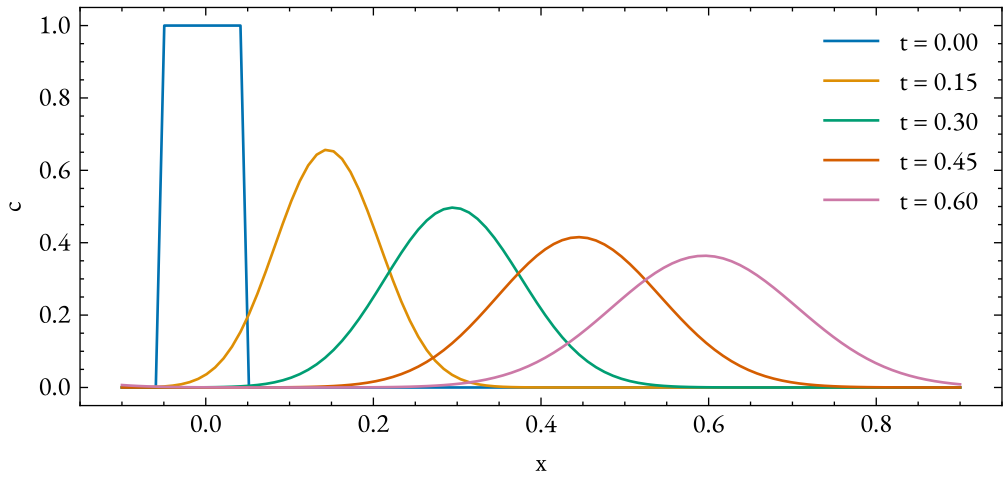

Figure A.5: Illustration of the advection-diffusion equation. The temporal evolution of a scalar quantity c is determined by an advection of $u = 1$ and a diffusion of $D = 0.01$.

A.3.2 Plume Masking in Single Scans

The correct masking and subsequent identification of emission plumes in images is ongoing research. Especially fully automated algorithms are under investigation since they are required to deal with the amount of data provided by satellites every day. Typical challenges are false positives in the enhancement maps, mostly due to scene heterogeneity, and disconnected plume fragments. The latter may appear due to turbulent transport, which either dilutes a plume part below the detection limit or disconnects a plume part completely.

Identifying the plume in the ground-based HySpex observations from the CoMF masking requires the separation of above-threshold patches into false positives and true plume signal. Be P_{jk} the mask in each pixel jk, with $P = 1$ above the threshold and $P = 0$ else. The algorithm used for both scanning and fixed geometry images in Chapter 5 follows several steps:

1. Sum P over all frames to gain the number of patch-pixels in each line.
2. Cluster consecutive lines with non-zero values, i.e., identify which connected lines contain potential plume pixels.
3. The plume is assigned to the cluster of lines with the highest density of patch-pixels.

Furthermore, patches upwind of the plume are excluded in the scanning geometry. This approach was found by testing different methods, and performs well in both the scanning and fixed geometry. Visual inspection suggests that nearly all plumes are identified correctly in the presented data. However, improvements are under way to consolidate the plume identification procedure. In the scanning geometry, choosing the patch closest to the known source location is a physically meaningful initial guess. The fixed geometry exhibits a tube of enhancements meandering through the single observations, such that connecting subsequent scans is a promising approach.

A.3.3 Time Series

Table A.1: The total number of performed scans at each observation day. The number of scans that passed the quality control is given in the second column, and the removed fraction [%] is in the third column. The following columns give the number of scans removed due to the different quality control criteria. These are the vicinity to the shaft, the downwind mass ratio, the plume travel direction, and the plume size (Section 5.2). Note that multiple criteria may flag a single scan, so the numbers do not necessarily add up.

Date	Scans	Passed	Removed	Vicinity	Ratio	Direction	Size
2022-06-17	317	247	22.1	38	44	14	7
2022-06-18	522	293	43.9	22	100	149	0
2022-06-19	555	457	17.7	16	27	4	4
2022-06-20	286	160	44.1	0	61	103	0
2023-06-08	290	275	5.2	0	0	0	0
2023-06-11	338	315	6.8	21	2	1	2
2023-06-12	449	436	2.9	7	2	2	0
2023-06-13	484	477	1.4	4	1	4	0

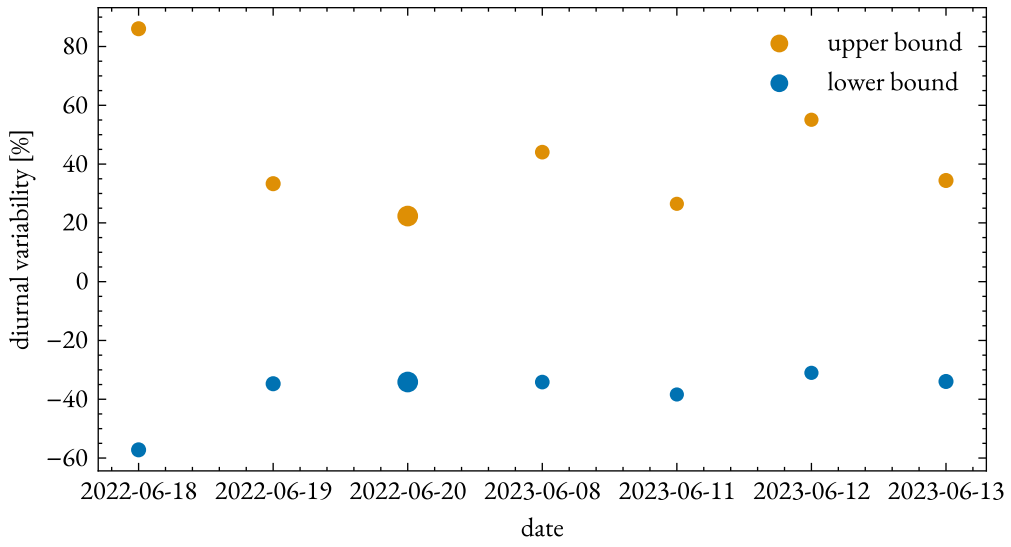

Figure A.6: Diurnal variability of the methane emissions from coal mine ventilation shafts during seven observation days. The change of the methane emissions is shown relative to the daily mean emissions, with the lower bound (blue) and the upper bound (orange) marker size proportional to the mean emissions.

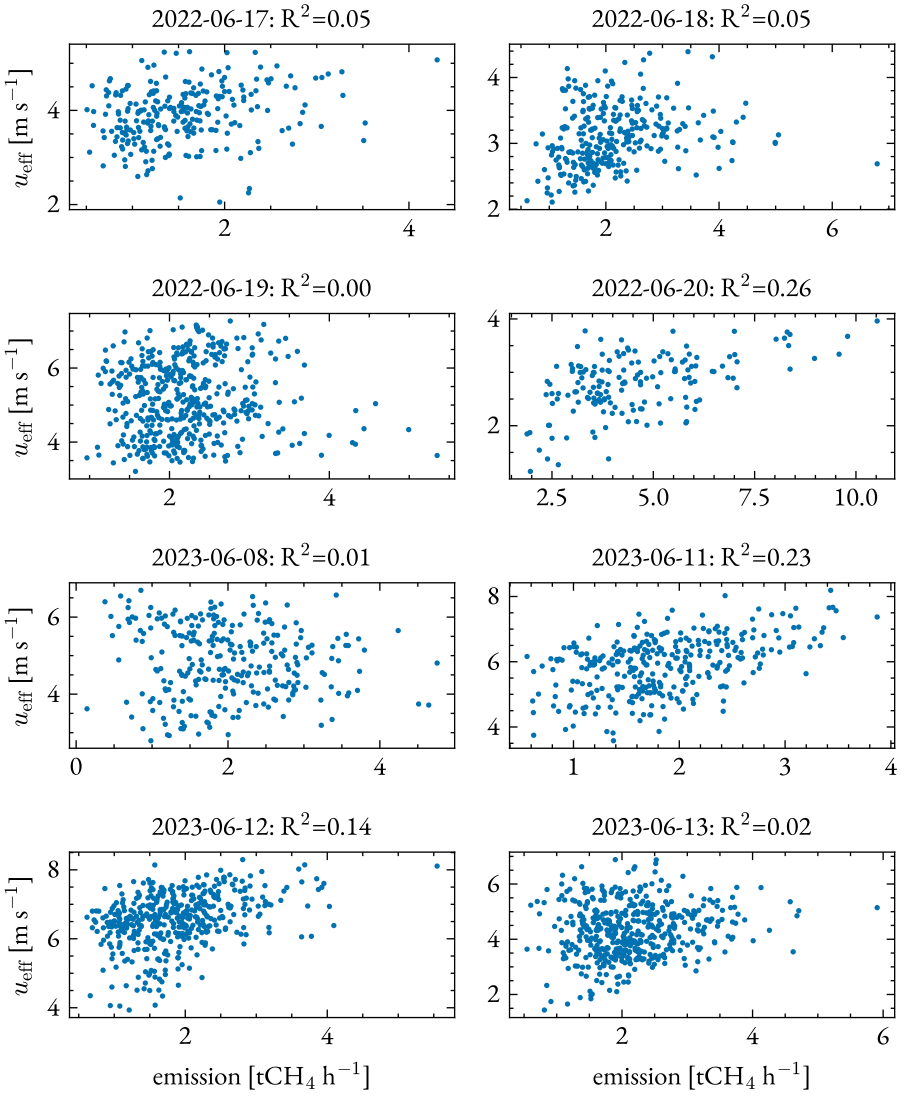

Figure A.7: Correlation of the methane emissions from coal mine ventilation shafts with the effective wind speed for each observation day. The Pearson correlation coefficient R^2 is given for each day.

Table A.2: For every experiment performed in the USCB campaigns, the effective plume speed u_{eff} [m s^{-1}] and the scan speed v_{scan} [m s^{-1}] are given. A scan speed of 0 m s^{-1} denotes a fixed viewing geometry experiment. These are used to calculate the factor $r = \left(1 - \frac{u_{\mathrm{eff}}}{v_{\mathrm{scan}}}\right)$, which determines the observed plume length d_{obs} [m] from the plume length in the image $d_{\mathrm{im,c}}$ [m]. The turbulent mixing length d_{turb} [m] is estimated from the Péclet Number $\mathrm{Pe} = 100$ and the diffusion coefficient K. Given a conservative estimate of $d_{\mathrm{turb}} = 3000$ m, the number of scans required to observe a plume of sufficient length is given by η.

Date: Experiment	v_{scan}	u_{eff}	r	d_{im}	$d_{\mathrm{im,c}}$	d_{obs}	d_{Pe}	η
2022-06-17: 1	3.6	3.9	-0.10	110	133	13	263	232
2022-06-18: 1	3.3	-3.2	1.98	119	210	417	318	7
2022-06-18: 2	3.3	-3.2	1.98	119	210	417	318	7
2022-06-19: 2	3.6	-4.9	2.35	93	110	260	210	12
2022-06-19: 4	3.4	-5.5	2.59	104	116	302	191	10
2022-06-20: 1	3.6	-2.7	1.77	98	106	187	370	16
2023-06-08: 3	10.3	4.2	0.59	223	231	137	242	22
2023-06-08: 4	0	4.5	-	-	-	153	-	20
2023-06-08: 6	0	5.7	-	-	-	196	-	15
2023-06-08: 9	6.2	5.0	0.18	222	226	41	199	73
2023-06-08: 10	7.4	4.5	0.39	221	222	88	225	34
2023-06-11: 1	9.8	6.3	0.35	240	243	86	160	35
2023-06-11: 2	9.3	6.7	0.28	222	224	64	150	47
2023-06-11: 4	9.3	5.6	0.40	242	246	99	182	30
2023-06-11: 5	9.3	5.8	0.38	241	245	93	179	32
2023-06-11: 7	7.7	5.9	0.23	240	248	57	172	52
2023-06-12: 1	7.7	6.5	0.16	240	242	40	156	76
2023-06-12: 2	9.3	6.6	0.29	240	242	69	152	43
2023-06-12: 3	9.3	7.1	0.24	237	239	58	142	52
2023-06-12: 4	0	6.7	-	-	-	249	-	12
2023-06-12: 6	7.1	5.3	0.25	233	242	62	192	49
2023-06-13: 1	7.1	3.0	0.57	241	269	154	347	20
2023-06-13: 2	9.3	4.3	0.54	242	260	140	244	21
2023-06-13: 3	7.1	5.4	0.25	242	253	62	190	48

A.4 Appendix to Carbon Dioxide Chapter

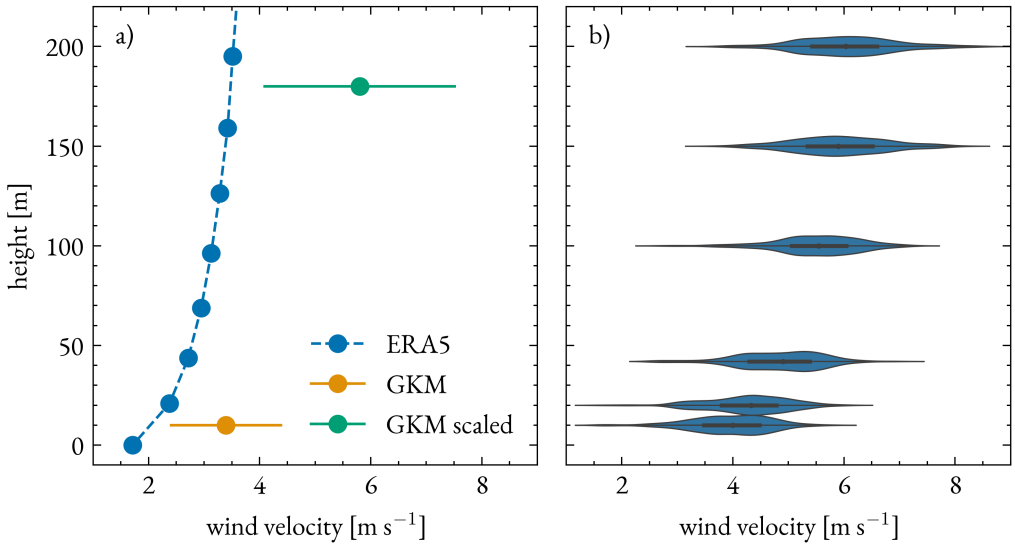

Figure A.8: Panel a) shows wind data from GKM measured at 10 m height on September 8th, 2021 (orange). The wind profile is taken from ERA5 and interpolated to the stack location in space and time (blue). The wind speed is scaled according to the profile to 180 m (green), the stack tip height of unit 9. Panel b) shows the vertically measured wind profile from the Windranger 200 on May 26, 2022. The distributions are the 2 min rolling mean values of the wind speeds during the time of observation. Image and caption as in Knapp et al. (2023b).

Table A.3: The table lists the GKM yearly electricity production [TW h] from their annual reports and reported carbon dioxide emissions [MtCO_2] from the E-PRTR. The power plant emits 955 gCO_2 kWh^{-1} on average.

Year	2015	2016	2017	2018	2019	2020	2021
Electric Power	7.779	8.633	7.363	7.185	4.974	4.158	5.167
CO_2 Emissions	7.32	7.88	6.86	6.74	4.92	4.18	5.00

Table A.4: Each day on which the camera observed the GKM chimneys. Columns one to three list the date, observed unit, and location of the camera. Bold dates mark the days that have been processed beyond the retrieval since they show either favorable conditions or illustrate the methods limitations. The abbreviations BR and KW denote Backofen-Riedwiesen and Kiefweiher, respectively. The next three columns list the camera settings of the observations, i.e., the exposure time t_{exp}, the number of co-additions HSNR, and the azimuth scan length ΔVAA. Column 7 lists the time t_{scan} it took to complete a full azimuth scan. The last column gives a short description of the measurement conditions.

Date	Target	Loc.	t_{exp} [ms]	HSNR	ΔVAA [°]	t_{scan} [s]	Measurement conditions
2021-04-28	Unit 8	BR	24.8	8	6	65	Clear sky, plume travels at an acute observation angle
2021-08-25	Unit 9	BR	10.8	8	11	70	Clouds appear shortly after beginning of observations
2021-09-06	Unit 9	BR	14.8	8	10	75	Low wind speeds cause plume to rise vertically
2021-09-08	Unit 9	BR	14.8	8	6	49	Clear sky, favorable winds
2022-03-23	Unit 9	KW	14.8	8	10	77	Plume condensation, acute observation angle
2022-03-24	Unit 9	KW	9.8	5	7.5	45	Plume condensation, high aerosol load, visually homogeneous but heterogeneity in observations
2022-03-26	Unit 9	BR	9.8	5	7	43	Plume condensation vanishes during observation period, high aerosol load, favorable wind
2022-03-28	Unit 9	KW	11.8	8	6	46	Plume condensation, high aerosol load, low wind speed
2022-04-20	Unit 6	BR	11.8	8	6.6	48	Plume condensation, clear sky, low ambient temperature (16 °C)
2022-05-13	Unit 6	BR	9.8	10	8.5	57	Clouds in image background, favorable wind
2023-05-03	Unit 9	KW	12	8	22	85	Clouds in image background, low GKM emissions
2023-07-07	Unit 9	BR	13.8	5	10	53	Clear sky, low winds, low GKM emissions

Table A.5: Collection of all *a priori* information as presented in Knapp et al. (2023b). Errors are given as the standard deviation of the quantity during the average time period of the measurement. The subscript a denotes ambient conditions, e denotes the initial plume conditions, and c_0 denotes the CO_2 concentration above the chimney.

Date and time	p_a [hPa]	T_a [°C]	RH_a [%]	u_a [m s^{-1}]	ϕ [°]	T_e [°C]	u_e [m/s]	c_0 [g m^{-3}]
2021-09-08 12:13-13:15	1016.5 ± 0.1	25.9 ± 0.3	45.5 ± 2.0	7.1 ± 2.2[a]	-53 ± 11[a]	63.1 ± 0.2	13.4 ± 0.1	188 ± 2
2021-09-08 13:17-14:23	1016.2 ± 0.5	26.8 ± 0.3	40.3 ± 0.9	8.1 ± 1.6[a]	-53 ± 11[a]	62.9 ± 0.3	13.4 ± 0.1	188 ± 2
2021-09-08 14:24-15:26	1015.3 ± 0.2	27.6 ± 0.2	38.3 ± 0.6	7.6 ± 1.7[a]	-51 ± 18[a]	63.1 ± 0.1	13.4 ± 0.1	188 ± 2
2021-09-08 15:27-16:35	1014.4 ± 0.2	27.9 ± 0.1	38.1 ± 0.5	7.8 ± 2.1[a]	-53 ± 12[a]	63.0 ± 0.2	13.3 ± 0.1	192 ± 2
2022-03-23 14:51-16:13	1029.4 ± 0.3	20.0 ± 0.2	25.5 ± 0.1	5.1 ± 0.9[b]	33 ± 30[b]	60.6 ± 0.1	12.5 ± 0.1	201 ± 2
2022-03-23 16:14-17:36	1028.7 ± 0.1	19.7 ± 0.2	25.1 ± 0.1	3.7 ± 0.9[b]	33 ± 25[b]	60.6 ± 0.1	12.4 ± 0.1	204 ± 2
2022-03-26 14:44-15:55	1028.2 ± 0.2	20.1 ± 0.1	28.7 ± 0.1	5.6 ± 0.8[b]	-97 ± 24[b]	61.0 ± 0.3	7.4 ± 0.4	131 ± 12
2022-03-26 15:56-17:36	1027.7 ± 0.0	19.9 ± 0.2	28.7 ± 0.3	6.0 ± 0.7[b]	-109 ± 23[b]	59.3 ± 0.2	11.1 ± 1.8	179 ± 55
2022-03-28 15:35-16:28	1019.9 ± 0.3	22.6 ± 0.2	33.4 ± 0.2	2.9 ± 0.7[b]	-60 ± 34[b]	59.0 ± 0.5	11.3 ± 0.5	185 ± 13
2022-05-13 12:21-14:01	1020.2 ± 0.1	25.4 ± 0.3	34.2 ± 1.5	5.4 ± 0.8[b]	72 ± 44[b]	62.3 ± 0.7	12.1 ± 0.1	427 ± 53
2022-05-13 14:02-15:39	1020.0 ± 0.1	25.3 ± 0.3	32.5 ± 0.4	5.6 ± 0.9[b]	80 ± 37[b]	61.9 ± 0.3	12.8 ± 1.1	259 ± 70

[a] from ERA5 scaling of the GKM 10 m wind field.
[b] from LIDAR observation

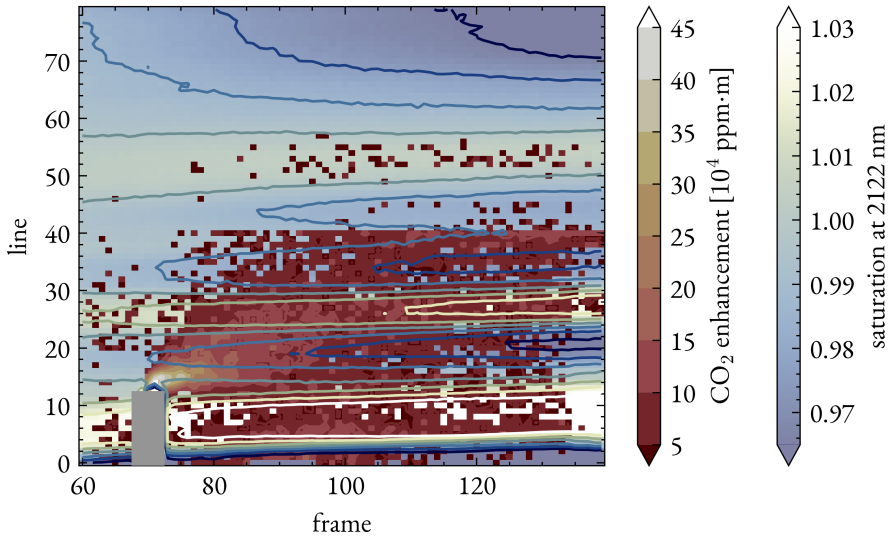

Figure A.9: Plume observation on May 13, 2022, between 12:21 and 14:01 UTC. The CO_2 enhancements (red to yellow) show a distinct plume. However, the saturation of the spectral vectors (blue to white, both background and contour lines) is not uniform, but shows some horizontal stripes. The saturation at 2122 nm is chosen as a transparent channel close to the CO_2 absorption. The plume observation correlates with these patterns, especially below and above the plume. Thus, the Gaussian plume model is not able to reproduce the observation correctly.

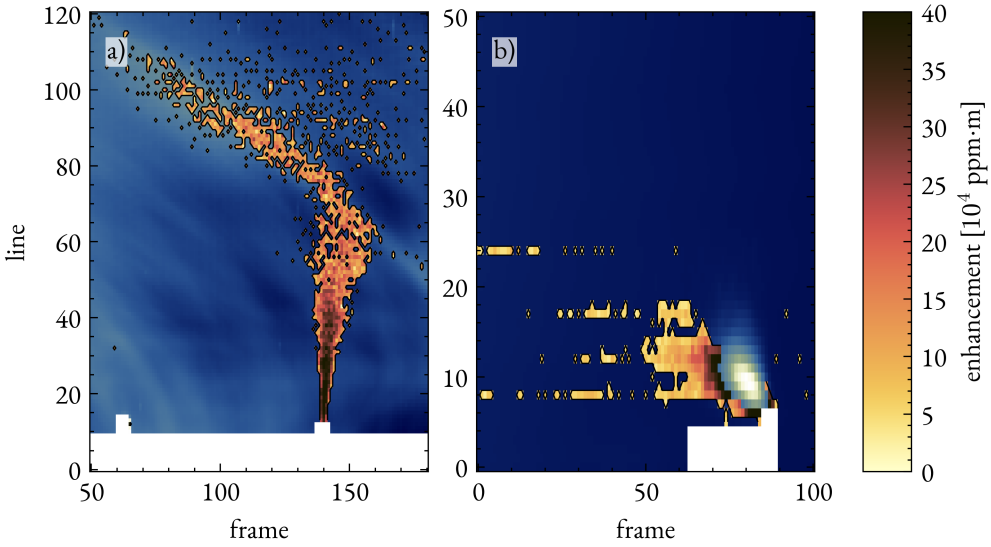

Figure A.10: Example of two plumes detected under conditions which prevent an emission estimation. Pixel saturation is shown in blue to white, enhancements in yellow to red. Panel a) shows a plume with unfavorable wind conditions, and some background correlated enhancements above and left of the plume. Panel b) shows a plume where most CO_2 is missing due to the condensation mask, and there is residual striping in the DMF retrieval. The plumes have been observed on September 6, 2021, and March 24, 2022, respectively.

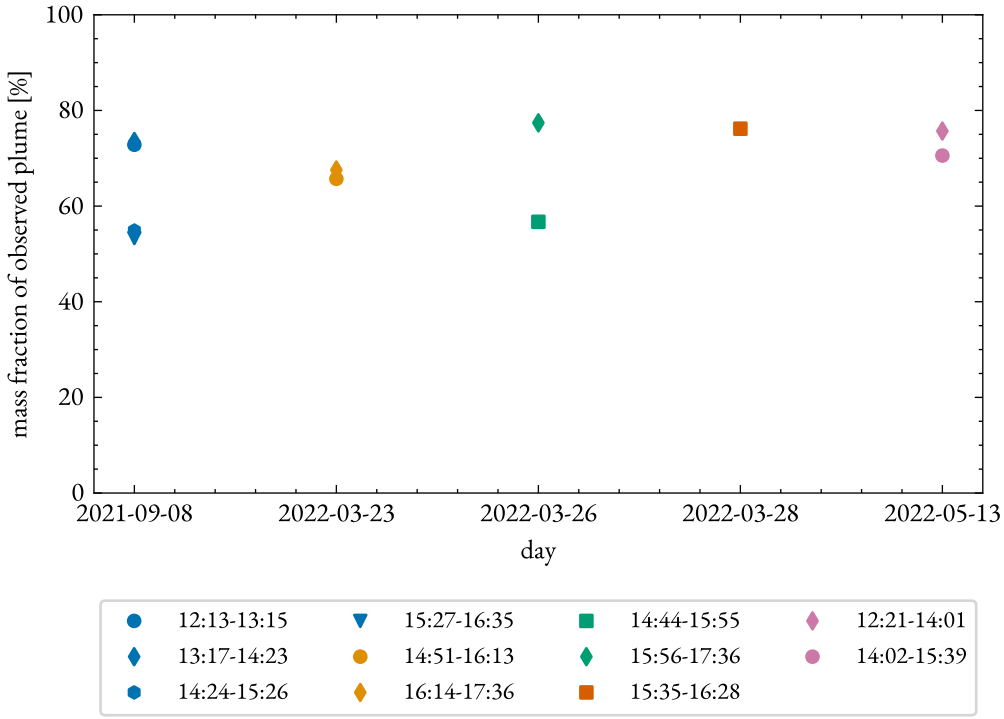

Figure A.11: The fraction of the observed plume mass divided by the simulated plume mass for each observation. The observed plume mass is the sum of all observed enhancements within the observation plume mask. The simulated plume mass is the sum of all modelled enhancements between the first and the last frame in which the plume is observed.

Glossary

ADC	Analog-to-digital converter
AERONET	AErosol RObotic NETwork
AHRS	Attitude and heading reference system
AOD	Aerosol optical depth
ASR	At-sensor radiance
AVIRIS	Airborne Visible/Infrared Imaging Spectrometer
BPM	Bad pixel mask
CAMS	Copernicus Atmosphere Monitoring Service
CLU	clustered differential matched filter
CMF	Classic matched filter
CO2M	CO2 Monitor
COCCON	COllaborative Carbon Column Observing Network
COMET	Carbon Dioxide and Methane
CoMF	Combo matched filter
DMF	Differential matched filter
DOAS	Differential optical absorption spectroscopy
E-PRTR	European Pollutant Release and Transfer Register
EnMAP	Environmental Mapping and Analysis Program
FOV	Field of view
FTIR	Fourier transform infrared
FWHM	Full width at half maximum
GHG	Greenhouse gas
GHGSat	Greenhouse Gas Satellite
GKM	Grosskraftwerk Mannheim
GOSAT	Greenhouse gases Observing SATellite
GPS	Global Positioning System
HITRAN	HIgh-resolution TRANsmission molecular absorption database
ILS	Instrument line shape
IMAP-DOAS	Iterative Maximum A Posteriori Differential Optical Absorption Spectroscopy
IME	Integrated mass enhancement
IMEO	International Methane Emissions Observatory
INS	Inertial navigation system
IPCC	Intergovernmental Panel on Climate Change
IRLS	Iteratively re-weighted least squares
ISE	Fraunhofer-Institut für Solare Energiesysteme

IUP	Institut für Umweltphysik
LIDAR	Light detection and ranging
LUT	Look-up table
MAG1C	Matched filter with Albedo correction and reweiGhted L1 sparsity Code
MAMAP	Methane Airborne MAPper
MCT	Mercury cadmium telluride
MVS	Monitoring and Verification Support
NASA	National Aeronautics and Space Administration
NEE	Noise equivalent enhancement
NEO	Norsk Elektro Optikk
NIR	Near infrared
OCO-2	Orbiting Carbon Observatory 2
OCO-3	Orbiting Carbon Observatory 3
OGI	Optical gas imaging
PRISMA	PRecursore IperSpettrale della Missione Applicativa
PSF	Point spread function
RMSE	Root mean square error
RTE	Radiative transfer equation
SAA	Solar azimuth angle
Sentinel-5P	Sentinel-5 Precursor
SNR	Signal-to-noise ratio
SSD	Spectral sampling distance
SWIR	Shortwave infrared
SZA	Solar zenith angle
TCCON	Total Carbon Column Observing Network
TDLAS	Tunable diode laser absorption spectroscopy
TIR	Thermal infrared
TROPOMI	TROPOspheric Monitoring Instrument
UAS	Unit absorption spectrum
UBA	Umweltbundesamt
UNEP	United Nations Environment Programme
UNFCCC	United Nations Framework Convention on Climate Change
USCB	Upper Silesian Coal Basin
UV	Ultraviolet
VAA	Viewing azimuth angle
VEA	Viewing elevation angle
VIS	Visible
VZA	Viewing zenith angle
XSF	Cross-sectional flux

Bibliography

Adler, B., A. Gohm, N. Kalthoff, N. Babić, U. Corsmeier, M. Lehner, M. W. Rotach, M. Haid, P. Markmann, E. Gast, G. Tsaknakis, and G. Georgoussis (2021). "CROSSINN: A Field Experiment to Study the Three-Dimensional Flow Structure in the Inn Valley, Austria". *Bulletin of the American Meteorological Society*. ISSN: 0003-0007, 1520-0477. DOI: 10.1175/BAMS-D-19-0283.1. URL: https://journals.ametsoc.org/view/journals/bams/102/1/BAMS-D-19-0283.1.xml (visited on 06/30/2022).

Andersen, T., K. Vinkovic, M. de Vries, B. Kers, J. Necki, J. Swolkien, A. Roiger, W. Peters, and H. Chen (2021). "Quantifying Methane Emissions from Coal Mining Ventilation Shafts Using an Unmanned Aerial Vehicle (UAV)-Based Active AirCore System". *Atmospheric Environment: X*. ISSN: 25901621. DOI: 10.1016/j.aeaoa.2021.100135. URL: https://linkinghub.elsevier.com/retrieve/pii/S2590162121000356 (visited on 05/28/2022).

Andersen, T., Z. Zhao, M. De Vries, J. Necki, J. Swolkien, M. Menoud, T. Röckmann, A. Roiger, A. Fix, W. Peters, and H. Chen (2023). "Local-to-Regional Methane Emissions from the Upper Silesian Coal Basin (USCB) Quantified Using UAV-based Atmospheric Measurements". *Atmospheric Chemistry and Physics*. ISSN: 1680-7324. DOI: 10.5194/acp-23-5191-2023. URL: https://acp.copernicus.org/articles/23/5191/2023/ (visited on 11/24/2023).

Anderson, G., S. Clough, F. Kneizys, J. Chetwyd, and E. Shettle (1986). *AFGL Atmospheric Constituent Profiles (0–120 Km). Air Force Geophysics Laboratory Tech. Rep*. AFGL-TR-86-0110.

Aster, R. C. and C. H. Thurber (2013). *Parameter Estimation and Inverse Problems*. 2nd ed. Academic Press, Waltham, MA. 360 pp. ISBN: 978-0-12-385048-5.

Ayasse, A. K., A. K. Thorpe, D. H. Cusworth, E. A. Kort, A. G. Negron, J. Heckler, G. Asner, and R. M. Duren (2022). "Methane Remote Sensing and Emission Quantification of Offshore Shallow Water Oil and Gas Platforms in the Gulf of Mexico". *Environmental Research Letters*. ISSN: 1748-9326. DOI: 10.1088/1748-9326/ac8566. URL: https://iopscience.iop.org/article/10.1088/1748-9326/ac8566 (visited on 11/07/2023).

Ayasse, A. K., D. Cusworth, K. O'Neill, J. Fisk, A. K. Thorpe, and R. Duren (2023). "Performance and Sensitivity of Column-Wise and Pixel-Wise Methane Retrievals for Imaging Spectrometers". *Atmospheric Measurement Techniques*. ISSN: 1867-8548. DOI: 10.5194/amt-16-6065-2023. URL: https://amt.copernicus.org/articles/16/6065/2023/.

Ayasse, A. K., A. K. Thorpe, D. A. Roberts, C. C. Funk, P. E. Dennison, C. Frankenberg, A. Steffke, and A. D. Aubrey (2018). "Evaluating the Effects of Surface Properties on Methane Retrievals Using a Synthetic Airborne Visible/Infrared Imaging Spectrometer next Generation (AVIRIS-NG) Image". *Remote Sensing of Environment*. ISSN: 00344257. DOI: 10.1016/j.rse.2018.06.018. URL: https://linkinghub.elsevier.com/retrieve/pii/S0034425718302967 (visited on 05/17/2022).

Bastviken, D., J. Wilk, N. T. Duc, M. Gålfalk, M. Karlson, T.-S. Neset, T. Opach, A. Enrich-Prast, and I. Sundgren (2022). "Critical Method Needs in Measuring Greenhouse Gas Fluxes". *En-*

vironmental Research Letters. ISSN: 1748-9326. DOI: 10.1088/1748-9326/ac8fa9. URL: https://iopscience.iop.org/article/10.1088/1748-9326/ac8fa9 (visited on 01/30/2023).

Basu, S., S. Guerlet, A. Butz, S. Houweling, O. Hasekamp, I. Aben, P. Krummel, P. Steele, R. Langenfelds, M. Torn, S. Biraud, B. Stephens, A. Andrews, and D. Worthy (2013). "Global CO $_2$ Fluxes Estimated from GOSAT Retrievals of Total Column CO $_2$". *Atmospheric Chemistry and Physics*. ISSN: 1680-7324. DOI: 10.5194/acp-13-8695-2013. URL: https://www.atmos-chem-phys.net/13/8695/2013/ (visited on 04/28/2020).

Baumgartner, A. (2022). "Traceable Imaging Spectrometer Calibration and Transformation of Geometric and Spectral Pixel Properties". In collab. with U. Osnabrück, U. Osnabrück, and P. D. P. Reinartz. DOI: 10.48693/38. URL: https://osnadocs.ub.uni-osnabrueck.de/handle/ds-202202076056 (visited on 11/03/2022).

Baumgartner, A., P. Gege, C. Köhler, K. Lenhard, and T. Schwarzmaier (2012). "Characterisation Methods for the Hyperspectral Sensor HySpex at DLR's Calibration Home Base". In: SPIE Remote Sensing. Ed. by R. Meynart, S. P. Neeck, and H. Shimoda. Edinburgh, United Kingdom. DOI: 10.1117/12.974664. URL: http://proceedings.spiedigitallibrary.org/proceeding.aspx?doi=10.1117/12.974664 (visited on 12/17/2019).

Bauwens, M., S. Compernolle, T. Stavrakou, J.-F. Müller, J. Van Gent, H. Eskes, P. F. Levelt, R. Van Der A, J. P. Veefkind, J. Vlietinck, H. Yu, and C. Zehner (2020). "Impact of Coronavirus Outbreak on NO $_2$ Pollution Assessed Using TROPOMI and OMI Observations". *Geophysical Research Letters*. ISSN: 0094-8276, 1944-8007. DOI: 10.1029/2020GL087978. URL: https://agupubs.onlinelibrary.wiley.com/doi/10.1029/2020GL087978 (visited on 01/02/2024).

Beirle, S., J. Lampel, C. Lerot, H. Sihler, and T. Wagner (2017). "Parameterizing the Instrumental Spectral Response Function and Its Changes by a Super-Gaussian and Its Derivatives". *Atmospheric Measurement Techniques*. ISSN: 1867-8548. DOI: 10.5194/amt-10-581-2017. URL: https://amt.copernicus.org/articles/10/581/2017/ (visited on 10/18/2023).

Bell, E., C. W. O'Dell, T. E. Taylor, A. Merrelli, R. R. Nelson, M. Kiel, A. Eldering, R. Rosenberg, and B. Fisher (2023). "Exploring Bias in the OCO-3 Snapshot Area Mapping Mode via Geometry, Surface, and Aerosol Effects". *Atmospheric Measurement Techniques*. ISSN: 1867-8548. DOI: 10.5194/amt-16-109-2023. URL: https://amt.copernicus.org/articles/16/109/2023/ (visited on 01/02/2024).

Berg, M., C. Sorensen, and A. Chakrabarti (2011). "A New Explanation of the Extinction Paradox". *Journal of Quantitative Spectroscopy and Radiative Transfer*. ISSN: 00224073. DOI: 10.1016/j.jqsrt.2010.08.024. URL: https://linkinghub.elsevier.com/retrieve/pii/S0022407310003420 (visited on 07/21/2020).

Berk, A., P. Conforti, R. Kennett, T. Perkins, F. Hawes, and J. Van Den Bosch (2014). "MODTRAN6: A Major Upgrade of the MODTRAN Radiative Transfer Code". In: SPIE Defense + Security. Ed. by M. Velez-Reyes and F. A. Kruse. Baltimore, Maryland, USA. DOI: 10.1117/12.2050433. URL: http://proceedings.spiedigitallibrary.org/proceeding.aspx?doi=10.1117/12.2050433 (visited on 10/27/2023).

Bevington, P. R., D. K. Robinson, J. M. Blair, A. J. Mallinckrodt, and S. McKay (1993). "Data Reduction and Error Analysis for the Physical Sciences". *Computers in Physics*. ISSN: 08941866. DOI: 10.1063/1.4823194. URL: https://pubs.aip.org/aip/cip/article/7/4/415-416/137145 (visited on 06/10/2023).

Bhardwaj, P., R. Kumar, D. A. Mitchell, C. A. Randles, N. Downey, D. Blewitt, and B. Kosovic (2022). "Evaluating the Detectability of Methane Point Sources from Satellite Observing Systems Using Microscale Modeling". *Scientific Reports*. ISSN: 2045-2322. DOI: 10.1038/s41598-022-20567-z. URL: https://www.nature.com/articles/s41598-022-20567-z (visited on 10/27/2022).

Borchardt, J., K. Gerilowski, S. Krautwurst, H. Bovensmann, A. K. Thorpe, D. R. Thompson, C. Frankenberg, C. E. Miller, R. M. Duren, and J. P. Burrows (2021). "Detection and Quantification of CH4 Plumes Using the WFM-DOAS Retrieval on AVIRIS-NG Hyperspectral Data". *Atmospheric Measurement Techniques*. ISSN: 1867-8548. DOI: 10.5194/amt-14-1267-2021. URL: https://amt.copernicus.org/articles/14/1267/2021/ (visited on 05/20/2022).

Borsdorff, T., J. Aan de Brugh, H. Hu, I. Aben, O. Hasekamp, and J. Landgraf (2018). "Measuring Carbon Monoxide With TROPOMI: First Results and a Comparison With ECMWF-IFS Analysis Data". *Geophysical Research Letters*. ISSN: 00948276. DOI: 10.1002/2018GL077045.

Bovensmann, H., M. Buchwitz, J. P. Burrows, M. Reuter, T. Krings, K. Gerilowski, O. Schneising, J. Heymann, A. Tretner, and J. Erzinger (2010). "A Remote Sensing Technique for Global Monitoring of Power Plant CO2 Emissions from Space and Related Applications". *Atmospheric Measurement Techniques*. ISSN: 1867-8548. DOI: 10.5194/amt-3-781-2010. URL: https://amt.copernicus.org/articles/3/781/2010/ (visited on 06/28/2023).

Bransden, B. H. and C. J. Joachain (2003). *Physics of Atoms and Molecules*. 2nd ed. Prentice Hall, Harlow, England ; New York. 1114 pp. ISBN: 978-0-582-35692-4.

Brasseur, G. P. and D. J. Jacob (2017). *Modeling of Atmospheric Chemistry*. 1st ed. Cambridge University Press. ISBN: 978-1-316-54475-4 978-1-107-14696-9. DOI: 10.1017/9781316544754. URL: https://www.cambridge.org/core/product/identifier/9781316544754/type/book (visited on 12/08/2023).

Brazile, J., R. A. Neville, K. Staenz, D. Schläpfer, L. Sun, and K. I. Itten (2008). "Toward Scene-Based Retrieval of Spectral Response Functions for Hyperspectral Imagers Using Fraunhofer Features". *Canadian Journal of Remote Sensing*, sup1. ISSN: 0703-8992, 1712-7971. DOI: 10.5589/m07-069. URL: http://www.tandfonline.com/doi/abs/10.5589/m07-069 (visited on 02/02/2024).

Brunner, D., G. Kuhlmann, S. Henne, E. Koene, B. Kern, S. Wolff, C. Voigt, P. Jöckel, C. Kiemle, A. Roiger, A. Fiehn, S. Krautwurst, K. Gerilowski, H. Bovensmann, J. Borchardt, M. Galkowski, C. Gerbig, J. Marshall, A. Klonecki, P. Prunet, R. Hanfland, M. Pattantyús-Ábrahám, A. Wyszogrodzki, and A. Fix (2023). "Evaluation of Simulated CO $_2$ Power Plant Plumes from Six High-Resolution Atmospheric Transport Models". *Atmospheric Chemistry and Physics*. ISSN: 1680-7324. DOI: 10.5194/acp-23-2699-2023. URL: https://acp.copernicus.org/articles/23/2699/2023/ (visited on 10/25/2023).

Buback, M., J. Schweer, and H. Tups (1986). "Near Infrared Absorption of Pure Carbon Dioxide up to 3100 Bar and 500 K. I. Wavenumber Range 3200 Cm $^{-1}$ to 5600 Cm $^{-1}$". *Zeitschrift für Naturforschung A*. ISSN: 1865-7109, 0932-0784. DOI: 10.1515/zna-1986-0308. URL: https://www.degruyter.com/document/doi/10.1515/zna-1986-0308/html (visited on 01/02/2024).

Butz, A., S. Guerlet, O. Hasekamp, D. Schepers, A. Galli, I. Aben, C. Frankenberg, J.-M. Hartmann, H. Tran, A. Kuze, G. Keppel-Aleks, G. Toon, D. Wunch, P. Wennberg, N. Deutscher, D. Griffith, R. Macatangay, J. Messerschmidt, J. Notholt, and T. Warneke (2011). "Toward Accurate CO2 and CH4 Observations from GOSAT". *Geophysical Research Letters*. ISSN:

00948276. DOI: 10.1029/2011GL047888. URL: http://doi.wiley.com/10.1029/2011GL047888 (visited on 12/17/2019).

Butz, A., S. Guerlet, O. P. Hasekamp, A. Kuze, and H. Suto (2013). "Using Ocean-Glint Scattered Sunlight as a Diagnostic Tool for Satellite Remote Sensing of Greenhouse Gases". *Atmospheric Measurement Techniques*. ISSN: 1867-8548. DOI: 10.5194/amt-6-2509-2013. URL: https://www.atmos-meas-tech.net/6/2509/2013/ (visited on 12/17/2019).

Butz, A., V. Hanft, R. Kleinschek, M. M. Frey, A. Müller, M. Knapp, I. Morino, A. Agusti-Panareda, F. Hase, J. Landgraf, S. Vardag, and H. Tanimoto (2022). "Versatile and Targeted Validation of Space-Borne XCO2, XCH4 and XCO Observations by Mobile Ground-Based Direct-Sun Spectrometers". *Frontiers in Remote Sensing*. ISSN: 2673-6187. DOI: 10.3389/frsen.2021.775805. URL: https://www.frontiersin.org/articles/10.3389/frsen.2021.775805/full (visited on 03/09/2023).

Candès, E. J., M. B. Wakin, and S. P. Boyd (2008). "Enhancing Sparsity by Reweighted L1 Minimization". *Journal of Fourier Analysis and Applications*. ISSN: 1069-5869, 1531-5851. DOI: 10.1007/s00041-008-9045-x. URL: http://link.springer.com/10.1007/s00041-008-9045-x (visited on 09/29/2021).

Carhart, R. and A. Policastro (1991). "A Second-Generation Model for Cooling Tower Plume Rise and Dispersion—I. Single Sources". *Atmospheric Environment. Part A. General Topics*. ISSN: 09601686. DOI: 10.1016/0960-1686(91)90015-Y. URL: https://linkinghub.elsevier.com/retrieve/pii/096016869190015Y (visited on 01/26/2022).

Chulakadabba, A., M. Sargent, T. Lauvaux, J. S. Benmergui, J. E. Franklin, C. Chan Miller, J. S. Wilzewski, S. Roche, E. Conway, A. H. Souri, K. Sun, B. Luo, J. Hawthrone, J. Samra, B. C. Daube, X. Liu, K. V. Chance, Y. Li, R. Gautam, M. Omara, J. S. Rutherford, E. D. Sherwin, A. Brandt, and S. C. Wofsy (2023). *Methane Point Source Quantification Using MethaneAIR: A New Airborne Imaging Spectrometer*. preprint. Gases/Remote Sensing/Validation and Intercomparisons. DOI: 10.5194/egusphere-2023-822. URL: https://egusphere.copernicus.org/preprints/2023/egusphere-2023-822/ (visited on 06/27/2023).

Ciais, P., A. J. Dolman, A. Bombelli, R. Duren, A. Peregon, P. J. Rayner, C. Miller, N. Gobron, G. Kinderman, G. Marland, N. Gruber, F. Chevallier, R. J. Andres, G. Balsamo, L. Bopp, F.-M. Bréon, G. Broquet, R. Dargaville, T. J. Battin, A. Borges, H. Bovensmann, M. Buchwitz, J. Butler, J. G. Canadell, R. B. Cook, R. DeFries, R. Engelen, K. R. Gurney, C. Heinze, M. Heimann, A. Held, M. Henry, B. Law, S. Luyssaert, J. Miller, T. Moriyama, C. Moulin, R. B. Myneni, C. Nussli, M. Obersteiner, D. Ojima, Y. Pan, J.-D. Paris, S. L. Piao, B. Poulter, S. Plummer, S. Quegan, P. Raymond, M. Reichstein, L. Rivier, C. Sabine, D. Schimel, O. Tarasova, R. Valentini, R. Wang, G. Van Der Werf, D. Wickland, M. Williams, and C. Zehner (2014). "Current Systematic Carbon-Cycle Observations and the Need for Implementing a Policy-Relevant Carbon Observing System". *Biogeosciences*. ISSN: 1726-4189. DOI: 10.5194/bg-11-3547-2014. URL: https://bg.copernicus.org/articles/11/3547/2014/ (visited on 02/16/2024).

Cogliati, S., F. Sarti, L. Chiarantini, M. Cosi, R. Lorusso, E. Lopinto, F. Miglietta, L. Genesio, L. Guanter, A. Damm, S. Pérez-López, D. Scheffler, G. Tagliabue, C. Panigada, U. Rascher, T. Dowling, C. Giardino, and R. Colombo (2021). "The PRISMA Imaging Spectroscopy Mission: Overview and First Performance Analysis". *Remote Sensing of Environment*. DOI: 10.1016/j.rse.2021.112499.

Collins, M., S.-I. An, W. Cai, A. Ganachaud, E. Guilyardi, F.-F. Jin, M. Jochum, M. Lengaigne, S. Power, A. Timmermann, G. Vecchi, and A. Wittenberg (2010). "The Impact of Global Warming on the Tropical Pacific Ocean and El Niño". *Nature Geoscience*. ISSN: 1752-0894, 1752-0908. DOI: 10.1038/ngeo868. URL: https://www.nature.com/articles/ngeo868 (visited on 02/15/2024).

Conway, E. K., A. H. Souri, J. Benmergui, K. Sun, X. Liu, C. Staebell, C. Chan Miller, J. Franklin, J. Samra, J. Wilzewski, S. Roche, B. Luo, A. Chulakadabba, M. Sargent, J. Hohl, B. Daube, I. Gordon, K. Chance, and S. Wofsy (2024). "Level0 to Level1B Processor for MethaneAIR". *Atmospheric Measurement Techniques*. ISSN: 1867-8548. DOI: 10.5194/amt-17-1347-2024. URL: https://amt.copernicus.org/articles/17/1347/2024/ (visited on 03/13/2024).

Crisp, D., B. M. Fisher, C. O'Dell, C. Frankenberg, R. Basilio, H. Bösch, L. R. Brown, R. Castano, B. Connor, N. M. Deutscher, A. Eldering, D. Griffith, M. Gunson, A. Kuze, L. Mandrake, J. McDuffie, J. Messerschmidt, C. E. Miller, I. Morino, V. Natraj, J. Notholt, D. M. O'Brien, F. Oyafuso, I. Polonsky, J. Robinson, R. Salawitch, V. Sherlock, M. Smyth, H. Suto, T. E. Taylor, D. R. Thompson, P. O. Wennberg, D. Wunch, and Y. L. Yung (2012). "The ACOS CO2 Retrieval Algorithm – Part II: Global CO2 Data Characterization". *Atmospheric Measurement Techniques*. ISSN: 1867-8548. DOI: 10.5194/amt-5-687-2012. URL: https://amt.copernicus.org/articles/5/687/2012/ (visited on 07/10/2023).

Cusworth, D. H., R. M. Duren, A. K. Thorpe, E. Tseng, D. Thompson, A. Guha, S. Newman, K. T. Foster, and C. E. Miller (2020). "Using Remote Sensing to Detect, Validate, and Quantify Methane Emissions from California Solid Waste Operations". *Environmental Research Letters*. ISSN: 1748-9326. DOI: 10.1088/1748-9326/ab7b99. URL: https://iopscience.iop.org/article/10.1088/1748-9326/ab7b99 (visited on 06/03/2022).

Cusworth, D. H., R. M. Duren, A. K. Thorpe, M. L. Eastwood, R. O. Green, P. E. Dennison, C. Frankenberg, J. W. Heckler, G. P. Asner, and C. E. Miller (2021a). "Quantifying Global Power Plant Carbon Dioxide Emissions With Imaging Spectroscopy". *AGU Advances*. ISSN: 2576-604X, 2576-604X. DOI: 10.1029/2020AV000350. URL: https://onlinelibrary.wiley.com/doi/10.1029/2020AV000350 (visited on 06/21/2021).

Cusworth, D. H., R. M. Duren, A. K. Thorpe, W. Olson-Duvall, J. Heckler, J. W. Chapman, M. L. Eastwood, M. C. Helmlinger, R. O. Green, G. P. Asner, P. E. Dennison, and C. E. Miller (2021b). "Intermittency of Large Methane Emitters in the Permian Basin". *Environmental Science & Technology Letters*. ISSN: 2328-8930, 2328-8930. DOI: 10.1021/acs.estlett.1c00173. URL: https://pubs.acs.org/doi/10.1021/acs.estlett.1c00173 (visited on 06/22/2023).

Cusworth, D. H., A. K. Thorpe, A. K. Ayasse, D. Stepp, J. Heckler, G. P. Asner, C. E. Miller, V. Yadav, J. W. Chapman, M. L. Eastwood, R. O. Green, B. Hmiel, D. R. Lyon, and R. M. Duren (2022). "Strong Methane Point Sources Contribute a Disproportionate Fraction of Total Emissions across Multiple Basins in the United States". *Proceedings of the National Academy of Sciences*. ISSN: 0027-8424, 1091-6490. DOI: 10.1073/pnas.2202338119. URL: https://pnas.org/doi/10.1073/pnas.2202338119 (visited on 10/27/2023).

D'Isidoro, M., A. Maurizi, and F. Tampieri (2010). "Effects of Resolution on the Relative Importance of Numerical and Physical Horizontal Diffusion in Atmospheric Composition Modelling". *Atmospheric Chemistry and Physics*. ISSN: 1680-7324. DOI: 10.5194/acp-10-2737-2010. URL: https://acp.copernicus.org/articles/10/2737/2010/ (visited on 12/08/2023).

Demtröder, W. (2013). *Elektrizität und Optik*. 6., überarb. und aktualisierte Aufl. Erscheinungsort nicht ermittelbar. 480 pp. ISBN: 978-3-642-29943-8.

– (2016). *Atome, Moleküle und Festkörper*. 5., neu bearbeitete und aktualisierte Auflage. Experimentalphysik / Wolfgang Demtröder. Springer Spektrum, Berlin Heidelberg. 586 pp. ISBN: 978-3-662-49093-8. DOI: 10.1007/978-3-662-49094-5.

Dennison, P. E., A. K. Thorpe, E. R. Pardyjak, D. A. Roberts, Y. Qi, R. O. Green, E. S. Bradley, and C. C. Funk (2013). "High Spatial Resolution Mapping of Elevated Atmospheric Carbon Dioxide Using Airborne Imaging Spectroscopy: Radiative Transfer Modeling and Power Plant Plume Detection". *Remote Sensing of Environment*. ISSN: 00344257. DOI: 10.1016/j.rse.2013.08.001. URL: https://linkinghub.elsevier.com/retrieve/pii/S0034425713002599 (visited on 01/06/2021).

Dietrich, F., J. Chen, B. Voggenreiter, P. Aigner, N. Nachtigall, and B. Reger (2021). "MUCCnet: Munich Urban Carbon Column Network". *Atmospheric Measurement Techniques*. ISSN: 1867-8548. DOI: 10.5194/amt-14-1111-2021. URL: https://amt.copernicus.org/articles/14/1111/2021/ (visited on 02/21/2024).

Dlugokencky, E. J., E. G. Nisbet, R. Fisher, and D. Lowry (2011). "Global Atmospheric Methane: Budget, Changes and Dangers". *Philosophical Transactions of the Royal Society A: Mathematical, Physical and Engineering Sciences*. ISSN: 1364-503X, 1471-2962. DOI: 10.1098/rsta.2010.0341. URL: https://royalsocietypublishing.org/doi/10.1098/rsta.2010.0341 (visited on 02/16/2024).

Dörner, S., S. Donner, L. Behrens, S. Beirle, and T. Wagner (2018). "MAX-DOAS Measurements of Tropospheric Trace Gases during the AQABA Campaign in Late Summer 2017." In: EGU General Assembly Conference Abstracts. URL: https://ui.adsabs.harvard.edu/abs/2018EGUGA..20.4978D (visited on 05/18/2022).

Dosio, A. (2005). *Turbulent Dispersion in the Atmospheric Convective Boundary Layer = Turbulente Dispersie in de Atmosferische Convectieve Grenslaag*. Wageningen University and Research, Wageningen. ISBN: 978-90-8504-171-9.

Duren, R. M., A. K. Thorpe, K. T. Foster, T. Rafiq, F. M. Hopkins, V. Yadav, B. D. Bue, D. R. Thompson, S. Conley, N. K. Colombi, C. Frankenberg, I. B. McCubbin, M. L. Eastwood, M. Falk, J. D. Herner, B. E. Croes, R. O. Green, and C. E. Miller (2019). "California's Methane Super-Emitters". *Nature*. ISSN: 0028-0836, 1476-4687. DOI: 10.1038/s41586-019-1720-3. URL: http://www.nature.com/articles/s41586-019-1720-3 (visited on 10/31/2022).

Eldering, A., P. O. Wennberg, D. Crisp, D. S. Schimel, M. R. Gunson, A. Chatterjee, J. Liu, F. M. Schwandner, Y. Sun, C. W. O'Dell, C. Frankenberg, T. Taylor, B. Fisher, G. B. Osterman, D. Wunch, J. Hakkarainen, J. Tamminen, and B. Weir (2017). "The Orbiting Carbon Observatory-2 Early Science Investigations of Regional Carbon Dioxide Fluxes". *Science*. ISSN: 0036-8075, 1095-9203. DOI: 10.1126/science.aam5745. URL: https://www.sciencemag.org/lookup/doi/10.1126/science.aam5745 (visited on 04/28/2020).

Eldering, A., T. E. Taylor, C. W. O'Dell, and R. Pavlick (2019). "The OCO-3 Mission: Measurement Objectives and Expected Performance Based on 1 Year of Simulated Data". *Atmospheric Measurement Techniques*. ISSN: 1867-8548. DOI: 10.5194/amt-12-2341-2019. URL: https://amt.copernicus.org/articles/12/2341/2019/ (visited on 10/26/2023).

Emde, C., R. Buras-Schnell, A. Kylling, B. Mayer, J. Gasteiger, U. Hamann, J. Kylling, B. Richter, C. Pause, T. Dowling, and L. Bugliaro (2016). "The libRadtran Software Package for Radia-

tive Transfer Calculations (Version 2.0.1)". *Geoscientific Model Development*. ISSN: 1991-9603. DOI: 10.5194/gmd-9-1647-2016. URL: https://gmd.copernicus.org/articles/9/1647/2016/ (visited on 10/27/2023).

Etminan, M., G. Myhre, E. J. Highwood, and K. P. Shine (2016). "Radiative Forcing of Carbon Dioxide, Methane, and Nitrous Oxide: A Significant Revision of the Methane Radiative Forcing". *Geophysical Research Letters*. ISSN: 0094-8276, 1944-8007. DOI: 10.1002/2016GL071930. URL: https://agupubs.onlinelibrary.wiley.com/doi/10.1002/2016GL071930 (visited on 11/22/2023).

Feng, L., P. I. Palmer, R. J. Parker, N. M. Deutscher, D. G. Feist, R. Kivi, I. Morino, and R. Sussmann (2016). "Estimates of European Uptake of CO2 Inferred from GOSAT XCO2 Retrievals: Sensitivity to Measurement Bias inside and Outside Europe". *Atmospheric Chemistry and Physics*. ISSN: 1680-7324. DOI: 10.5194/acp-16-1289-2016. URL: https://acp.copernicus.org/articles/16/1289/2016/ (visited on 02/16/2024).

Fiehn, A., J. Kostinek, M. Eckl, T. Klausner, M. Gałkowski, J. Chen, C. Gerbig, T. Röckmann, H. Maazallahi, M. Schmidt, P. Korbeń, J. Nęcki, P. Jagoda, N. Wildmann, C. Mallaun, R. Bun, A.-L. Nickl, P. Jöckel, A. Fix, and A. Roiger (2020). "Estimating CH4, CO2 and CO Emissions from Coal Mining and Industrial Activities in the Upper Silesian Coal Basin Using an Aircraft-Based Mass Balance Approach". *Atmospheric Chemistry and Physics*. ISSN: 1680-7324. DOI: 10.5194/acp-20-12675-2020. URL: https://acp.copernicus.org/articles/20/12675/2020/ (visited on 10/31/2022).

Flores, B. M., E. Montoya, B. Sakschewski, N. Nascimento, A. Staal, R. A. Betts, C. Levis, D. M. Lapola, A. Esquível-Muelbert, C. Jakovac, C. A. Nobre, R. S. Oliveira, L. S. Borma, D. Nian, N. Boers, S. B. Hecht, H. Ter Steege, J. Arieira, I. L. Lucas, E. Berenguer, J. A. Marengo, L. V. Gatti, C. R. C. Mattos, and M. Hirota (2024). "Critical Transitions in the Amazon Forest System". *Nature*. ISSN: 0028-0836, 1476-4687. DOI: 10.1038/s41586-023-06970-0. URL: https://www.nature.com/articles/s41586-023-06970-0 (visited on 02/15/2024).

Foote, M. D., P. E. Dennison, P. R. Sullivan, K. B. O'Neill, A. K. Thorpe, D. R. Thompson, D. H. Cusworth, R. Duren, and S. C. Joshi (2021). "Impact of Scene-Specific Enhancement Spectra on Matched Filter Greenhouse Gas Retrievals from Imaging Spectroscopy". *Remote Sensing of Environment*. ISSN: 00344257. DOI: 10.1016/j.rse.2021.112574. URL: https://linkinghub.elsevier.com/retrieve/pii/S0034425721002947 (visited on 07/16/2021).

Foote, M. D., P. E. Dennison, A. K. Thorpe, D. R. Thompson, S. Jongaramrungruang, C. Frankenberg, and S. C. Joshi (2020). "Fast and Accurate Retrieval of Methane Concentration From Imaging Spectrometer Data Using Sparsity Prior". *IEEE Transactions on Geoscience and Remote Sensing*. ISSN: 0196-2892, 1558-0644. DOI: 10.1109/TGRS.2020.2976888. URL: https://ieeexplore.ieee.org/document/9034492/ (visited on 05/31/2022).

Foulds, A., G. Allen, J. T. Shaw, P. Bateson, P. A. Barker, L. Huang, J. R. Pitt, J. D. Lee, S. E. Wilde, P. Dominutti, R. M. Purvis, D. Lowry, J. L. France, R. E. Fisher, A. Fiehn, M. Pühl, S. J. B. Bauguitte, S. A. Conley, M. L. Smith, T. Lachlan-Cope, I. Pisso, and S. Schwietzke (2022). "Quantification and Assessment of Methane Emissions from Offshore Oil and Gas Facilities on the Norwegian Continental Shelf". *Atmospheric Chemistry and Physics*. ISSN: 1680-7324. DOI: 10.5194/acp-22-4303-2022. URL: https://acp.copernicus.org/articles/22/4303/2022/ (visited on 01/26/2023).

Frankenberg, C., U. Platt, and T. Wagner (2005). "Iterative Maximum a Posteriori (IMAP)-DOAS for Retrieval of Strongly Absorbing Trace Gases: Model Studies for CH_4 and CO_2 Retrieval from near Infrared Spectra of SCIAMACHY Onboard ENVISAT". *Atmospheric Chemistry and Physics*. ISSN: 1680-7324. DOI: 10.5194/acp-5-9-2005. URL: http://www.atmos-chem-phys.net/5/9/2005/ (visited on 03/24/2020).

Frankenberg, C., A. K. Thorpe, D. R. Thompson, G. Hulley, E. A. Kort, N. Vance, J. Borchardt, T. Krings, K. Gerilowski, C. Sweeney, S. Conley, B. D. Bue, A. D. Aubrey, S. Hook, and R. O. Green (2016). "Airborne Methane Remote Measurements Reveal Heavy-Tail Flux Distribution in Four Corners Region". *Proceedings of the National Academy of Sciences*. ISSN: 0027-8424, 1091-6490. DOI: 10.1073/pnas.1605617113. URL: https://pnas.org/doi/full/10.1073/pnas.1605617113 (visited on 06/30/2022).

Frey, M., M. K. Sha, F. Hase, M. Kiel, T. Blumenstock, R. Harig, G. Surawicz, N. M. Deutscher, K. Shiomi, J. E. Franklin, H. Bösch, J. Chen, M. Grutter, H. Ohyama, Y. Sun, A. Butz, G. Mengistu Tsidu, D. Ene, D. Wunch, Z. Cao, O. Garcia, M. Ramonet, F. Vogel, and J. Orphal (2019). "Building the COllaborative Carbon Column Observing Network (COCCON): Long-Term Stability and Ensemble Performance of the EM27/SUN Fourier Transform Spectrometer". *Atmospheric Measurement Techniques*. ISSN: 1867-8548. DOI: 10.5194/amt-12-1513-2019. URL: https://www.atmos-meas-tech.net/12/1513/2019/ (visited on 12/17/2019).

Friedlingstein, P. et al. (2023). "Global Carbon Budget 2023". *Earth System Science Data*. ISSN: 1866-3516. DOI: 10.5194/essd-15-5301-2023. URL: https://essd.copernicus.org/articles/15/5301/2023/ (visited on 12/06/2023).

Fuentes Andrade, B., M. Buchwitz, M. Reuter, H. Bovensmann, A. Richter, H. Boesch, and J. P. Burrows (2023). *A Method for Estimating Localized CO_2 Emissions from Co-Located Satellite XCO_2 and NO_2 Images*. preprint. Gases/Remote Sensing/Data Processing and Information Retrieval. DOI: 10.5194/egusphere-2023-2085. URL: https://egusphere.copernicus.org/preprints/2023/egusphere-2023-2085/ (visited on 10/25/2023).

Funk, C., J. Theiler, D. Roberts, and C. Borel (2001). "Clustering to Improve Matched Filter Detection of Weak Gas Plumes in Hyperspectral Thermal Imagery". *IEEE Transactions on Geoscience and Remote Sensing*. ISSN: 01962892. DOI: 10.1109/36.934073. URL: http://ieeexplore.ieee.org/document/934073/ (visited on 03/18/2020).

Gålfalk, M. and D. Bastviken (2018). "Remote Sensing of Methane and Nitrous Oxide Fluxes from Waste Incineration". *Waste Management*. ISSN: 0956053X. DOI: 10.1016/j.wasman.2018.01.031. URL: https://linkinghub.elsevier.com/retrieve/pii/S0956053X18300527 (visited on 01/26/2023).

Gålfalk, M., G. Olofsson, and D. Bastviken (2017). "Approaches for Hyperspectral Remote Flux Quantification and Visualization of GHGs in the Environment". *Remote Sensing of Environment*. ISSN: 00344257. DOI: 10.1016/j.rse.2017.01.012. URL: https://linkinghub.elsevier.com/retrieve/pii/S0034425717300123 (visited on 01/29/2023).

Gålfalk, M., G. Olofsson, P. Crill, and D. Bastviken (2016). "Making Methane Visible". *Nature Climate Change*. ISSN: 1758-678X, 1758-6798. DOI: 10.1038/nclimate2877. URL: http://www.nature.com/articles/nclimate2877 (visited on 01/27/2021).

Gålfalk, M., S. N. Påledal, R. Sehlén, and D. Bastviken (2022). "Ground-Based Remote Sensing of CH4 and N2O Fluxes from a Wastewater Treatment Plant and Nearby Biogas Production with Discoveries of Unexpected Sources". *Environmental Research*. ISSN: 00139351. DOI: 10.

1016/j.envres.2021.111978. URL: https://linkinghub.elsevier.com/retrieve/pii/S0013935121012731 (visited on 01/30/2023).

Gałkowski, M., A. Jordan, M. Rothe, J. Marshall, F.-T. Koch, J. Chen, A. Agusti-Panareda, A. Fix, and C. Gerbig (2021). "In Situ Observations of Greenhouse Gases over Europe during the CoMet 1.0 Campaign Aboard the HALO Aircraft". *Atmospheric Measurement Techniques*. ISSN: 1867-8548. DOI: 10.5194/amt-14-1525-2021. URL: https://amt.copernicus.org/articles/14/1525/2021/ (visited on 11/27/2023).

Gao, B.-C., M. J. Montes, and C. O. Davis (2004). "Refinement of Wavelength Calibrations of Hyperspectral Imaging Data Using a Spectrum-Matching Technique". *Remote Sensing of Environment*. ISSN: 00344257. DOI: 10.1016/j.rse.2003.09.002. URL: https://linkinghub.elsevier.com/retrieve/pii/S0034425703002530 (visited on 02/02/2024).

Gege, P., J. Fries, P. Haschberger, P. Schötz, H. Schwarzer, P. Strobl, B. Suhr, G. Ulbrich, and W. Jan Vreeling (2009). "Calibration Facility for Airborne Imaging Spectrometers". *ISPRS Journal of Photogrammetry and Remote Sensing*. ISSN: 09242716. DOI: 10.1016/j.isprsjprs.2009.01.006. URL: https://linkinghub.elsevier.com/retrieve/pii/S0924271609000124 (visited on 06/17/2020).

Geladi, P., J. Burger, and T. Lestander (2004). "Hyperspectral Imaging: Calibration Problems and Solutions". *Chemometrics and Intelligent Laboratory Systems*. ISSN: 01697439. DOI: 10.1016/j.chemolab.2004.01.023. URL: https://linkinghub.elsevier.com/retrieve/pii/S0169743904000371 (visited on 12/17/2019).

Gerilowski, K., A. Tretner, T. Krings, M. Buchwitz, P. P. Bertagnolio, F. Belemezov, J. Erzinger, J. P. Burrows, and H. Bovensmann (2011). "MAMAP – a New Spectrometer System for Column-Averaged Methane and Carbon Dioxide Observations from Aircraft: Instrument Description and Performance Analysis". *Atmospheric Measurement Techniques*. ISSN: 1867-8548. DOI: 10.5194/amt-4-215-2011. URL: https://amt.copernicus.org/articles/4/215/2011/ (visited on 10/26/2023).

Gifford, F. A. Jr. (1968). *AN OUTLINE OF THEORIES OF DIFFUSION IN THE LOWER LAYERS OF THE ATMOSPHERE*. DOI: 10.2172/4501607. URL: http://www.osti.gov/servlets/purl/4501607-85l5s9/ (visited on 12/08/2023).

Gordon, I., L. Rothman, C. Hill, R. Kochanov, Y. Tan, P. Bernath, M. Birk, V. Boudon, A. Campargue, K. Chance, B. Drouin, J.-M. Flaud, R. Gamache, J. Hodges, D. Jacquemart, V. Perevalov, A. Perrin, K. Shine, M.-A. Smith, J. Tennyson, G. Toon, H. Tran, V. Tyuterev, A. Barbe, A. Császár, V. Devi, T. Furtenbacher, J. Harrison, J.-M. Hartmann, A. Jolly, T. Johnson, T. Karman, I. Kleiner, A. Kyuberis, J. Loos, O. Lyulin, S. Massie, S. Mikhailenko, N. Moazzen-Ahmadi, H. Müller, O. Naumenko, A. Nikitin, O. Polyansky, M. Rey, M. Rotger, S. Sharpe, K. Sung, E. Starikova, S. Tashkun, J. V. Auwera, G. Wagner, J. Wilzewski, P. Wcisło, S. Yu, and E. Zak (2017). "The HITRAN2016 Molecular Spectroscopic Database". *Journal of Quantitative Spectroscopy and Radiative Transfer*. ISSN: 00224073. DOI: 10.1016/j.jqsrt.2017.06.038. URL: https://linkinghub.elsevier.com/retrieve/pii/S0022407317301073 (visited on 04/13/2020).

Green, R., B. Pavri, and T. Chrien (2003). "On-Orbit Radiometric and Spectral Calibration Characteristics of EO-1 Hyperion Derived with an Underflight of AVIRIS and in Situ Measurements at Salar de Arizaro, Argentina". *IEEE Transactions on Geoscience and Remote Sensing*.

ISSN: 0196-2892, 1558-0644. DOI: 10.1109/TGRS.2003.813204. URL: https://ieeexplore.ieee.org/document/1220227/ (visited on 02/02/2024).

Green, R. O., M. L. Eastwood, C. M. Sarture, T. G. Chrien, M. Aronsson, B. J. Chippendale, J. A. Faust, B. E. Pavri, C. J. Chovit, M. Solis, M. R. Olah, and O. Williams (1998). "Imaging Spectroscopy and the Airborne Visible/Infrared Imaging Spectrometer (AVIRIS)". *Remote Sensing of Environment*. ISSN: 00344257. DOI: 10.1016/S0034-4257(98)00064-9. URL: https://linkinghub.elsevier.com/retrieve/pii/S0034425798000649 (visited on 07/02/2022).

Grosskraftwerk, M. (2015). *Geschäftsbericht 2015*. annual report. Grosskraftwerk Mannheim. URL: https://www.gkm.de/unternehmen/.

Guanter, L., I. Irakulis-Loitxate, J. Gorroño, E. Sánchez-García, D. H. Cusworth, D. J. Varon, S. Cogliati, and R. Colombo (2021). "Mapping Methane Point Emissions with the PRISMA Spaceborne Imaging Spectrometer". *Remote Sensing of Environment*. ISSN: 00344257. DOI: 10.1016/j.rse.2021.112671.

Guanter, L., H. Kaufmann, K. Segl, S. Foerster, C. Rogass, S. Chabrillat, T. Kuester, A. Hollstein, G. Rossner, C. Chlebek, C. Straif, S. Fischer, S. Schrader, T. Storch, U. Heiden, A. Mueller, M. Bachmann, H. Mühle, R. Müller, M. Habermeyer, A. Ohndorf, J. Hill, H. Buddenbaum, P. Hostert, S. Van Der Linden, P. Leitão, A. Rabe, R. Doerffer, H. Krasemann, H. Xi, W. Mauser, T. Hank, M. Locherer, M. Rast, K. Staenz, and B. Sang (2015). "The EnMAP Spaceborne Imaging Spectroscopy Mission for Earth Observation". *Remote Sens.* DOI: 10.3390/rs70708830. URL: http://www.mdpi.com/2072-4292/7/7/8830 (visited on 10/26/2023).

Hakkarainen, J., I. Ialongo, T. Oda, M. E. Szeląg, C. W. O'Dell, A. Eldering, and D. Crisp (2023). "Building a Bridge: Characterizing Major Anthropogenic Point Sources in the South African Highveld Region Using OCO-3 Carbon Dioxide Snapshot Area Maps and S5P/ TROPOMI Nitrogen Dioxide Columns". *Environmental Research Letters*. ISSN: 1748-9326. DOI: 10.1088/1748-9326/acb837. URL: https://iopscience.iop.org/article/10.1088/1748-9326/acb837 (visited on 01/02/2024).

Hamlin, L., R. O. Green, P. Mouroulis, M. Eastwood, D. Wilson, M. Dudik, and C. Paine (2011). "Imaging Spectrometer Science Measurements for Terrestrial Ecology: AVIRIS and New Developments". In: *2011 Aerospace Conference*. 2011 IEEE Aerospace Conference. IEEE, Big Sky, USA. ISBN: 978-1-4244-7350-2. DOI: 10.1109/AERO.2011.5747395. URL: http://ieeexplore.ieee.org/document/5747395/ (visited on 07/02/2022).

Haveresch, H. (2023). "Ground-Based Hyperspectral Imaging of Greenhouse Gases Using a Physics Inversion Algorithm". Universität Heidelberg.

Hill, T. and R. Nassar (2019). "Pixel Size and Revisit Rate Requirements for Monitoring Power Plant CO2 Emissions from Space". *Remote Sensing*. ISSN: 2072-4292. DOI: 10.3390/rs11131608. URL: https://www.mdpi.com/2072-4292/11/13/1608 (visited on 02/05/2021).

Hochstaffl, P., F. Schreier, C. H. Köhler, A. Baumgartner, and D. Cerra (2023). "Methane Retrievals from Airborne HySpex Observations in the Shortwave Infrared". *Atmospheric Measurement Techniques*. ISSN: 1867-8548. DOI: 10.5194/amt-16-4195-2023. URL: https://amt.copernicus.org/articles/16/4195/2023/ (visited on 09/26/2023).

Holben, B., T. Eck, I. Slutsker, D. Tanré, J. Buis, A. Setzer, E. Vermote, J. Reagan, Y. Kaufman, T. Nakajima, F. Lavenu, I. Jankowiak, and A. Smirnov (1998). "AERONET—A Federated Instrument Network and Data Archive for Aerosol Characterization". *Remote Sensing of En-*

vironment. ISSN: 00344257. DOI: 10.1016/S0034-4257(98)00031-5. URL: https://linkinghub.elsevier.com/retrieve/pii/S0034425798000315 (visited on 01/17/2024).

Holmgren, F., C. W. Hansen, and M. A. Mikofski (2018). "Pvlib Python: A Python Package for Modeling Solar Energy Systems". *Journal of Open Source Software*. ISSN: 2475-9066. DOI: 10.21105/joss.00884. URL: http://joss.theoj.org/papers/10.21105/joss.00884 (visited on 06/30/2022).

Hu, H., J. Landgraf, R. Detmers, T. Borsdorff, J. Aan de Brugh, I. Aben, A. Butz, and O. Hasekamp (2018). "Toward Global Mapping of Methane With TROPOMI: First Results and Intersatellite Comparison to GOSAT". *Geophysical Research Letters*. DOI: 10.1002/2018GL077259. URL: http://doi.wiley.com/10.1002/2018GL077259 (visited on 04/28/2020).

Humlíček, J. (1982). "Optimized Computation of the Voigt and Complex Probability Functions". *Journal of Quantitative Spectroscopy and Radiative Transfer*. ISSN: 00224073. DOI: 10.1016/0022-4073(82)90078-4. URL: https://linkinghub.elsevier.com/retrieve/pii/0022407382900784 (visited on 10/12/2023).

IEA (2018). "Global Energy and CO2 Status Report 2018". *Energy Demand*.

Inness, A., M. Ades, A. Agustí-Panareda, J. Barré, A. Benedictow, A.-M. Blechschmidt, R. Engelen, J. J. Dominguez, H. Eskes, J. Flemming, V. Huijnen, L. Jones, Z. Kipling, S. Massart, M. Parrington, V.-H. Peuch, M. Razinger, S. Remy, M. Schulz, and M. Suttie (2019). "The CAMS Reanalysis of Atmospheric Composition". *Atmospheric Chemistry and Physics*. ISSN: 1680-7324. DOI: 10.5194/acp-19-3515-2019. URL: https://www.atmos-chem-phys.net/19/3515/2019/ (visited on 12/17/2019).

IPCC (2023). *Climate Change 2021 – The Physical Science Basis: Working Group I Contribution to the Sixth Assessment Report of the Intergovernmental Panel on Climate Change*. 1st ed. Cambridge University Press. ISBN: 978-1-00-915789-6. DOI: 10.1017/9781009157896. URL: https://www.cambridge.org/core/product/identifier/9781009157896/type/book (visited on 11/15/2023).

Jacob, D. J., D. J. Varon, D. H. Cusworth, P. E. Dennison, C. Frankenberg, R. Gautam, L. Guanter, J. Kelley, J. McKeever, L. E. Ott, B. Poulter, Z. Qu, A. K. Thorpe, J. R. Worden, and R. M. Duren (2022). "Quantifying Methane Emissions from the Global Scale down to Point Sources Using Satellite Observations of Atmospheric Methane". *Atmospheric Chemistry and Physics*. ISSN: 1680-7324. DOI: 10.5194/acp-22-9617-2022. URL: https://acp.copernicus.org/articles/22/9617/2022/ (visited on 04/22/2023).

Janicke, U. and L. Janicke (2001). "A Three-Dimensional Plume Rise Model for Dry and Wet Plumes". *Atmospheric Environment*. ISSN: 13522310. DOI: 10.1016/S1352-2310(00)00372-1. URL: https://linkinghub.elsevier.com/retrieve/pii/S1352231000003721 (visited on 10/13/2021).

Janssens-Maenhout, G., B. Pinty, M. Dowell, H. Zunker, E. Andersson, G. Balsamo, J.-L. Bézy, T. Brunhes, H. Bösch, B. Bojkov, D. Brunner, M. Buchwitz, D. Crisp, P. Ciais, P. Counet, D. Dee, H. Denier van der Gon, H. Dolman, M. Drinkwater, O. Dubovik, R. Engelen, T. Fehr, V. Fernandez, M. Heimann, K. Holmlund, S. Houweling, R. Husband, O. Juvyns, A. Kentarchos, J. Landgraf, R. Lang, A. Löscher, J. Marshall, Y. Meijer, M. Nakajima, P. Palmer, P. Peylin, P. Rayner, M. Scholze, B. Sierk, J. Tamminen, and P. Veefkind (2020). "Towards an Operational Anthropogenic CO $_2$ Emissions Monitoring and Verification Support Capacity". *Bulletin of the American Meteorological Society*. ISSN: 0003-0007, 1520-0477. DOI: 10.1175/BAMS-D-19-

0017.1. URL: http://journals.ametsoc.org/doi/10.1175/BAMS-D-19-0017.1 (visited on 05/21/2020).

Jervis, D., J. McKeever, B. O. A. Durak, J. J. Sloan, D. Gains, D. J. Varon, A. Ramier, M. Strupler, and E. Tarrant (2021). "The GHGSat-D Imaging Spectrometer". *Atmospheric Measurement Techniques*. ISSN: 1867-8548. DOI: 10.5194/amt-14-2127-2021. URL: https://amt.copernicus.org/articles/14/2127/2021/ (visited on 12/15/2023).

Jiang, F., W. Ju, W. He, M. Wu, H. Wang, J. Wang, M. Jia, S. Feng, L. Zhang, and J. M. Chen (2022). "A 10-Year Global Monthly Averaged Terrestrial Net Ecosystem Exchange Dataset Inferred from the ACOS GOSAT v9 XCO $_2$ Retrievals (GCAS2021)". *Earth System Science Data*. ISSN: 1866-3516. DOI: 10.5194/essd-14-3013-2022. URL: https://essd.copernicus.org/articles/14/3013/2022/ (visited on 02/16/2024).

Jongaramrungruang, S., C. Frankenberg, G. Matheou, A. K. Thorpe, D. R. Thompson, L. Kuai, and R. M. Duren (2019). "Towards Accurate Methane Point-Source Quantification from High-Resolution 2-D Plume Imagery". *Atmospheric Measurement Techniques*. DOI: 10.5194/amt-12-6667-2019. URL: https://amt.copernicus.org/articles/12/6667/2019/ (visited on 09/22/2021).

Jongaramrungruang, S., A. K. Thorpe, G. Matheou, and C. Frankenberg (2022). "MethaNet – An AI-driven Approach to Quantifying Methane Point-Source Emission from High-Resolution 2-D Plume Imagery". *Remote Sensing of Environment*. ISSN: 00344257. DOI: 10.1016/j.rse.2021.112809.

Jungmann, M., S. N. Vardag, F. Kutzner, F. Keppler, M. Schmidt, N. Aeschbach, U. Gerhard, A. Zipf, S. Lautenbach, A. Siegmund, T. Goeschl, and A. Butz (2022). "Zooming-in for Climate Action—Hyperlocal Greenhouse Gas Data for Mitigation Action?" *Climate Action*. ISSN: 2731-3263. DOI: 10.1007/s44168-022-00007-4. URL: https://link.springer.com/10.1007/s44168-022-00007-4 (visited on 06/30/2022).

Kasten, F. and A. T. Young (1989). "Revised Optical Air Mass Tables and Approximation Formula". *Applied Optics*. ISSN: 0003-6935, 1539-4522. DOI: 10.1364/AO.28.004735. URL: https://opg.optica.org/abstract.cfm?URI=ao-28-22-4735 (visited on 06/18/2022).

Kirschke, S., P. Bousquet, P. Ciais, M. Saunois, J. G. Canadell, E. J. Dlugokencky, P. Bergamaschi, D. Bergmann, D. R. Blake, L. Bruhwiler, P. Cameron-Smith, S. Castaldi, F. Chevallier, L. Feng, A. Fraser, M. Heimann, E. L. Hodson, S. Houweling, B. Josse, P. J. Fraser, P. B. Krummel, J.-F. Lamarque, R. L. Langenfelds, C. Le Quéré, V. Naik, S. O'Doherty, P. I. Palmer, I. Pison, D. Plummer, B. Poulter, R. G. Prinn, M. Rigby, B. Ringeval, M. Santini, M. Schmidt, D. T. Shindell, I. J. Simpson, R. Spahni, L. P. Steele, S. A. Strode, K. Sudo, S. Szopa, G. R. van der Werf, A. Voulgarakis, M. van Weele, R. F. Weiss, J. E. Williams, and G. Zeng (2013). "Three Decades of Global Methane Sources and Sinks". *Nature Geoscience*. ISSN: 1752-0894, 1752-0908. DOI: 10.1038/ngeo1955. URL: http://www.nature.com/articles/ngeo1955 (visited on 12/16/2022).

Klappenbach, F., M. Bertleff, J. Kostinek, F. Hase, T. Blumenstock, A. Agusti-Panareda, M. Razinger, and A. Butz (2015). "Accurate Mobile Remote Sensing of XCO $_2$ and XCH $_4$ Latitudinal Transects from Aboard a Research Vessel". *Atmospheric Measurement Techniques*. ISSN: 1867-8548. DOI: 10.5194/amt-8-5023-2015. URL: https://www.atmos-meas-tech.net/8/5023/2015/ (visited on 12/17/2019).

Klein, A., P. Lübcke, N. Bobrowski, J. Kuhn, and U. Platt (2017). "Plume Propagation Direction Determination with SO2 Cameras". *Atmospheric Measurement Techniques*. ISSN: 1867-8548. DOI: 10.5194/amt-10-979-2017. URL: https://amt.copernicus.org/articles/10/979/2017/ (visited on 01/19/2022).

Knapp, M., L. Scheidweiler, F. Külheim, R. Kleinschek, J. Necki, P. Jagoda, and A. Butz (2023a). "Spectrometric Imaging of Sub-Hourly Methane Emission Dynamics from Coal Mine Ventilation". *Environmental Research Letters*. ISSN: 1748-9326. DOI: 10.1088/1748-9326/acc346. URL: https://iopscience.iop.org/article/10.1088/1748-9326/acc346 (visited on 04/18/2023).

Knapp, M., R. Kleinschek, F. Hase, A. Agustí-Panareda, A. Inness, J. Barré, J. Landgraf, T. Borsdorff, S. Kinne, and A. Butz (2021). "Shipborne Measurements of XCO2, XCH4, and XCO above the Pacific Ocean and Comparison to CAMS Atmospheric Analyses and Sentinel-5P/TROPOMI". *Earth System Science Data*. ISSN: 1866-3516. DOI: 10.5194/essd-13-199-2021. URL: https://essd.copernicus.org/articles/13/199/2021/ (visited on 06/22/2021).

Knapp, M., R. Kleinschek, S. N. Vardag, F. Külheim, H. Haveresch, M. Sindram, T. Siegel, B. Burger, and A. Butz (2023b). *Quantitative Imaging of Carbon Dioxide Plumes Using a Ground-Based Shortwave Infrared Spectral Camera*. preprint. Atmospheric Measurement Techniques (Gases/Remote Sensing/Data Processing and Information Retrieval). DOI: 10.5194/egusphere-2023-1857. URL: https://egusphere.copernicus.org/preprints/2023/egusphere-2023-1857/ (visited on 11/07/2023).

Kochanov, R., I. Gordon, L. Rothman, P. Wcisło, C. Hill, and J. Wilzewski (2016). "HITRAN Application Programming Interface (HAPI): A Comprehensive Approach to Working with Spectroscopic Data". *Journal of Quantitative Spectroscopy and Radiative Transfer*. DOI: 10.1016/j.jqsrt.2016.03.005. URL: https://linkinghub.elsevier.com/retrieve/pii/S0022407315302466 (visited on 02/26/2024).

Köhler, P., L. Guanter, and J. Joiner (2015). "A Linear Method for the Retrieval of Sun-Induced Chlorophyll Fluorescence from GOME-2 and SCIAMACHY Data". *Atmospheric Measurement Techniques*. ISSN: 1867-8548. DOI: 10.5194/amt-8-2589-2015. URL: https://amt.copernicus.org/articles/8/2589/2015/ (visited on 06/10/2023).

Kokka, A., T. Pulli, E. Honkavaara, L. Markelin, P. Kärhä, and E. Ikonen (2019). "Flat-Field Calibration Method for Hyperspectral Frame Cameras". *Metrologia*. ISSN: 0026-1394, 1681-7575. DOI: 10.1088/1681-7575/ab3261. URL: https://iopscience.iop.org/article/10.1088/1681-7575/ab3261 (visited on 12/17/2019).

Kort, E. A., C. Frankenberg, C. E. Miller, and T. Oda (2012). "Space-Based Observations of Megacity Carbon Dioxide: SPACE-BASED OBSERVATIONS OF MEGACITY CO_2". *Geophysical Research Letters*. ISSN: 00948276. DOI: 10.1029/2012GL052738. URL: http://doi.wiley.com/10.1029/2012GL052738 (visited on 06/30/2022).

Kostinek, J., A. Roiger, M. Eckl, A. Fiehn, A. Luther, N. Wildmann, T. Klausner, A. Fix, C. Knote, A. Stohl, and A. Butz (2021). "Estimating Upper Silesian Coal Mine Methane Emissions from Airborne in Situ Observations and Dispersion Modeling". *Atmospheric Chemistry and Physics*. ISSN: 1680-7324. DOI: 10.5194/acp-21-8791-2021. URL: https://acp.copernicus.org/articles/21/8791/2021/ (visited on 10/26/2022).

Krautwurst, S., K. Gerilowski, J. Borchardt, N. Wildmann, M. Gałkowski, J. Swolkień, J. Marshall, A. Fiehn, A. Roiger, T. Ruhtz, C. Gerbig, J. Necki, J. P. Burrows, A. Fix, and H. Bovens-

mann (2021). "Quantification of CH4 Coal Mining Emissions in Upper Silesia by Passive Airborne Remote Sensing Observations with the Methane Airborne MAPper (MAMAP) Instrument during the CO2 and Methane (CoMet) Campaign". *Atmospheric Chemistry and Physics*. ISSN: 1680-7324. DOI: 10.5194/acp-21-17345-2021. URL: https://acp.copernicus.org/articles/21/17345/2021/ (visited on 10/31/2022).

Krautwurst, S., K. Gerilowski, H. H. Jonsson, D. R. Thompson, R. W. Kolyer, L. T. Iraci, A. K. Thorpe, M. Horstjann, M. Eastwood, I. Leifer, S. A. Vigil, T. Krings, J. Borchardt, M. Buchwitz, M. M. Fladeland, J. P. Burrows, and H. Bovensmann (2017). "Methane Emissions from a Californian Landfill, Determined from Airborne Remote Sensing and in Situ Measurements". *Atmospheric Measurement Techniques*. ISSN: 1867-8548. DOI: 10.5194/amt-10-3429-2017. URL: https://amt.copernicus.org/articles/10/3429/2017/ (visited on 07/07/2022).

Krings, T., K. Gerilowski, M. Buchwitz, J. Hartmann, T. Sachs, J. Erzinger, J. P. Burrows, and H. Bovensmann (2013). "Quantification of Methane Emission Rates from Coal Mine Ventilation Shafts Using Airborne Remote Sensing Data". *Atmospheric Measurement Techniques*. ISSN: 1867-8548. DOI: 10.5194/amt-6-151-2013. URL: https://amt.copernicus.org/articles/6/151/2013/ (visited on 10/26/2023).

Krings, T., K. Gerilowski, M. Buchwitz, M. Reuter, A. Tretner, J. Erzinger, D. Heinze, U. Pflüger, J. P. Burrows, and H. Bovensmann (2011). "MAMAP – a New Spectrometer System for Column-Averaged Methane and Carbon Dioxide Observations from Aircraft: Retrieval Algorithm and First Inversions for Point Source Emission Rates". *Atmospheric Measurement Techniques*. ISSN: 1867-8548. DOI: 10.5194/amt-4-1735-2011. URL: https://amt.copernicus.org/articles/4/1735/2011/ (visited on 04/29/2023).

Kuhlmann, G., G. Broquet, J. Marshall, V. Clément, A. Löscher, Y. Meijer, and D. Brunner (2019). "Detectability of CO2 Emission Plumes of Cities and Power Plants with the Copernicus Anthropogenic CO2 Monitoring (CO2M) Mission". *Atmospheric Measurement Techniques*. ISSN: 1867-8548. DOI: 10.5194/amt-12-6695-2019. URL: https://amt.copernicus.org/articles/12/6695/2019/ (visited on 09/21/2021).

Kuhlmann, G., S. Henne, Y. Meijer, L. Emmenegger, and D. Brunner (2021). *Quantifying CO2 Emissions of Power Plants with the CO2M Mission*. other. pico. DOI: 10.5194/egusphere-egu21-3260. URL: https://meetingorganizer.copernicus.org/EGU21/EGU21-3260.html (visited on 09/21/2021).

Kuhn, L., J. Kuhn, T. Wagner, and U. Platt (2022). "The NO2 Camera Based on Gas Correlation Spectroscopy". *Atmospheric Measurement Techniques*. ISSN: 1867-8548. DOI: 10.5194/amt-15-1395-2022. URL: https://amt.copernicus.org/articles/15/1395/2022/ (visited on 06/19/2022).

Kumar, P., C. Caldow, G. Broquet, A. Shah, O. Laurent, C. Yver-Kwok, S. Ars, S. Defratyka, S. Gichuki, L. Lienhardt, M. Lozano, J.-D. Paris, F. Vogel, C. Bouchet, E. Allegrini, R. Kelly, C. Juery, and P. Ciais (2023). *Detection and Long-Term Quantification of Methane Emissions from an Active Landfill*. preprint. Gases/In Situ Measurement/Data Processing and Information Retrieval. DOI: 10.5194/amt-2023-124. URL: https://amt.copernicus.org/preprints/amt-2023-124/ (visited on 02/20/2024).

Kuze, A., H. Suto, M. Nakajima, and T. Hamazaki (2009). "Thermal and near Infrared Sensor for Carbon Observation Fourier-transform Spectrometer on the Greenhouse Gases Observing Satellite for Greenhouse Gases Monitoring". *Applied Optics*. ISSN: 0003-6935, 1539-4522.

DOI: 10.1364/AO.48.006716. URL: https://www.osapublishing.org/abstract.cfm?URI=ao-48-35-6716 (visited on 04/28/2020).

Lauvaux, T., C. Giron, M. Mazzolini, A. d'Aspremont, R. Duren, D. Cusworth, D. Shindell, and P. Ciais (2022). "Global Assessment of Oil and Gas Methane Ultra-Emitters". *Science*. ISSN: 0036-8075, 1095-9203. DOI: 10.1126/science.abj4351. URL: https://www.science.org/doi/10.1126/science.abj4351 (visited on 10/27/2023).

Lenhard, K., A. Baumgartner, and T. Schwarzmaier (2015). "Independent Laboratory Characterization of NEO HySpex Imaging Spectrometers VNIR-1600 and SWIR-320m-e". *IEEE Transactions on Geoscience and Remote Sensing*. ISSN: 0196-2892, 1558-0644. DOI: 10.1109/TGRS.2014.2349737. URL: http://ieeexplore.ieee.org/document/6891322/ (visited on 08/12/2020).

Lenton, T. M., C. Xu, J. F. Abrams, A. Ghadiali, S. Loriani, B. Sakschewski, C. Zimm, K. L. Ebi, R. R. Dunn, J.-C. Svenning, and M. Scheffer (2023). "Quantifying the Human Cost of Global Warming". *Nature Sustainability*. ISSN: 2398-9629. DOI: 10.1038/s41893-023-01132-6. URL: https://www.nature.com/articles/s41893-023-01132-6 (visited on 06/22/2023).

Levelt, P., D. Stein, S.-E. Martinez, W. Tang, H. Worden, L. Emmons, B. Gaubert, H. Eskes, R. Van Der A, and P. Veefkind (2023). *Investigating Expanding Air Pollution and Climate Change on the African Continent Using TROPOMI Data*. DOI: 10.5194/egusphere-egu23-10385. URL: https://meetingorganizer.copernicus.org/EGU23/EGU23-10385.html (visited on 01/02/2024).

Liu, M., R. van der A, M. van Weele, H. Eskes, X. Lu, P. Veefkind, J. de Laat, H. Kong, J. Wang, J. Sun, J. Ding, Y. Zhao, and H. Weng (2021). "A New Divergence Method to Quantify Methane Emissions Using Observations of Sentinel-5P TROPOMI". *Geophysical Research Letters*. ISSN: 0094-8276, 1944-8007. DOI: 10.1029/2021GL094151.

Luther, A., R. Kleinschek, L. Scheidweiler, S. Defratyka, M. Stanisavljevic, A. Forstmaier, A. Dandocsi, S. Wolff, D. Dubravica, N. Wildmann, J. Kostinek, P. Jöckel, A.-L. Nickl, T. Klausner, F. Hase, M. Frey, J. Chen, F. Dietrich, J. Necki, J. Swolkień, A. Fix, A. Roiger, and A. Butz (2019). "Quantifying CH_4 Emissions from Hard Coal Mines Using Mobile Sun-Viewing Fourier Transform Spectrometry". *Atmospheric Measurement Techniques*. ISSN: 1867-8548. DOI: 10.5194/amt-12-5217-2019. URL: https://www.atmos-meas-tech.net/12/5217/2019/ (visited on 12/17/2019).

Luther, A., J. Kostinek, R. Kleinschek, S. Defratyka, M. Stanisavljević, A. Forstmaier, A. Dandocsi, L. Scheidweiler, D. Dubravica, N. Wildmann, F. Hase, M. M. Frey, J. Chen, F. Dietrich, J. Necki, J. Swolkień, C. Knote, S. N. Vardag, A. Roiger, and A. Butz (2022). "Observational Constraints on Methane Emissions from Polish Coal Mines Using a Ground-Based Remote Sensing Network". *Atmospheric Chemistry and Physics*. ISSN: 1680-7324. DOI: 10.5194/acp-22-5859-2022. URL: https://acp.copernicus.org/articles/22/5859/2022/ (visited on 06/30/2022).

Maasakkers, J. D., D. J. Jacob, M. P. Sulprizio, T. R. Scarpelli, H. Nesser, J.-X. Sheng, Y. Zhang, M. Hersher, A. A. Bloom, K. W. Bowman, J. R. Worden, G. Janssens-Maenhout, and R. J. Parker (2019). "Global Distribution of Methane Emissions, Emission Trends, and OH Concentrations and Trends Inferred from an Inversion of GOSAT Satellite Data for 2010–2015". *Atmospheric Chemistry and Physics*. ISSN: 1680-7324. DOI: 10.5194/acp-19-7859-2019. URL: https://www.atmos-chem-phys.net/19/7859/2019/ (visited on 12/17/2019).

Maasakkers, J. D., D. J. Varon, A. Elfarsdóttir, J. McKeever, D. Jervis, G. Mahapatra, S. Pandey, A. Lorente, T. Borsdorff, L. R. Foorthuis, B. J. Schuit, P. Tol, T. A. van Kempen, R. van Hees, and I. Aben (2022). "Using Satellites to Uncover Large Methane Emissions from Landfills". *Science Advances*. ISSN: 2375-2548. DOI: 10.1126/sciadv.abn9683. URL: https://www.science.org/doi/10.1126/sciadv.abn9683 (visited on 10/31/2022).

Manolakis, D., E. Truslow, M. Pieper, T. Cooley, and M. Brueggeman (2014). "Detection Algorithms in Hyperspectral Imaging Systems: An Overview of Practical Algorithms". *IEEE Signal Processing Magazine*. ISSN: 1053-5888. DOI: 10.1109/MSP.2013.2278915. URL: http://ieeexplore.ieee.org/document/6678280/ (visited on 05/20/2022).

Masson-Delmotte, V., P. Zhai, A. Pirani, S. L. Connors, C. Péan, S. Berger, N. Chaud, Y. Chen, L. Goldfarb, M. Gomis, M. Huang, K. Leitzell, E. Lonnoy, J. Metthews, T. Maycook, T. Waterfield, O. Yelekci, R. Yu, and B. Zhou (2021). *Climate Change 2021: The Physical Science Basis. Contribution of Working Group I to the Sixth Assessment Report of the Intergovernmental Panel on Climate Change*. Cambridge, United Kingdom and New York, NY, USA. DOI: https://doi.org/10.1017/9781009157896.

Metz, E.-M., S. N. Vardag, S. Basu, M. Jung, B. Ahrens, T. El-Madany, S. Sitch, V. K. Arora, P. R. Briggs, P. Friedlingstein, D. S. Goll, A. K. Jain, E. Kato, D. Lombardozzi, J. E. M. S. Nabel, B. Poulter, R. Séférian, H. Tian, A. Wiltshire, W. Yuan, X. Yue, S. Zaehle, N. M. Deutscher, D. W. T. Griffith, and A. Butz (2023). "Soil Respiration–Driven CO_2 Pulses Dominate Australia's Flux Variability". *Science*. ISSN: 0036-8075, 1095-9203. DOI: 10.1126/science.add7833. URL: https://www.science.org/doi/10.1126/science.add7833 (visited on 10/26/2023).

Miller, S. M. and A. M. Michalak (2017). "Constraining Sector-Specific CO2 and CH4 Emissions in the US". *Atmospheric Chemistry and Physics*. ISSN: 1680-7324. DOI: 10.5194/acp-17-3963-2017. URL: https://acp.copernicus.org/articles/17/3963/2017/ (visited on 10/27/2023).

Mouroulis, P. and R. O. Green (2018). "Review of High Fidelity Imaging Spectrometer Design for Remote Sensing". *Optical Engineering*. ISSN: 0091-3286. DOI: 10.1117/1.OE.57.4.040901. URL: https://www.spiedigitallibrary.org/journals/optical-engineering/volume-57/issue-04/040901/Review-of-high-fidelity-imaging-spectrometer-design-for-remote-sensing/10.1117/1.OE.57.4.040901.full (visited on 07/02/2020).

Nassar, R., T. G. Hill, C. A. McLinden, D. Wunch, D. B. A. Jones, and D. Crisp (2017). "Quantifying CO_2 Emissions From Individual Power Plants From Space". *Geophysical Research Letters*. ISSN: 0094-8276, 1944-8007. DOI: 10.1002/2017GL074702.

NEO (2014). *HySpex User Manual v4.1*. Norsk Elektro Optikk AS.

Nesme, N., P.-Y. Foucher, and S. Doz (2020). "DETECTION AND QUANTIFICATION OF INDUSTRIAL METHANE PLUME WITH THE AIRBORNE HYSPEX-NEO CAMERA AND APPLICATIONS TO SATELLITE DATA". *The International Archives of the Photogrammetry, Remote Sensing and Spatial Information Sciences*. ISSN: 2194-9034. DOI: 10.5194/isprs-archives-XLIII-B3-2020-821-2020. URL: https://www.int-arch-photogramm-remote-sens-spatial-inf-sci.net/XLIII-B3-2020/821/2020/ (visited on 03/24/2023).

Nesser, H., D. J. Jacob, J. D. Maasakkers, A. Lorente, Z. Chen, X. Lu, L. Shen, Z. Qu, M. P. Sulprizio, M. Winter, S. Ma, A. A. Bloom, J. R. Worden, R. N. Stavins, and C. A. Randles (2023). *High-Resolution U.S. Methane Emissions Inferred from an Inversion of 2019 TROPOMI Satellite Data: Contributions from Individual States, Urban Areas, and Landfills*. DOI: 10.5194/

egusphere-2023-946. URL: https://egusphere.copernicus.org/preprints/2023/egusphere-2023-946/ (visited on 12/14/2023).

Ngo, N., D. Lisak, H. Tran, and J.-M. Hartmann (2013). "An Isolated Line-Shape Model to Go beyond the Voigt Profile in Spectroscopic Databases and Radiative Transfer Codes". *Journal of Quantitative Spectroscopy and Radiative Transfer*. ISSN: 00224073. DOI: 10.1016/j.jqsrt.2013.05.034. URL: https://linkinghub.elsevier.com/retrieve/pii/S0022407313002422 (visited on 05/21/2020).

Nieuwstadt, F. (1992). "A Large-Eddy Simulation of a Line Source in a Convective Atmospheric Boundary Layer—II. Dynamics of a Buoyant Line Source". *Atmospheric Environment. Part A. General Topics*. ISSN: 09601686. DOI: 10.1016/0960-1686(92)90332-F. URL: https://linkinghub.elsevier.com/retrieve/pii/096016869290332F (visited on 12/22/2023).

NIR (2018). *POLAND'S NATIONAL INVENTORY REPORT 2018*. URL: https://www.kobize.pl/uploads/materialy/materialy_do_pobrania/krajowa_inwentaryzacja_emisji/NIR_2018_POL.pdf.

Nisbet, E. G., R. E. Fisher, D. Lowry, J. L. France, G. Allen, S. Bakkaloglu, T. J. Broderick, M. Cain, M. Coleman, J. Fernandez, G. Forster, P. T. Griffiths, C. P. Iverach, B. F. J. Kelly, M. R. Manning, P. B. R. Nisbet-Jones, J. A. Pyle, A. Townsend-Small, A. al-Shalaan, N. Warwick, and G. Zazzeri (2020). "Methane Mitigation: Methods to Reduce Emissions, on the Path to the Paris Agreement". *Reviews of Geophysics*. DOI: 10.1029/2019RG000675. URL: https://onlinelibrary.wiley.com/doi/abs/10.1029/2019RG000675 (visited on 10/31/2022).

Nisbet, E. G., E. J. Dlugokencky, R. E. Fisher, J. L. France, D. Lowry, M. R. Manning, S. E. Michel, and N. J. Warwick (2021). "Atmospheric Methane and Nitrous Oxide: Challenges Alongthe Path to Net Zero". *Philosophical Transactions of the Royal Society A: Mathematical, Physical and Engineering Sciences*. ISSN: 1364-503X, 1471-2962. DOI: 10.1098/rsta.2020.0457. URL: https://royalsocietypublishing.org/doi/10.1098/rsta.2020.0457 (visited on 10/31/2022).

O'Dell, C. W., B. Connor, H. Bösch, D. O'Brien, C. Frankenberg, R. Castano, M. Christi, D. Eldering, B. Fisher, M. Gunson, J. McDuffie, C. E. Miller, V. Natraj, F. Oyafuso, I. Polonsky, M. Smyth, T. Taylor, G. C. Toon, P. O. Wennberg, and D. Wunch (2012). "The ACOS CO2 Retrieval Algorithm – Part 1: Description and Validation against Synthetic Observations". *Atmospheric Measurement Techniques*. ISSN: 1867-8548. DOI: 10.5194/amt-5-99-2012. URL: https://amt.copernicus.org/articles/5/99/2012/ (visited on 07/10/2023).

O'Dell, C. W., A. Eldering, P. O. Wennberg, D. Crisp, M. R. Gunson, B. Fisher, C. Frankenberg, M. Kiel, H. Lindqvist, L. Mandrake, A. Merrelli, V. Natraj, R. R. Nelson, G. B. Osterman, V. H. Payne, T. E. Taylor, D. Wunch, B. J. Drouin, F. Oyafuso, A. Chang, J. McDuffie, M. Smyth, D. F. Baker, S. Basu, F. Chevallier, S. M. R. Crowell, L. Feng, P. I. Palmer, M. Dubey, O. E. García, D. W. T. Griffith, F. Hase, L. T. Iraci, R. Kivi, I. Morino, J. Notholt, H. Ohyama, C. Petri, C. M. Roehl, M. K. Sha, K. Strong, R. Sussmann, Y. Te, O. Uchino, and V. A. Velazco (2018). "Improved Retrievals of Carbon Dioxide from Orbiting Carbon Observatory-2 with the Version 8 ACOS Algorithm". *Atmospheric Measurement Techniques*. ISSN: 1867-8548. DOI: 10.5194/amt-11-6539-2018. URL: https://amt.copernicus.org/articles/11/6539/2018/ (visited on 07/10/2023).

Ocko, I. B., T. Sun, D. Shindell, M. Oppenheimer, A. N. Hristov, S. W. Pacala, D. L. Mauzerall, Y. Xu, and S. P. Hamburg (2021). "Acting Rapidly to Deploy Readily Available Methane Mitigation Measures by Sector Can Immediately Slow Global Warming". *Environmental Research*

Letters. ISSN: 1748-9326. DOI: 10.1088/1748-9326/abf9c8. URL: https://iopscience.iop.org/article/10.1088/1748-9326/abf9c8 (visited on 10/31/2022).

Palmer, P. I., L. Feng, M. F. Lunt, R. J. Parker, H. Bösch, X. Lan, A. Lorente, and T. Borsdorff (2021). "The Added Value of Satellite Observations of Methane Forunderstanding the Contemporary Methane Budget". *Philosophical Transactions of the Royal Society A: Mathematical, Physical and Engineering Sciences*. ISSN: 1364-503X, 1471-2962. DOI: 10.1098/rsta.2021.0106. URL: https://royalsocietypublishing.org/doi/10.1098/rsta.2021.0106 (visited on 10/27/2023).

Pandey, S., R. Gautam, S. Houweling, H. D. van der Gon, P. Sadavarte, T. Borsdorff, O. Hasekamp, J. Landgraf, P. Tol, T. van Kempen, R. Hoogeveen, R. van Hees, S. P. Hamburg, J. D. Maasakkers, and I. Aben (2019). "Satellite Observations Reveal Extreme Methane Leakage from a Natural Gas Well Blowout". *Proceedings of the National Academy of Sciences*. ISSN: 0027-8424, 1091-6490. DOI: 10.1073/pnas.1908712116. URL: https://pnas.org/doi/full/10.1073/pnas.1908712116 (visited on 10/31/2022).

Pandolfi, M., L. Alados-Arboledas, A. Alastuey, M. Andrade, C. Angelov, B. Artiñano, J. Backman, U. Baltensperger, P. Bonasoni, N. Bukowiecki, M. Collaud Coen, S. Conil, E. Coz, V. Crenn, V. Dudoitis, M. Ealo, K. Eleftheriadis, O. Favez, P. Fetfatzis, M. Fiebig, H. Flentje, P. Ginot, M. Gysel, B. Henzing, A. Hoffer, A. Holubova Smejkalova, I. Kalapov, N. Kalivitis, G. Kouvarakis, A. Kristensson, M. Kulmala, H. Lihavainen, C. Lunder, K. Luoma, H. Lyamani, A. Marinoni, N. Mihalopoulos, M. Moerman, J. Nicolas, C. O'Dowd, T. Petäjä, J.-E. Petit, J. M. Pichon, N. Prokopciuk, J.-P. Putaud, S. Rodríguez, J. Sciare, K. Sellegri, E. Swietlicki, G. Titos, T. Tuch, P. Tunved, V. Ulevicius, A. Vaishya, M. Vana, A. Virkkula, S. Vratolis, E. Weingartner, A. Wiedensohler, and P. Laj (2018). "A European Aerosol Phenomenology – 6: Scattering Properties of Atmospheric Aerosol Particles from 28 ACTRIS Sites". *Atmospheric Chemistry and Physics*. ISSN: 1680-7324. DOI: 10.5194/acp-18-7877-2018. URL: https://acp.copernicus.org/articles/18/7877/2018/ (visited on 11/06/2023).

Pei, Z., G. Han, H. Mao, C. Chen, T. Shi, K. Yang, X. Ma, and W. Gong (2023). "Improving Quantification of Methane Point Source Emissions from Imaging Spectroscopy". *Remote Sensing of Environment*. ISSN: 00344257. DOI: 10.1016/j.rse.2023.113652. URL: https://linkinghub.elsevier.com/retrieve/pii/S0034425723002031 (visited on 06/19/2023).

Peters, G. (2018). "Reliable Data - Continuous Wave Lidars Can Provide More Accurate Wind Measurements with High Resolution at Short Distances". *Meteorological Technology International*. URL: http://www.ukimediaevents.com/publication/8511a42f/1.

Peters, G. P., C. Le Quéré, R. M. Andrew, J. G. Canadell, P. Friedlingstein, T. Ilyina, R. B. Jackson, F. Joos, J. I. Korsbakken, G. A. McKinley, S. Sitch, and P. Tans (2017). "Towards Real-Time Verification of CO2 Emissions". *Nature Climate Change*. ISSN: 1758-678X, 1758-6798. DOI: 10.1038/s41558-017-0013-9. URL: http://www.nature.com/articles/s41558-017-0013-9 (visited on 01/27/2022).

Petty, G. W. (2006). *A First Course in Atmospheric Radiation*. 2. ed. Sundog Publ, Madison, Wisc. 459 pp. ISBN: 978-0-9729033-1-8.

Platt, U. and T. Wagner (1998). "Satellite Mapping of Enhanced BrO Concentrations in the Troposphere". *Nature*. ISSN: 0028-0836, 1476-4687. DOI: 10.1038/26723. URL: https://www.nature.com/articles/26723 (visited on 11/03/2023).

Platt, U. (2017). "Air Monitoring by Differential Optical Absorption Spectroscopy". In: *Encyclopedia of Analytical Chemistry*. Ed. by R. A. Meyers. 1st ed. Wiley. ISBN: 978-0-471-97670-7 978-0-470-02731-8. DOI: 10.1002/9780470027318.a0706.pub2. URL: https://onlinelibrary.wiley.com/doi/10.1002/9780470027318.a0706.pub2 (visited on 11/03/2023).

Pöhler, D. (2011). *Noise Tests to Determine the Instrument Performance and Lowest Achievable Detection Limit*.

Prahl, S. (2023). *Miepython: Pure Python Implementation of Mie Scattering*. Version v2.5.3. Zenodo. DOI: 10.5281/ZENODO.8218010. URL: https://zenodo.org/record/8218010 (visited on 10/16/2023).

Prather, M. J., C. D. Holmes, and J. Hsu (2012). "Reactive Greenhouse Gas Scenarios: Systematic Exploration of Uncertainties and the Role of Atmospheric Chemistry". *Geophysical Research Letters*. ISSN: 0094-8276, 1944-8007. DOI: 10.1029/2012GL051440. URL: https://agupubs.onlinelibrary.wiley.com/doi/10.1029/2012GL051440 (visited on 11/22/2023).

Pregger, T. and R. Friedrich (2009). "Effective Pollutant Emission Heights for Atmospheric Transport Modelling Based on Real-World Information". *Environmental Pollution*. ISSN: 02697491. DOI: 10.1016/j.envpol.2008.09.027. URL: https://linkinghub.elsevier.com/retrieve/pii/S0269749108004466 (visited on 09/28/2021).

Radman, A., M. Mahdianpari, D. J. Varon, and F. Mohammadimanesh (2023). "S2MetNet: A Novel Dataset and Deep Learning Benchmark for Methane Point Source Quantification Using Sentinel-2 Satellite Imagery". *Remote Sensing of Environment*. ISSN: 00344257. DOI: 10.1016/j.rse.2023.113708. URL: https://linkinghub.elsevier.com/retrieve/pii/S0034425723002596 (visited on 02/26/2024).

Roberts, D. A., E. S. Bradley, R. Cheung, I. Leifer, P. E. Dennison, and J. S. Margolis (2010). "Mapping Methane Emissions from a Marine Geological Seep Source Using Imaging Spectrometry". *Remote Sensing of Environment*. ISSN: 00344257. DOI: 10.1016/j.rse.2009.10.015. URL: https://linkinghub.elsevier.com/retrieve/pii/S0034425709003241 (visited on 10/27/2023).

Rodgers, C. D. (2000). *Inverse Methods for Atmospheric Sounding: Theory and Practice*. Series on Atmospheric, Oceanic and Planetary Physics. World Scientific, Singapore. ISBN: 978-981-02-2740-1.

Roedel, W. and T. Wagner (2011). *Physik unserer Umwelt: die Atmosphäre*. 4. Aufl., 1. korrigierter Nachdr. Springer, Berlin. 589 pp. ISBN: 978-3-642-15728-8.

Roger, J., L. Guanter, J. Gorroño, and I. Irakulis-Loitxate (2023a). *Exploiting the Entire Near-Infrared Spectral Range to Improve the Detection of Methane Plumes with High-Resolution Imaging Spectrometers*. preprint. Gases/Remote Sensing/Data Processing and Information Retrieval. DOI: 10.5194/amt-2023-168. URL: https://amt.copernicus.org/preprints/amt-2023-168/amt-2023-168.pdf (visited on 02/26/2024).

Roger, J., I. Irakulis-Loitxate, A. Valverde, J. Gorroño, S. Chabrillat, M. Brell, and L. Guanter (2023b). *High-Resolution Methane Mapping with the EnMAP Satellite Imaging Spectroscopy Mission*. preprint. Atmospheric Sciences. DOI: 10.31223/X5M65Z. URL: https://eartharxiv.org/repository/view/5235/ (visited on 04/24/2023).

Sadavarte, P., S. Pandey, J. D. Maasakkers, A. Lorente, T. Borsdorff, H. Denier van der Gon, S. Houweling, and I. Aben (2021). "Methane Emissions from Superemitting Coal Mines in Australia Quantified Using TROPOMI Satellite Observations". *Environmental Science & Technol-*

ogy. ISSN: 0013-936X, 1520-5851. DOI: 10.1021/acs.est.1c03976. URL: https://pubs.acs.org/doi/10.1021/acs.est.1c03976 (visited on 10/31/2022).

Sandau, F., S. Timme, C. Baumgarten, R. Beckers, D. W. Bretschneider, S. Briem, J. Frauenstein, C. Gibis, P. Gniffke, S. Grimm, C. Herbstritt, and K. Juhrich (2021). "Daten und Fakten zu Braun- und Steinkohlen: Stand und Perspektiven 2021". ISSN: 1862-4804. URL: https://www.umweltbundesamt.de/publikationen.

Saunois, M., P. Bousquet, B. Poulter, A. Peregon, P. Ciais, J. G. Canadell, E. J. Dlugokencky, G. Etiope, D. Bastviken, S. Houweling, G. Janssens-Maenhout, F. N. Tubiello, S. Castaldi, R. B. Jackson, M. Alexe, V. K. Arora, D. J. Beerling, P. Bergamaschi, D. R. Blake, G. Brailsford, V. Brovkin, L. Bruhwiler, C. Crevoisier, P. Crill, K. Covey, C. Curry, C. Frankenberg, N. Gedney, L. Höglund-Isaksson, M. Ishizawa, A. Ito, F. Joos, H.-S. Kim, T. Kleinen, P. Krummel, J.-F. Lamarque, R. Langenfelds, R. Locatelli, T. Machida, S. Maksyutov, K. C. McDonald, J. Marshall, J. R. Melton, I. Morino, V. Naik, S. O'Doherty, F.-J. W. Parmentier, P. K. Patra, C. Peng, S. Peng, G. P. Peters, I. Pison, C. Prigent, R. Prinn, M. Ramonet, W. J. Riley, M. Saito, M. Santini, R. Schroeder, I. J. Simpson, R. Spahni, P. Steele, A. Takizawa, B. F. Thornton, H. Tian, Y. Tohjima, N. Viovy, A. Voulgarakis, M. van Weele, G. R. van der Werf, R. Weiss, C. Wiedinmyer, D. J. Wilton, A. Wiltshire, D. Worthy, D. Wunch, X. Xu, Y. Yoshida, B. Zhang, Z. Zhang, and Q. Zhu (2016). "The Global Methane Budget 2000–2012". *Earth System Science Data*. ISSN: 1866-3516. DOI: 10.5194/essd-8-697-2016. URL: https://www.earth-syst-sci-data.net/8/697/2016/ (visited on 12/17/2019).

Saunois, M., A. R. Stavert, B. Poulter, P. Bousquet, J. G. Canadell, R. B. Jackson, P. A. Raymond, E. J. Dlugokencky, S. Houweling, P. K. Patra, P. Ciais, V. K. Arora, D. Bastviken, P. Bergamaschi, D. R. Blake, G. Brailsford, L. Bruhwiler, K. M. Carlson, M. Carrol, S. Castaldi, N. Chandra, C. Crevoisier, P. M. Crill, K. Covey, C. L. Curry, G. Etiope, C. Frankenberg, N. Gedney, M. I. Hegglin, L. Höglund-Isaksson, G. Hugelius, M. Ishizawa, A. Ito, G. Janssens-Maenhout, K. M. Jensen, F. Joos, T. Kleinen, P. B. Krummel, R. L. Langenfelds, G. G. Laruelle, L. Liu, T. Machida, S. Maksyutov, K. C. McDonald, J. McNorton, P. A. Miller, J. R. Melton, I. Morino, J. Müller, F. Murguia-Flores, V. Naik, Y. Niwa, S. Noce, S. O'Doherty, R. J. Parker, C. Peng, S. Peng, G. P. Peters, C. Prigent, R. Prinn, M. Ramonet, P. Regnier, W. J. Riley, J. A. Rosentreter, A. Segers, I. J. Simpson, H. Shi, S. J. Smith, L. P. Steele, B. F. Thornton, H. Tian, Y. Tohjima, F. N. Tubiello, A. Tsuruta, N. Viovy, A. Voulgarakis, T. S. Weber, M. van Weele, G. R. van der Werf, R. F. Weiss, D. Worthy, D. Wunch, Y. Yin, Y. Yoshida, W. Zhang, Z. Zhang, Y. Zhao, B. Zheng, Q. Zhu, Q. Zhu, and Q. Zhuang (2020). "The Global Methane Budget 2000–2017". *Earth System Science Data*. ISSN: 1866-3516. DOI: 10.5194/essd-12-1561-2020. URL: https://essd.copernicus.org/articles/12/1561/2020/ (visited on 10/26/2022).

Schaum, A. (2021). "A Uniformly Most Powerful Detector of Gas Plumes against a Cluttered Background". *Remote Sensing of Environment*. ISSN: 00344257. DOI: 10.1016/j.rse.2021.112443. URL: https://linkinghub.elsevier.com/retrieve/pii/S0034425721001619 (visited on 06/21/2023).

Schuit, B. J., J. D. Maasakkers, P. Bijl, G. Mahapatra, A.-W. Van Den Berg, S. Pandey, A. Lorente, T. Borsdorff, S. Houweling, D. J. Varon, J. McKeever, D. Jervis, M. Girard, I. Irakulis-Loitxate, J. Gorroño, L. Guanter, D. H. Cusworth, and I. Aben (2023). "Automated Detection and Monitoring of Methane Super-Emitters Using Satellite Data". *Atmospheric Chemistry and Phy-*

sics. ISSN: 1680-7324. DOI: 10.5194/acp-23-9071-2023. URL: https://acp.copernicus.org/articles/23/9071/2023/ (visited on 09/28/2023).

Schwandner, F. M., M. R. Gunson, C. E. Miller, S. A. Carn, A. Eldering, T. Krings, K. R. Verhulst, D. S. Schimel, H. M. Nguyen, D. Crisp, C. W. O'Dell, G. B. Osterman, L. T. Iraci, and J. R. Podolske (2017). "Spaceborne Detection of Localized Carbon Dioxide Sources". *Science*. ISSN: 0036-8075, 1095-9203. DOI: 10.1126/science.aam5782. URL: https://www.sciencemag.org/lookup/doi/10.1126/science.aam5782 (visited on 01/06/2021).

Shaw, G. A. and H.-h. K. Burke (2003). "Spectral Imaging for Remote Sensing".

Sherwin, E. D., J. S. Rutherford, Y. Chen, S. Aminfard, E. A. Kort, R. B. Jackson, and A. R. Brandt (2023). "Single-Blind Validation of Space-Based Point-Source Detection and Quantification of Onshore Methane Emissions". *Scientific Reports*. ISSN: 2045-2322. DOI: 10.1038/s41598-023-30761-2. URL: https://www.nature.com/articles/s41598-023-30761-2 (visited on 05/11/2023).

Shi, T., Z. Han, G. Han, X. Ma, H. Chen, T. Andersen, H. Mao, C. Chen, H. Zhang, and W. Gong (2022). "Retrieving CH $_4$ -Emission Rates from Coal Mine Ventilation Shafts Using UAV-based AirCore Observations and the Genetic Algorithm–Interior Point Penalty Function (GA-IPPF) Model". *Atmospheric Chemistry and Physics*. ISSN: 1680-7324. DOI: 10.5194/acp-22-13881-2022. URL: https://acp.copernicus.org/articles/22/13881/2022/ (visited on 01/26/2023).

Siegel, T. (2023). "Matched Filter Sensitivity Studies for Spectral Greenhouse Gas Imagery". BA thesis. Universität Heidelberg.

Sierk, B., J.-L. Bezy, A. Löscher, and Y. Meijer (2019). "The European CO2 Monitoring Mission: Observing Anthropogenic Greenhouse Gas Emissions from Space". In: *International Conference on Space Optics — ICSO 2018*. International Conference on Space Optics - ICSO 2018. Ed. by N. Karafolas, Z. Sodnik, and B. Cugny. SPIE, Chania, Greece. ISBN: 978-1-5106-3077-2 978-1-5106-3078-9. DOI: 10.1117/12.2535941. URL: https://www.spiedigitallibrary.org/conference-proceedings-of-spie/11180/2535941/The-European-CO2-Monitoring-Mission--observing-anthropogenic-greenhouse-gas/10.1117/12.2535941.full (visited on 12/21/2021).

Sindram, M. (2021). "Qualifizierung Und Charakterisierung Eines Lagesensors Für Stationäre Hyperspektralkameras". BA thesis. Universität Heidelberg.

Slater, J. A. and S. Malys (1998). "WGS 84 — Past, Present and Future". In: *Advances in Positioning and Reference Frames*. Ed. by F. K. Brunner. Red. by K.-P. Schwarz. Springer Berlin Heidelberg, Berlin, Heidelberg. ISBN: 978-3-642-08425-6 978-3-662-03714-0. DOI: 10.1007/978-3-662-03714-0_1. URL: http://link.springer.com/10.1007/978-3-662-03714-0_1 (visited on 05/20/2022).

Smith, C. J., R. J. Kramer, G. Myhre, P. M. Forster, B. J. Soden, T. Andrews, O. Boucher, G. Faluvegi, D. Fläschner, Ø. Hodnebrog, M. Kasoar, V. Kharin, A. Kirkevåg, J.-F. Lamarque, J. Mülmenstädt, D. Olivié, T. Richardson, B. H. Samset, D. Shindell, P. Stier, T. Takemura, A. Voulgarakis, and D. Watson-Parris (2018). "Understanding Rapid Adjustments to Diverse Forcing Agents". *Geophysical Research Letters*. ISSN: 0094-8276, 1944-8007. DOI: 10.1029/2018GL079826. URL: https://agupubs.onlinelibrary.wiley.com/doi/10.1029/2018GL079826 (visited on 11/22/2023).

Stamnes, K., G. E. Thomas, and J. J. Stamnes (2017). *Radiative Transfer in the Atmosphere and Ocean*. 2nd ed. Cambridge university press, Cambridge. ISBN: 978-1-107-09473-4.

Strandgren, J., D. Krutz, J. Wilzewski, C. Paproth, I. Sebastian, K. R. Gurney, J. Liang, A. Roiger, and A. Butz (2020). "Towards Spaceborne Monitoring of Localized CO2 Emissions: An Instrument Concept and First Performance Assessment". *Atmospheric Measurement Techniques*. ISSN: 1867-8548. DOI: 10.5194/amt-13-2887-2020. URL: https://amt.copernicus.org/articles/13/2887/2020/ (visited on 01/06/2021).

Swolkień, J. (2020). "Polish Underground Coal Mines as Point Sources of Methane Emission to the Atmosphere". *International Journal of Greenhouse Gas Control*. ISSN: 17505836. DOI: 10.1016/j.ijggc.2019.102921. URL: https://linkinghub.elsevier.com/retrieve/pii/S175058361930266X (visited on 01/30/2023).

Swolkień, J., A. Fix, and M. Gałkowski (2022). "Factors Influencing the Temporal Variability of Atmospheric Methane Emissions from Upper Silesia Coal Mines: A Case Study from the CoMet Mission". *Atmospheric Chemistry and Physics*. ISSN: 1680-7324. DOI: 10.5194/acp-22-16031-2022. URL: https://acp.copernicus.org/articles/22/16031/2022/ (visited on 02/22/2023).

Taylor, G. I. (1922). "Diffusion by Continuous Movements". *Proceedings of the London Mathematical Society*. ISSN: 00246115. DOI: 10.1112/plms/s2-20.1.196. URL: http://doi.wiley.com/10.1112/plms/s2-20.1.196 (visited on 12/22/2023).

Tennyson, J., P. F. Bernath, A. Campargue, A. G. Császár, L. Daumont, R. R. Gamache, J. T. Hodges, D. Lisak, O. V. Naumenko, L. S. Rothman, H. Tran, N. F. Zobov, J. Buldyreva, C. D. Boone, M. D. De Vizia, L. Gianfrani, J.-M. Hartmann, R. McPheat, D. Weidmann, J. Murray, N. H. Ngo, and O. L. Polyansky (2014). "Recommended Isolated-Line Profile for Representing High-Resolution Spectroscopic Transitions (IUPAC Technical Report)". *Pure and Applied Chemistry*. ISSN: 1365-3075, 0033-4545. DOI: 10.1515/pac-2014-0208. URL: http://www.degruyter.com/view/j/pac.2014.86.issue-12/pac-2014-0208/pac-2014-0208.xml (visited on 05/25/2020).

Theiler, J. P. and G. Gisler (1997). "Contiguity-Enhanced k-Means Clustering Algorithm for Unsupervised Multispectral Image Segmentation". In: Optical Science, Engineering and Instrumentation '97. Ed. by B. Javidi and D. Psaltis. San Diego, CA. DOI: 10.1117/12.279444. URL: http://proceedings.spiedigitallibrary.org/proceeding.aspx?articleid=930271 (visited on 11/03/2023).

Thompson, D. R., I. Leifer, H. Bovensmann, M. Eastwood, M. Fladeland, C. Frankenberg, K. Gerilowski, R. O. Green, S. Kratwurst, T. Krings, B. Luna, and A. K. Thorpe (2015). "Real-Time Remote Detection and Measurement for Airborne Imaging Spectroscopy: A Case Study with Methane". *Atmospheric Measurement Techniques*. ISSN: 1867-8548. DOI: 10.5194/amt-8-4383-2015. URL: https://www.atmos-meas-tech.net/8/4383/2015/ (visited on 12/17/2019).

Thorpe, A. K., R. M. Duren, S. Conley, K. R. Prasad, B. D. Bue, V. Yadav, K. T. Foster, T. Rafiq, F. M. Hopkins, M. L. Smith, M. L. Fischer, D. R. Thompson, C. Frankenberg, I. B. McCubbin, M. L. Eastwood, R. O. Green, and C. E. Miller (2020). "Methane Emissions from Underground Gas Storage in California". *Environmental Research Letters*. ISSN: 1748-9326. DOI: 10.1088/1748-9326/ab751d. URL: https://iopscience.iop.org/article/10.1088/1748-9326/ab751d (visited on 07/07/2022).

Thorpe, A. K., C. Frankenberg, A. Aubrey, D. Roberts, A. Nottrott, T. Rahn, J. Sauer, M. Dubey, K. Costigan, C. Arata, A. Steffke, S. Hills, C. Haselwimmer, D. Charlesworth, C. Funk, R. Green, S. Lundeen, J. Boardman, M. Eastwood, C. Sarture, S. Nolte, I. Mccubbin, D. Thompson, and J. McFadden (2016). "Mapping Methane Concentrations from a Controlled Release Experiment Using the next Generation Airborne Visible/Infrared Imaging Spectrometer". *Remote Sensing of Environment*. ISSN: 00344257. DOI: 10.1016/j.rse.2016.03.032. URL: https://linkinghub.elsevier.com/retrieve/pii/S0034425716301250 (visited on 07/07/2022).

Thorpe, A. K., C. Frankenberg, D. R. Thompson, R. M. Duren, A. D. Aubrey, B. D. Bue, R. O. Green, K. Gerilowski, T. Krings, J. Borchardt, E. A. Kort, C. Sweeney, S. Conley, D. A. Roberts, and P. E. Dennison (2017). "Airborne DOAS Retrievals of Methane, Carbon Dioxide, and Water Vapor Concentrations at High Spatial Resolution: Application to AVIRIS-NG". *Atmospheric Measurement Techniques*. ISSN: 1867-8548. DOI: 10.5194/amt-10-3833-2017. URL: https://www.atmos-meas-tech.net/10/3833/2017/ (visited on 03/25/2020).

Thorpe, A. K., C. O'Handley, G. D. Emmitt, P. L. DeCola, F. M. Hopkins, V. Yadav, A. Guha, S. Newman, J. D. Herner, M. Falk, and R. M. Duren (2021). "Improved Methane Emission Estimates Using AVIRIS-NG and an Airborne Doppler Wind Lidar". *Remote Sensing of Environment*. ISSN: 00344257. DOI: 10.1016/j.rse.2021.112681. URL: https://linkinghub.elsevier.com/retrieve/pii/S0034425721004016 (visited on 07/07/2022).

Thorpe, A. K., D. A. Roberts, E. S. Bradley, C. C. Funk, P. E. Dennison, and I. Leifer (2013). "High Resolution Mapping of Methane Emissions from Marine and Terrestrial Sources Using a Cluster-Tuned Matched Filter Technique and Imaging Spectrometry". *Remote Sensing of Environment*. ISSN: 00344257. DOI: 10.1016/j.rse.2013.03.018. URL: https://linkinghub.elsevier.com/retrieve/pii/S0034425713000977 (visited on 12/17/2019).

Tu, Q., M. Schneider, F. Hase, F. Khosrawi, B. Ertl, J. Necki, D. Dubravica, C. J. Diekmann, T. Blumenstock, and D. Fang (2022). "Quantifying CH_4 Emissions in Hard Coal Mines from TROPOMI and IASI Observations Using the Wind-Assigned Anomaly Method". *Atmospheric Chemistry and Physics*. ISSN: 1680-7324. DOI: 10.5194/acp-22-9747-2022. URL: https://acp.copernicus.org/articles/22/9747/2022/ (visited on 01/26/2023).

UNFCCC (2015). *United Nations Framework Convention on Climate Change, The Paris Agreement*. Letter.

Van de Hulst, H. (1981). *Light Scattering by Small Particles*. Dover publication, New York.

Van Westen, R. M., M. Kliphuis, and H. A. Dijkstra (2024). "Physics-Based Early Warning Signal Shows That AMOC Is on Tipping Course". *Science Advances*. ISSN: 2375-2548. DOI: 10.1126/sciadv.adk1189. URL: https://www.science.org/doi/10.1126/sciadv.adk1189 (visited on 02/21/2024).

Varon, D. J., J. McKeever, D. Jervis, J. D. Maasakkers, S. Pandey, S. Houweling, I. Aben, T. Scarpelli, and D. J. Jacob (2019). "Satellite Discovery of Anomalously Large Methane Point Sources From Oil/Gas Production". *Geophysical Research Letters*. ISSN: 0094-8276, 1944-8007. DOI: 10.1029/2019GL083798. URL: https://onlinelibrary.wiley.com/doi/10.1029/2019GL083798 (visited on 10/31/2022).

Varon, D. J., D. J. Jacob, B. Hmiel, R. Gautam, D. R. Lyon, M. Omara, M. Sulprizio, L. Shen, D. Pendergrass, H. Nesser, Z. Qu, Z. R. Barkley, N. L. Miles, S. J. Richardson, K. J. Davis, S. Pandey, X. Lu, A. Lorente, T. Borsdorff, J. D. Maasakkers, and I. Aben (2023). "Continuous Weekly Monitoring of Methane Emissions from the Permian Basin by Inversion of TROPOMI

Satellite Observations". *Atmospheric Chemistry and Physics*. ISSN: 1680-7324. DOI: 10.5194/acp-23-7503-2023. URL: https://acp.copernicus.org/articles/23/7503/2023/ (visited on 12/05/2023).

Varon, D. J., D. J. Jacob, J. McKeever, D. Jervis, B. O. A. Durak, Y. Xia, and Y. Huang (2018). "Quantifying Methane Point Sources from Fine-Scale Satellite Observations of Atmospheric Methane Plumes". *Atmospheric Measurement Techniques*. ISSN: 1867-8548. DOI: 10.5194/amt-11-5673-2018. URL: https://amt.copernicus.org/articles/11/5673/2018/ (visited on 05/17/2022).

Varon, D. J., D. Jervis, J. McKeever, I. Spence, D. Gains, and D. J. Jacob (2021). "High-Frequency Monitoring of Anomalous Methane Point Sources with Multispectral Sentinel-2 Satellite Observations". *Atmospheric Measurement Techniques*. ISSN: 1867-8548. DOI: 10.5194/amt-14-2771-2021.

Veefkind, J., I. Aben, K. McMullan, H. Förster, J. de Vries, G. Otter, J. Claas, H. Eskes, J. de Haan, Q. Kleipool, M. van Weele, O. Hasekamp, R. Hoogeveen, J. Landgraf, R. Snel, P. Tol, P. Ingmann, R. Voors, B. Kruizinga, R. Vink, H. Visser, and P. Levelt (2012). "TROPOMI on the ESA Sentinel-5 Precursor: A GMES Mission for Global Observations of the Atmospheric Composition for Climate, Air Quality and Ozone Layer Applications". *Remote Sensing of Environment*. ISSN: 00344257. DOI: 10.1016/j.rse.2011.09.027. URL: https://linkinghub.elsevier.com/retrieve/pii/S0034425712000661 (visited on 04/28/2020).

Verhulst, K. R., A. Karion, J. Kim, P. K. Salameh, R. F. Keeling, S. Newman, J. Miller, C. Sloop, T. Pongetti, P. Rao, C. Wong, F. M. Hopkins, V. Yadav, R. F. Weiss, R. M. Duren, and C. E. Miller (2017). "Carbon Dioxide and Methane Measurements from the Los Angeles Megacity Carbon Project – Part 1: Calibration, Urban Enhancements, and Uncertainty Estimates". *Atmospheric Chemistry and Physics*. ISSN: 1680-7324. DOI: 10.5194/acp-17-8313-2017. URL: https://acp.copernicus.org/articles/17/8313/2017/ (visited on 02/16/2024).

Wang, Y., C. Zhou, Z. Lou, H. Zhang, A. Hussain, L. Zhan, K. Yin, M. Fang, and X. Fei (2024). "Underestimated Methane Emissions from Solid Waste Disposal Sites Reveal Missed Greenhouse Gas Mitigation Opportunities". *Engineering*. ISSN: 20958099. DOI: 10.1016/j.eng.2023.12.011. URL: https://linkinghub.elsevier.com/retrieve/pii/S2095809924000651 (visited on 03/05/2024).

Wang, Y., G. Broquet, F.-M. Bréon, F. Lespinas, M. Buchwitz, M. Reuter, Y. Meijer, A. Loescher, G. Janssens-Maenhout, B. Zheng, and P. Ciais (2020). "PMIF v1.0: Assessing the Potential of Satellite Observations to Constrain CO2 Emissions from Large Cities and Point Sources over the Globe Using Synthetic Data". *Geoscientific Model Development*. ISSN: 1991-9603. DOI: 10.5194/gmd-13-5813-2020. URL: https://gmd.copernicus.org/articles/13/5813/2020/ (visited on 11/23/2023).

Watanabe, M., A. Oba, Y. Saito, G. Purevjav, B. Gankhuyag, M. Byamba-Ochir, B. Zamba, and T. Shishime (2023). "Enhancing Scientific Transparency in National CO2 Emissions Reports via Satellite-Based a Posteriori Estimates". *Scientific Reports*. ISSN: 2045-2322. DOI: 10.1038/s41598-023-42664-3. URL: https://www.nature.com/articles/s41598-023-42664-3 (visited on 10/02/2023).

Watine-Guiu, M., D. J. Varon, I. Irakulis-Loitxate, N. Balasus, and D. J. Jacob (2023). "Geostationary Satellite Observations of Extreme and Transient Methane Emissions from Oil and Gas Infrastructure". *Proceedings of the National Academy of Sciences*. ISSN: 0027-8424, 1091-6490.

DOI: 10.1073/pnas.2310797120. URL: https://pnas.org/doi/10.1073/pnas.2310797120 (visited on 02/16/2024).

Weil, J. C., W. H. Snyder, R. E. Lawson, and M. S. Shipman (2002). "Experiments On Buoyant Plume Dispersion In A Laboratory Convection Tank". *Boundary-Layer Meteorology*. ISSN: 0006-8314, 1573-1472. DOI: 10.1023/A:1013874816509. URL: http://link.springer.com/10.1023/A:1013874816509 (visited on 12/22/2023).

Wild, M., A. Ohmura, C. Schär, G. Müller, D. Folini, M. Schwarz, M. Z. Hakuba, and A. Sanchez-Lorenzo (2017). *The Global Energy Balance Archive (GEBA) Version 2017: A Database for Worldwide Measured Surface Energy Fluxes*. preprint. Atmosphere – Atmospheric Chemistry and Physics. DOI: 10.5194/essd-2017-28. URL: https://essd.copernicus.org/preprints/essd-2017-28/essd-2017-28.pdf (visited on 12/31/2023).

Wilzewski, J. S., A. Roiger, J. Strandgren, J. Landgraf, D. G. Feist, V. A. Velazco, N. M. Deutscher, I. Morino, H. Ohyama, Y. Té, R. Kivi, T. Warneke, J. Notholt, M. Dubey, R. Sussmann, M. Rettinger, F. Hase, K. Shiomi, and A. Butz (2020). "Spectral Sizing of a Coarse-Spectral- Resolution Satellite Sensor for XCO2". *Atmospheric Measurement Techniques*. ISSN: 1867-8548. DOI: 10.5194/amt-13-731-2020. URL: https://amt.copernicus.org/articles/13/731/2020/ (visited on 10/18/2023).

Woitischek, J., M. Edmonds, and A. W. Woods (2021a). "On the Fluctuations in Volcanic Plumes". *Geophysical Research Letters*. ISSN: 0094-8276, 1944-8007. DOI: 10.1029/2020GL090594. URL: https://agupubs.onlinelibrary.wiley.com/doi/10.1029/2020GL090594.

Woitischek, J., N. Mingotti, M. Edmonds, and A. W. Woods (2021b). "On the Use of Plume Models to Estimate the Flux in Volcanic Gas Plumes". *Nature Communications*. ISSN: 2041-1723. DOI: 10.1038/s41467-021-22159-3. URL: http://www.nature.com/articles/s41467-021-22159-3.

Wunch, D., G. C. Toon, J.-F. L. Blavier, R. A. Washenfelder, J. Notholt, B. J. Connor, D. W. T. Griffith, V. Sherlock, and P. O. Wennberg (2011). "The Total Carbon Column Observing Network". *Philosophical Transactions of the Royal Society A: Mathematical, Physical and Engineering Sciences*. ISSN: 1364-503X, 1471-2962. DOI: 10.1098/rsta.2010.0240. URL: https://royalsocietypublishing.org/doi/10.1098/rsta.2010.0240 (visited on 12/17/2019).

Yu, J., B. Hmiel, D. R. Lyon, J. Warren, D. H. Cusworth, R. M. Duren, Y. Chen, E. C. Murphy, and A. R. Brandt (2022). "Methane Emissions from Natural Gas Gathering Pipelines in the Permian Basin". *Environmental Science & Technology Letters*. ISSN: 2328-8930, 2328-8930. DOI: 10.1021/acs.estlett.2c00380. URL: https://pubs.acs.org/doi/10.1021/acs.estlett.2c00380 (visited on 10/27/2023).

Zeng, Y. and J. Morris (2019). "Detection Limits of Optical Gas Imagers as a Function of Temperature Differential and Distance". *Journal of the Air & Waste Management Association*. ISSN: 1096-2247, 2162-2906. DOI: 10.1080/10962247.2018.1540366. URL: https://www.tandfonline.com/doi/full/10.1080/10962247.2018.1540366 (visited on 01/31/2023).

Zhang, J., G. Han, H. Mao, Z. Pei, X. Ma, W. Jia, and W. Gong (2022). "The Spatial and Temporal Distribution Patterns of XCH4 in China: New Observations from TROPOMI". *Atmosphere*. ISSN: 2073-4433. DOI: 10.3390/atmos13020177. URL: https://www.mdpi.com/2073-4433/13/2/177 (visited on 06/22/2023).

Zhang, Y., D. J. Jacob, X. Lu, J. D. Maasakkers, T. R. Scarpelli, J.-X. Sheng, L. Shen, Z. Qu, M. P. Sulprizio, J. Chang, A. A. Bloom, S. Ma, J. Worden, R. J. Parker, and H. Boesch (2021). "At-

tribution of the Accelerating Increase in Atmospheric Methane during 2010–2018 by Inverse Analysis of GOSAT Observations". *Atmospheric Chemistry and Physics*. DOI: 10.5194/acp-21-3643-2021. URL: https://acp.copernicus.org/articles/21/3643/2021/ (visited on 01/02/2024).

Zheng, T., R. Nassar, and M. Baxter (2019). "Estimating Power Plant CO_2 Emission Using OCO-2 XCO_2 and High Resolution WRF-Chem Simulations". *Environmental Research Letters*. ISSN: 1748-9326. DOI: 10.1088/1748-9326/ab25ae. URL: https://iopscience.iop.org/article/10.1088/1748-9326/ab25ae (visited on 11/23/2023).

Zimmerle, D., T. Vaughn, C. Bell, K. Bennett, P. Deshmukh, and E. Thoma (2020). "Detection Limits of Optical Gas Imaging for Natural Gas Leak Detection in Realistic Controlled Conditions". *Environmental Science & Technology*. ISSN: 0013-936X, 1520-5851. DOI: 10.1021/acs.est.0c01285. URL: https://pubs.acs.org/doi/10.1021/acs.est.0c01285 (visited on 01/31/2023).

Acknowledgements

This thesis would not have been possible without the help, ideas, and support of many resourceful people who accompanied and guided me along the journey. Here, I want to acknowledge their contributions, and many thanks go to:

Prof. Dr. André Butz for supervising this thesis and always taking the time to discuss my work. For guiding my ideas as I investigated the potential of the camera while giving me the necessary creative space. For providing a supportive and respectful environment to work and study.

Dr. Sanam Vardag for freely sharing insights and advice in all scientific and academia-related regards. For supporting my research with an ever-lasting optimism and enthusiasm that is just catching.

Ralph Kleinschek for advising me on all matters concerning the instrument and the laboratory. For providing useful and practical ideas, saving me a lot of trouble and time when I couldn't see the wood for the trees.

My office mates, Benedikt Löw, Lukas Pilz, and Dr. Tobias Schmitt for their willingness to delve into any physics- or IT-related problem. Sharing a workspace led to fruitful discussions about physics, proper coding techniques, and engaging conversations about politics and life in general. They made going to work (almost) every day easy and enjoyable.

Leonie Scheidweiler, Felix Külheim, and Helge Haveresch for their support during the Poland field campaigns. For relentless motivation to observe spectra, even when I was grounded after catching COVID. For fun evenings at the Pustelnik with duck, dumplings, and Tyskie.

Moritz Sindram and Tim Siegel for their work on the HySpex field instrumentation and retrieval algorithm.

Dr. Harikrish Charuvil, Valentin Hanft, Helge Haveresch, Ralph Kleinschek, Dr. Benedikt Herkommer, Robert Maiwald, Eva Metz, Lukas Pilz, Thomas Plewa, Lennart Resch, Dr. Tobias Schmitt, Leonie Scheidweiler, Moritz Sindram, and Dr. Sanam Vardag for reading the manuscript of this thesis and providing truly helpful feedback.

Angelika Gassama, Rebekka Benetatos, and Karolin Thomas for keeping the institute running and patiently answering my questions concerning travel forms, order forms, vacation forms, and many more forms.

Ralph Pfeifer and the IUP's workshop for always finding a solution to technical challenges in short time.

Dr. Jarosław Nęcki, Paweł Jagoda, and Dr. Justyna Swolkień for their support during the Poland field campaigns. Without their knowledge, contacts, and enthusiasm the whole endeavor would have been impossible.

Dr. Robert Field from UNEP's IMEO program for coordinating 2023's field campaign and his engagement that allowed me to show some preliminary data.

Bruno Burger from the Fraunhofer Institute for Solar Energy Systems for providing energy production rates of the GKM.

Roland Krupp, representing the GKM, for providing invaluable data for validating the presented methods.

Bernhard Vogel and Frank Wagner for their effort in establishing and maintaining AERONET site in Karlsruhe, Germany, and Aleksander Pietruczuk and Michal Posyniak for their effort in establishing and maintaining AERONET site in Raciborz, Poland.

Philine, for supporting me in every way imaginable. For long discussions on physics, philosophy, and politics. For motivating me to go on and give it my best, always leading by example.

Tina W. for making Heidelberg my home, loaded with wonderful memories. For countless games of Commander, over 1000 rounds of Billiards, and exploring fantastic planes as the Pentakauppias. For renting a palace and staying up until the sun rises. For traveling the world and for jumping down cliffs.

My sister, Caroline, for her enthusiastic and joyful view on life, that is so refreshing and inspiring to me.

My parents, Annette and Harald, for none of this would have been possible without their unconditional support and constant encouragement throughout my life.

Marvin Knapp Heidelberg, March 2024